Synthesis of Siliceous Materials Using Vortex Fluidic Devices (VFDs)

by

Chee Ling Tong

Dissertation Submitted to the

Faculty of Science & Engineering of Flinders University in Candidacy for the

Degree of Doctor of Philosophy in Chemistry

School of Chemical and Physical Sciences

Flinders University

February 2015

Table of Contents

Abstract

Santa Barbara Amorphous, SBA-15, has a hexagonally ordered array of mesoporous silica, discovered at the University of California Santa Barbara in 1988. SBA-15 exhibits high surface area, large and controllable pore sizes, and better hydrothermal stability over Mobil Crystalline Materials, MCM-41. In consequence SBA-15 has attracted much attention for developing the materials for a variety of applications such as separation, catalysis, drug delivery, adsorption, and biosensors.

Over the decades, research on SBA-15, has focused either on improving the synthesis methods or to use it as a support in different applications. However, the synthesis has not diverted much from the original hydrothermal process, which is a very successful and mature process. This is despite the process is lengthy and is highly temperature dependent, which represent some disadvantages.

This dissertation focuses on the formation of SBA-15 using a novel vortex fluidic device (VFD) without the need for hydrothermal treatment, under room temperature and atmospheric pressure. The vortex fluidic device enables the synthesis to be performed in a continuous mode, at ambient conditions, and reduces the processing time by at least half relative to the conventional method. Moreover, by fine-tuning the processing controls such as rotational speed, there is the ability to control the pore size of the periodic mesostructure which is without precedent.

In situ incorporation of palladium oxide (PdO) within the pore channels of SBA-15 was successfully achieved using the VFD. The resulting material served as a heterogeneous catalyst and was tested for its catalytic performance in Suzuki cross-coupling reactions. In addition, this VFD processing can be set up to operate under a hydrogen gas environment which results in spontaneous reduction of metal oxides to metal. This allowed a one-pot synthesis of Pd(0)/SBA-15 material, which is effective in the removal of 41% of the initial nitrate-nitrogen ions [NO_3-N] from aqueous media with good recyclability, yielding 36% removal efficiency after being recycled.

The research was extended further in preparing silica hydrogel using the VFD, effectively creating a new paradigm in sol-gel technology. A benign aqueous synthesis of silica hydrogel can be achieved under continuous processing, without the need for a solvent or the addition of an acid or base, and under ambient conditions. The simplicity of this process greatly enhances the applicability of the use of silica as a drug delivery vehicle, in minimising the use of chemicals involved throughout the process. This was established for the in situ incorporation of curcumin within the silica network, which greatly enhanced its bioavailability, improving the bacterial growth inhibition of gram-positive bacterium *Staphylococcus aureus*.

Overall the work has established a breakthrough in process enhancement in making functional siliceous materials. It defies the orthodox process and the ability to make silica under more benign processing conditions, presumably involving less energy input, while significantly reducing the processing time and the generation of waste. The work establishes the ability of VFD processing in improving the green chemistry metrics of silica manufacturing in general.

Overview

In this dissertation, discussion is mainly focused on the synthesis of siliceous materials, as Santa Barbara Amorphous (SBA-15) and silica xerogel, using a vortex fluidic device (VFD), along with applications of the materials. Sol-gel chemistry is the backbone of all the aforementioned syntheses. The fundamentals of the reaction kinetics have been studied for decades by many researchers, from the chemistry point of view. The studies reported herein establish a new paradigm in making siliceous materials in a greener and more cost effective approach, by applying external shear force during the synthesis. The focus is on process enhancement by studying the micromixing effect at the molecular level. Using VFD processing avoids hydrothermal treatment, the use of co-solvents, and refluxing associated with conventional processing. The synthesis time is drastically reduced, with the cost of the material with more tunable properties destined to be significantly reduced.

Chapter 1 provides a succinct history and development of ordered mesoporous silica, SBA-15 and silica xerogel chronologically.

Chapter 2 provides the introduction to the new-patented vortex fluidic device (VFD). It reviews many successful applications in different fields and discusses the technicality involved in this device, which is unique to the synthesis of siliceous materials. In addition, various analytical techniques applied in this project are elaborated.

Chapter 3 reports a feasibility study of preparing ordered mesoporous silica, SBA-15 using a vortex fluidic device (VFD). The chapter includes the method of synthesis, characterization data, and results and discussion.

Chapter 4 presents the synthesis of heterogeneous catalyst with *in situ* incorporation of palladium nanoparticles into the pore channel of SBA-15, the performance of the heterogeneous catalyst being tested in the Suzuki Miyaura cross-coupling reaction. The catalytic activity is compared against a commercial catalyst.

Chapter 5 presents the versatility of the VFD, in incorporating palladium nanoparticles into the pores of SBA-15 during the synthesis, with hydrogen gas used to purge the system simultaneously to reduce the palladium nanoparticles to metal. A zero-valent Pd/SBA-15 was synthesized within 5 hours, with the material effective for nitrate removal from waste water.

Chapter 6 reports a successful incorporation of magnetic nanoparticles within the network of mesocellular siliceous foams (MCFs) using hexane as a swelling agent. The pore diameter is enlarged to 28 nm and renders the materials as an effective adsorbent for phosphate removal.

Chapter 7 presents a benign aqueous synthesis of silica hydrogel without using co-solvent or acid/ base catalyst. The synthesis involves only a silica precursor, namely tetramethyl orthosilicate (TMOS) and water, within the vortex fluidic device (VFD), with the silica hydrogel formed in just 3.5 hours. Curcumin nanoparticles were embedded within the silica network using this method, in improving its bioavailability of the compound, as shown in the growth inhibition test of gram-positive bacteria.

Chapter 8 presents the synthesis of a donut-like SBA-15 material using a VFD, which forms only at a specific set of operating parameters. It establishes that the shear in the VFD can be adjusted in controlling the morphology of SBA-15, without the need for the addition of surfactants, co-solvents or inorganic salts.

Chapter 9 introduces the concept of utilizing the tube in the VFD itself as a catalyst support in organic synthesis. A thin silica coating was formed in a 20 mm OD NMR tube, with the hydroxyl group functionalized with thiol moieties for binding palladium. Dehydration reactions of boronic acid were effective under ambient conditions without the need of a purification process, as there is minimal leaching of the palladium catalyst into the product.

Chapter 10 provides a treatise of the results and significance of the research, along with some insight into future directions, particularly with respect to potential applications.

Declaration

I certify that this thesis does not incorporate without acknowledgment any material previously submitted for a degree or diploma in any university; and that to the best of my knowledge and belief it does not contain any material previously published or written by another person except where due reference is made in the text.

This thesis contains published work and/ or work prepared for publication, some of which has been co-authored. The details of the work and where it appears in the thesis are outlined below.

Chapter 3 – **Tong, C. L.**, Raston, Colin L., Boulos, R. A., Yu, Chengzhong, & Iyer, K.S., **2013**, "Continuous flow tuning of ordered mesoporous silica under ambient conditions", *RSC Advances*, (3), pp. 18767-18770.
Author Contributions: CLT and CLR designed the research, CLT undertook all of the research, RB undertook chemical modelling, CLT, CLR, RB, CY, and IKS finalised the manuscript. (Overall contribution by CLT: 90%)

Chapter 5 – **Tong, C.L.**, Eroglu, E., Raston, C.L., Duan, X., Lamb, R.N., Jarrett, K., & Buckley, C.E., **2015**, "Nitrate uptake using mesoporous silica embedded with zero-valent palladium nanoparticles", *submitted*
Author Contributions: CLT and CLR designed the research, CLT and EE undertook all of the research, CLT, EE, CLR, XD, RNL, KJ, and BEC finalised the manuscript. (Overall contribution by CLT: 85%)

Chapter 6 – **Tong, C.L.**, Eroglu, E., & Raston, C.L., **2014**, "In situ synthesis of phosphate binding mesocellular siliceous foams impregnated with iron oxide nanoparticles", *RSC Advances*, vol. 4(87), pp. 46718-46722.
Author Contributions: CLT and CLR designed the research, CLT and EE undertook all of the research, CLT, EE, and CLR finalised the manuscript. (Overall contribution by CLT: 85%)

Chapter 7 – **Tong, C.L.**, Stroeher, U.H., Brown, M.H., & Raston, C.L., **2015**, "Continuous flow vortex fluidic synthesis of silica xerogel as a delivery vehicle for curcumin", *RSC Advances*, (5), pp. 7953-7958.
Author Contributions: CLT and CLR designed the research, CLT and UHS undertook all of the research, CLT, UHS, MHB, and CLR finalised the manuscript. (Overall contribution by CLT: 85%)

____

Chee Ling Tong

Date: ____________________

Acknowledgement

It is a very exciting moment when comes to writing up this part of my dissertation. To me, it is a symbolic moment that my PhD journey has coming to an end and I am all ready to begin a whole new chapter of my life. I would like to take this opportunity to acknowledge and express my sincere gratitude to all of those who helped and supported me physically or mentally, towards the completion of my research throughout the years.

My PhD journey was not easy and smooth, rather rocky journey indeed. It all started with my commencement under the degree of Doctor of Philosophy in Chemical Engineering but after 1.5 years into my research, I have to quit the research due to unforseen issues. I was petrified and completely lost at time. Within weeks, I had to look for a new supervisor, propose a new research project and start new research from scratch. I am an atheist, but I now believed in the saying "when God shuts a door, he opens a window". I am truly blessed to meet Prof. Colin L. Raston, else, I would not have come to this far. I owe my deepest gratitude to my supervisor, Prof. Colin L. Raston. From the time he agrees to take me as his student and throughout my three years PhD journey, he has endlessly provides invaluable guidance and support. I truly appreciated the confidence he has in me; also his willingness to altruistically shares his entire intellectual and life experiences, which inspired me very much. There are no words that could fully express my deepest respect and gratitude to Prof. Colin L. Raston, THANK YOU!

I am also indebted to Prof. Chengzhong Yu (Michael) at The University of Queensland. Being an expert in mesoporous silica, he has generously shared his expertise and guided me in compiling my works and published my first paper. Special thanks for Dr. Ela Eroglu. She is one of the most enthusiastic researcher that I ever worked with. I am truly lucky to know her and to collaborate with her. She is always very keen in giving respond/feedback (receiving her feedback within the same day at 3 am), very supportive and always offering help. She is a mentor but also close friend; very best wishes to Ela and thanks for everything you have done for me, truly appreciated.

My research would not be successful without the generous help and support from all collaborators, particularly Dr. Xiaofei Duan and Prof. Robert N. Lamb for all the help and training in XPS anaylsis; Dr. Kevin Jarrett and Prof. Craig E. Buckley in SAXS analysis;

Dr. Uwe H. Stroeher and Prof. Mellisa H. Brown for antimicrobial studies. Last but not least, I have to thanks all my colleagues at Raston research group especially Dr. Ramiz Boulos, for being great support at all time.

I would like to acknowledge my funding sources, which allowed me to solely focus on my research without financial pressure. I was awarded the Australia Postgraduate Awards (APA) under Research Higher Degrees (RHD) scheme, which provided a stipend and full tuition waiver for my 3.5 years candidature. Also, special thanks to the South Australia government funding in supporting my candidature extension from the time I relocated from The University of Western Australia to Flinders University.

It requires lot of perseverance to have come this far and fortunately I have my best buddies, Wooi Sin and Chien Yee that are always by my side, your mental support is priceless. Thank you for listening to me, cheering me up when I am down, and being happy for each other for good news. Special thanks to Dr. Shanti In for believing in me, I can never imagine myself doing PhD but you lead the way and you are always my role model.

Lastly and most importantly, my deepest gratitude goes to my family. To Mom and Dad, you have raised me with unconditioned love and supports. As Chinese proverb says “give a man a fish and you feed him for a day; teach a man to fish and you feed him for a lifetime”. You have given me the best wealth in life- knowledge. I am proud to say I have the greatest parents and I love you both so much. To my sis, I Ling, my apology for the selfishness and petulant decision in pursuing my dream overseas, leaving you with family responsibilities. Yet, you have been so considerate, forgiving and supportive. Thanks for always being with me. To my lovely nieces, Annabelle and Evangeline, you are my angels and your lovely smiles cheer me up always through the hardship. I am blessed to have a caring and wonderful family, a main driving force for me to face all challenges without fear.

I may have missed out some names, once again, thank you everyone. I truly appreciated the opportunity to experience this enriching PhD journey.

Chee Ling Tong
Flinders University
February 2015

List of Publications

Refereed Journal Articles

1. ***Chee Ling Tong,*** Ela Eroglu, Xiaofei Duan, Robert N. Lamb, Kevin Jarrett, Craig E. Buckley, and Colin L. Raston. Nitrate uptake using mesoporous silica embedded with zero-valent palladium nanoparticles. *RSC Advances,* submitted December 2014.

2. ***Chee Ling Tong,*** Uwe H. Stroeher, Melissa H. Brown, and Colin L. Raston. Continuous flow vortex fluidic synthesis of silica xerogel as a delivery vehicle for curcumin. *RSC Advances*, **2015**, (5), pp. 7953-7958

3. ***Chee Ling Tong,*** Ela Eroglu, and Colin L. Raston. In situ synthesis of phosphate binding mesocellular siliceous foams impregnated with iron oxide nanoparticles. *RSC Advances*, **2014**, vol. 4(87), pp. 46718-46722.

4. ***Chee Ling Tong,*** Ramiz A. Boulos, Chengzhong Yu, Swaminathan K. Iyer, and Colin L. Raston. Continuous flow tuning of ordered mesoporous silica under ambient conditions. *RSC Advances*, **2013**, (3), pp. 18767-18770.

Conference Proceedings

1. ***Chee Ling Tong***, Colin L. Raston. Vortex Fluidic Device (VFD): A new platform for the benign aqueous synthesis of silica. *Proceedings of the Royal Australian Chemical Institute National Congress (RACI 2014), Adelaide, Australia,* 7 – 12 December 2014.

2. ***Chee Ling Tong,*** Uwe H. Stroeher, Melissa H. Brown, and Colin L. Raston. Continuous flow vortex fluidic synthesis of silica xerogel as delivery vehicle for curcumin. *Proceedings of the 4th Flinders Centre for Nanoscale Science and Technology (FCNST) Annual Conference*, *Adelaide, Australia,* 18 June 2014.

3. ***Chee Ling Tong***, Ramiz A. Boulos, Chengzhong Yu, Swaminathan K. Iyer, Colin L. Raston. Synthesis of ordered mesoporous silica (OMS) using a vortex fluidic device (VFD): Controlling the core structure and shape, and shortening the processing time. *Proceedings of the Material Research Society Spring Meeting & Exhibit (MRS 2014), San Francisco, United States,* 21 – 25 April 2014.

4. ***Chee Ling Tong***, Rebecca E. Norman, Craig L. Francis, Michael V. Perkins, Chengzhong Yu, Colin L. Raston. One-pot synthesis of Pd/SBA-15 using a vortex fluidic device (VFD) at neutral pH under ambient conditions. *Proceedings of the International Conference on Nanoscience and Nanotechnology (ICONN 2014)*, *Adelaide, Australia,* 2 – 6 February 2014.

5. ***Chee Ling Tong***, Colin L. Raston. Vortex Fluidic Device: A new platform for ordered mesoporous silica and silica nanoparticles synthesis. *Proceedings of the International Workshop and School on Nanotechnology (NanoS-E3 2013)*, *Airlie Beach, Australia,* 15 – 20 September 2013.

6. ***Chee Ling Tong***, Ramiz A. Boulos, Chengzhong Yu, Swaminathan K. Iyer, Colin L. Raston. Continuous Flow Tuning of Ordered Mesoporous Silica Under Ambient Conditions. *Proceedings of the 3rd Flinders Centre for Nanoscale Science and Technology (FCNST) Annual Conference*, *Adelaide, Australia,* 19 June 2013.

7. ***Chee Ling Tong***, Iyer K. Swaminathan, Colin. L. Raston. Process Intensification Synthesis of Mesoporous SBA-15 at Room Temperature. *Proceedings of the International Conference on Nanoscience and Nanotechnology (ICONN 2012)*, *Perth, Australia,* 5 – 9 February 2012.

List of Figures

List of Tables

List of Acronyms

APTES	(Aminopropyl)triethoxysilane
APTMS	3-(aminopropyl)trimethoxysilane
ATR-FTIR	Attenuated total reflectance- Fourier transform infra-red
BDBA	Benzene-1,4-diboronic acid
BET	Braunauer–Emmett–Teller
CCDC	The Cambridge Crystallographic Data Centre
CNOs	Carbon nano onions
CNTs	Carbon nanotubes
DDSs	Drug-delivery systems
DET	Direct electron transfer
DLS	Dynamic light scattering
DSC	Differential scanning calorimetry
DTA	Differential thermal analysis
EDAX	Energy-dispersive x-ray spectroscopy
EDCs	Endocrine disrupting compounds
EELS	Electron energy-loss spectroscopy
EO	Ethylene oxide
HPLC	High performance liquid chromatography
ICP-AES	Inductively coupled plasma atomic emission spectroscopy
ICP-MS	Inductively coupled plasma mass spectrometry
IEP	Isoelectric point
IUPAC	International Union of Pure and Applied Chemistry
JCPDS	Joint Committee on Powder Diffraction Standards
ICDD	International Center for Diffraction Data
MCFs	Mesocellular foams
MCM-41	Mobil Crystalline Materials
MPTMS	3-mercaptopropyltrimethoxysilane
Na_2SiO_3	Sodium silicate
NPs	Nanoparticles
$PhB(OH)_2$	Phenylboronic acid

Pluronic® P-123	Poly(ethylene glycol)-poly(propylene glycol)-poly(ethylene glycol)
PO	Propylene oxide
rpm	Revolutions per minute
RTP	Rotating tube processor
SAED	Selected area electron diffraction
SBA-15	Santa Barbara Amorphous
S_{BET}	Specific surface area
$ScCO_2$	Supercritical carbon dioxide
SEM	Scanning electron microscopy
SPD	Spinning disc processor
SWCNTs	Single walled carbon nanotubes
TBOS	Tetrabutyl orthosilicate
TEM	Transmission electron microscopy
TEOS	Tetraethyl orthosilicate
TGA	Thermogravimetric analysis
TMB	1,3,5-trimethylbenzene
TMOS	Tetramethyl orthosilicate
TNT	2,4,6-trinitrotoluene
VFD	Vortex fluidic device
XPS	X-ray photoelectron spectroscopy
XRD	X-ray diffraction

Chapter One

Introduction

1.1. Chemistry of porous silica

The synthesis of siliceous materials has been widely practiced for decades using solution-gelation ("sol-gel") technology. Such sol-gel reactions involve the hydrolysis of alkoxysilanes, followed by room temperature condensation, which is summarized in equations (1.1 – 1.3).[1, 2]

Hydrolysis:

$$Si(OR)_4 + H_2O \rightarrow Si(OH)_4 + 4ROH \qquad (1.1)$$

Alcohol condensation:

$$Si(OR)_4 + Si(OH)_4 \rightarrow (Si-O-Si)_n + 4ROH \qquad (1.2)$$

Water condensation:

$$Si(OH)_4 + Si(OH)_4 \rightarrow (Si-O-Si)_n + 4H_2O \qquad (1.3)$$

Typically the hydrolysis and condensation takes place at the same time and thus, the rate of polymerization can be complicated.[3] The pH plays an important role in determining whether the rate of hydrolysis or condensation is governing the reaction, which would result in the formation of different morphologies of the porous silica. Acid catalysts promote the rate of hydrolysis but hinders the condensation; in contrast, base catalysts promote the rate of condensation, which consequently determines the size and shape of the silica particles.[4, 5] All factors that influence the chemistry of sol-gel synthesis will be discussed in the following sections.

According to International Union of Pure and Applied Chemistry (IUPAC), siliceous material can be classified into three categories, based on pore sizes. In general, macroporous materials have pore diameter > 50 nm, mesoporous materials have pore diameter in the range from 2 to 50 nm, and microporous materials have pore diameter < 2 nm (Figure 1.1).[6] Nitrogen adsorption-desorption analysis is commonly used to determine the porosity of the materials.

This dissertation focuses on the synthesis of two categories of mesoporous silica, in particular ordered mesoporous silica, Santa Barbara Amorphous (SBA-15), as well as its applications, as the main focus, and silica alcogel/hydrogel.

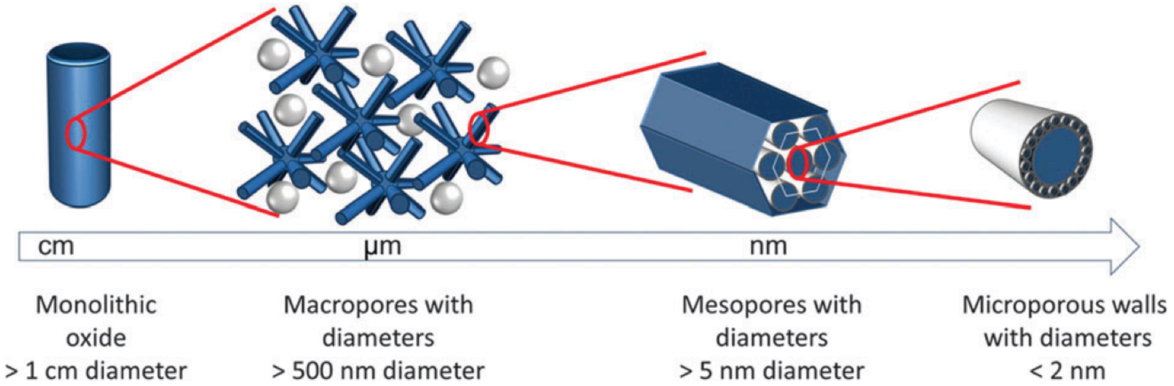

Figure 1.1. *Schematic representation of a silica monolith exhibiting two or more separated pore size regimes; in this case macropores and periodically arranged mesopores are depicted. Taken from the review article "Chemical phase separation strategies towards silica monoliths with hierarchical porosity".[6]*

1.2. Type of mesoporous silica

1.2.1. Ordered mesoporous silica, SBA-15

Mesoporous silica was discovered and patented in 1970. However, it did not get much attention until 1990s when Mobil Corporation produced mesoporous nanoparticles (NPs), which were named as Mobil Crystalline Materials (MCM-41).[7] MCM-41 is a periodic mesoporous silica material which has attracted considerable attention because of its remarkable features, consisting of a well-ordered, hexagonal array of parallel pore channels with diameters varying within the range 1.5 to 10 nm, depending on the length of the alkyl chain of the templating surfactants used in the synthesis, pore walls thickness of 1 to 2 nm, and high surface areas typically >1000 m^2/g.[8-11]

In 1988, Zhao and co-workers discovered Santa Barbara Amorphous (SBA-15), a hexagonal array mesoporous silica synthesized using a non-ionic copolymer template.[12] Similar to MCM-41, SBA-15 has well-ordered structures, high surface area, but much larger and controllable pore sizes, from 5 nm to 30 nm in diameter, and thicker pore wall, ranging from 3.1 to 6.4 nm.[12] The materials have better hydrothermal stability over MCM-41 due to the thicker pore walls. Thus, they are well suited as supports for number of applications such as catalysis, adsorption, separation, biosensing, drug delivery, chromatography, and gas storage.[13-16] A review article has pointed that there are 1007 papers related to SBA-15 published in 2013 alone (Figure 1.2), which can be considered a leading topic of interest in chemical and material sciences research.[17]

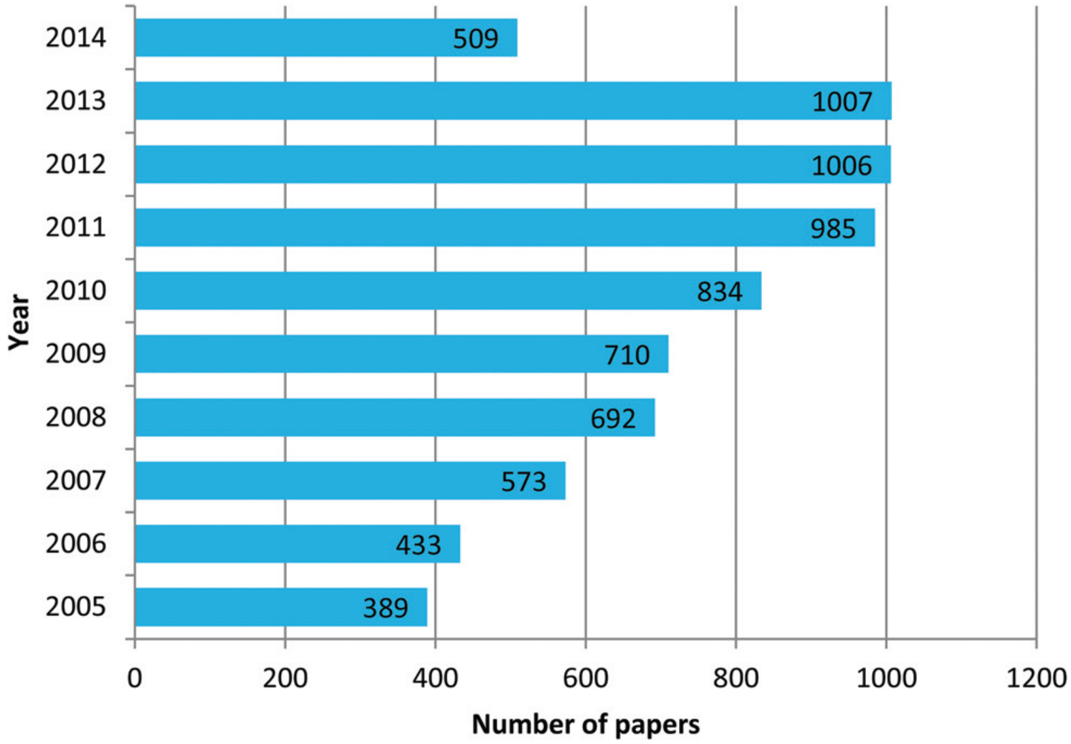

Figure 1.2. *Bar graph of number of SBA-15 related papers published from year 2005 to mid 2014. Taken from review article "Incredible pace of research on mesoporous silica nanoparticle".[17]*

Typical synthesis of SBA-15 uses a non-ionic triblock copolymers, poly(ethylene glycol)-poly(propylene glycol)-poly(eyhtlene glycol), which is commercially known as Pluronic® P123, as the structure-directing agent, with tetraethyl orthosilicate (TEOS) as the silica precursor. Syntheses are carried out under acidic conditions at reaction temperatures in the range 35 ºC to 110 ºC, with aging required under autogenous pressure in an autoclave from 1 to 3 days.[12, 18-20]

1.2.2. Non-ordered silica alcogel

Sol–gel synthesis has been widely studied over the decades, for gaining access to silica. Typically, the sol–gel synthesis of silica involves the use of TEOS or tetramethyl orthosilicate (TMOS) as the silica precursor, a co-solvent such as ethanol or methanol, an acid or base catalyst and water in a closed system.[21] Silica gel can be in a form of monolith, paste, granules, powder, or even thin film. The gelation is defined as the clustering and linking of the nucleated particles forming a three-dimensional network. The phase transformation from sol-to-gel can be observed via a change in viscosity. Gelation point of the continuous structural evolution of the sol-gel materials can be determined using dynamic and steady shear flow measurements.[22] There are substantial studies on the process of formation of silica gel, which depend on the nature of catalyst, the choice of solvents, and temperature of the processing. The synthesis of silica and silica monoliths and glasses, which encompass the materials featuring herein, has a number of contemporary issues to be addressed, including (1) reduction in the processing time, (2) avoiding fracturing during the drying process, and (3) reduction of the reagents used and the generation of any waste stream, and (4) exploring new methods to functional glasses.[23] They feature in the body of research in this thesis.

1.3. Research evolution of SBA-15

1.3.1. Physicochemical properties and stabilities studies of SBA-15

The discovery of SBA-15 in 1988 attracted a lot of attention from researchers. Over the years, hundreds of publications relating to SBA-15 have appeared. Initially, Zhao and co-workers established that the choice of structure directing agent in terms of chain architecture and the reaction temperature are able to control the physicochemical properties of SBA-15.[12] From Table 1.1 it is evident that using the same type of structure directing agent, higher aging temperature increases the pore diameter, however, pore wall thickness decreases at the same time, affecting the stability of the materials. In addition, the EO:PO ratio greatly influences the architectures of SBA-15, where lower EO:PO ratio favoured the *p6mm* hexagonal morphology and higher EO:PO ratio favoured the formation of cubic mesoporous silica.[12, 24]

Table 1.1. Physicochemical properties of hexagonal SBA-15 at different reaction temperatures. Taken from Zhao *et al.*[12]

Block copolymer	Reaction Temperature	BET surface area (m^2/g)	Pore size (Å)	Pore volume (cm^3/g)	Wall thickness (Å)
$EO_5PO_{70}EO_5$	35	630	100	1.04	35
$EO_{20}PO_{70}EO_{20}$	35	690	47	0.56	64
$EO_{20}PO_{70}EO_{20}$	35, 80*	820	77	1.03	38
$EO_{20}PO_{70}EO_{20}$	35, 90*	920	85	1.23	36
$EO_{20}PO_{70}EO_{20}$	35, 100*	850	89	1.17	31
$EO_{17}PO_{55}EO_{17}$	40	770	46	0.70	47
$EO_{20}PO_{30}EO_{20}$	60	1000	51	1.26	39
$EO_{26}PO_{39}EO_{26}$	40	960	60	1.08	42
$EO_{13}PO_{70}EO_{13}$	60	950	59	1.19	34
$EO_{19}PO_{33}EO_{19}$	60	1040	48	1.15	34

* Reaction at 35 ˚C for 20 hours, then heating to the higher temperature for 24 hours, or for the second entry for 80 ˚C, 48 hours.

In 2000, reports revealed that the primary mesopores of SBA-15 can be tailored by carefully controlling the synthesis and aging temperature, albeit with a significant amount of disordered micropores and small mesopores (Table 1.2). Studies using nitrogen and argon adsorption showed that the large mesopores in SBA-15 are accompanied by significantly smaller pores, which are about 3.4 nm, providing the connectivity between order channels.[18, 25]

Table 1.2. Structural parameters of the SBA-15*. Taken from Kruk *et al.*[18]

Sample/ (aging time, Temperature)	a (nm)	S_{BET} (m^2/g)	V_t (m^3/g)	V_p (m^3/g)	V_{mi} (m^3/g)	S_{ex} (m^2/g)
S0 (no aging)	8.3	520	0.44	0.33	0.08	20
S1 (1 day, 80 ˚C)	9.7	780	0.81	0.62	0.12	40
S2 (2 days, 80 ˚C)	10.4	870	0.96	0.75	0.12	60
S3 (1 day, 90 ˚C)	10.2	850	1.02	0.84	0.08	60
S4 (2 days, 100 ˚C)	10.6	850	1.08	0.92	0.06	70

*a, XRD unit-cell parameter; S_{BET}, BET specific surface area; V_t, total pore volume; V_p, primary mesopore volume; V_{mi}, micropore volume; S_{ex}, external surface area.

Since SBA-15 can be used in wide range of applications such as catalysis, adsorption, and separation with the thermal, hydrothermal, and mechanical stabilities of SBA-15 an important consideration. As thermal stability is strongly related the pore wall thickness of the mesostructure framework, SBA-15 is known to exhibit thicker pore walls relative to MCM-41 which is an advantage.[26] Similarly, SBA-15 has a better hydrothermal stability over MCM-41, which is influenced by both the pore wall thickness and degree of polymerization,[26] which is defined by the ratio of Q_4 [$Si(OSi)_4$] to Q_3 [$Si(OSi)_3(OH)$] band of the solid-state ^{29}Si nuclear magnetic resonance (NMR) spectra under magic-angle spinning (MAS) conditions.[27] However, there are two distinctive claims presented by two groups of researchers in regard to the mechanical stability of SBA-15. Cassiers and co-workers claimed that SBA-15 showed only a 10% decrease in surface area, a 15% decrease in mesopore volume, and a 4% decrease in pore diameter, after compression at 296 MPa. It is rationalized that the influence of the compression is minimal due to the thicker pore walls and highly polymerized walls, with a high portion of Q_4 [$Si(OSi)_4$] band presence in the sample, determined by solid-state NMR.[26, 27] Martin and co-workers also observed the similar trend where increasing the compression pressure leads to a decrease in surface area and pore volume. Nonetheless, since SBA-15 contains secondary mico- and/ or mesopore regimes,[25, 28] the pore diameter is largely underestimated.[29] Thus, Martin and co-workers have proposed that the ratio of wall thickness and pore diameter would be a better measure of mechanical stability of SBA-15. Under this proposal, SBA-15 possess a rather low mechanical stability compared to MCM-41, which is due to the unfavourable ratio between pore wall thickness and pore diameter, which influences by the presence of micropores.[29]

According to the findings, the existence of micropores in SBA-15 influences the estimation of pore diameter, and an extensive evaluation of SBA-15 porosity was subsequently undertaken, with a conclusion that the increase in the synthesis temperature would lead to an increase in mesopore size and a decrease in microporous volume[30] and thus, SBA-15 without micropores can be synthesized at 130 ˚C.[19] The synthesis at higher temperature produces SBA-15 with larger pores without the presence of micropore, and thus the mechanical stability of SBA-15 can be improved. Che and co-workers also confirmed that the hydrothermal treatment at 130 ˚C further played an important role in self-repairing processes of the defect regions, allowing the occurrence of recrystallization of the mesostructure, which promotes the mesoregularity of the materials.[11]

1.3.2. Factors affecting the synthesis of SBA-15

The synthesis of SBA-15 involves (1) lengthy processing times, up to 3 days, and (2) multiple-steps, which includes hydrothermal treatment, the synthesis being pH and temperature dependent. All these issues are challenging, in controlling the mesostructure and improving the overall stabilities (thermal, hydrothermal, and mechanical) of SBA-15.

Temperature

As previously discussed, higher temperature during the synthesis can increase the pore diameter, eliminating the micropores and enhancing the mesorugarity.[11, 19, 30] In 2005, Zhang and co-workers introduced two post-synthesis thermal treatment methods, high-temperature treatment and carbon-propping thermal treatment, to improve the hydrothermal stability of SBA-15. In the former method, the as-synthesized SBA-15 is calcined at a much higher temperature, up to 900 ˚C, and it greatly increased the pore wall thickness where most of the silanols of the sample dehydrolyzed to $\equiv Si - O - Si \equiv$, thus effectively enhancing the degree of polymerization and minimizing the structural recombination reactions and the structural destruction when exposing to pure steam under 800 ˚C at prolonged period.[31] Nevertheless, high temperature calcination caused shrinkage of the mesopores, which can be overcome by carbon-propping method. This method is carried out by impregnating glucose into the pores of calcined SBA-15, followed by carbonization at 900 ˚C and calcination to remove the carbon from the carbonized composite, and thus shrinkage can be prevented as the mesopores are propped with carbon rods.[31] Pu and co-workers proposed a method to synthesized SBA-15 without micropores by recrystallizing SBA-15 using the diluted solution of aluminosilicate sol-gel and glycerol that eventually enhanced the hydrothermal stability of SBA-15.[32] The microporosity of SBA-15 can be controlled by varying the temperature and the ratio between the silica precursor and structure-directing agent.[33] There are many more reports disclosing the effect of temperature for the SBA-15 synthesis that cannot be fully covered. Generally, the pore size and pore wall thickness can be controlled, the degree of polymerization of the siloxanes can be enhanced, and the microporosity can be eliminated by manipulating the temperature during or after the synthesis of SBA-15, which leads to better hydrothermal and mechanical stability.

pH of the solution

SBA-15 is typically prepared under acidic conditions, pH< 1, mainly because highly acidic concentration results in a faster precipitation rate.[34] Isoelectric point (IEP) is used to represent the pH at which an immersed solid oxide surface has zero net charge, and the difference of average IEP for quartz, gels, and sols for SiO_2 is insignificant, hence an IEP $\leq$ pH 2.0 ± 0.2 is assumed.[35] At pH 2 to 6, above the isoelectric point of silica (pH ~2), no occurrence of silica gel precipitation or formation is observed.[12] In 2000, Kim and co-workers successfully synthesized ordered mesoporous silica with non-ionic surfactant over a wide range of pH, from 0 to 9, with the addition of fluoride ions during the synthesis. Fluoride ions promote precipitation, which dramatically increases the rate of silica condensation, especially at isoelectric point of silica.[36] Later in year 2005, Cui and co-workers reported the successfully synthesized SBA-15 at pH 2.7 to 5 by pre-hydrolyzing TEOS at pH ~3, followed by the self-assembly of pre-hydrolyzed TEOS and Pluronic® P-123 at pH ~5.[37] In addition, there is an increase in pore wall thickness with the increase in pH.[37] These findings provide valuable information in better understanding the effect of pH over the spectrum of processing conditions.

Silica precursor

TEOS can be replaced by a cheaper silica source, such as water soluble sodium silicate[38, 39] or clay[40] in synthesizing SBA-15, without compromising on the physicochemical parameters. For example, Fulvio and co-workers established that the self-assembly time can be significantly reduced from 24 hours to 2 hours using sodium metasilicate ($Na_2.SiO_3.9H_2O$), with the material having a thicker pore wall compared to that obtained using TEOS.[39] Although this scope of the literature may not be bringing as much impact towards improving the quality of SBA-15 as the choice of temperature and pH, cheaper sources of raw materials is important for making a process commercially viable.

1.4. Synthetic routes in SBA-15 synthesis

Of all the process conditions, one major challenge or necessary improvement that has been studied widely is to reduce the time of the synthesis/processing. While SBA-15 is widely recognised in possessing great potential in many applications, the conventional hydrothermal synthesis is not industrially viable due to the lengthy processing times required.

1.4.1 Microwave-assisted synthesis

The use of microwave-hydrothermal treatment in the synthesis of SBA-15 dramatically reduces the aging time to *ca.* 120 min, form 1 – 3 days for the conventional method.[41] Using the same treatment, now in the presence of an ionic salt, NaCl, and a co-solvent such as ethanol, not only can the crystallization of SBA-15 be formed within two hours, but the pore size and microporosity of the material can be tuned under the microwave-hydrothermal conditions at 373 K.[42, 43] Subsequently in 2006, implementing a temperature-programmed microwave system, Celer and co-workers further developed the microwave-assisted synthesis of SBA-15, for the entire process from gel formation to hydrothermal processing.[44]

1.4.2 Dry-gel conversion versus hydrothermal treatment

An alternative to hydrothermal treatment under acidic conditions is the use of dry-gel conversion processing, whereby the gel initially formed by the hydrolysis of TEOS is filtered and dried, and then treated with steam at 100 ˚C.[45]

1.4.3 Synthesis under shear flow using a Couette cell

Kim and co-workers have studied the formation of mesoporous silica using cationic surfactant under shear at relatively low temperature.[46] The shear effect was generated within a Couette cell, which resulted in long twisted wormy micelles, in establishing a method for the controlled formation of helical mesoporous silica structures.[46]

Despite the above development of different approaches for the synthesis of SBA-15, the common practice is to use hydrothermal treatment. Such treatment is thought to be necessary to improve the mesostructure of SBA-15, with no reports to the contrary. The dissertation herein focuses on a new method of preparing SBA-15 using vortex fluidic device (VFD) processing (Chapter 3), which avoids hydrothermal treatment, as a breakthrough in the synthesis of material, with scalability addressed upfront given the continuous flow processing capabilities of the device.

1.5. Pore expansion

Depending on the application, controlling the pore size and particle morphologies of SBA-15 can be important. For example, the application of mesoporous silica in different catalysis relies heavily on the pore structure and the morphology of the materials and these two factors influence the catalytic efficiencies.[47] Enzyme immobilization efficiency and capability within the pore channels of SBA-15 relates highly to the pore diameter of the support.[48] Thus, the ability to control these two parameters whilst preparing the mesoporous materials represents a significant and challenging research endeavour. Typical SBA-15 synthesis using the hydrothermal method proposed by Zhao and co-workers has a pore sizes up to 9 nm, which can be used in immobilizing small to medium size enzymes, such as proteases, lipases and peroxidases.[48-51] In order to utilize SBA-15 as host for bio-macromolecules such as proteins, which the molecular size can be up to 30 nm,[49] pore expansion is required.

1.5.1. Pore expansion using swelling agent

Schmidt-Winkel and co-workers established that the pore size of SBA-15 can be increased up to 33 nm by introducing an organic co-solvent, 1,3,5-trimethylbenzene (TMB).[52] Controlling the pore size can be achieved by adjusting the hydrophobic volume, and the TMB can induce a phase transformation from SBA-15 type mesostructure to ultra large cavities mesostructured cellular foams, namely MCFs.[52]

Expanding the pore size using TMB without a phase transformation from hexagonally to mesocellular foam, pore diameters up to 12 nm have been achieved.[53] Cao and co-workers used 1,3,5-triisopropylbenzene as a swelling agent, successfully preparing SBA-15 with pore size ranging from 10 to 26 nm.[54] They later claimed a breakthrough in the reduction of the processing time ranges from 2.5 to 7.5 hours, in contrast to one or more days required conventionally processing. This involved the initial processing at 12 – 17 ˚C and then hydrothermal treatment at 150 to 170 ˚C.[55] Aliphatic hydrocarbons from hexane to dodecane have also been used as swelling agent in preparing larger pore size SBA-15.[56-62]

1.5.2. Pore expansion by changing the silica source

Other attempts have also been made to enlarge the pore size of SBA-15 by varying the nature of the silica precursors. Different types of alkoxysilanes used in the synthesis of SBA-15 have been investigated in determining the effect of pore size using the well established conventional processing conditions.[63] Although TBOS is capable of expanding the pore size, there is a lost in mesoregularity, the sample prepared with TBOS showed a three-dimensional interconnected wormhole-like pore structure due to the slow hydrolysis rate of TBOS.[63] Large pore sizes for SBA-15, in the range of 10 – 16 nm, can be prepared by controlling the composition of a mixture of TEOS and Na_2SiO_3 in acetic acid/sodium acetate buffer solution, where TEOS has a dual function, both as a swelling agent and also a silica source.[64]

1.6. Surface modification or functionalization of the pore walls

Surface modification or functionalization of SBA-15 is a pre-requisite for tailoring the property of the material for particular applications. This has been carried out using two approaches, namely post-grafting and direct synthesis.[65] Functionalizing the surface of SBA-15 improves the interaction between the surface of the framework and metal particles or biomolecules which can be incorporated onto SBA-15 for many differing applications. This will be discussed in the following sections.

1.6.1. Methods for surface modification or functionalization

Post- synthesis grafting

Post-synthesis grafting was the first method used for surface modification of mesoporous silica. This is a multi-step method, where SBA-15 is prepared under the well-established hydrothermal process and then calcined to remove the polymeric template, whereupon the desired functional groups are attached to the surface as a separate process. If the latter is carried out using a solvent, which occasionally is under reflux conditions, the surface silanol groups become covalently bond to the functional groups.[66] Many reports have pointed out a number of downsides of this method, including (1) difficulties in controlling the surface uniformity and loading of the grafted functional groups, (2) the use of multiple steps and the time required to prepare the functional material, and (3) the tendency for pore size reduction, possibly due to the localized distribution of functional groups in the material.[65, 67, 68]

Direct synthesis

A direct synthesis for preparing functionalized hybrid materials with ordered mesopores was first proposed by Burkett and co-workers, in mimicking the methodology used in sol–gel chemistry for functionalizing amorphous silica.[69] A direct synthesis for functionalised SBA-15 is widely used. It involves co-condensation of alkoxysilanes such as TEOS or TMOS with organotrialkoxysilanes such as APTES, MPTMS, carboxylic groups, or materials containing arenesulfonic groups.[70-73] This has advantages over the grafting method in its simplicity in being a one-pot synthesis, and more control over the loading and distribution of functional groups, which allows control over the type and position of the functional groups at the molecular level.[65, 68]

1.6.2. Importance of the surface modification or functionalization

Apart from its excellent physical properties and great stability, the flexibility and simplicity in modifying the silanol groups on the surface of SBA-15 makes it a popular candidate as a supporting material. Many reports show that surface modification or functionalization is crucial for performance enhancement. For example, without surface modification, SBA-15 supported Pd catalyst show a high performance in oxidation of benzyl alcohol, however, the catalytic activity drops dramatically for subsequent consecutive cycles.[74] This is improved by modifying the surface with bipyridyl ligand, which prevents the leaching and agglomerating of Pd NPs, as well as enhancing the activity and durability of the catalyst.[74] In catalysis, it is a common practice to use amino- or thiol-functionalized SBA-15 as the host matrix as these functional groups are known to have strong affinity to metal ions, thus, reduces the likelihood of leaching and agglomeration.[75, 76]

Surface modification or functionalization plays a major role and influence in drug delivery systems. The adsorption capacity and release properties of a drug is highly depends on both its own properties and also the properties of the functional groups of the surface, which lead to the influence of interaction between the drug molecules and the surface groups.[77] Needless to say, material such as SBA-15 which possess ordered and tuneable cavities, also the ease of functionalize the hydroxyl surface to withhold different size of drug molecules, has attracted much attention in aiming to tailor better performance materials, as well as utilizing the materials in wider range of applications.

1.7. Incorporation of metals into SBA-15

SBA-15 is known as a molecular sieve or support. Enormous effort has focused on studying mesoporous silica for a wide range of applications, with a substantial number of reports over a sustained period. Incorporating different metal oxides into mesoporous silica for catalysis is most popular among all applications. For example, doping platinum with TiO_2 and ZrO_2 into the pores of the ordered mesoporous silica significantly increases both the activity and selectivity of ethyl acetate combustion.[78] Using a series of catalysts based on Ni–Mo, Ni–W, Pt and triflic acid (TFA) supported on mesoporous SBA-15, good performance in hydrocracking of unsaturated oil has been established.[79] SBA-15-supported palladium serves as catalysts for the Heck reaction, with performance test carried out on the reaction of 4-nitrobromobenzene and methyl acrylate, resulting in 98%

conversion, and the catalyst can be recycled up to three cycles for the same experiment, with a slightly reduced 96% conversion.[80] In addition, many reports highlight the success of utilizing mesoporous silica in encapsulated drugs, as a delivery channel in medicine.[81-83]

There are two general methods for introducing metals into the SBA-15 support, a direct synthesis and a post-synthesis treatment. In the direct synthesis, metal precursors are added during the synthesis of silica gel before aging, or added into the micelle solution, allowing the metals to be stabilized inside the template micelles during the self-assembly of the surfactants.[84, 85] For post-synthesis treatment, the metal precursors are added into the pores of calcined SBA-15, as discussed in the following sections.

1.7.1. Incipient wetness impregnation

Incipient wetness impregnation is the most commonly practiced method for incorporating metals into mesoporous silica. Firstly, a solution of the metal complex precursor is prepared in aqueous or an organic solvent. Then, the calcined SBA-15 is added into the metal-containing solution under vigorous stirring for a prolong period. The treated SBA-15 is then washed and dried to remove the excess solution. There is minimal control of the concentration of metals loaded using this approach and often time consuming, multiple cycles are required to achieve the desired metal loadings. Highly dispersed and uniformly distributed Pd and Pt NPs or Au and Ag nanowires have been prepared using this method.[86]

1.7.2. Ion exchange

The template-ions exchange method was first developed for MCM-14 where the as-synthesized material involves exchange reactions with metal cations such as those of Al, Ti, Cr, Mn, Zn, and Zr in aqueous media, resulting in a high dispersion of metal ions incorporated in the pores of MCM-41.[87] Given the synthesis of SBA-15 uses a non-ionic surfactant under acidic conditions, the interaction between the protonated surfactant (S^0H^+) and cationic silica species is very weak and can be easily broken by addition of inorganic cations.[88] Similarly, this method proposes the low charge density, S^0H^+ can be replaced by cations of high charge density, with the ion exchange reaction as follows:[88]

$$2(S^0H^+)(X^-I^+) + M^{2+} \rightarrow (I^+X^-)M^{2+}(X^-I^+) + 2(S^0H^+) \qquad (1.4)$$

1.7.3. Vapour phase deposition

This method is carried out by reacting a volatile organometallic precursor with the surface of the mesoporous silica in the gas phase, then carried on with reduction and generating a highly dispersed metal particles deposition.[89, 90]

1.7.4. Other methods

Sonochemical methods can be used to introduce nanocatalysts into mesoporous material.[91] Rioux and co-workers applied low power sonication for incorporating metal, for example, on adding colloidal Pt in water and ethanol to SBA-15 followed by sonication for 3 hours.[92] In addition, Wang and co-workers successfully established a two-solvent method in producing high metal loading nanocomposite of Pd clusters supported in the SBA-15 (up to 3 wt%), with the majority of metal NPs incorporated in the porous host matrix made possible by using both hydrophobic and hydrophilic solvents during the post-synthesis treatment.[93] Dissolving the metal precursor in supercritical CO_2 ($ScCO_2$), offers a process for impregnating Pd NPs into the support under rather mild conditions, at 40 ˚C and 85 bar pressure.[94]

1.8. Applications

The robust properties of SBA-15 render it useful as support for many applications. A review of some of the most widely reported applications of nanocomposite material prepared using SBA-15 as the support is now provided. It will be categorized into four areas of discussion: catalysis, sensors, medicine, and other applications.

1.8.1. Heterogeneous catalysis

Many reports can be found using various supported metal NPs in SBA-15 for catalysis. The commonly used metals are Au, Ag, Pd and Pt. Table 1.3 summarizes some of these applications.

Table 1.3. Summary of heterogeneous catalysts using SBA-15 as support in different reactions.

C–C coupling reactions		
Mizoroki–Heck coupling reaction	Pd	[93, 95-101]
Suzuki–Miyaura coupling reaction	Pd	[99, 102-105]
Sonogashira coupling reaction	Ni	[106]
Ullmann coupling reaction	Pd	[107]
Oxidation reactions		
Alcohols	Au, Au-Pd, Ag	[108, 109]
	Co	[110]
	Pd, Pt	[74, 111, 112]
Alkenes	Ag, Pd	[113, 114]
Aromatics	Co, Co/Ce	[115-119]
	Pd, Pt, Pd/Ti	[113, 120, 121]
CO	Ag	[122, 123]
	Au, Au/Ti, Au-Cu	[124-130]
	Co, Cu	[131, 132]
	Pd	[133]
Methane	Co-Cu	[134]
	Pd	[135]
Other catalytic reactions		
Catalytic cracking of biomass	Pd	[136]
Catalytic deoxygenation of stearic acid	Pd	[137]
Direct synthesis of H_2O_2	Pd	[138, 139]
Hydrogenation reactions	Pd	[76, 140-143]
Methane combustion	Pd	[144]
Synthesis of 2-functionalized indoles	Pd	[145]

1.8.2. Sensors

Biosensing has attracted much attention over the past years. Direct electron transfer (DET) from biomolecules to the electrode surface is achievable with the aid of metal NPs, without additional mediators.[146] To develop an enzyme-based sensor, a good chemical, mechanical, thermal stability, and large surface area immobilization matrix is required.[147] The unique physical properties of mesoporous silica, which fulfils the aforementioned requirements, makes it an attractive candidate for biosensors.

A high performance glucose biosensor has been devised using composite material prepared derived from calcined SBA-15, followed by functionalized with APTMS and then loading with gold NPs.[147] A study showed that the immobilization of hemoglobin onto SBA-15 exhibits a fast amperometric response, a low detection limit and good stability for H_2O_2 detection.[148] Similarly, encapsulating Pd NPs into amino functionalized SBA-15 enhances the DET between hemoglobin and the electrode surface, and thus the modified electrode with Hb/Pd/SBA-15 composite exhibits a response towards the reduction of H_2O_2.[149] Other examples of the potential of SBA-15 for use in electrochemical biosensors involve preparing a composite of SBA-15/ polyaniline for detection of uric acid,[150] immobilizing tyrosinase onto CuO/SBA-15 for detection of phenolic compounds,[151] and developing a method for an immunosensing array based on labelling of amino-functionalized SBA-15 and Pt (Pt/SBA-15) composite in determining endocrine disrupting compounds (EDCs).[152]

1.8.3. Drug delivery

Over the last ten years there have been an increasing number of research groups involved in the synthesis of mesoporous silica as host matrices for drugs delivery applications. Mesoporous silica with uniform pore size, large surface area, large pore volume, and ease of surface functionalization, allows better control release of various drugs, which comes the field of controlled drug delivery systems (DDSs).[153] The aim of DDSs focuses on precise control of time-release dosage of drugs, which targets specific area of the body to achieve a maximum therapeutic effect.[153] Depending on the type of drug and the conditions of target tissue, formulations of drugs loading into the carrier can be tailored accordingly, to achieve the best stimuli-response systems.

The therapeutic performance of SBA-15 loaded with model drugs such as atenolol,[154] ibuprofen,[155] collagen-polyvinylpyrrolidon,[156] naproxen,[157] amoxicillin,[158] and heparin are evaluated by studying the release kinetics of the drugs over time. It is worth noting that surface modification or functionalization of SBA-15 plays an important role in facilitating the loading of a drug, as well as sustained release.[77, 155, 157-159] Modification or functionalization of the silanol groups on the surface of SBA-15 through functional groups, increases the drug–surface interaction, consequently allowing an increase in drug loading.[153] Another strategy involves modification of the surface hydrophobicity of SBA-15, for which the release of drug can be impeded by a decrease in wettability of the pore wall surface by the aqueous media.[153] Examples of different drugs loaded into functionalized SBA-15, extracted from review article by Vallet-Regí and co-workers, are listed in table below.

Table 1.4. Drugs, adsorption conditions, and maximum drug load adsorbed into functionalized SBA-15. Adapted from Vallet-Regí *et al.*[153]

Drug	Mesoporous matrix	Solvent	Max. load (%)
Gentamicin	SBA-15	Water	20
Erythromycin	SBA-15	Acetonitrile	34
Erythromycin	SBA-15-C8 [a]	Acetonitrile	13
Erythromycin	SBA-15-C18 [b]	Acetonitrile	18
Alendronate	SBA-15	Water	8
Alendronate	SBA-15-NH_2 [c]	Water	22
Amoxicillin	SBA-15	Water	24
Captopril	SBA-15	Water	22.6

[a] Organically modified with trimethoxyoctylsilane.
[b] Organically modified with trimethoxyoctadecylsilane.
[c] Organically modified with amino groups.

1.8.4. Adsorption

Amino- and thiol-functionalized SBA-15 can be used as a scavenger for heavy metal ions such as Au^{2+}, Cd^{2+}, Co^{2+}, Cr^{3+}, Cu^{2+}, Hg^{2+}, Ni^{2+}, Pb^{2+}, and Zn^{2+}.[70, 160-162] For example, Au^{2+} and Hg^{2+} have strong affinity to thiolated SBA-15, whereas Cu^{2+}, Ni^{2+}, and Zn^{2+} have strong affinity to aminated SBA-15, which is an exceptional adsorbent for waste water treatment.[161-163] Similarly, Huang and co-workers discovered a simple method to recover lithium from waste lithium ion battery by using thiol-functionalized SBA-15.[164] SBA-15 also possess adsorption potential towards light hydrocarbons, noting that the adsorption selectivity of SBA-15 is highly influenced by the microporosity of the framework.[165] The presence of Cu atoms in SBA-15 increases the adsorption selectivity towards propylene.[166] In addition, modified SBA-15 or metals supported SBA-15 composite show an uptake capability for H_2S,[167] CO_2,[168, 169] and sulphur-containing compounds.[170]

1.8.5. Other applications

There are many other applications of SBA-15 where it is employed as a host matrix. It can be an excellent candidate for HPLC stationary phase to separate biomolecules such as peptides, proteins, cysteine, glutathione, dopamine, 6-thiopurine, and vitamin E isomers.[171-173] In addition, Liu and co-workers developed an efficient method for removing lignin in corn straw, using MgO/SBA-15 as molecular sieves.[174] Surely there are many more latest research focuses on exploring the wide applications relating to the used of SBA-15 as the host matrix that are recently published may not be included.

1.9. Factors affecting the synthesis and properties of alcogel

1.9.1. Effects of co-solvent

The sol–gel polymerization of silicon alkoxides forms silica gel. Hydrolysis occurs when TEOS or TMOS and water are mixed, however, tetraalkoxysilanes are immiscible with water and thus, a mutual solvent is required, generally ethanol.[175] A homogeneous solution formed under the aid of mutual solvent, initiates the hydrolysis of the alkyl groups to form silanol monomers, which then condense and cross-link to form silica gel.[176] The role of the co-solvent is to serve as a bridging medium so that the biphasic silicon alkoxides-water mixture can be homogenized. Avnir and co-worker claimed that the addition of alcohol is unnecessary as the generation of alcohol during hydrolysis is sufficient to convert the biphasic system into a single phase system.[177] However, this report has limited characterization data to support the claim and there hasn't been any follow up relevant report. Thus, all studies since this report have focused on the use of a co-solvent during the synthesis of silica gel. Šefčík and McCormick presented a tertiary miscibility diagram to determine the range of compositions that provide a homogeneous solution immediately after adding and mixing the tetraalkoxysilanes, before any reaction takes place.[178] The diagram in Figure 1.3, clearly shows that a mutual solvent such as ethanol is necessary for the low miscibility compositions of silica gel synthesis.[178]

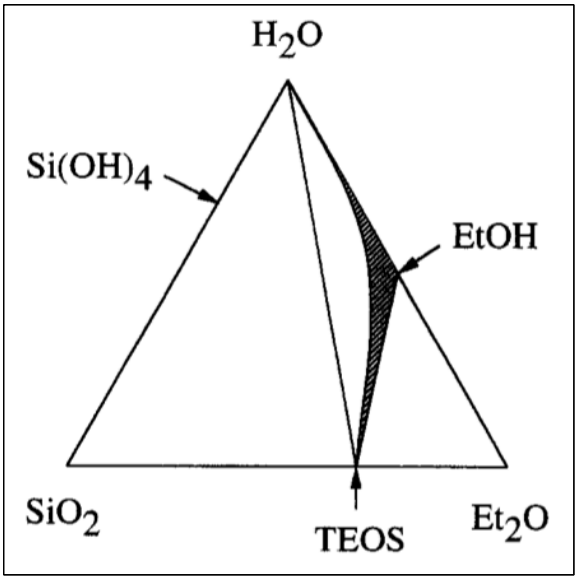

Figure 1.3. *Miscibility diagram of TEOS/EtOH/H_2O inserted into the oxide composition simplex SiO_2–EtOH–H_2O. The black area corresponds to initially miscible composition. Taken from Šefčík et al.*[178-180]

In 2009, Kajihara and co-workers reported the development of a method to prepare macroporous silica gels that are free from addition of alcohols. However, this method involves multistep mixing at different pH ranges, and requires a processing time up to four days.[181]

1.9.2. Effects of catalysts and pH

The role of catalyst in sol–gel synthesis is the most widely studied area. Numerous papers have published on the effects of catalyst on the silica gel synthesis. The pH of the starting sol mixture not only affects the properties of the gel but also dramatically influences the gelation process.[182] In acid-catalyzed synthesis, at pH < 2, the hydrolysis rate is fast but the condensation rate is slow, and vice versa for base-catalyzed synthesis. The acid and base-catalyzed mechanisms are outlined as below:[183]

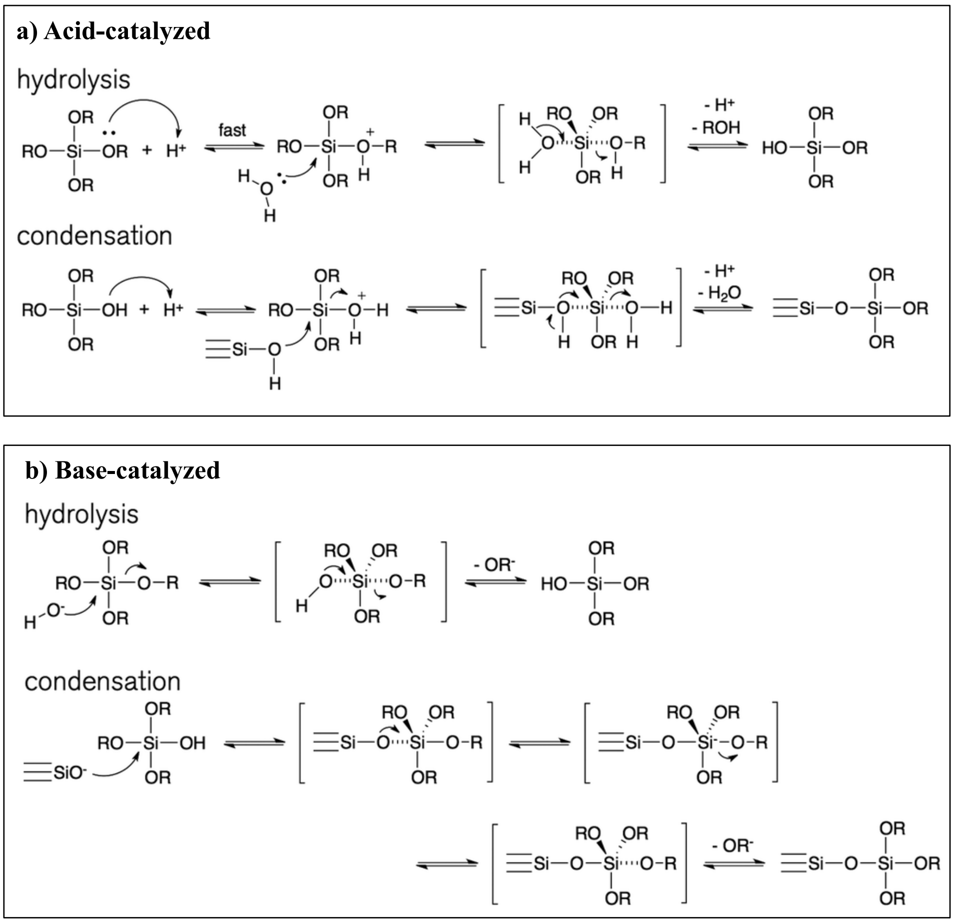

Figure 1.4. *General mechanisms of hydrolysis and condensation of (a) acid-catalyzed conditions and (b) base-catalyzed conditions, where condensation involves both water condensation and alcohol condensation. Taken from review article by Lofgree and Ozin.*[183]

Researchers have related the catalytic mechanisms of the gelation process to the properties of the silica gel formed and concluded that at low pH regimes, there is a favourable linear chain growth which results in the formation of a low cross-linking and less stiff gel.[182] On the other hand, increasing the pH leads to an increase in the rate of polymerization and thus a low gelation time. This results in gels with microstructures consisting of large spherical particles.[182] Gelation is not observed but precipitates form once the particles reach a certain size. These particles are electrostatically stabilized and prevent particles from condensing with other particles, but it does not preclude continuous condensation of monomeric species, unlike in the Stöber process.[1] These differences in microstructures are summarised in Figure 1.5.

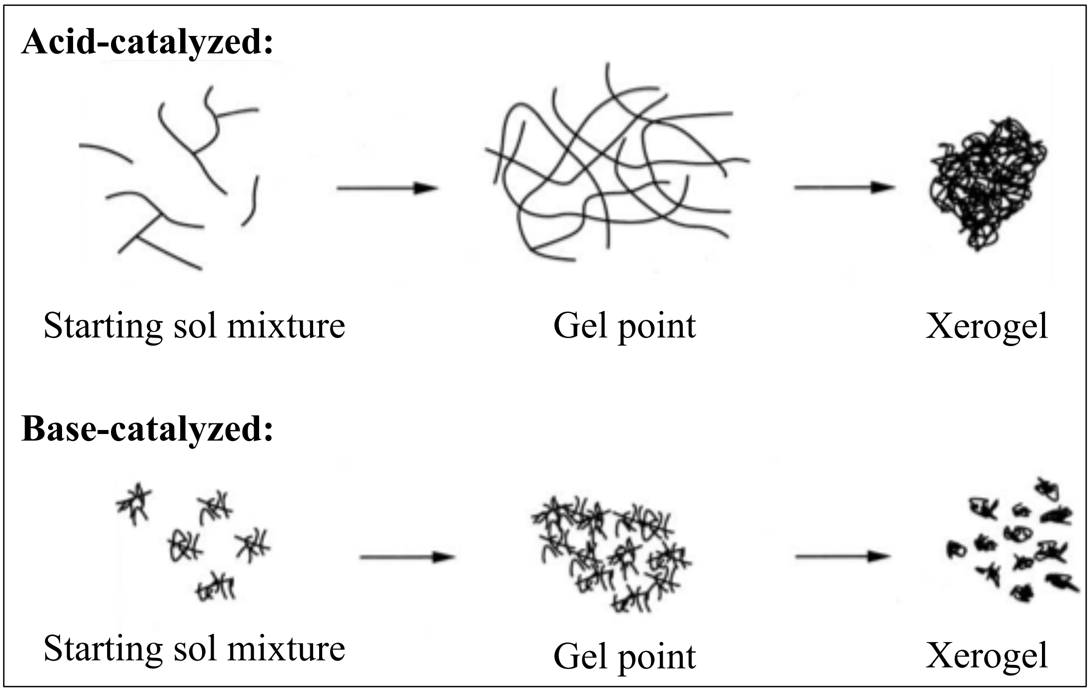

Figure 1.5. *Effects on the microstructure of the silica gel under acid and base-catalyzed conditions. Taken from Buckley and Greenblatt.*[175]

Without the presence of a catalyst, the gelation time at room temperature can be anywhere from several days to weeks. Once a catalyst is added, a rapid gelation occurs. The gelation time may vary depends on the type of catalysts used. Pope and Mackenzie have summarized the effects of the choice of catalyst for the formation of the silica, synthesis as show in Table 1.5.

Table 1.5. Examples of published silica work on the effects of catalysts. Extracted directly from reference.[182]

Catalyst	Comments
HCl	• slow hydrolysis relative to the condensation reaction: small pores • high bulk density: no particles observed • accelerated hydrolysis and retarded polymerization
NH_4OH	• low bulk density: spherical particles observed • “limited hydrolysis”
NH_3OH	• rapid hydrolysis relative to the condensation reaction: large pores
NH_4Cl	• “postponed hydrolysis” followed by rapid gelation

Based on the summary in Table 1.5, Pope and Mackenzie conducted a systematic study to look at the role of catalysts, in controlling the gelation time of the initial sol mixture, with the results summarized in Table 1.6.

Table 1.6. Gelation time and pH of solutions for six catalysts. Taken from the work by Pope and Mackenzie.[182]

Catalyst	Concentration (mol.: TEOS)	Initial pH of solution	Gelation time (hr)
HF	0.05	1.90	12
HCl	0.05	0.05[a]	92
HNO_3	0.05	0.05[a]	100
H_2SO_4	0.05	0.05[a]	106
HOAc	0.05	3.70	72
NH_4OH	0.05	9.95	107
No catalyst	–	5.00	1000

[a] between 0.01 and 0.05.

The results in Table 1.6 clearly show a great variation in gelation time at different pH. However, the gelation time cannot be solely explained on the basis of pH, but also on the mechanism of the acid or base-catalyzed hydrolysis (Figure 1.3), with acid-catalyzed and base-catalyzed hydrolysis being governed by the concentration of hydronium and concentration of hydroxyl in starting solution mixture respectively.[182] In 2002, Buisson and co-workers proposed that addition of lipase from *Burkholderia cepacia* to the starting sol could accelerate the gelation kinetics, and stressed out the difference in the gelation mechanism between lipase and the traditional catalysts.[184] All these findings provide an in-depth understanding on how a different type and concentrations of catalysts can govern the nucleation rate of the system and thus, influence the microstructure formation.

1.9.3. Effect of temperature

Typically, sol–gel synthesis is carried out under room temperature. By far, the greatest interest has been on the effects of catalysts during the preparation of silica gel. From the aforementioned discussion, gelation of silica is a very time consuming process in the absence of catalyst, under room temperature. This can be improved by introducing an acid or base catalyst during the process. Likewise, the gelation time can be highly dependence on temperature.[21] Yamane and co-workers reported that by applying heat-treatment, carefully controlling the temperature at an increment rate of 2 ˚C/ min up to predetermined setpoint (tested under temperature ranging from 100 ˚C to 900 ˚C) and maintained at the setpoint temperature for 18 hours, a crack-free silica monolith glass can be generated.[185] Thus far, there are limited studies focused on the effect of temperature on the gelation of silica. In 1986, Colby and co-workers undertook a systematic study on both acid and based-catalyzed silica gel synthesis, involving changing the reactions temperature from from 0 ˚C to 70 ˚C. For both TEOS-EtOH and TMOS-MeOH systems, the gelation times significantly decreased with an increase in reaction temperature.[21] This study was based on the assumption that with the aid of catalysts, the hydrolysis is completed within a short period of time after the initial mixing, and thus the condensation is the rate-determining process of gelation.[21]

1.9.4. Drying process

After the formation and aging process, the silica-wet gel goes through a drying process to remove excess solvents in order to obtain a material with sufficient mechanical and chemical stability.[186] Generally this process is carried out using two methods, namely drying under atmospheric pressure and drying under supercritical conditions.

Silica gels that go through drying via thermal evaporation of pore liquid near ambient pressure are named xerogels. Shrinkage occurs during this process due to the capillary pressure, and subsequently cracking occurs due to the stress arising from the large degree of shrinkage, which is attributed to the small volume fraction.[23, 186, 187] Depending on the synthetic conditions, xerogels typically are porous with small pore diameters (1–10 nm), with reasonably high surface area, high densities, and good mechanical properties, and are transparent to visible light when pore radii are smaller than 4 nm.[186, 187] Shrinkage of base-catalyzed gels during drying is less pronounced compared to the acid-catalyzed gels, mainly because gels formed under basic conditions have larger pore radii and thus, lower capillary pressure.[23]

Using a supercritical drying process, the gel is placed in an autoclave, the pore liquid is replaced via solvent exchange, and the material is treated at temperatures and pressures above the critical point of the exchanged solvent.[186] The dried gel produce is named aerogels. Although this method can produces a fracture-free gel with the least shrinkage and lowest densities, this material has poor mechanical properties and the process is uneconomical.[186]

Many methods have been proposed to tailor and produce silica gels with specific properties, in targeting particular applications. For example, Sen and Bruce developed a tri-phasic reverse emulsion (TPRE) method for surface functionalization of silica NPs functionalised as high efficient biosensors.[188] Choi introduced the molecular-level hybridization method in the preparation of polysilsesquioxanes, which show novel optical properties.[189] Zhou and co-workers have successfully synthesized hydrophobic modified silica aerogel/activated carbon composite materials, which show an adsorption rate of TNT up to 96.5%.[190] The mechanisms and methods for surface modification or functionalization of silica gel will not be further discussed, as they are similar to the those in the discussion for the modification or functionalization of SBA-15 in section 1.5 and 1.6.

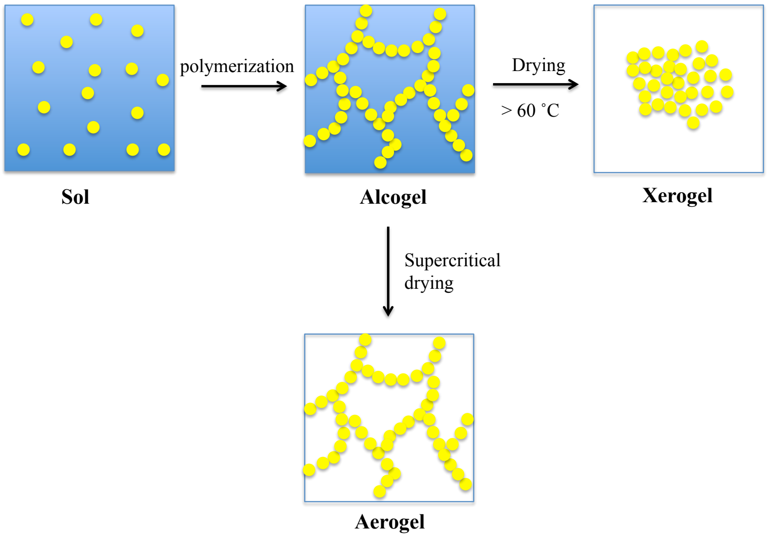

Figure 1.6. *Sol–gel synthesis scheme demonstrated the formation and structure of the gels under two different drying approaches.*[191]

1.10. Thesis Hypotheses

In this dissertation, the synthesis and potential application of two different categories of mesoporous silica have been investigated, an ordered mesoporous silica and disordered silica alcogel. This is with a goal to overcome the existing downside for existing processes and methods. Research focuses on improving the synthesis of SBA-15 and silica gel, in devising an unorthodox continuous flow method as a new paradigm in the field. This involves the use of the VFD, where high shear is created with a thin film regime that is able to control the nucleation and growth of the reactions down to molecular level, with scalability addressed at the inception of the science.

Remarkably, using the VFD in the processing, SBA-15 can be prepared under ambient conditions, thereby avoiding the abiding hydrothermal processing. This approach not only shortens the synthesis time drastically, but the pore sizes distribution can be readily tuned. Moreover, the VFD processing allows the synthesis of SBA-15 carried out under neutral condition, which makes *in situ* metals incorporation during the SBA-15 synthesis easily achievable under such benign environment. Overall, this new processing provides a wide range of possibilities and flexibility that potentially allows SBA-15 to be tailored and synthesized for specific application. Results of these works will be discussed in the subsequent chapters.

Using VFD processing, silica gel can also be synthesized without acid or base catalyst and mutual solvent under ambient conditions. Yet, rapid gelation time of the silica gel is achievable. This is a significant advantage in the development of silica-based functionalized glasses that are difficult to form by conventional melt-quench and vapour-phase method.[23] The new method greatly improves the green chemistry metrics of the processing,[192-194] with minimal utilities usage and chemical waste generation.

1.11. References

1. C. J. Brinker, Hydrolysis and condensation of silicates: Effects on structure, *J. Non-Cryst. Solids*, 1988, **100**, 31-50.

2. F. Surivet, M. Lam Thanh, J. P. Pascault and T. Pham Quang, Organic-inorganic hybrid materials. 1. Hydrolysis and condensation mechanisms involved in alkoxysilane-terminated macromonomers, *Macromolecules*, 1992, **25**, 4309-4320.

3. N. A. J. M. S. J.D. Wright, *Sol Gel Materials: Chemistry and Applications*, CRC Press, Florida, 2001.

4. R. Ciriminna, M. Sciortino, G. Alonzo, A. d. Schrijver and M. Pagliaro, From Molecules to Systems: Sol−Gel Microencapsulation in Silica-Based Materials, *Chem. Rev.*, 2010, **111**, 765-789.

5. R. K. Iler, *The Chemistry of Silica: Solubility, Polymerization, Colloid and Surface Properties and Biochemistry of Silica*, John Wiley and Sons, NY, 1979.

6. C. Triantafillidis, M. S. Elsaesser and N. Husing, Chemical phase separation strategies towards silica monoliths with hierarchical porosity, *Chem. Soc. Rev.*, 2013, **42**, 3833-3846.

7. C. T. Kresge, M. E. Leonowicz, W. J. Roth, J. C. Vartuli and J. S. Beck, Ordered mesoporous molecular sieves synthesized by a liquid-crystal template mechanism, *Nature*, 1992, **359**, 710-712.

8. V.-T. Hoang, Q. Huang, M. Ei*f*á, T.-O. Do and S. Kaliaguine, Structure and Diffusion Characterization of SBA-15 Materials, *Langmuir*, 2005, **21**, 2051-2057.

9. A. Y. Khodakov, V. L. Zholobenko, R. Bechara and D. Durand, Impact of aqueous impregnation on the long-range ordering and mesoporous structure of cobalt containing MCM-41 and SBA-15 materials, *Microporous Mesoporous Mater.*, 2005, **79**, 29-39.

10. W. Guo, X. Li and X. S. Zhao, Understanding the hydrothermal stability of large-pore periodic mesoporous organosilicas and pure silicas, *Microporous Mesoporous Mater.*, 2006, **93**, 285-293.

11. R. Che, D. Gu, L. Shi and D. Zhao, Direct imaging of the layer-by-layer growth and rod-unit repairing defects of mesoporous silica SBA-15 by cryo-SEM, *J. Mater. Chem.*, 2011, **21**, 17371-17381.

12. D. Zhao, J. Feng, Q. Huo, N. Melosh, G. H. Fredrickson, B. F. Chmelka and G. D. Stucky, Triblock Copolymer Syntheses of Mesoporous Silica with Periodic 50 to 300 Angstrom Pores, *Science*, 1998, **279**, 548-552.

13. L. Y. Chen, S. Jaenicke and G. K. Chuah, Thermal and hydrothermal stability of framework-substituted MCM-41 mesoporous materials, *Microporous Mater.*, 1997, **12**, 323-330.

14. J. r. P. Thielemann, F. Girgsdies, R. Schlögl and C. Hess, Pore structure and surface area of silica SBA-15: influence of washing and scale-up, *Beilstein J. Nanotechnol.*, 2011, **2**, 110-118.

15. S. Lin, L. Shi, M. M. L. Ribeiro Carrott, P. J. M. Carrott, J. Rocha, M. R. Li and X. D. Zou, Direct synthesis without addition of acid of Al-SBA-15 with controllable porosity and high hydrothermal stability, *Microporous Mesoporous Mater.*, 2011, **142**, 526-534.

16. C. Gerardin, J. Reboul, M. Bonne and B. Lebeau, Ecodesign of ordered mesoporous silica materials, *Chem. Soc. Rev.*, 2013, **42**, 4217-4255.

17. S. A. Jadhav, Incredible pace of research on mesoporous silica nanoparticles, *Inor. Chem. Front.*, 2014.

18. M. Kruk, M. Jaroniec, C. H. Ko and R. Ryoo, Characterization of the Porous Structure of SBA-15, *Chem. Mater.*, 2000, **12**, 1961-1968.

19. A. Galarneau, H. Cambon, F. Di Renzo and F. Fajula, True Microporosity and Surface Area of Mesoporous SBA-15 Silicas as a Function of Synthesis Temperature, *Langmuir*, 2001, **17**, 8328-8335.

20. M. S. Morey, S. O'Brien, S. Schwarz and G. D. Stucky, Hydrothermal and Postsynthesis Surface Modification of Cubic, MCM-48, and Ultralarge Pore SBA-15 Mesoporous Silica with Titanium, *Chem. Mater.*, 2000, **12**, 898-911.

21. M. W. Colby, A. Osaka and J. D. Mackenzie, Effects of temperature on formation of silica gel, *J. Non-Cryst. Solids*, 1986, **82**, 37-41.

22. M. D. Sacks and R.-S. Sheu, Rheological properties of silica sol-gel materials, *J. Non-Cryst. Solids*, 1987, **92**, 383-396.

23. K. Kajihara, Recent advances in sol–gel synthesis of monolithic silica and silica-based glasses, *Journal of Asian Ceramic Societies*, 2013, **1**, 121-133.

24. D. Zhao, Q. Huo, J. Feng, B. F. Chmelka and G. D. Stucky, Nonionic Triblock and Star Diblock Copolymer and Oligomeric Surfactant Syntheses of Highly Ordered, Hydrothermally Stable, Mesoporous Silica Structures, *J. Am. Chem. Soc.*, 1998, **120**, 6024-6036.

25. R. Ryoo, C. H. Ko, M. Kruk, V. Antochshuk and M. Jaroniec, Block-Copolymer-Templated Ordered Mesoporous Silica: Array of Uniform Mesopores or Mesopore-Micropore Network?, *J. Phys. Chem. B.*, 2000, **104**, 11465-11471.

26. K. Cassiers, T. Linssen, M. Mathieu, M. Benjelloun, K. Schrijnemakers, P. Van Der Voort, P. Cool and E. F. Vansant, A Detailed Study of Thermal, Hydrothermal, and Mechanical Stabilities of a Wide Range of Surfactant Assembled Mesoporous Silicas, *Chem. Mater.*, 2002, **14**, 2317-2324.

27. L. Chen, T. Horiuchi, T. Mori and K. Maeda, Postsynthesis Hydrothermal Restructuring of M41S Mesoporous Molecular Sieves in Water, *J. Phys. Chem. B.*, 1999, **103**, 1216-1222.

28. W. W. Lukens, P. Schmidt-Winkel, D. Zhao, J. Feng and G. D. Stucky, Evaluating Pore Sizes in Mesoporous Materials: A Simplified Standard Adsorption Method and a Simplified Broekhoff−de Boer Method, *Langmuir*, 1999, **15**, 5403-5409.

29. M. Hartmann and A. Vinu, Mechanical Stability and Porosity Analysis of Large-Pore SBA-15 Mesoporous Molecular Sieves by Mercury Porosimetry and Organics Adsorption, *Langmuir*, 2002, **18**, 8010-8016.

30. A. Galarneau, H. Cambon, F. Di Renzo, R. Ryoo, M. Choi and F. Fajula, Microporosity and connections between pores in SBA-15 mesostructured silicas as a function of the temperature of synthesis, *New J. Chem.*, 2003, **27**, 73-79.

31. F. Zhang, Yan, H. Yang, Y. Meng, C. Yu, B. Tu and D. Zhao, Understanding Effect of Wall Structure on the Hydrothermal Stability of Mesostructured Silica SBA-15, *J. Phys. Chem. B.*, 2005, **109**, 8723-8732.

32. H. P. Pu, H. Wang, S. X. Xu, C. Y. Han, L. Y. Zhang, Y. Y. Zhang, D. Q. Du and Y. M. Luo, in *Particulate Materials: Synthesis, Characterisation, Processing and Modelling*, The Royal Society of Chemistry, 2012, pp. 46-51.

33. K. Miyazawa and S. Inagaki, Control of the microporosity within the pore walls of ordered mesoporous silica SBA-15, *Chem. Commun.*, 2000, 2121-2122.

34. Y. Wan and D. Zhao, On the Controllable Soft-Templating Approach to Mesoporous Silicates, *Chem. Rev.*, 2007, **107**, 2821-2860.

35. G. A. Parks, The Isoelectric Points of Solid Oxides, Solid Hydroxides, and Aqueous Hydroxo Complex Systems, *Chem. Rev.*, 1965, **65**, 177-198.

36. J. M. Kim, Y.-J. Han, B. F. Chmelka and G. D. Stucky, One-step synthesis of ordered mesocomposites with non-ionic amphiphilic block copolymers: implications of isoelectric point, hydrolysis rate and fluoride, *Chem. Commun.*, 2000, 2437-2438.

37. X. Cui, W.-C. Zin, W.-J. Cho and C.-S. Ha, Nonionic triblock copolymer synthesis of SBA-15 above the isoelectric point of silica (pH = 2–5), *Mater. Lett.*, 2005, **59**, 2257-2261.

38. K. Kosuge, T. Sato, N. Kikukawa and M. Takemori, Morphological Control of Rod- and Fiberlike SBA-15 Type Mesoporous Silica Using Water-Soluble Sodium Silicate, *Chem. Mater.*, 2004, **16**, 899-905.

39. P. F. Fulvio, S. Pikus and M. Jaroniec, Short-time synthesis of SBA-15 using various silica sources, *J. Colloid Interface Sci.*, 2005, **287**, 717-720.

40. Liliane Andrade Lima, Gustavo Medeiros de Paula, Meiry Glaúcia Freire Rodrigues, SBA-15 Molecular Sieve Using Clay as Silicon Sources, *Mater. Sci. Forum*, 2014, **798-799**, 116-120.

41. B. L. Newalkar, S. Komarneni and H. Katsuki, Rapid synthesis of mesoporous SBA-15 molecular sieve by a microwave-hydrothermal process, *Chem. Commun.*, 2000, 2389-2390.

42. B. L. Newalkar and S. Komarneni, Control over Microporosity of Ordered Microporous−Mesoporous Silica SBA-15 Framework under Microwave-Hydrothermal Conditions: Effect of Salt Addition, *Chem. Mater.*, 2001, **13**, 4573-4579.

43. B. L. Newalkar and S. Komarneni, Simplified synthesis of micropore-free mesoporous silica, SBA-15, under microwave-hydrothermal conditions, *Chem. Commun.*, 2002, 1774-1775.

44. E. B. Celer and M. Jaroniec, Temperature-Programmed Microwave-Assisted Synthesis of SBA-15 Ordered Mesoporous Silica, *J. Am. Chem. Soc.*, 2006, **128**, 14408-14414.

45. S. Shen, F. Chen, P. S. Chow, P. Phanapavudhikul, K. Zhu and R. B. H. Tan, Synthesis of SBA-15 mesoporous silica via dry-gel conversion route, *Microporous Mesoporous Mater.*, 2006, **92**, 300-308.

46. W.-J. Kim and S.-M. Yang, Preparation of Mesoporous Materials from the Flow-Induced Microstructure in Aqueous Surfactant Solutions, *Chem. Mater.*, 2000, **12**, 3227-3235.

47. S. Gandhi, S. Sethuraman and U. Krishnan, Influence of polyhydric solvents on the catalytic & adsorption properties of self-oriented mesoporous SBA-15 silica, *J. Porous Mater.*, 2011, **18**, 329-336.

48. Y. Kang, J. He, X. GuoGuo, Guo and Z. Song, Influence of Pore Diameters on the Immobilization of Lipase in SBA-15, *Ind. Eng. Chem. Res.*, 2007, **46**, 4474-4479.

49. H. H. P. Yiu and P. A. Wright, Enzymes supported on ordered mesoporous solids: a special case of an inorganic-organic hybrid, *J. Mater. Chem.*, 2005, **15**, 3690-3700.

50. H. H. P. Yiu, P. A. Wright and N. P. Botting, Enzyme immobilisation using SBA-15 mesoporous molecular sieves with functionalised surfaces, *J. Mol. Catal. B: Enzym.*, 2001, **15**, 81-92.

51. J. Lei, J. Fan, C. Yu, L. Zhang, S. Jiang, B. Tu and D. Zhao, Immobilization of enzymes in mesoporous materials: controlling the entrance to nanospace, *Microporous Mesoporous Mater.*, 2004, **73**, 121-128.

52. P. Schmidt-Winkel, W. W. Lukens, D. Zhao, P. Yang, B. F. Chmelka and G. D. Stucky, Mesocellular Siliceous Foams with Uniformly Sized Cells and Windows, *J. Am. Chem. Soc.*, 1998, **121**, 254-255.

53. J. S. Lettow, Y. J. Han, P. Schmidt-Winkel, P. Yang, D. Zhao, G. D. Stucky and J. Y. Ying, Hexagonal to Mesocellular Foam Phase Transition in Polymer-Templated Mesoporous Silicas, *Langmuir*, 2000, **16**, 8291-8295.

54. L. Cao, T. Man and M. Kruk, Synthesis of Ultra-Large-Pore SBA-15 Silica with Two-Dimensional Hexagonal Structure Using Triisopropylbenzene As Micelle Expander, *Chem. Mater.*, 2009, **21**, 1144-1153.

55. L. Cao and M. Kruk, Short synthesis of ordered silicas with very large mesopores, *RSC Adv.*, 2014, **4**, 331-339.

56. H. Zhang, J. Sun, D. Ma, X. Bao, A. Klein-Hoffmann, G. Weinberg, D. Su and R. Schlögl, Unusual Mesoporous SBA-15 with Parallel Channels Running along the Short Axis, *J. Am. Chem. Soc.*, 2004, **126**, 7440-7441.

57. J. Sun, H. Zhang, D. Ma, Y. Chen, X. Bao, A. Klein-Hoffmann, N. Pfänder and D. S. Su, Alkanes-assisted low temperature formation of highly ordered SBA-15 with large cylindrical mesopores, *Chem. Commun.*, 2005, 5343-5345.

58. H. Zhang, J. Sun, D. Ma, G. Weinberg, D. S. Su and X. Bao, Engineered Complex Emulsion System: Toward Modulating the Pore Length and Morphological Architecture of Mesoporous Silicas, *J. Phys. Chem. B.*, 2006, **110**, 25908-25915.

59. J. Sun, D. Ma, H. Zhang, C. Wang, X. Bao, D. S. Su, A. Klein-Hoffmann, G. Weinberg and S. Mann, Phase evolution in the alkane-P123-water-TEOS quadru-component system: a feasible route to different complex mesostructured materials, *J. Mater. Chem.*, 2006, **16**, 1507-1510.

60. M. Kruk and L. Cao, Pore Size Tailoring in Large-Pore SBA-15 Silica Synthesized in the Presence of Hexane, *Langmuir*, 2007, **23**, 7247-7254.

61. J. Sun, D. Ma, H. Zhang, F. Jiang, Y. Cui, R. Guo and X. Bao, Organic Molecule-Modulated Phase Evolution of Inorganic Mesostructures, *Langmuir*, 2008, **24**, 2372-2380.

62. E. M. Johansson, J. M. Córdoba and M. Odén, The effects on pore size and particle morphology of heptane additions to the synthesis of mesoporous silica SBA-15, *Microporous Mesoporous Mater.*, 2010, **133**, 66-74.

63. K.-K. Kang and H.-K. Rhee, Synthesis and characterization of novel mesoporous silica with large wormhole-like pores: Use of TBOS as silicon source, *Microporous Mesoporous Mater.*, 2005, **84**, 34-40.

64. J. Liu, Q. Yang, X. S. Zhao and L. Zhang, Pore size control of mesoporous silicas from mixtures of sodium silicate and TEOS, *Microporous Mesoporous Mater.*, 2007, **106**, 62-67.

65. X. S. Zhao, A. S. M. Chong and G. Q. Lu, Surface functionalization of ordered nanoporous silicates, *Ser. Chem. Eng.*, 2004, **4**, 393-426.

66. J. S. Valenstein, K. Kandel, F. Melcher, I. I. Slowing, V. S. Y. Lin and B. G. Trewyn, Functional Mesoporous Silica Nanoparticles for the Selective Sequestration of Free Fatty Acids from Microalgal Oil, *ACS Appl. Mater. Interfaces*, 2012, **4**, 1003-1009.

67. L. Mercier and T. J. Pinnavaia, Direct Synthesis of Hybrid Organic−Inorganic Nanoporous Silica by a Neutral Amine Assembly Route: Structure−Function Control by Stoichiometric Incorporation of Organosiloxane Molecules, *Chem. Mater.*, 1999, **12**, 188-196.

68. M. H. Lim and A. Stein, Comparative Studies of Grafting and Direct Syntheses of Inorganic−Organic Hybrid Mesoporous Materials, *Chem. Mater.*, 1999, **11**, 3285-3295.

69. S. L. Burkett, S. D. Sims and S. Mann, Synthesis of hybrid inorganic-organic mesoporous silica by co-condensation of siloxane and organosiloxane precursors, *Chem. Commun.*, 1996, 1367-1368.

70. E. Da'na and A. Sayari, Adsorption of heavy metals on amine-functionalized SBA-15 prepared by co-condensation: Applications to real water samples, *Desalination*, 2012, **285**, 62-67.

71. Q. Wei, Z. Nie, Y. Hao, Z. Chen, J. Zou and W. Wang, Direct synthesis of thiol-ligand-functionalized SBA-15: Effect of 3-mercaptopropyltrimethoxysilane concentration on pore structure, *Mater. Lett.*, 2005, **59**, 3611-3615.

72. J. A. Melero, G. D. Stucky, R. van Grieken and G. Morales, Direct syntheses of ordered SBA-15 mesoporous materials containing arenesulfonic acid groups, *J. Mater. Chem.*, 2002, **12**, 1664-1670.

73. S. Fiorilli, B. Onida, B. Bonelli and E. Garrone, In Situ Infrared Study of SBA-15 Functionalized with Carboxylic Groups Incorporated by a Co-condensation Route, *J. Phys. Chem. B*, 2005, **109**, 16725-16729.

74. B. Karimi, S. Abedi, J. H. Clark and V. Budarin, Highly Efficient Aerobic Oxidation of Alcohols Using a Recoverable Catalyst: The Role of Mesoporous Channels of SBA-15 in Stabilizing Palladium Nanoparticles, *Angew. Chem. Int. Ed.*, 2006, **45**, 4776-4779.

75. G. Zhang, P. Wang and X. Wei, Palladium supported on functionalized mesoporous silica: synthesis, structure and catalytic properties in Suzuki-Miyaura coupling reactions, *Adv. Mater. Res. (Durnten-Zurich, Switz.)*, 2013, **750-752**, 1083-1086, 1085 pp.

76. J. Zhang, G. Huang, C. Zhang, Q. He, C. Huang, X. Yang, H. Song, Z. Liang, L. Du and S. Liao, Immobilization of highly active Pd nano-catalysts on functionalized mesoporous silica supports using mercapto groups as anchoring sites and their catalytic performance for phenol hydrogenation, *Cuihua Xuebao*, 2013, **34**, 1519-1526.

77. S. K. Natarajan and S. Selvaraj, Mesoporous silica nanoparticles: importance of surface modifications and its role in drug delivery, *RSC Adv.*, 2014, **4**, 14328-14334.

78. X. Wang, M. V. Landau, H. Rotter, L. Vradman, A. Wolfson and A. Erenburg, TiO_2 and ZrO_2 crystals in SBA-15 silica: performance of Pt/TiO_2(ZrO_2)/SBA-15 catalysts in ethyl acetate combustion, *J. Catal.*, 2004, **222**, 565-571.

79. A. E. Barrón C., J. A. Melo-Banda, J. M. Dominguez E., E. Hernández M., R. Silva R., A. I. Reyes T. and M. A. Meraz M., Catalytic hydrocracking of vegetable oil for agrofuels production using Ni–Mo, Ni–W, Pt and TFA catalysts supported on SBA-15, *Catal. Today*, 2011, **166**, 102-110.

80. X. J. Feng, M. Yan, X. Zhang and M. Bao, Preparation and application of SBA-15-supported palladium catalyst for Heck reaction in supercritical carbon dioxide, *Chin. Chem. Lett.*, 2011, **22**, 643-646.

81. N. W. Clifford, K. S. Iyer and C. L. Raston, Encapsulation and controlled release of nutraceuticals using mesoporous silica capsules, *J. Mater. Chem.*, 2008, **18**, 162-165.

82. M. Moritz and M. Łaniecki, Application of SBA-15 mesoporous material as the carrier for drug formulation systems. Papaverine hydrochloride adsorption and release study, *Powder Technol.*, 2012, **230**, 106-111.

83. A. L. Doadrio, E. M. B. Sousa, J. C. Doadrio, J. Pérez Pariente, I. Izquierdo-Barba and M. Vallet-Regí, Mesoporous SBA-15 HPLC evaluation for controlled gentamicin drug delivery, *J. Controlled Release*, 2004, **97**, 125-132.

84. L. Li, J. L. Shi, L. X. Zhang, L. M. Xiong and J. N. Yan, A Novel and Simple In-Situ Reduction Route for the Synthesis of an Ultra-Thin Metal Nanocoating in the Channels of Mesoporous Silica Materials, *Adv. Mater.*, 2004, **16**, 1079-1082.

85. P. Han, X. Wang, X. Qiu, X. Ji and L. Gao, One-step synthesis of palladium/SBA-15 nanocomposites and its catalytic application, *J. Mol. Catal. A: Chem.*, 2007, **272**, 136-141.

86. Z.-j. Wang, Y. Xie and C.-j. Liu, Synthesis and Characterization of Noble Metal (Pd, Pt, Au, Ag) Nanostructured Materials Confined in the Channels of Mesoporous SBA-15, *J. Phys. Chem. C*, 2008, **112**, 19818-19824.

87. M. Iwamoto and Y. Tanaka, Preparation of Metal Ion-Planted Mesoporous Silica by Template Ion-Exchange Method and Its Catalytic Activity for Asymmetric Oxidation of Sulfide, *Catalysis Surveys from Japan*, 2001, **5**, 25-36.

88. S. Wang, D. G. Choi and S. M. Yang, Incorporation of CdS Nanoparticles Inside Ordered Mesoporous Silica SBA-15 via Ion Exchange, *Adv. Mater.*, 2002, **14**, 1311-1314.

89. C. P. Mehnert, D. W. Weaver and J. Y. Ying, Heterogeneous Heck Catalysis with Palladium-Grafted Molecular Sieves, *J. Am. Chem. Soc.*, 1998, **120**, 12289-12296.

90. Y. Zhang, F. L.-Y. Lam, X. Hu, Z. Yan and P. Sheng, Fabrication of Copper Nanowire Encapsulated in the Pore Channels of SBA-15 by Metal Organic Chemical Vapor Deposition, *J. Phys. Chem. C.*, 2007, **111**, 12536-12541.

91. A. Gedanken, X. Tang, Y. Wang, N. Perkas, Y. Koltypin, M. V. Landau, L. Vradman and M. Herskowitz, Using Sonochemical Methods for the Preparation of Mesoporous Materials and for the Deposition of Catalysts into the Mesopores, *Chem. –Eur. J.*, 2001, **7**, 4546-4552.

92. R. M. Rioux, H. Song, J. D. Hoefelmeyer, P. Yang and G. A. Somorjai, High-Surface-Area Catalyst Design: Synthesis, Characterization, and Reaction Studies of Platinum Nanoparticles in Mesoporous SBA-15 Silica, *J. Phys. Chem. B.*, 2004, **109**, 2192-2202.

93. P. Wang, X. Luo, X. Wu, X. Wei, L. Zhou and X. Zheng, Structure and catalytic properties of Pd encapsulated in mesoporous silica SBA-15 fabricated by two-solvent strategy, *J. Porous Mater.*, 2013, **20**, 1-6.

94. J. Morère, M. J. Tenorio, M. J. Torralvo, C. Pando, J. A. R. Renuncio and A. Cabañas, Deposition of Pd into mesoporous silica SBA-15 using supercritical carbon dioxide, *J. Supercrit. Fluids*, 2011, **56**, 213-222.

95. L. Li, J.-l. Shi and J.-n. Yan, A highly efficient heterogeneous catalytic system for Heck reactions with a palladium colloid layer reduced in situ in the channel of mesoporous silica materials, *Chem. Commun.*, 2004, 1990-1991.

96. L. Li, L.-X. Zhang, J.-L. Shi, J.-N. Yan and J. Liang, New and efficient heterogeneous catalytic system for Heck reaction: palladium colloid layer in situ reduced in the channel of mesoporous silica materials, *Appl. Catal., A-Gen.*, 2005, **283**, 85-89.

97. P. Wang, Z. Wang, J. Li and Y. Bai, Preparation, characterizations, and catalytic characteristics of Pd nanoparticles encapsulated in mesoporous silica, *Microporous Mesoporous Mater.*, 2008, **116**, 400-405.

98. P. Wang and X. Zheng, Pd/SBA-15 nanocomposite: Synthesis, structure and catalytic properties in Heck reactions, *Powder Technol.*, 2011, **210**, 115-121.

99. *C. M. Crudden, M. Sateesh and A. Blanc,* WO2006094392A1, 2006.

100. J. Demel, M. Lamac, J. Cejka and P. Stepnicka, Palladium Catalysts Supported on Mesoporous Molecular Sieves Bearing Nitrogen Donor Groups: Preparation and Use in Heck and Suzuki C-C Bond-Forming Reactions, *ChemSusChem*, 2009, **2**, 442-451.

101. J.-Y. Jung, A. Taher, H.-J. Kim, W.-S. Ahn and M.-J. Jin, Heck reaction catalyzed by mesoporous SBA-15-supported ionic liquid-$Pd(OAc)_2$, *Synlett*, 2009, 39-42.

102. W. Zhang, Q. Wang, F. Qin, H. Zhou, Z. Lu and R. Chen, Microwave-assisted facile synthesis of palladium nanoparticles in HEPES solution and their size-dependent catalytic activities to Suzuki reaction, *J. Nanosci. Nanotechnol.*, 2011, **11**, 7794-7801.

103. A. Fallah, D. Kordestani, A. Alizadeh and S. Endud, Supported palladium catalysis using a biguanide N-donor motif on mesoporous silica for Suzuki-Miyaura coupling reaction, *Adv. Mater. Res. (Durnten-Zurich, Switz.)*, 2013, **622-623**, 757-761, 756 pp.

104. W. Chang, G. H. Chae, S. R. Jang, J. Shin and B. J. Ahn, An efficient microwave-assisted Suzuki reaction using Pd/MCM-41 and Pd/SBA-15 as catalysts in solvent-free condition, *J. Ind. Eng. Chem. (Amsterdam, Neth.)*, 2012, **18**, 581-585.

105. T. Zhang, X.-j. Feng, M. Yan and M. Bao, Preparation and application of SBA-15-supported palladium catalyst for Suzuki coupling reactions in supercritical carbon dioxide, *Fenzi Kexue Xuebao*, 2008, **24**, 1-5.

106. J. Yin, W. Chai, F. Zhang and H. Li, Periodic mesoporous silica-supported Ni(II) organometallic complex as an active and reusable nanocatalyst for water-medium Sonogashira coupling reaction, *Appl. Organomet. Chem.*, 2013, **27**, 512-518.

107. H. Li, W. Chai, F. Zhang and J. Chen, Water-medium Ullmann reaction over a highly active and selective Pd/Ph-SBA-15 catalyst, *Green Chem.*, 2007, **9**, 1223-1228.

108. C. Y. Ma, B. J. Dou, J. J. Li, J. Cheng, Q. Hu, Z. P. Hao and S. Z. Qiao, Catalytic oxidation of benzyl alcohol on Au or Au-Pd nanoparticles confined in mesoporous silica, *Appl. Catal., B*, 2009, **92**, 202-208.

109. L. Jia, X. Guo and L. Ma*,* CN103497093A, 2014.

110. R. Hosseinpour, A. Pineda, M. Ojeda, A. Garcia, A. A. Romero and R. Luque, Microwave-assisted oxidation of benzyl alcohols using supported cobalt based nanomaterials under mild reaction conditions, *Green Process. Synth.*, 2014, **3**, 133-139.

111. C. M. A. Parlett, D. W. Bruce, N. S. Hondow, A. F. Lee and K. Wilson, Support-Enhanced Selective Aerobic Alcohol Oxidation over Pd/Mesoporous Silicas, *ACS Catal.*, 2011, **1**, 636-640.

112. C. S. Chen, Y. T. Lai, T. C. Chen, C. H. Chen, J. F. Lee, C. W. Hsu and H. M. Kao, Synthesis and characterization of Pt nanoparticles with different morphologies in mesoporous silica SBA-15 for methanol oxidation reaction, *Nanoscale*, 2014, **6**, 12644-12654.

113. C. He, J. Li, J. Cheng, L. Li, P. Li, Z. Hao and Z. P. Xu, Comparative Studies on Porous Material-Supported Pd Catalysts for Catalytic Oxidation of Benzene, Toluene, and Ethyl Acetate, *Ind. Eng. Chem. Res.*, 2009, **48**, 6930-6936.

114. Z. Qu, S. Shen, D. Chen and Y. Wang, Highly active Ag/SBA-15 catalyst using post-grafting method for formaldehyde oxidation, *J. Mol. Catal. A: Chem.*, 2012, **356**, 171-177.

115. Y.-H. Kim and Y.-B. Son, Environmentally friendly liquid phase oxidation of p-xylene using SBA-15 supported transition metal ions, *Nonmunjip - Ch'ungnam Taehakkyo Sanop Kisul Yon'guso*, 2003, **18**, 92-103.

116. G. Centi, P. Lanzafame and S. Perathoner, Performances of Co-based catalysts for the selective side chain oxidation of toluene in the gas phase, *Catal. Today*, 2005, **99**, 161-170.

117. H. Ma, J. Xu, C. Chen, Q. Zhang, J. Ning, H. Miao, L. Zhou and X. Li, Catalytic aerobic oxidation of ethylbenzene over Co/SBA-15, *Catal. Lett.*, 2007, **113**, 104-108.

118. Z. Mu, J. J. Li, H. Tian, Z. P. Hao and S. Z. Qiao, Synthesis of mesoporous Co/Ce-SBA-15 materials and their catalytic performance in the catalytic oxidation of benzene, *Mater. Res. Bull.*, 2008, **43**, 2599-2606.

119. X. Bai and J. Shen, Study on the performance of Co-SBA-15 catalyst for catalytic oxidation of styrene to benzaldehyde, *Shiyou Lianzhi Yu Huagong*, 2011, **42**, 23-27.

120. K. Bendahou, L. Cherif, S. Siffert, H. L. Tidahy, H. Benaissa and A. Aboukais, The effect of the use of lanthanum-doped mesoporous SBA-15 on the performance of Pt/SBA-15 and Pd/SBA-15 catalysts for total oxidation of toluene, *Appl. Catal., A*, 2008, **351**, 82-87.

121. C. He, P. Li, J. Cheng, J. Li and Z. Hao, Preparation and investigation of Pd/Ti-SBA-15 catalysts for catalytic oxidation of benzene, *Environ. Prog. Sustainable Energy*, 2010, **29**, 435-442.

122. C. Tu, A. Wang, M. Zheng, Y. Meng, J. Shan and T. Zhang, A novel active catalyst Ag/SBA-15 for CO oxidation, *Cuihua Xuebao*, 2005, **26**, 631-633.

123. X. Zhang, Z. Qu, X. Li, Q. Zhao, Y. Wang and X. Quan, Low temperature CO oxidation over Ag/SBA-15 nanocomposites prepared via in-situ "pH-adjusting" method, *Catal. Commun.*, 2011, **16**, 11-14.

124. C.-m. Yang, M. Kalwei, F. Schuth and K.-j. Chao, Gold nanoparticles in SBA-15 showing catalytic activity in CO oxidation, *Appl. Catal., A*, 2003, **254**, 289-296.

125. C.-W. Chiang, A. Wang, B.-Z. Wan and C.-Y. Mou, High Catalytic Activity for CO Oxidation of Gold Nanoparticles Confined in Acidic Support Al-SBA-15 at Low Temperatures, *J. Phys. Chem. B*, 2005, **109**, 18042-18047.

126. Y.-S. Chi, H.-P. Lin and C.-Y. Mou, CO oxidation over gold nanocatalyst confined in mesoporous silica, *Appl. Catal., A*, 2005, **284**, 199-206.

127. H. Zhu, C. Liang, W. Yan, S. H. Overbury and S. Dai, Preparation of Highly Active Silica-Supported Au Catalysts for CO Oxidation by a Solution-Based Technique, *J. Phys. Chem. B*, 2006, **110**, 10842-10848.

128. C.-W. Chiang, A. Wang and C.-Y. Mou, CO oxidation catalyzed by gold nanoparticles confined in mesoporous aluminosilicate Al-SBA-15: Pretreatment methods, *Catal. Today*, 2006, **117**, 220-227.

129. M. Ruszel, B. Grzybowska, M. Laniecki and M. Wojtowski, Au/Ti-SBA-15 catalysts in CO and preferential (PROX) CO oxidation, *Catal. Commun.*, 2007, **8**, 1284-1286.

130. X. Liu, A. Wang, X. Wang, C.-Y. Mou and T. Zhang, Au-Cu Alloy nanoparticles confined in SBA-15 as a highly efficient catalyst for CO oxidation, *Chem. Comm.*, 2008, 3187-3189.

131. C.-H. Tu, A.-Q. Wang, M.-Y. Zheng, X.-D. Wang and T. Zhang, Factors influencing the catalytic activity of SBA-15-supported copper nanoparticles in CO oxidation, *Appl. Catal., A*, 2006, **297**, 40-47.

132. X. Xu, J. Li, Z. Hao, W. Zhao and C. Hu, Characterization and catalytic performance of Co/SBA-15 supported gold catalysts for CO oxidation, *Mater. Res. Bull.*, 2006, **41**, 406-413.

133. H. Wang and C.-j. Liu, Preparation and characterization of SBA-15 supported Pd catalyst for CO oxidation, *Appl. Catal., B*, 2011, **106**, 672-680.

134. S. V. Kolotilov, K. S. Gavrilenko, M. R. Kantserova, A. V. Yakovenko, N. N. Stepanenko, N. V. Kas'yan and A. V. Shvets, Catalytic activity of nanosized Co-Cu oxide systems in the deep oxidation of methane, *Theor. Exp. Chem.*, 2005, **41**, 347-351.

135. I. Yuranov, L. Kiwi-Minsker and A. Renken, Structured combustion catalysts based on sintered metal fibre filters, *Appl. Catal., B*, 2003, **43**, 217-227.

136. Q. Lu, Z. Tang, Y. Zhang and X.-f. Zhu, Catalytic Upgrading of Biomass Fast Pyrolysis Vapors with Pd/SBA-15 Catalysts, *Ind. Eng. Chem. Res.*, 2010, **49**, 2573-2580.

137. S. Lestari, P. Maeki-Arvela, K. Eraenen, J. Beltramini, G. Q. Max Lu and D. Y. Murzin, Diesel-like Hydrocarbons from Catalytic Deoxygenation of Stearic Acid over Supported Pd Nanoparticles on SBA-15 Catalysts, *Catal. Lett.*, 2010, **134**, 250-257.

138. S. Abate, K. Barbera, P. Lanzafame, S. Perathoner and G. Centi, Direct H_2O_2 synthesis from H_2 and O_2 using Pd-SBA-15 and CO_2-expanded solvents, *Prepr. - Am. Chem. Soc., Div. Pet. Chem.*, 2008, **53**, 227-229.

139. S. Park, T. J. Kim, Y.-M. Chung, S.-H. Oh and I. K. Song, Direct Synthesis of Hydrogen Peroxide from Hydrogen and Oxygen over Palladium Catalyst Supported on SO_3H-Functionalized SBA-15, *Catal. Lett.*, 2009, **130**, 296-300.

140. S.-S. Lee, B.-K. Park, S.-H. Byeon, F. Chang and H. Kim, Mesoporous Silica-Supported Pd Nanoparticles; Highly Selective Catalyst for Hydrogenation of Olefins in Supercritical Carbon Dioxide, *Chem. Mater.*, 2006, **18**, 5631-5633.

141. J. Liu, H. Lu, Z. Ling, L. Shi, B. Xu and Y. Fan, Catalytic properties of supported Pd/SBA-15 catalyst for selective hydrogenation of alkadienes, *Cuihua Xuebao*, 2008, **29**, 206-208.

142. D. Liu, Research on catalytic hydrogenation performance of Pd/SBA-15 supported catalyst, *Huaxue Gongye Yu Gongcheng Jishu*, 2012, **33**, 7-9.

143. S.-H. Chung, Y.-M. Park, M.-S. Kim and K.-Y. Lee, The effect of textural properties on the hydrogenation of succinic acid using palladium incorporated mesoporous supports, *Catal. Today*, 2012, **185**, 205-210.

144. I. Yuranov, P. Moeckli, E. Suvorova, P. Buffat, L. Kiwi-Minsker and A. Renken, Pd/SiO_2 catalysts: synthesis of Pd nanoparticles with the controlled size in mesoporous silicas, *J. Mol. Catal. A: Chem.*, 2003, **192**, 239-251.

145. L. Djakovitch, V. Dufaud and R. Zaidi, Heterogeneous palladium catalysts applied to the synthesis of 2- and 2,3-functionalised indoles, *Adv. Synth. Catal.*, 2006, **348**, 715-724.

146. X. Hu and S. Dong, Metal nanomaterials and carbon nanotubes-synthesis, functionalization and potential applications towards electrochemistry, *J. Mater. Chem.*, 2008, **18**, 1279-1295.

147. Y. Bai, H. Yang, W. Yang, Y. Li and C. Sun, Gold nanoparticles-mesoporous silica composite used as an enzyme immobilization matrix for amperometric glucose biosensor construction, *Sensor Actuat. B-Chem.*, 2007, **124**, 179-186.

148. Y. Liu, Q. Xu, X. Feng, J.-J. Zhu and W. Hou, Immobilization of hemoglobin on SBA-15 applied to the electrocatalytic reduction of H_2O_2, *Anal Bioanal Chem*, 2007, **387**, 1553-1559.

149. L. Yuge, Z. Jingjing, H. Wenhua and Z. Jun-Jie, A Pd/SBA-15 composite: synthesis, characterization and protein biosensing, *Nanotechnology*, 2008, **19**, 135707.

150. S. Weng, Z. Lin, Y. Zhang, L. Chen and J. Zhou, Facile synthesis of SBA-15/polyaniline nanocomposites with high electrochemical activity under neutral and acidic conditions, *React. Funct. Polym.*, 2009, **69**, 130-136.

151. Y. Liu, J. Lei and H. Ju, CuO-doped mesoporous silica hybrid for rapid and sensitive amperometric detection of phenolic compounds, *Electroanalysis*, 2010, **22**, 2407-2412.

152. H. Ma, K. Mao, H. Li, D. Wu, Y. Zhang, B. Du and Q. Wei, Ultrasensitive multiplexed immunosensors for the simultaneous determination of endocrine disrupting compounds using Pt@SBA-15 as a non-enzymatic label, *J. Mater. Chem. B*, 2013, **1**, 5137-5142.

153. M. Vallet-Regí, F. Balas and D. Arcos, Mesoporous Materials for Drug Delivery, *Angew. Chem. Int. Ed.*, 2007, **46**, 7548-7558.

154. L. B. Fagundes, T. G. F. Sousa, A. Sousa, V. V. Silva and E. M. B. Sousa, SBA-15-collagen hybrid material for drug delivery applications, *J. Non-Cryst. Solids*, 2006, **352**, 3496-3501.

155. D. H. Hwang, D. Lee, H. Lee, D. Choe, S. H. Lee and K. Lee, Surface functionalization of SBA-15 particles for ibuprofen delivery, *Korean J. Chem. Eng.*, 2010, **27**, 1087-1092.

156. T. Lopez, E. Krotzsch, E. Ortiz-Islas, M. Alvarez-Lemus, E. Balsadella, J. M. Martinez-Blanes and J. A. Odriozola, Release properties and acute biosecurity determination of collagen-polyvinylpyrrolidone loaded in ordered mesoporous silica, *Key Eng. Mater.*, 2009, **391**, 169-184.

157. D. Halamova, M. Badanicova, V. Zelenak, T. Gondova and U. Vainio, Naproxen drug delivery using periodic mesoporous silica SBA-15, *Appl. Surf. Sci.*, 2010, **256**, 6489-6494.

158. F. Sevimli and A. Yilmaz, Surface functionalization of SBA-15 particles for amoxicillin delivery, *Microporous Mesoporous Mater.*, 2012, **158**, 281-291.

159. W. J. Qian, M. M. Wan, W. G. Lin and J. H. Zhu, Fabricating a sustained releaser of heparin using SBA-15 mesoporous silica, *J. Mater. Chem. B*, 2014, **2**, 92-101.

160. L. Hajiaghababaei, T. Tajmiri, A. Badiei, M. R. Ganjali, Y. Khaniani and G. M. Ziarani, Heavy metals determination in water and food samples after preconcentration by a new nanoporous adsorbent, *Food Chem.*, 2013, **141**, 1916-1922.

161. A. M. Liu, K. Hidajat, S. Kawi and D. Y. Zhao, A new class of hybrid mesoporous materials with functionalized organic monolayers for selective adsorption of heavy metal ions, *Chem. Commun. (Cambridge)*, 2000, 1145-1146.

162. R. A. Sperling and W. J. Parak, Surface modification, functionalization and bioconjugation of colloidal inorganic nanoparticles, *Philosophical Transactions of the Royal Society A: Mathematical, Physical and Engineering Sciences*, 2010, **368**, 1333-1383.

163. A. Arencibia, J. Aguado and J. M. Arsuaga, Regeneration of thiol-functionalized mesostructured silica adsorbents of mercury, *Appl. Surf. Sci.*, 2010, **256**, 5453-5457.

164. *H. Huang, C. Dong, D. Zhao, H. Yang, G. Zhang, Y. Liu, Y. Xue, W. Bai, B. Liang, Z. Liu, Y. Song, L. Du and Z. Zhang,* CN103981368A, 2014.

165. B. L. Newalkar, Choudary, Nettem V., Turaga, Uday T., Vijayalakshmi, R. P., Kumar, Prakash, Komarneni, S., Bhat, Thirumaleshwara S. G., Potential Adsorbent for Light Hydrocarbon Separation: Role of SBA-15 Framework Porosity, *Chem. Mater.*, 2003, **15**, 1474-1479.

166. E. I. Basaldella, J. C. Tara, G. A. Armenta and M. E. P. Iglesias, Cu/SBA-15 as adsorbent for propane/propylene separation, *J. Porous Mater.*, 2007, **14**, 273-278.

167. W. Ren, S. Chen, Y. Zhang and G. Li, Preparation of Zn/SBA-15 mesoporous adsorbent and its property for H_2S removal, *Huagong Jinzhan*, 2011, **30**, 2304-2309.

168. J. Hu and H. Liu, CO_2 adsorption on porous materials: experimental and simulation study, *ACS Symp. Ser.*, 2010, **1056**, 209-232.

169. G. Calleja, R. Sanz, A. Arencibia and E. S. Sanz-Perez, Influence of drying conditions on amine-functionalized SBA-15 as adsorbent of CO_2, *Top. Catal.*, 2011, **54**, 135-145.

170. J.-h. Shan and X.-q. Liu, Adsorption of sulfur-containing compounds on CuCl/SBA-15 molecular sieve prepared by the thermal diffusion method, *Gongneng Cailiao*, 2010, **41**, 2194-2197.

171. J. Zhao, F. Gao, Y. Fu, W. Jin, P. Yang and D. Zhao, Biomolecule separation using large pore mesoporous SBA-15 as a substrate in high performance liquid chromatography, *Chem. Comm.*, 2002, 752-753.

172. F. Gao, J.-W. Zhao, S. Zhang, F. Zhou, W. Jin, X.-M. Zhang, P.-Y. Yang and D.-Y. Zhao, Application of C18-modified mesoporous SBA-15 as the substrate for high performance liquid chromatography, *Gaodeng Xuexiao Huaxue Xuebao*, 2002, **23**, 1494-1497.

173. J. Zhou, H.-Y. Zhong, L. Yin, X.-D. Yu and H.-Y. Chen, Separation of vitamin E isomers using mesoporous SBA-15 as stationary phase by high performance liquid chromatography, *Fenxi Huaxue*, 2011, **39**, 777-780.

174. Y. Liu, M. Ju, W. Li, Y. Jiang, D. Zhang and X. Chen, CN104047197A, 2014.

175. A. M. Buckley and M. Greenblatt, The Sol-Gel Preparation of Silica Gels, *J. Chem. Educ.*, 1994, **71**, 599.

176. W. M. Jones and D. B. Fischbach, Novel processing of silica hydrosols and gels, *J. Non-Cryst. Solids*, 1988, **101**, 123-126.

177. D. Avnir and V. R. Kaufman, Alcohol is an unnecessary additive in the silicon alkoxide sol-gel process, *J. Non-Cryst. Solids*, 1987, **92**, 180-182.

178. J. Šefčik and A. V. McCormick, Kinetic and thermodynamic issues in the early stages of sol-gel processes using silicon alkoxides, *Catal. Today*, 1997, **35**, 205-223.

179. M. Prassas, Hench, L. L, Ultrastructure processing of ceramics, glasses and composites, *by L.L Hench, D.R Ulrich, Wiley, New York*, 1984, 100.

180. B. E. Yoldas, Effect of molecular separation on the hydrolytic polycondensation of $Si(OC_2H_5)_4$, *J. Non-Cryst. Solids*, 1986, **82**, 11-23.

181. K. Kajihara, M. Hirano and H. Hosono, Sol-gel synthesis of monolithic silica gels and glasses from phase-separating tetraethoxysilane-water binary system, *Chem. Commun.*, 2009, 2580-2582.

182. E. J. A. Pope and J. D. Mackenzie, Sol-gel processing of silica: II. The role of the catalyst, *J. Non-Cryst. Solids*, 1986, **87**, 185-198.

183. J. E. Lofgreen and G. A. Ozin, Controlling morphology and porosity to improve performance of molecularly imprinted sol-gel silica, *Chem. Soc. Rev.*, 2014, **43**, 911-933.

184. P. Buisson, H. El Rassy, S. Maury and A. C. Pierre, Biocatalytic Gelation of Silica in the Presence of a Lipase, *J. Sol-Gel Sci. Technol.*, 2003, **27**, 373-379.

185. M. Yamane, S. Aso, S. Okano and T. Sakaino, Low temperature synthesis of a monolithic silica glass by the pyrolysis of a silica gel, *Journal of Materials Science*, 1979, **14**, 607-611.

186. L. L. Hench and W. Vasconcelos, Gel-Silica Science, *Annu. Rev. Mater. Sci.*, 1990, **20**, 269-298.

187. J. Estella, J. C. Echeverría, M. Laguna and J. J. Garrido, Silica xerogels of tailored porosity as support matrix for optical chemical sensors. Simultaneous effect of pH, ethanol:TEOS and water:TEOS molar ratios, and synthesis temperature on gelation time, and textural and structural properties, *J. Non-Cryst. Solids*, 2007, **353**, 286-294.

188. T. Sen and I. J. Bruce, Surface engineering of nanoparticles in suspension for particle based bio-sensing, *Sci. Rep.*, 2012, **2**.

189. M. C. Kyung, in *Optical Devices in Communication and Computation*, ed. P. Xi, InTech, 2012, ch. 10, p. 230.

190. X. Zhou, S. Cui, Y. Liu, X. Liu, X. Shen and Z. Wu, Adsorption capacity of hydrophobic SiO2 aerogel/activated carbon composite materials for TNT, *Science China Technological Sciences*, 2013, **56**, 1767-1772.

191. C. J. Brinker and G. W. Scherer, *Sol-gel science: the physics and chemistry of sol-gel processing*, Gulf Professional Publishing, 1990.

192. L. Yasmin, X. Chen, K. A. Stubbs and C. L. Raston, Optimising a vortex fluidic device for controlling chemical reactivity and selectivity, *Sci. Rep.*, 2013, **3**, 2282.

193. J. Britton and C. L. Raston, Continuous flow vortex fluidic production of biodiesel, *RSC Adv.*, 2014, **4**, 49850-49854.

194. R. A. Boulos, C. L. Raston, F. Zhang, E. S. Tjandra, D. Spagnoli and A. D. Martin, Spinning up the polymorphs of calcium carbonate, *Sci. Rep.*, 2014, **4**, 3616.

Chapter Two

Synthetic Strategies

2.1. Process intensification

2.1.1. Brief overview for process intensification modules

Process intensification is a strategy employed to enhance the transport properties by understanding the hydrodynamic behaviour of a system, which is beneficial for enhancing the production throughput, product quality, and reducing the production cost. As opposed to the batch processing, process intensification creates a thin film spread across a surface that significantly increases the surface to volume ratio, which leads to more influential interactions between the film and its surroundings.[1] These intensified modules include the spinning disc processor (SDP) and the rotating tube processor (RTP), Figure 2.1.[2]

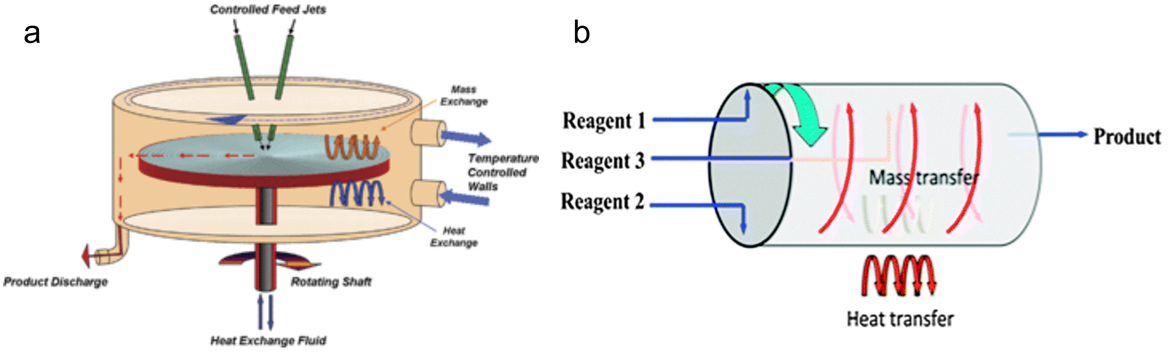

Figure 2.1. *Schematic of (a) spinning disc processor (SDP) and (b) rotating tube processor (RTP). Taken from review article "Controlling nanomaterial synthesis, chemical reactions and self assembly in dynamic thin films".*[2]

Both SDP and RTP provide excellent micro-mixing efficiency, have high heat and mass transfer properties, and they are energy efficient continuous processing platforms for chemical reactions such as polymerization and crystallization.[2] RTP has an advantage over the SDP with the ability to control the residence time for the reactions within the thin film.[2]

There are number of reports on the success of using SDP or RTP in nanofabrication. For example, SDP has been used to uniformly coat fullerene C_{60} fibres with silver, forming a silver-C_{60} nano-hybrid.[3] In addition, SDP can be used to exfoliate pristine graphite flakes and hexagonal boron nitride, which simultaneously forms carbon and boron nitride nano-scrolls.[4] SDP and RTP have been used in fabricating ultrathin single-crystalline rhabdophane lanthanide phosphate ($LnPO_4$) nanowires at room temperature in water, with controllable aspect ratio of the nano-crystals arising from suppression of the Ostwald ripening phenomenon.[5] RTP has been used in the preparation of gold nanorods,[6] curcumin nanoparticles of less than 50 nm in diameter,[7] and semicrystalline meloxicam nanoparticles of less than 100 nm in diameter without the use of organic solvent,[8] and more.[2] However, there are drawbacks on the use of the SDP and RTP. They strictly operate under continuous flow conditions requiring large volumes of liquids, typically up to 500 mL, to probe the effects of intense shearing within the dynamic thin films.[1] They are also inherently expensive to construct.

2.1.2. Introduction to the vortex fluidic device (VFD)

In addressing the drawbacks of SDP and RTP and incorporating additional operational parameters, Colin L. Raston developed a hybrid device where a thin film is formed within a cylindrical surface, closed at one end and open at the other, along the longitudinal axis, with the angle of the longitudinal axis relative to the horizontal is variable from 0 to 90 degrees, Figure 2.2.[1] This device was patented in 2010 and is officially named as a vortex fluidic device (VFD), and can be constructed for less than \$5k (AUS) for the basic unit. The VFD can operates at an angle relative to the horizontal axis using relatively low volumes (< 1 mL) while maintaining the shear forces of the type in thin films generated in the SDP and RTP.[1] Moreover, it can operate under either batch mode or continuous flow mode without losing the micro-mixing efficiency. The difference between two operation modes are, under batch mode, a reaction is carried out with finite volume of reagents for a specific duration, whereas in continuous flow mode, the reagents are introduced into the system using pumps, and reaction is carried out continuously.

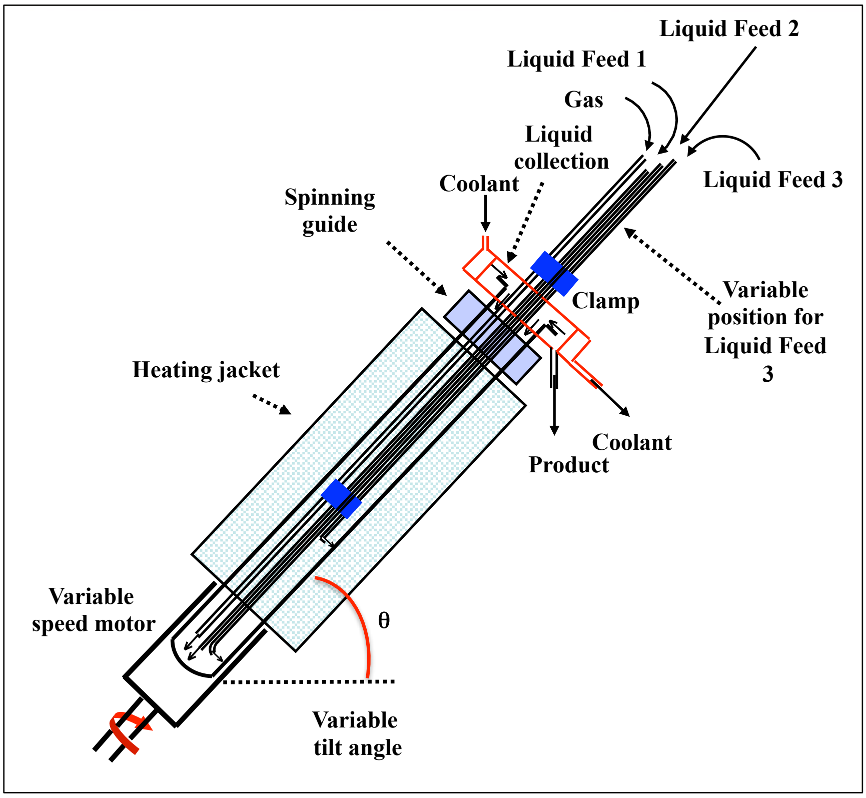

Figure 2.2. *Schematic drawing of the vortex fluidic device.*[1]

The VFD is fabricated in two prototypes, having a 10 mm or 20 mm OD (8.45 mm and 18 mm ID), rotating tubes, typically as borosilicate glass. They are equipped with multiple feed jets made of 1/8” stainless steel tubing, a variable speed motor, and a heating jacket. Liquid reactants can be fed separately via the feed jets entering the closed end of the rotating cylinder. With the variable rotational speed up to 10,000 rpm, the centrifugal forces within the system form a homogeneous thin film in the inner surface of the cylinder creating an annular flow,[1] and the products can be collected at the open end when operating under continuous flow, as show in Figure 2.1. Thin film generated within the tubes results in even micro-mixing and high mass transfer rates throughout the entire system. This is a significant advantage over the conventional round bottom flask reactions, which often suffer from uneven mixing in a large-scale reaction, and also uneven heat transfer. Process controls such as the nature of the reactants, feed rates and rotational speed greatly influence the effect of mass transfer, with these parameters dictating the reaction residence times and the thickness of the thin film. Accordingly, optimization studies are necessary for every reaction, and may require significantly different conditions for even closely related reactions. Moreover, VFD processing can also include the implementation of field effects, as in the use of standard light sources, lasers, plasmas, magnetic fields, and acoustic energy.

2.1.3. Overview of VFD research

Thus far, twenty publications have appeared on using the VFD for a different number of fields, all arising from Colin L. Raston's laboratory.[9-28] Of these, a major focus has been on the use of the VFD in organic synthesis, in particular in controlling chemical reactivity and selectivity that is not possible using conventional round bottom flask, and indeed the use of the VFD here can circumvent the need for heating. The VFD is effective in accelerating Diels-Alder dimerization of cyclopentadienes, and sequential aldol and Michael addition reactions.[17] As discussed in the previous section, the VFD has different shear regimes that arise from the difference in the film thickness, which depends on the rotational speed and tilt angle θ, and flow rates, if any. The influence of average film thickness for a finite volume of liquid at various rotating speed and tilting angle is determined mathematically from the surface coverage of the film for 1 mL water containing a low concentration of dye, Figure 2.3.[17]

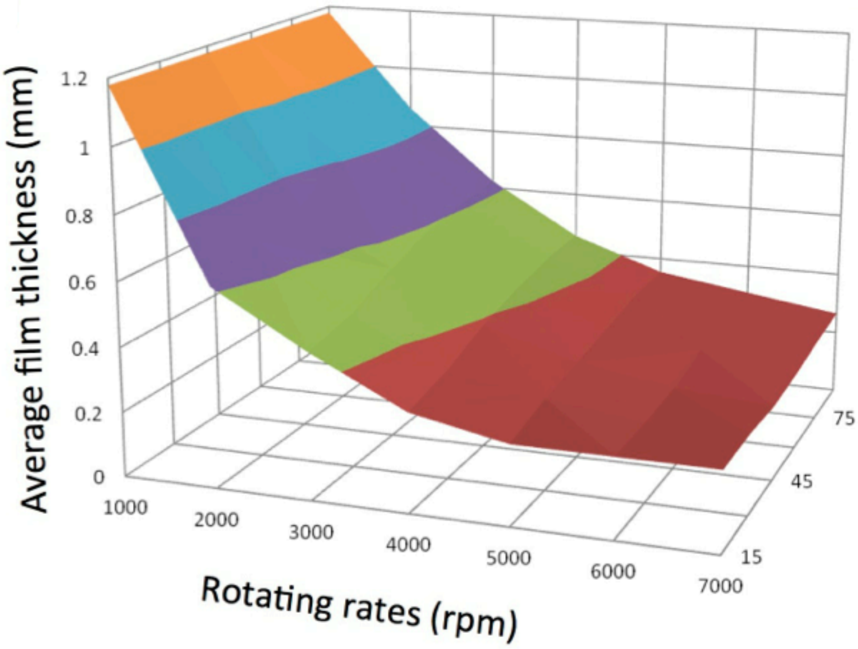

Figure 2.3. *Average film thickness (mm) versus tilt angle θ and rotational speed in a standard 10 mm prototype VFD, operating under the confined mode. Taken from Yasmin et.al.*[17]

By understanding of the effect of VFD on molecular reactions, other organic syntheses can be carried out using this platform, with often remarkable outcomes. For example, the VFD allows high reactivity and selectivity, under continuous flow conditions, in the synthesis of resorcin[4]arenes and pyrogallol[4]arenes with minimal catalyst amount, with the preferred stereochemistry.[18] Other reactions include highly efficient Diels-Alder reactions for different 9-substituted anthracenes and N-maleimides in an aqueous medium,[25] the synthesis of alkylaminopyrazines without the need for the addition of a transition metal catalyst,[21] and the single pass synthesis of polysubstituted and 2,4,6-trisubstituted pyridines.[24] These results promote chemical synthesis towards a focus on environmental concern, quality control, safety and economical perspective.[25] This is highlighted by the recent success on converting sunflower oil to biodiesel in > 99% yield in room temperature, under continuous flow using VFD,[20] and similarly in converting free fatty acids into biodiesel.[28]

Organic synthesis aside, the VFD is also effective in top-down and bottom-up syntheses of nanomaterials such as exfoliation of graphite and boron nitride under confined mode,[9] and the methodology has been applied in fabricating a biohybrid materials composed of the multi-layer graphene and *Cholorella vulgaris* cells or entrapping the microalgae cells within graphene oxide layers, which are effective for nitrate removal from liquid effluent.[15, 16] VFD processing is effective in preparing superparamagnetic particles,[12] and in the control over the growth of nanoparticles. This is demonstrated by decorating the carbon nano onions (CNOs) with Pd nanoparticles[10] and Pt nanoparticles,[13] with control over the size and distribution of the nanoparticles. A similar approach has been used (1) to decorate the ultrafine Pd nanoparticles on non-covalently functionalized graphene sheets,[11] (2) to decorate carbon nanotubes (CNTs) and CNOs with Pd nanoparticles.[14] Given palladium nanoparticles possess hydrogen adsorption capabilities, the materials in (1) and (2) have been incorporated into a hydrogen sensing device via drop casting techniques, with promising electrocatalytic properties.[11, 14]

More notably, the VFD has been used to control the formation of calcium carbonate polymorphs by varying the shear and temperature of the process.[19] Interestingly, the ability to selectively generate the different polymorphs, namely aragonite, calcite, or vaterite, provides insight into understanding the effect of more hostile conditions on marine organisms under different environmental conditions in the oceans.[19] With this finding, the same approach was used to prepare stable, monodispersed amorphous calcium carbonate at room temperature without using additives.[22] Then there is the intensity and influence of shear forces within the thin film in the VFD to facilitate exfoliation of individual SWCNTs, in overcoming the Van der Waals forces between the bundles of single walled carbon nanotubes (SWCNTs). This results in compacting and intertwining the SWCNTs, in generating nanorings.[23]

2.2. Research methodology using VFD

Intrigued by the versatility of the VFD in a number of scientific endeavours, the possibility of using the platform to prepare silica, in particular SBA-15 was considered, noting the applications of the material, for example as a molecular sieve, and that the current method of synthesis involves lengthy processing which is not energy efficiency. Overall, the aim of this research was to develop a new synthesis method for SBA-15 using VFD, from a process enhancement perspective. The proposed method has the potential to drastically shorten the synthesis time, avoid hydrothermal processing, provide a way of tuning the properties of the material in terms of pore size, micropore volume and surface area of the final product. This relates to the mechanical shearing forces and the ability to carry out the synthesis under ambient conditions and continuous flow. Apart from synthesizing SBA-15, the preparation of silica hydrogel using aqueous medium, without the additive of co-solvent and catalyst, was also explored using VFD processing.

2.2.1. VFD method for preparing SBA-15

In general, 4.0 g of Pluronic® P-123 is stirred and dissolved in 50 mL deionized water and 10 mL of 32 – 37 wt% HCl in a water bath at 40 to 45 ˚C for an hour. The dissolved micelles solution is then fed into VFD, which is inclined at 45˚ angle and various rotational speeds. This initial step of pre-stressing the micelles is important in determining the pore diameter, which will be discussed in Chapter 3. The pre-stressed micelles are collected and then fed into the VFD together with TEOS via separate feed jets. The collected product consists of sol-gel material with some along with some precipitates. To improve the homogeneity, the sol-gel is fed through VFD again and the product is collected and is subsequently referred to as-synthesized SBA-15. This material was filtered under vacuum and washed with deionized water, then dried in an oven at 120 ˚C for at least 12 hours. Lastly, the material is calcined in air at 550 ˚C to remove the polymer template. The overall process is summarised in Figure 2.4.

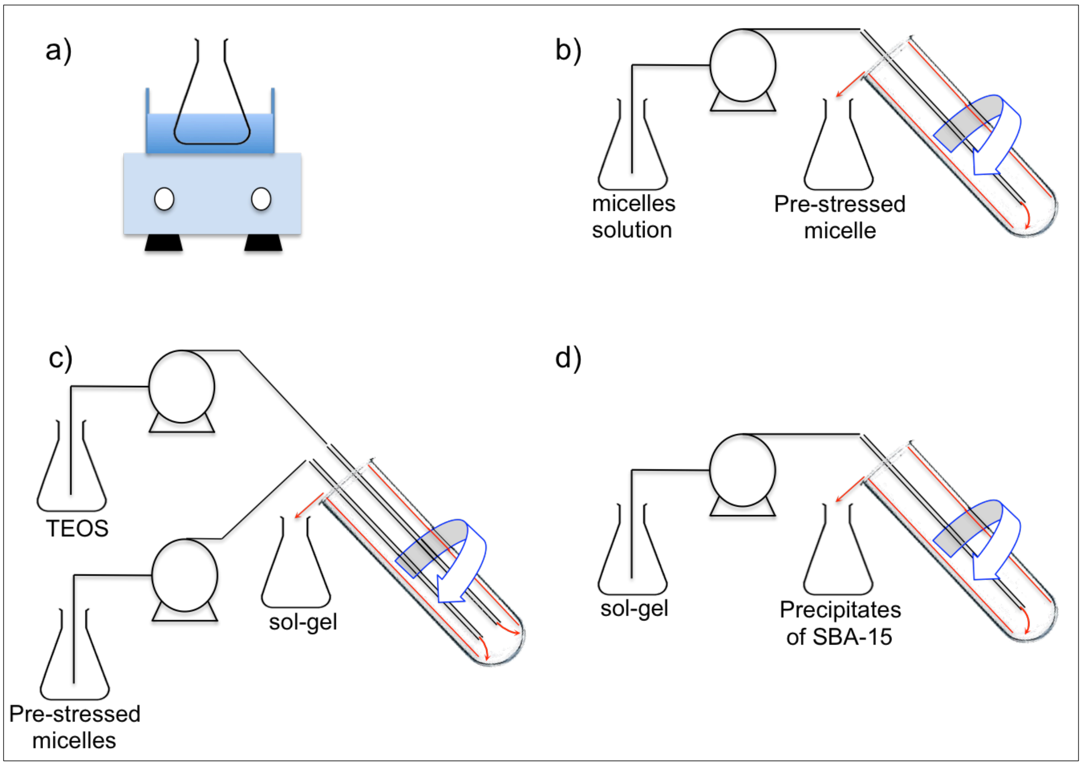

Figure 2.4. *Drawing of overall process steps in synthesizing SBA-15 using VFD.*

2.2.2. Incorporation of metal oxides into SBA-15 using VFD

Incorporation of metals oxide in SBA-15 is carried out simultaneously during the synthesis of SBA-15. The overall process setup is similar to the synthesis of SBA-15 with slight modifications. The metals oxides precursor is added into the dissolved micelles solutions and mixed for 30 min using a magnetic stirrer, at 40 to 45 ˚C. The metals oxide/micelles solution is then fed into VFD to pre-stress the micelles, followed by the same procedures as stated above. In addition, the incorporated metals oxide can be reduced at the same time and this is demonstrated and discussed in detail in Chapter 5.

2.2.3. Synthesis of silica hydrogel using VFD

Synthesis of the silica hydrogel is time and cost efficient using VFD. The process only involves using TMOS and water. In the study, TMOS and water were fed into the VFD at different flow rate based on the desired H_2O/Si molar ratio, under 45˚ tilt angle, at various rotational speeds. The product was collected in a vial and allowed to gel, with the material collected by filtration and dried in air to remove the excess solvents, for then characterised. Functionalized silica gel can also be prepared by co-condensation of alkoxysilanes and organosilanes with water using the same method, and similarly for the preparation of curcumin/SiO_2 composite as summarised in Figure 2.5. This benign synthesis condition is necessary for preparation of curcumin/SiO_2 composite as curcumin is a pH, temperature, and light sensitive compound. This work is detailed in Chapter 7.

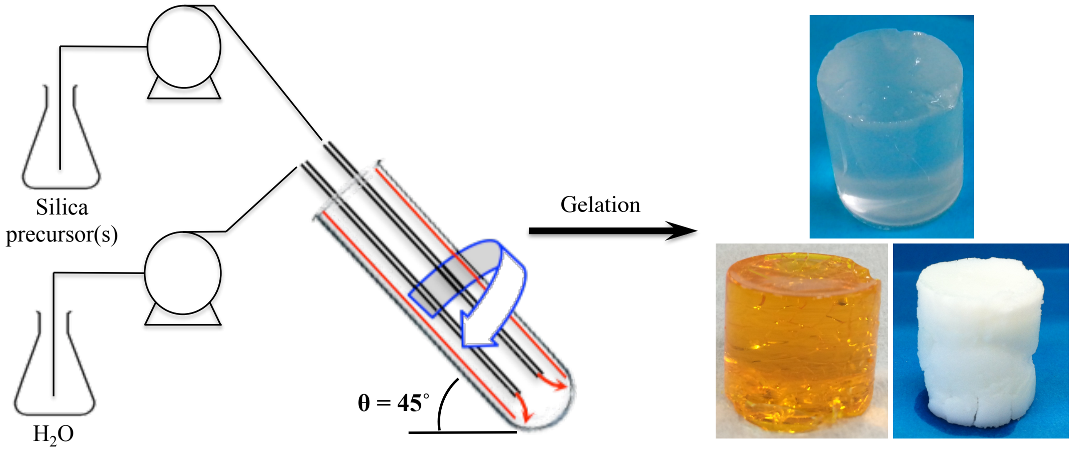

Figure 2.5. *Drawing of the synthesis process of silica hydrogel (top), curcumin/*SiO_2 *composite (bottom left), or hybrid silica (bottom right) using VFD.*

2.3. Characterization techniques

The progress in nanoscience and nanomaterials cannot advance without the use of sophisticated physical characterization methods such as electron miscroscopy, x-ray or neutron diffraction, x-ray scattering, atomic force microscopy, and various spectroscopies.[29] The characterization of nanomaterials includes determination of size and shape, atomic and electronic structure, surface properties, composition, and many other physicochemical properties.[29, 30] Although every characterization technique is unique in providing a specific structural details or properties of the nanomaterials, often the conclusion about the nature of the material can only be made or illustrated based on the analytical results of a combination of techniques. There are many characterization techniques that are involved in this dissertation research program, of which, they can be categorized into (1) surface morphology and structure at nano-scale, (2) molecular and solid state structure, (3) physical and thermal analysis, (4) elemental analysis, and (5) chemical speciation.

2.3.1. Surface morphology and structure at nano scale

Scanning electron microscopy (SEM)

In SEM, the electron beam is scanned over a relatively large surface area of the material, then signals of the electrons that are scattered back from the interaction of the incident electrons with the object's surface is detected and converted by the detector system to generate an image.[31] SEM images have great depth of field, yielding characteristics three-dimensional appearance that is useful for understanding the surface morphology of the sample.[29] However, samples that are nonconductive tend to acquire charge and not deflecting the electron beam, potentially leading to imaging artifacts.[30] This can be solved by spin coating an ultra thin layer (3 – 5 nm) of an electrically conducting material, such as Pt or Au, onto the sample prior imaging. Typically, SEM is coupled with energy-dispersive x-ray spectroscopy (EDAX) system that allowed elemental analysis.[29]

Herein, the research utilized two different models of SEM instrument, ZEISS 1555 and Quanta 450; images are typically taken using secondary electron detector, at an accelerating voltage of 5 – 15 kV. Figure 2.6 shows the images of calcined SBA-15 synthesized with VFD at different tilting angle, which is elaborated in Chapter 8.

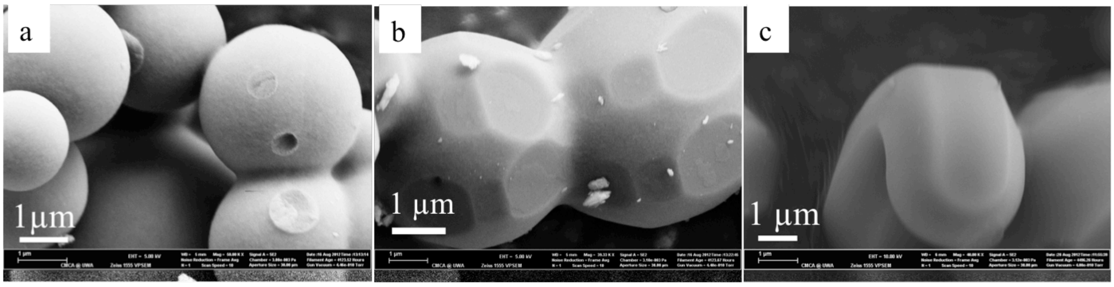

Figure 2.6. *SEM images showing the changes in surface morphology of calcined SBA-15 synthesized using VFD at 8500 rpm rotational speed and (a) 0° tilt angle, (b) 15° tilt angle, and (c) 45° tilt angle.*

Transmission electron microscopy (TEM)

In TEM, the electron beam is transmitted at high accelerating voltage through the sample, where the accelerating voltage can be set from 100 kV to 300 kV, depending on the instrument, and the interactions between the electron beam and the sample give rise to the image.[32] TEM generates atomic level images that also provide the size and shape of the nanomaterial. Moreover, coupled with the functionality such as selected area electron diffraction (SAED) and electron energy loss spectroscopy (EELS), sample crystallography and chemical bonding in the narrow regions of interest can be quantitatively investigated.[29, 32] Similarly, TEM also have the capability of performing elemental analysis and obtain the chemical composition using EDAX. Figure 2.7 shows the TEM analysis of mesocellular siliceous foam loaded with iron oxide, which is detailed in chapter 6.

TEM images obtained in this dissertation use several different EM instruments, FEI Tecnai

TM G^2 Spirit, JEOL 2100, and JEOL 3000, operates at accelerating voltage of 120 kV, 200 kV, and 300 kV respectively.

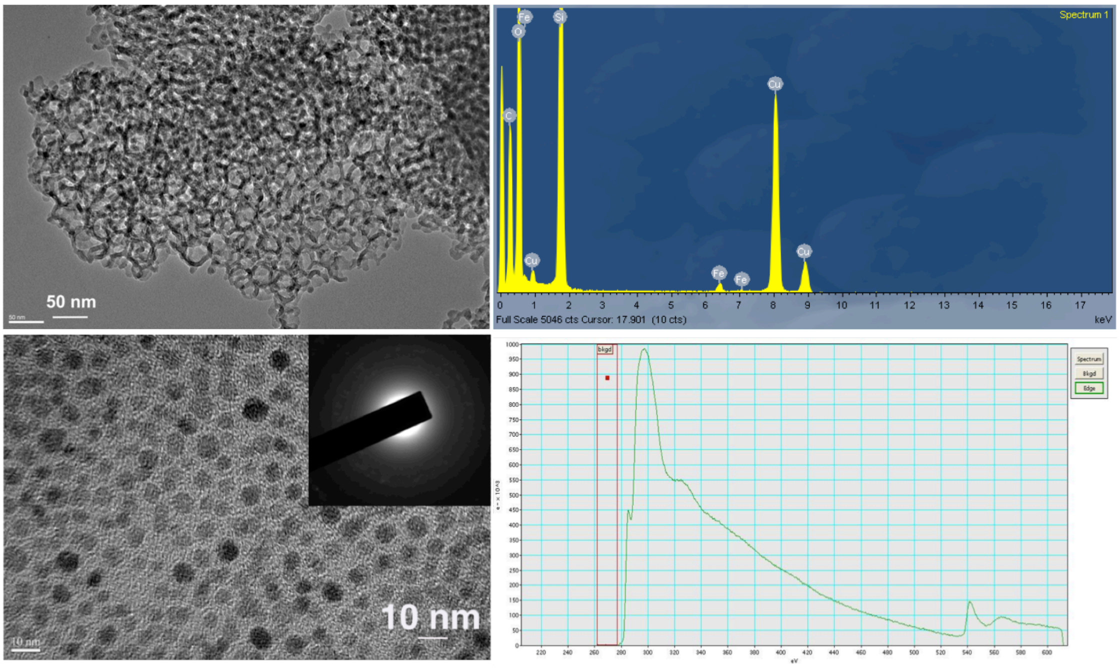

Figure 2.7. *Images of samples synthesized for this research showing results of different TEM techniques: (top left) TEM image, (top right) EDAX of the TEM image, (bottom left) high resolution TEM image of magnetite nanoparticles with the diffraction pattern (inset), and (bottom right) EELS of calcined SBA-15.*

2.3.2. Molecular and solid state structure

Powder X-ray diffraction (XRD)

It is essential to evaluate the crystal structure of nanomaterials using XRD. The principle of XRD is based on Bragg's law and the most commonly used database for the identification of crystal structures is the Joint Committee on Powder Diffraction Standards-International Center for Diffraction Data (JCPDS-ICDD) system.[29]

This dissertation will focus only on powder or polycrystalline diffraction rather than single crystal diffraction. The characterization is carried out using a PANalytic Empyrean diffractometer system with Nickel-filtered Cu Kα radiation operating at 40 kV and 40 mA. This diffractometer set up in the Bragg-Brentano, or reflection geometry where the focal spot of the tube, the sample surface and the detector slit are positioned on the so-called focusing circle as show in Figure 2.8.[33]

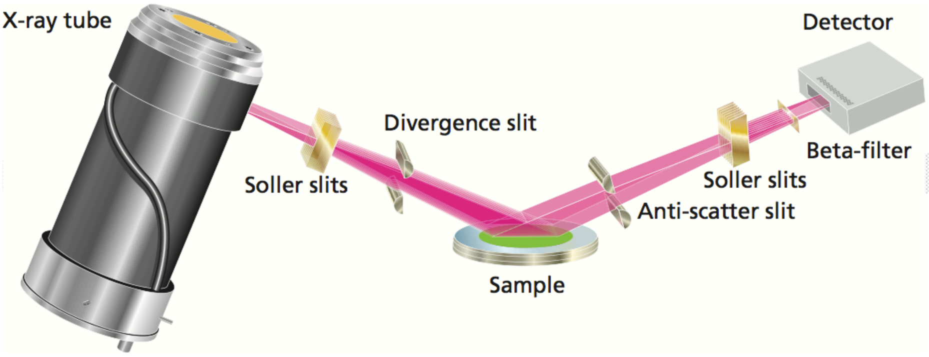

Figure 2.8. *Classical powder diffractometer setup in Bragg-Brentano geometry with components for reflection measurements. Taken from Ermrich and Opper.[33]*

The diffractometer uses the THETA:THETA goniometer where the sample always stays horizontal and tube and detector perform a 1:1 movement, however, the deviations of sample height may lead to a shift in reflection position.[33] Thus, the sample is ground and pressed on to the slightly hollowed sample holder, ensuring a flat smooth surface. As mentioned, the principle of XRD is based on Bragg's Law with the equation expressed as below:[33]

$$n\lambda = 2dsin\theta \tag{2.1}$$

where n is the is order of the interference, normally n = 1; λ is the x-ray wavelength, 1.54 Å for the Ni-filtered Cu Kα radiation; d is the interplanar spacing of the atoms; and θ is the Bragg angle, which is half of the angle between the incident reflected beam (Figure 2.9).[33]

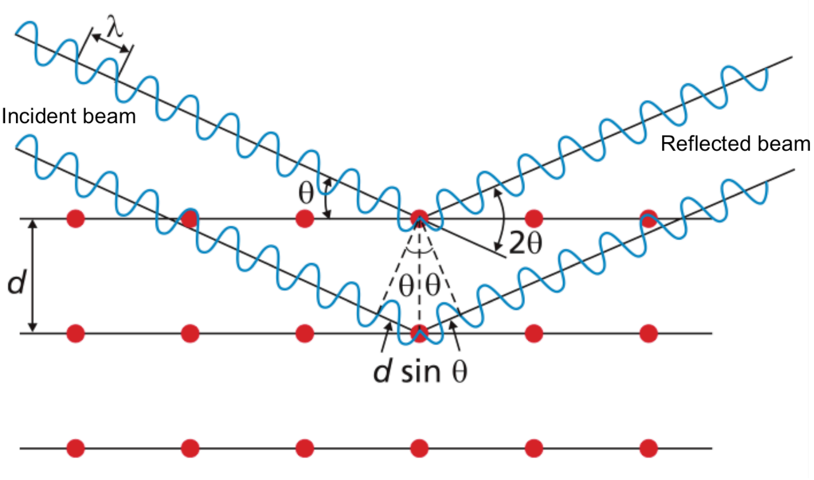

Figure 2.9. *Scheme of the diffraction geometry using Bragg's law. Adapted from Ermrich and Opper.[33]*

A diffractogram or diffraction pattern is obtained by measuring the intensity of reflected waved as a function of the scattering angle. The 2 theta value for the peak can be used to determine the interplanar spacing *d*, which cut the axes lengths a, b, c or the axis intercepts in the reciprocal space a/h, b/k and c/l, respectively (Figure 2.10), known as Miller indices.[33]

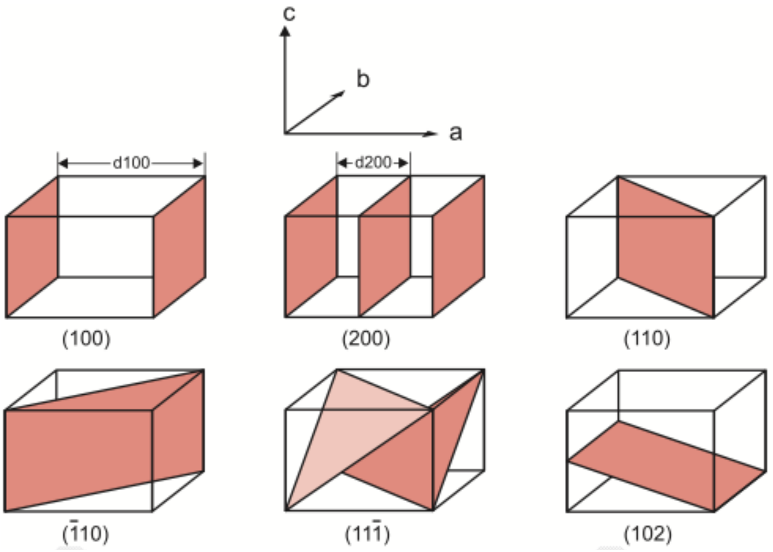

Figure 2.10. *Example of different lattice planes. Taken from Ermrich and Opper.*[33]

Once the *d*-spacing and the corresponding indices *h, k, l* is determined, the dimension of unit cell can be calculated depending of the crystal systems or shapes. There are seven crystal systems with fourteen different Bravais lattices, which are illustrated in Figure 2.11.

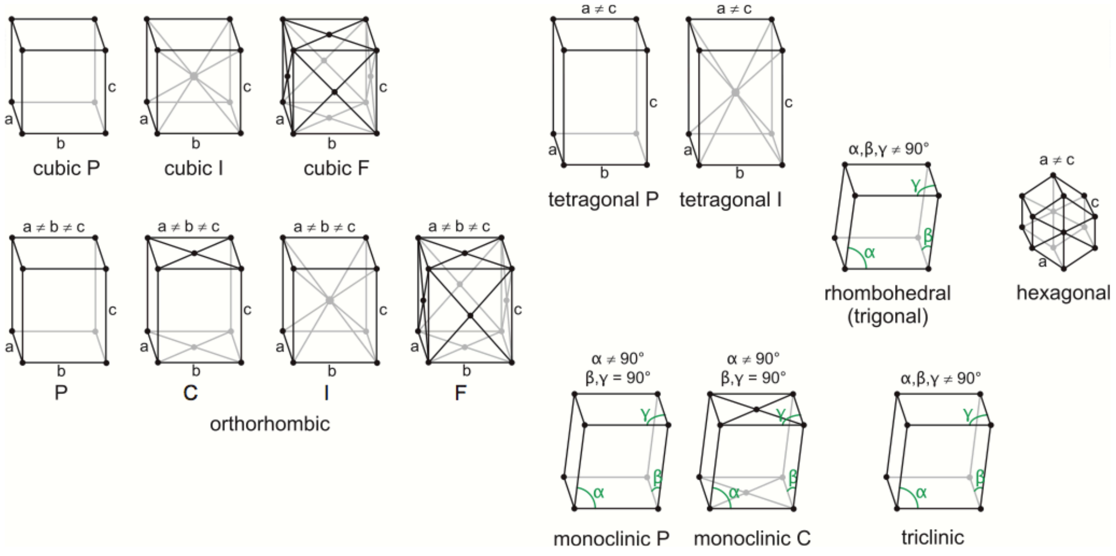

Figure 2.11. *Graphical presentation of seven crystal systems and fourteen different Bravais lattices. Taken from Ermrich and Opper.*[33]

Once the crystal structure and lattice is known, unit cell parameter a can be determined using equation. Equations for few general crystal systems are:[33-35]

Cubic $$\frac{1}{d_{hkl}^2} = (h^2 + k^2 + l^2)\frac{1}{a^2} \tag{2.2}$$

Hexagonal $$\frac{1}{d_{hkl}^2} = \left[\frac{4}{3}\,(h^2 + k^2 + hk\,) + l^2\left(\frac{a}{c}\right)^2\right]\frac{1}{a^2} \tag{2.3}$$

Tetragonal $$\frac{1}{d_{hkl}^2} = \left[h^2 + k^2 + l^2\left(\frac{a}{c}\right)^2\right]\frac{1}{a^2} \tag{2.4}$$

Small-angle X-ray scattering (SAXS)

SAXS includes both the diffraction of large lattice spacing, and can be up to the order of thousands of interatomic distances, as well as the scattering by nonperiodic structures of amorphous and mesormorphic materials,[36] which can be used to evaluate not only crystalline materials but also for amorphous materials, polymers, and biomolecules.[29] This method determines the structure of the particle systems in terms of averaged particle sizes or shape, with the materials analysed in the solid or liquid forms.[37]

In contrast to microscopy, where only a small part of the sample is magnified and investigated, the scattering technique investigates the whole illuminated volume of the sample and provides an average values of the structure parameters of the sample.[37] In the dissertation research, the SAXS analysis is carried out using the Bruker AXS NanoStar system (Figure 2.12). The basic principle of the system involves illuminating a sample with radiation of known wavelength, then detecting the intensity scattered by the sample with respect to the incident radiation at a given observation angle.[38]

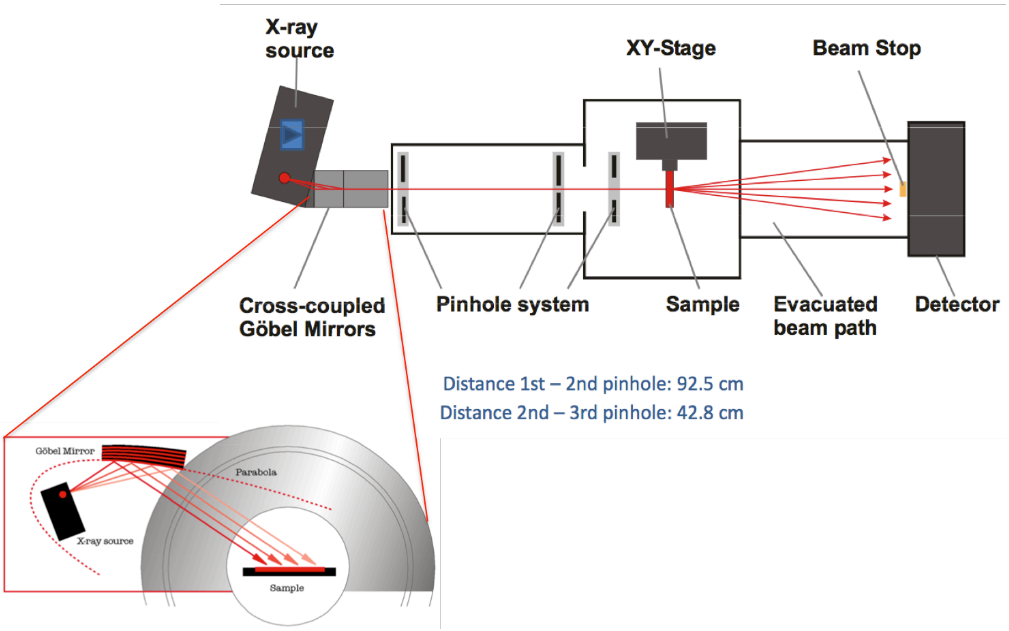

Figure 2.12. *Schematics showing the key components in the Bruker AXS NanoStar system.*[39]

In brief, when X-rays are scattered on atoms and every atom emits spherical waves radiating from the position of the respective atom, constructive or destructive interferences would occur depending on the 2θ angle, the orientation and the distance r of the light-emitting atoms (Figure 2.13).[37]

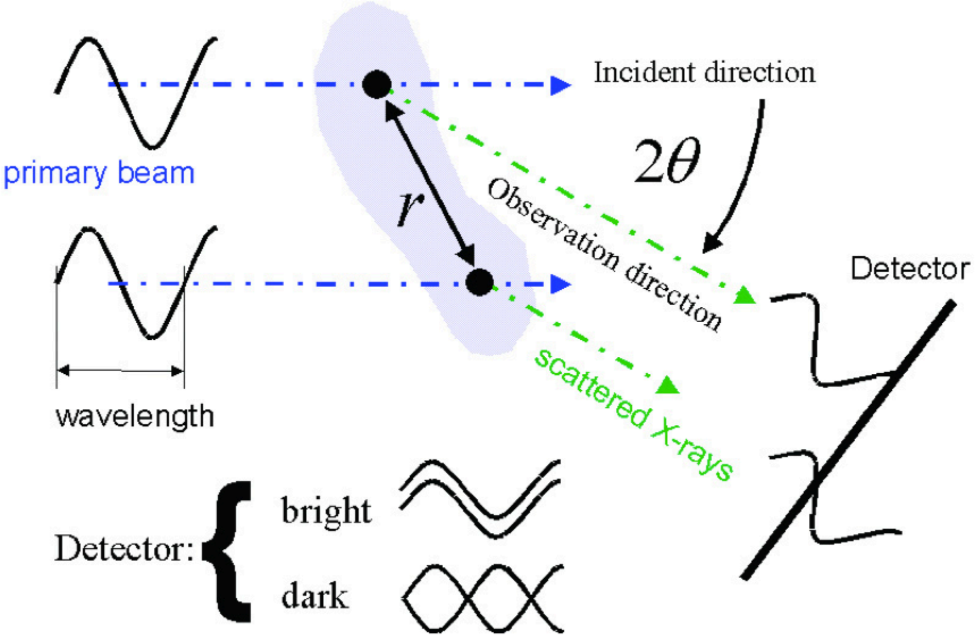

Figure 2.13. *Drawing illustrating the interferences of scattered of X-rays. When the interfering waves arrive parallel, the detector receives brightness (constructive interferences) and when arrive anti-parallel, the detector receives darkness (destructive interferences).*[37]

Generally, the wavelength λ of the scattered x-rays are known and every distance r is measured relative to the wavelength, a scattering wave vector, q can be defined by the following equation:[37]

$$q = 4\pi \, sin \, \theta / \lambda \qquad (2.5)$$

The interference pattern is often represents by plotting the scattered intensity as a function of scattering wave vector, and is characteristic to the orientation and distances of the atoms relative to each other.[37] The d-spacing of the reflections can then be calculated from Bragg's law expressing sin (θ) in terms of scattering vector q, as follow:

$$\lambda = 2 \, d_{hkl} \cdot \frac{q\lambda}{4\pi} \qquad (2.6)$$

$$d_{hkl} = \frac{q}{2\pi} \qquad (2.7)$$

Once d-spacing is determined, the unit cell parameter, a, can be calculated using the equations stated under XRD sections.

2.3.3. Physical and thermal analysis

Nitrogen adsorption-desorption

Measuring the porosity of nanomaterial can be done via gas adsorption or mercury porosimetry. The dissertation research involves using gas adsorption technique to determine the porosity of all the lab-synthesized samples. All analyses are carried out using a Micromeritics TriStar^{TM} II 3020 system, which adapted the concept of physical adsorption. Physisorption may lead to surface coverage by more than one layer of adsorbate, thus, pores can be filled by the adsorbate for pore volume measurements, with no disruptive structural change occurring during the measurement.[40] In addition, physical adsorption is fully reversible and this allows both adsorption and desorption process to be studied.[40]

An isotherm is a measure of the volume of gas adsorbed at a constant temperature as a function of gas pressure, and they are grouped into six standard isotherms according to International Union of Pure and Applied Chemistry (IUPAC) as show below. Type I isotherm corresponds to a complete monolayer adsorption which is typically exhibited by microporous solids; Type II isotherm with a sigmoidal shape corresponds to unrestricted monolayer-multilayer adsorption, the inflection point B of the isotherm indicates the completion of first adsorbed monolayer or changeover from monolayer to multilayer adsorption occurs, which is typically exhibits by nonporous solids or macroporous solids.[40, 41] Type III isotherm also known as Flory-Huggins isotherm, with a convex to the relative pressure axis corresponds to vapour adsorption and characteristic of weak adsorbate-adsorbent interaction which is exhibited by nonporous solids.[42, 43] Type IV isotherm exhibits initial inflection similar to Type II, which generally occurs near completion of the first monolayer. Type IV isotherm features a hysteresis loop generated by the capillary condensation that commonly associated with the presence of mesoporosity.[40, 42] Type V isotherm features a hysteresis loop which is associated with mesoporosity, and also features an initial convex to the relative pressure axis similar to Type III that result from weak adsorbate-adsorbent interaction, which is indicative of microporous or mesoporous solids, as observed in the water adsorption on carbon.[40, 42, 43] A rare isotherm, Type VI isotherm exhibits a series of steps that can be arise from adsorption of extremely homogenous, nonporous surfaces where the monolayer capacity corresponds to the step height.[40, 42]

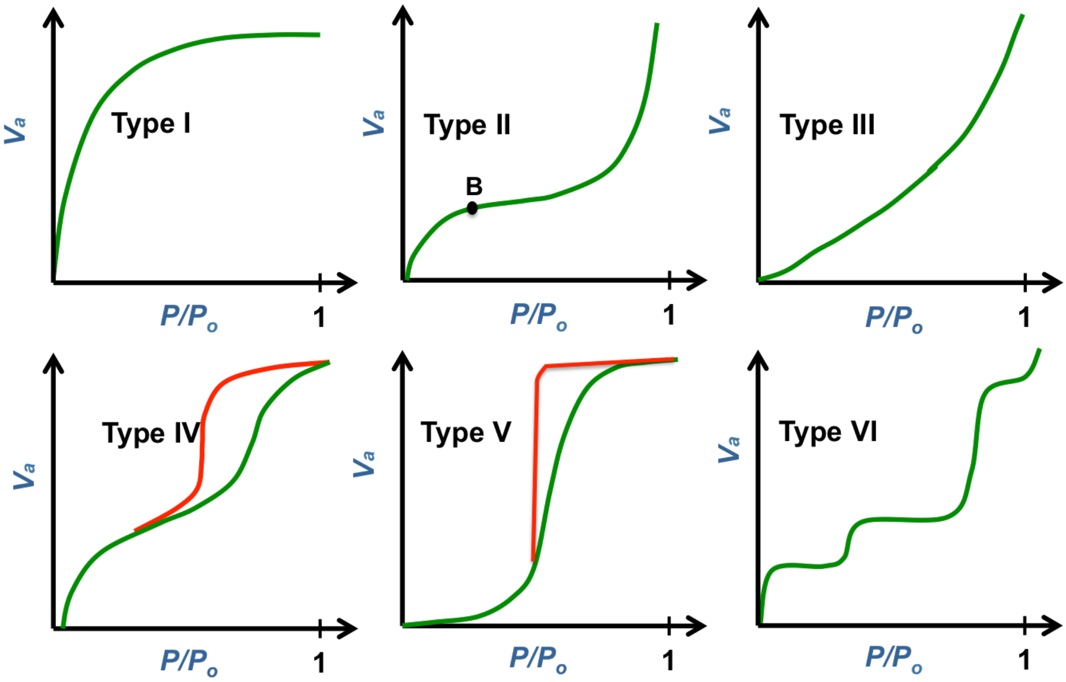

Figure 2.14. *Six IUPAC classifications of adsorption isotherm, which is a measure of the volume of gas adsorbed at standard temperature and pressure (STP) as a function of relative pressure, P/P_0. Adapted from Lowell et.al.*[40]

Physicochemical properties such as the specific surface area, total pore volume and pore diameter of a sample can be determined using nitrogen adsorption-desorption analysis. Prior to the analysis, degassing is mandatory and for this procedure it is important to remove water, gases or vapours, and other contaminants that may be physically adsorbed onto the surface of the sample after manufacture, in order to achieve high accuracy in the measurements. The calculation of specific surface area is based on the Brunauer–Emmett–Teller (BET) theory, as an extension of Langmuir theory, with the fundamental assumption that the forces active in the condensation of gases also are responsible for the binding energy in multi-molecular adsorption.[40] By equating the rate of condensation of gas molecules onto an adsorbed layer to the rate of evaporation from the same layer and summing for an infinite number of layers, it can be expressed in the equation:[40]

$$\frac{P}{V_a(P_o-P)} = \frac{1}{V_m C} + \frac{C-1}{V_m C}\left(\frac{P}{P_o}\right) \tag{2.8}$$

The parameters in the equation are defined as follow:

P = Partial vapour pressure of adsorbate gas in equilibrium with the surface at 77.4 K,

P_o = saturated pressure of adsorbate gas,

V_a = volume of gas adsorbed at STP (273.15 K and 1.013×10^5 Pa),

V_m = volume of gas adsorbed at STP to produce an apparent monolayer on the sample surface,

C = dimensionless constant that is related to the enthalpy of adsorption of the adsorbate gas on the powder sample.

The data collected is based on multi-point measurements, ideally five data points, and BET value is plotted against the P/P_o according to equation (2.8), yielding a linear plot in the approximate relative pressure ranging from 0.05 to 0.3.[40] According to the linear plot, slope and intercept can be obtained using least square regression, and the monolayer capacity, V_m , S_{total}, S_{BET} are calculated based on these equations:[40, 44]

$$V_m = \frac{1}{A+I} \tag{2.9}$$

$$S_{total} = \frac{V_m N A_m}{M_v} \tag{2.10}$$

$$S_{BET} = \frac{S_{total}}{m} \tag{2.11}$$

where A refers to the slope and I refers to the intercept of the BET plot. For equation (10), N is Avogadro constant (6.022×10^{23} mol^{-1}), A_m is cross-sectional area of one adsorbate molecule and equals to 0.162 nm^2 for nitrogen molecule, and M_v is the molar volume occupied by one mole of the adsorbate gas at STP and equals to 22414 mL. To obtain a specific surface area, S_{BET}, the total surface area is divided by the mass of the solid sample, m.

Based on the aforementioned theory, the associated software of the equipment is used to calculate and determines all parameters such as specific surface area, pore volume, and pore diameter upon analysis.

Dynamic light scattering (DLS)

DLS is also known as photon correlation spectroscopy,[45] and is commonly used to determine the size distribution of small particles in suspension, in the submicron regime. DLS measurements provide the average hydrodynamic diameter of the particles, effectively providing an average of the different dimensions within a particle to give the equivalent of the diameter of a spherical particle in solution. In brief, a laser imposes a monochromatic incident light onto a solution with small particles in Brownian motion, resulting in a Doppler shift between the frequency of incident light and the frequency of scattered light, which is related to the size of the particle.[45] As the particles move and change distance with respect to each other, it can be reflect by the fluctuation in intensity as a function of time, of which the size distribution can be computed by processing the fluctuations of the intensity of the scattered light (Figure 2.15).[46]

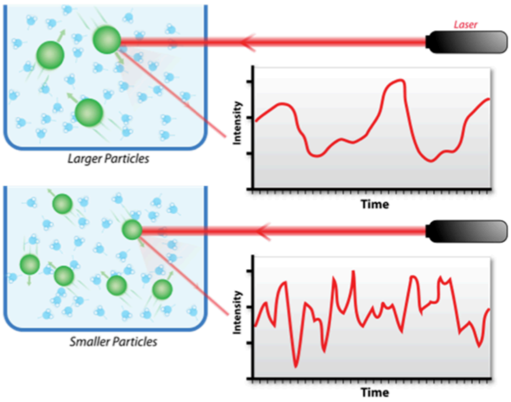

Figure 2.15. *Hypothetical fluctuation of scattering intensity of large particles and small particles.*[46]

The fluctuation of intensity is mathematically processed based on several principles and equations in determining the particle size in solution, which will not be elaborated as the DLS instrument used herein, Malvern Instrument 'High Performance Particle Sizer' model HPP5001, provides the software to facilitate with the measurement. However, it is important to understand the parameter required for each measurement such as wavelength of laser light source, viscosity, and refraction index of the solution.[46] As DLS actually measures the hydrodynamic radius of the particles, the size from DLS measurement is larger than the size measurement from TEM or atomic force microscopy (AFM).[46] Thus, it is always recommended to combine different analytical techniques such as SEM, TEM, AFM, and DLS to perform size distribution analysis and get complimentary information from different aspects.[46]

Thermogravimetric analysis (TGA) / Differential scanning calorimetry (DSC)

TGA and the associated differential thermal analysis (DTA) is commonly used in monitoring the thermal stability of a sample by recording the change in mass of a sample over the change in temperature under a reactive or inert atmosphere.[47] TGA can determine selected characteristics of materials that exhibits a loss or gain in mass due to chemical phenomena such as dehydration, decomposition, and degradation.[48] In addition to recording the change in mass using TGA, associated DTA information can be obtained simultaneously. The DTA measures the difference in temperature between the sample and the reference when they are subjected to the same heat and shows if there is any phase transition within the sample over the temperature change.[47] Where DTA is constant, this means there is no phase change whereas a dip in DTA curve indicates an endotherm and a peak in DTA signifies an exotherm.[47]

DSC is a thermoanalytical technique that measures the change of difference in heat flow rate to the sample and to the reference sample as a function of temperature.[49] DSC provides similar information as DTA by measuring the enthalpy energy changes or heat capacity changes associated with phase transition at same temperature.[49, 50] In this dissertation, a Simultaneous Thermal Analyzer (STA) is used, that combines both TGA and DSC techniques to analyse the sample.

2.3.4. Elemental Analysis

Inductively coupled plasma atomic emission spectroscopy (ICP-AES) and inductively coupled plasma mass spectrometry (ICP-MS)

Both inductively coupled plasma atomic emission spectroscopy (ICP-AES) and inductively coupled plasma mass spectroscopy (ICP-MS) techniques can precisely determine the elemental compositions of a sample and quantify the elemental concentration within the sample.[51, 52] Although both techniques can be used for elemental analysis, there are differences in the basic operations. In ICP-AES ions are excited by vertical plasma and the emitting photons are separated on the basis of their emission wavelengths, whereby in ICP-MS, ions are excited by horizontal plasma and separated on the basis of their mass-to-charge ratio (m/z).[51, 52] These difference in ions generation and detection impacts on the relative sensitivities. ICP-MS provides a detection limit range from 1 to 10 ppt and works over eight orders of magnitude detection level, compared to the detection limit range from 1 to 10 ppb for ICP-AES that works over six orders of magnitude.[52] Elemental analyses throughout the dissertation are conducted either by TSW Analytical Pty. Ltd. (Perth, WA) or Marine and Freshwater Research Laboratory Environmental Science at Murdoch University (Perth, WA).

X-ray photoelectron spectroscopy (XPS)

XPS is an excellent surface technique for quantitatively measuring the elemental composition, empirical formula, chemical state, and electronic state of the elements embedded within a nanomaterial.[29] This is a non-destructive method where the material is irritated with Al or Mg X-rays, which is then absorbed by an atom, causing the lowest energy shell electron (K-shell) to be ejected from the top 1 to 10 nm of the material. [29] The binding energy of the ejected electron can be calculated as the ejected electron has a kinetic energy (KE) that is related to the energy of the incident beam (hv), and the work function of the spectrometer (ϕ).[53] Each ejected electron and the orbital from which the electron is ejected has its specific binding energy, or XPS peak positions, which is characteristic of each element, depending on its oxidation state.[53] Thus, the chemical environment and oxidation state of the atom can be determined through shifts of the peaks within the expected range of binding energy, which can be looked up in a number of database.[53]

XPS only measures up to 10 nm in depth of the surface. In the case where a sample is not homogenous with the consistent composition throughout or certain element is embedding in specific areas in a sample, depth profile analysis can be carried out where Ar^+ ion beam is sputtered onto the sample surface and forms a crater, allowing the X-rays to reach the layers that would not have otherwise been analysed.[53] This technique is used in the work in this dissertation and was conducted by through the Surface and Chemical Analysis Network (SCAN) at the University of Melbourne.

Fluorescence Spectroscopy

Fluorescence spectroscopy analyses fluorescence from a sample that contains a fluorophore, using an ultraviolet (UV) light to excite the electrons in the molecules of the compound, which can re-emit the light upon excitation, and the amount and wavelength of the emitted energy depends on both the fluorophore and the chemical environment of the fluorophore.[54] In the present work, fluorescence spectroscopy is applied to analyse the concentration of a fluorescence compound in a composite nanomaterial. A Varian Cary Eclipse fluorescence spectrophotometer is used and the associated software provides ease to build a concentration profile as reference. Samples with fixed concentration are prepared and analysed to obtain a calibration plot of the intensity versus concentration. Ideally, five concentrations are needed for better accuracy and the correlation coefficient of the calibration should be 0.9 or better. Then, the concentration of fluorescence compound within the composite nanomaterials is analysed and calculated using the calibration equation.

2.3.5. Chemical Speciation

Attenuated total reflectance- Fourier transform infrared (ATR-FTIR)

Infrared spectroscopy (IR) is based on the principle that every molecule has its distinctive spectra due to the molecular vibrations caused by the oscillation of molecular dipoles, in which depends on the atoms in the bond, the number of bonds, and the orientation of the bonds with respect to the rest of the molecule.[55] Fourier transform is a common algorithm required to process the raw data into the actual spectrum, thus emerges the term Fourier transform infrared spectroscopy (FTIR). Characteristic IR vibration modes for different compounds can be found from the NIST Chemistry WebBook. As all molecules have distinct absorption region in the IP spectrum, which is generally presented in the form of both wavenumber and absorption intensity or percent transmittance, this technique can be used in distinguishing products or identifying unknown substance to certain extent.[55]

Nicolet Nexus 870 FT-IR, equipped with a Thermo Scientific ATR-IR 'Smart Orbit Attachment' is used in the dissertation research, for all IR analysis. ATR-FTIR is method of a compositional analysis that builds upon the traditional FTIR, enabling samples to be examined directly in the form of solid or liquid without further preparation and is thus optimised for reproducibility.[55]

Solid-state nuclear magnetic resonance spectroscopy (SSNMR)

NMR is ubiquitous in organic chemistry as a powerful tool for identifying molecular structures. Initially, NMR is used in liquids and solutions but as technology progressed, solid-state NMR can now be used for compounds that pose problems in solutions, such as in powder and complex proteins.[56] SSNMR has become an important tool in determining the structure of molecular sieves, providing information about local environment of atoms, including silicon, aluminium and phosphorus.[56]

As the molecules are fixed in a lattice for solid sample, different peaks will be produced depending on how the molecules are oriented in the magnetic field, resulting in a chemical shift anisotropy.[56] In addition, the large dipolar interactions in solid sample that is not averaged out due to lack of randomized movement, is another source of line broadening.[56] To counteract these effects, magic angle spinning (MAS) is used, whereby the sample is tilted at a specific angle, 54.74°, to eliminate the line broadening effects by decreasing the geometric factor ($3\cos^2\theta-1$) to 0.[56]

In this dissertation ^{29}Si MAS NMR is performed using a Bruker 400 instrument, single pulse at 5000 Hz rotating speed to determine the poly-condensation degree of the silica. ^{29}Si MAS NMR spectrum of a silica nanoparticle (Figure 2.16) shows the Q unit region, where Q^n represent silicon entities with different bonding environments as such: Q^4 ([SiO_4], -111 ppm), Q^3 ([$SiO_3(OH)$], -102 ppm) and Q^2 ([$SiO_2(OH)_2$], -92 ppm),[57] Q^1 denotes a silicon with one Si-O-Si linkage and Q^0 denotes a silicon with no Si-O-Si linkages. As the silica gel obtained has at least partial condensation, Q^1 and Q^2 entities are not usually observed.[58] Q- values are obtained from the NMR peak area and degree of condensation can be calculated based on the following equation:[59, 60]

$$D_c = \frac{[1.0(\%\ area\ Q^1)+2.0(\%\ area\ Q^2)+3.0(\%\ area\ Q^3)+4.0(\%\ area\ Q^4)}{4} \qquad (2.12)$$

However, the relative CP-MAS NMR peak areas may not correspond to relative amounts of species present as Q^4 sites cross polarize less efficient than Q^2 and Q^3 sites, thus giving much smaller relative ^{29}Si CP MAS signals.[61] This is because cross polarization involves transfer of magnetization from ^{1}H to the X-nucleus (^{29}Si or ^{13}C) via a dipole-dipole mechanism, which is critically dependent on the distance between the proton and the X nucleus.[61] Therefore, ^{29}Si SP-MAS spectra is used to calculate the degree of condensation (equation 12) rather than ^{29}Si CP-MAS.

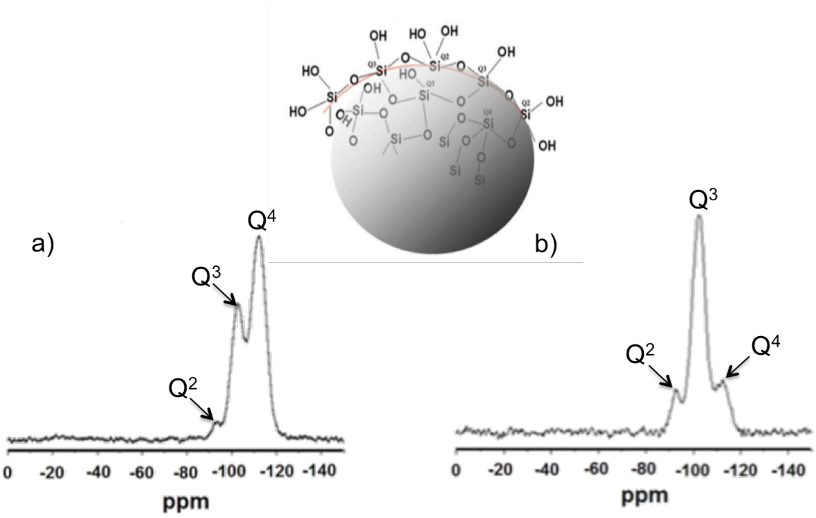

Figure 2.16. *(a) ^{29}Si single pulse (SP) and (b) ^{29}Si-^{1}H cross polarization (CP) magical angle spinning (MAS) spectra of a silica nanoparticle. Adapted from Sen and Bruce.*[62]

Superconducting quantum interference device (SQUID)

Magnetic characterization of nanomaterials is performed using SQUID, in which information of magnetization versus temperature or magnetization versus field data can be obtained.[29] SQUID is an extremely low impedance, high sensitivity flux magnetometer that uses a combination of superconducting materials and Josephson junction to measure magnetic fields with resolutions up to approximately 10^{-14} kG or greater.[29, 63] During measurement, the induced current is independent of rate of flux change and provides an uniform response over a wide range of frequencies.[63] Typically, helium gas is passed through the sample slowly to control the temperature so that measurement can be made over a wide range of temperature, 5 to 300 K in our study.

Magnetic hysteresis can be obtained through a SQUID measurement if a material responds to the field, which can then be interpreted and determined the type of magnetic interactions within the sample.[63] Paramagnetic and diamagnetic materials can be easily recognized (Figure 2.17), whereby ferromagnetic materials exhibit hysteresis curves (Figure 2.18) and values such as saturation magnetization, remnant magnetization, and coercivity is observed.[63]

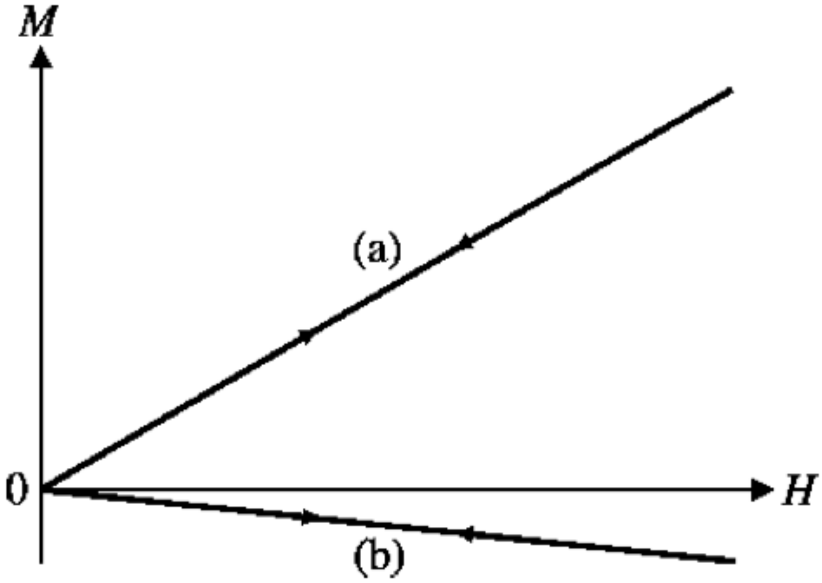

Figure 2.17. Typical effect of the magnetization, M, of an applied magnetic field, H, on (a) a paramagnetic system and (b) a diamagnetic system. Taken from Bland thesis.[64]

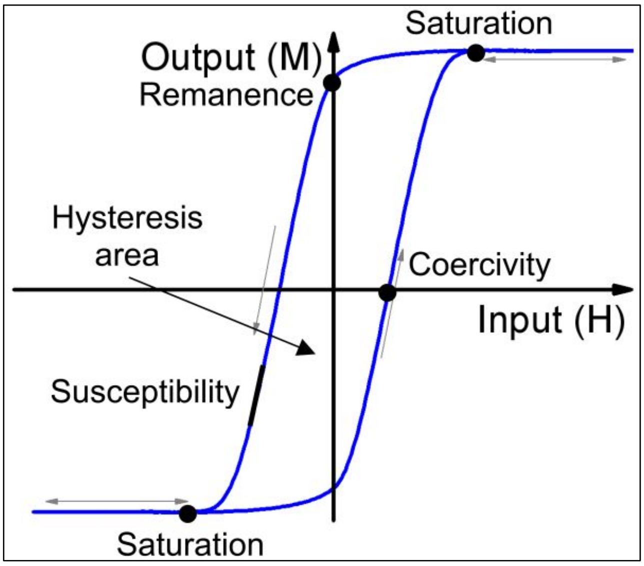

Figure 2.18. Characteristic of a hysteresis loop in a ferromagnetic material showing a saturation magnetization, M_s, coercive field, H_c, and remnant magnezation, M_r. Taken from Béron et al.[65]

Having a clear picture of the proposed research methodology and analytical techniques, which are involved in fulfilling objectives of the research, the following chapters will be discussed on the results obtained throughout the candidature.

2.4. References

1. C. L. Raston*,* WO2012034164A2, 2012.

2. X. Chen, N. M. Smith, K. S. Iyer and C. L. Raston, Controlling nanomaterial synthesis, chemical reactions and self assembly in dynamic thin films, *Chem. Soc. Rev.*, 2014, **43**, 1387-1399.

3. K. S. Iyer, C. L. Raston and M. Saunders, Hierarchical aqueous self-assembly of C60 nano-whiskers and C60-silver nano-hybrids under continuous flow, *Lab Chip*, 2007, **7**, 1121-1124.

4. X. Chen, R. A. Boulos, J. F. Dobson and C. L. Raston, Shear induced formation of carbon and boron nitride nano-scrolls, *Nanoscale*, 2013, **5**, 498-502.

5. J. Fang, Y. Guo, G. Lu, C. L. Raston and K. S. Iyer, Instantaneous crystallization of ultrathin one-dimensional fluorescent rhabdophane nanowires at room temperature, *Green Chem.*, 2011, **13**, 817-819.

6. C. Bullen, M. J. Latter, N. J. D'Alonzo, G. J. Willis and C. L. Raston, A seedless approach to continuous flow synthesis of gold nanorods, *Chem. Commun.*, 2011, **47**, 4123-4125.

7. S. Dev, P. Prabhakaran, L. Filgueira, K. S. Iyer and C. L. Raston, Microfluidic fabrication of cationic curcumin nanoparticles as an anti-cancer agent, *Nanoscale*, 2012, **4**, 2575-2579.

8. S. Dev, J. Toster, S. Vadhan Prasanna, M. Fitzgerald, K. Swaminathan Iyer and C. L. Raston, Suppressing regrowth of microfluidic generated drug nanocrystals using polyelectrolyte coatings, *RSC Adv.*, 2013, **3**, 695-698.

9. X. Chen, J. F. Dobson and C. L. Raston, Vortex fluidic exfoliation of graphite and boron nitride, *Chem. Commun.*, 2012, **48**, 3703-3705.

10. F. M. Yasin, R. A. Boulos, B. Y. Hong, A. Cornejo, K. S. Iyer, L. Gao, H. T. Chua and C. L. Raston, Microfluidic size selective growth of palladium nano-particles on carbon nano-onions, *Chem. Commun.*, 2012, **48**, 10102-10104.

11. X. Chen, F. M. Yasin, P. K. Eggers, R. A. Boulos, X. Duan, R. N. Lamb, K. S. Iyer and C. L. Raston, Non-covalently modified graphene supported ultrafine nanoparticles of palladium for hydrogen gas sensing, *RSC Adv.*, 2013, **3**, 3213-3217.

12. E. Eroglu, N. J. D'Alonzo, S. M. Smith and C. L. Raston, Vortex fluidic entrapment of functional microalgal cells in a magnetic polymer matrix, *Nanoscale*, 2013, **5**, 2627-2631.

13. Y. A. Goh, X. Chen, F. M. Yasin, P. K. Eggers, R. A. Boulos, X. Wang, H. T. Chua and C. L. Raston, Shear flow assisted decoration of carbon nano-onions with platinum nanoparticles, *Chem. Commun.*, 2013, **49**, 5171-5173.

14. F. Md. Yasin, K. S. Iyer and C. L. Raston, Palladium nano-carbon-calixarene based devices for hydrogen sensing, *New J. Chem.*, 2013, **37**, 3289-3293.

15. M. H. Wahid, E. Eroglu, X. Chen, S. M. Smith and C. L. Raston, Entrapment of *Chlorella vulgaris* cells within graphene oxide layers, *RSC Adv.*, 2013, **3**, 8180-8183.

16. M. H. Wahid, E. Eroglu, X. Chen, S. M. Smith and C. L. Raston, Functional multi-layer graphene-algae hybrid material formed using vortex fluidics, *Green Chem.*, 2013, **15**, 650-655.

17. L. Yasmin, X. Chen, K. A. Stubbs and C. L. Raston, Optimising a vortex fluidic device for controlling chemical reactivity and selectivity, *Sci. Rep.*, 2013, **3**, 2282.

18. L. Yasmin, T. Coyle, K. A. Stubbs and C. L. Raston, Stereospecific synthesis of resorcin[4]arenes and pyrogallol[4]arenes in dynamic thin films, *Chem. Commun.*, 2013, **49**, 10932-10934.

19. R. A. Boulos, C. L. Raston, F. Zhang, E. S. Tjandra, D. Spagnoli and A. D. Martin, Spinning up the polymorphs of calcium carbonate, *Sci. Rep.*, 2014, **4**, 3616.

20. J. Britton and C. L. Raston, Continuous flow vortex fluidic production of biodiesel, *RSC Adv.*, 2014, **4**, 49850-49854.

21. M. N. Gandy, C. L. Raston and K. A. Stubbs, Towards aryl C-N bond formation in dynamic thin films, *Org. Biomol. Chem.*, 2014, **12**, 4594-4597.

22. W. Peng, X. Chen, S. Zhu, C. Guo and C. L. Raston, Room temperature vortex fluidic synthesis of monodispersed amorphous proto-vaterite, *Chem. Commun.*, 2014, **50**, 11764-11767.

23. K. Vimalanathan, X. Chen and C. L. Raston, Shear induced fabrication of intertwined single walled carbon nanotube rings, *Chem. Commun.*, 2014, **50**, 11295-11298.

24. L. Yasmin, P. K. Eggers, B. W. Skelton, K. A. Stubbs and C. L. Raston, Thin film microfluidic synthesis of fluorescent highly substituted pyridines, *Green Chem.*, 2014, **16**, 3450-3453.

25. L. Yasmin, K. A. Stubbs and C. L. Raston, Vortex fluidic promoted Diels–Alder reactions in an aqueous medium, *Tetrahedron Lett.*, 2014, **55**, 2246-2248.

26. X. Chen, P. K. Eggers, A. D. Slattery, S. G. Ogden and C. L. Raston, Template-free assembly of three-dimensional networks of graphene hollow spheres at the water/toluene interface, *J. Colloid Interface Sci.*, 2014, **430**, 174-177.

27. J. Britton, S. B. Dalziel and C. L. Raston, Continuous flow Fischer esterifications harnessing vibrational-coupled thin film fluidics, *RSC Adv.*, 2015, **5**, 1655-1660.

28. J. Britton and C. L. Raston, Rapid high conversion of high free fatty acid feedstock into biodiesel using continuous flow vortex fluidics, *RSC Adv.*, 2015, **5**, 2276-2280.

29. C. N. R. Rao and K. Biswas, Characterization of Nanomaterials by Physical Methods, *Annual Review of Analytical Chemistry*, 2009, **2**, 435-462.

30. P.-C. Lin, S. Lin, P. C. Wang and R. Sridhar, Techniques for physicochemical characterization of nanomaterials, *Biotechnol. Adv.*, 2014, **32**, 711-726.

31. D. E. N. Joseph I. Goldstein, Patrick Echlin, David C. Joy, Charles E. Lyman, Eric Lifshin, Linda Sawyer, Joseph R. Michael, *Scanning Electron Microscopy and X-ray Microanalysis*, Springer US, New York, 2003.

32. D. Williams and C. B. Carter, in *Transmission Electron Microscopy*, Springer United States, 1996, ch. 1, pp. 3-17.

33. Martin Ermrich and D. Opper, *XRD for the analyst*, PANalytical GmbH, Germany, 2011.

34. B. Nasiri-Tabrizi and A. Fahami, Structural Characterization of Nanocrystalline Ni(50-x)Ti50Cux (X = 5, 9 wt%) Alloys Produced by Mechanical Alloying, *Adv. Nanoparticles*, 2013, **2**, 71-77.

35. A. R. a. S. M. F. Rahimi, Determination and Analysis of Structural and Optical Properties for Thermally Evaporated ZnO Thin Films, *SNL*, 2014, **5**, 1-5.

36. B. Chu and B. S. Hsiao, Small-angle X-ray scattering of polymers, *Chem. Rev.*, 2001, **101**, 1727-1762.

37. H. Schnablegger; and Y. Singh, *The SAXS Guide- Getting acquainted with the principles*, Anton Paar GmbH, Austria, 2011.

38. J. P. Patterson, M. P. Robin, C. Chassenieux, O. Colombani and R. K. O'Reilly, The analysis of solution self-assembled polymeric nanomaterials, *Chem. Soc. Rev.*, 2014, **43**, 2412-2425.

39. Z. Denchev, unpublished work.

40. S. Lowell and J. E. Shields, *Powder Surface Area and Porosity*, Springer, 1991.

41. K. Sing, The use of nitrogen adsorption for the characterisation of porous materials, *Colloids Surf., A*, 2001, **187–188**, 3-9.

42. A. J. Fletcher, Porosity and sorption behaviour http://personal.strath.ac.uk/ashleigh.fletcher/adsorption.htm, 2008.

43. R. D. Andrade P, R. Lemus M and C. E. Pérez C, Models of sorption isotherms for food: uses and limitations, *Vitae*, 2011, **18**, 325-334.

44. N. Hwang and A. R. Barron, in *Physical Methods in Chemistry and Nano Science*, ed. A. R. Barron, United States, 2014, ch. 2, pp. 176-186.

45. M. Sartor, Dynamic light scattering, *University of California–San Diego.* http://physics.ucsd.edu/neurophysics/courses/physics_173_273/dynamic_light_scattering_03.pdf, 2003.

46. Y. Li and A. R. Barron, in *Physical Methods in Chemistry and Nano Science*, ed. A. R. Barron, United States, 2014, ch. 2, pp. 187-198.

47. C. d. Fréin, N. Soultanidis and A. R. Barrom, in *Physical Methods in Chemistry and Nano Science*, ed. A. R. Barron, United States, 2014, ch. 2, pp. 198-223.

48. A. W. Coats and J. P. Redfern, Thermogravimetric analysis. A review, *Analyst*, 1963, **88**, 906-924.

49. G. Höhne, W. Hemminger and H. J. Flammersheim, *Differential Scanning Calorimetry*, Springer, 2003.

50. B. Shadfan and A. R. Barron, in *Physical Methods in Chemistry and Nano Science*, ed. A. R. Barron, United States, 2014, ch. 2, pp. 224-228.

51. A. Orbaek and A. R. Barron, in *Physical Methods in Chemistry and Nano Science*, United States, 2014, pp. 34-42.

52. M. Jebb and A. R. Barron, in *Physical Methods in Chemistry and Nano Science*, United States, 2014, pp. 42-47.

53. L. Harrison and A. R. Barron, in *Physical Methods in Chemistry and Nano Science*, ed. A. R. Barron, United States, 2014, pp. 103-112.

54. M. Sauer, J. Hofkens and J. Enderlein, in *Handbook of Fluorescence Spectroscopy and Imaging*, WILEY-VCH Verlag GmbH & Co, Weinheim, 2011, ch. 1, pp. 1-30.

55. A. Miranda, J. Li, P. Derry, X. Wen and A. R. Barron, in *Physical Methods in Chemistry and Nano Science*, ed. A. R. Barron, United States, 2014, pp. 313-351.

56. G. Oaxaca and A. R. Barron, in *Physical Methods in Chemistry and Nano Science*, ed. A. R. Barron, United States, 2014, pp. 433-440.

57. K. Finnie, D. Waller, F. Perret, A. Krause-Heuer, H. Lin, J. Hanna and C. Barbé, Biodegradability of sol–gel silica microparticles for drug delivery, *J. Sol-Gel Sci. Technol.*, 2009, **49**, 12-18.

58. R. Viitala, M. Jokinen, S. L. Maunu, H. Jalonen and J. B. Rosenholm, Chemical characterization of bioresorbable sol–gel derived SiO_2 matrices prepared at protein-compatible pH, *J. Non-Cryst. Solids*, 2005, **351**, 3225-3234.

59. L. S. Connell, F. Romer, M. Suarez, E. M. Valliant, Z. Zhang, P. D. Lee, M. E. Smith, J. V. Hanna and J. R. Jones, Chemical characterisation and fabrication of chitosan-silica hybrid scaffolds with 3-glycidoxypropyl trimethoxysilane, *J. Mater. Chem. B*, 2014, **2**, 668-680.

60. D. J. Boday, T. U. o. A. M. Science and Engineering, *Silica Aerogel-polymer Nanocomposites and New Nanoparticle Syntheses*, University of Arizona, 2009.

61. J. D. Brennan, J. S. Hartman, E. I. Ilnicki and M. Rakic, Fluorescence and NMR Characterization and Biomolecule Entrapment Studies of Sol−Gel-Derived Organic−Inorganic Composite Materials Formed by Sonication of Precursors, *Chem. Mater.*, 1999, **11**, 1853-1864.

62. T. Sen and I. J. Bruce, Surface engineering of nanoparticles in suspension for particle based bio-sensing, *Sci. Rep.*, 2012, **2**.

63. S. Maguire-Boyle and A. R. Barron, in *Physical Methods in Chemistry and Nano Science*, ed. A. R. Barron, United States, 2014, pp. 285-313.

64. M. P. H. John Bland, Doctor of Philosophy, University of Liverpool, 2002.

65. Fanny Béron, Louis-Philippe Carignan, David Ménard and A. Yelon, in *Extracting Individual Properties from Global Behaviour: First-order Reversal Curve Method Applied to Magnetic Nanowire Arrays, Electrodeposited Nanowires and their Applications*, ed. N. Lupu, InTech, 2010, ch. 7.

Chapter Three

Continuous Flow Tuning of Ordered Mesoporous Silica Under Ambient Conditions

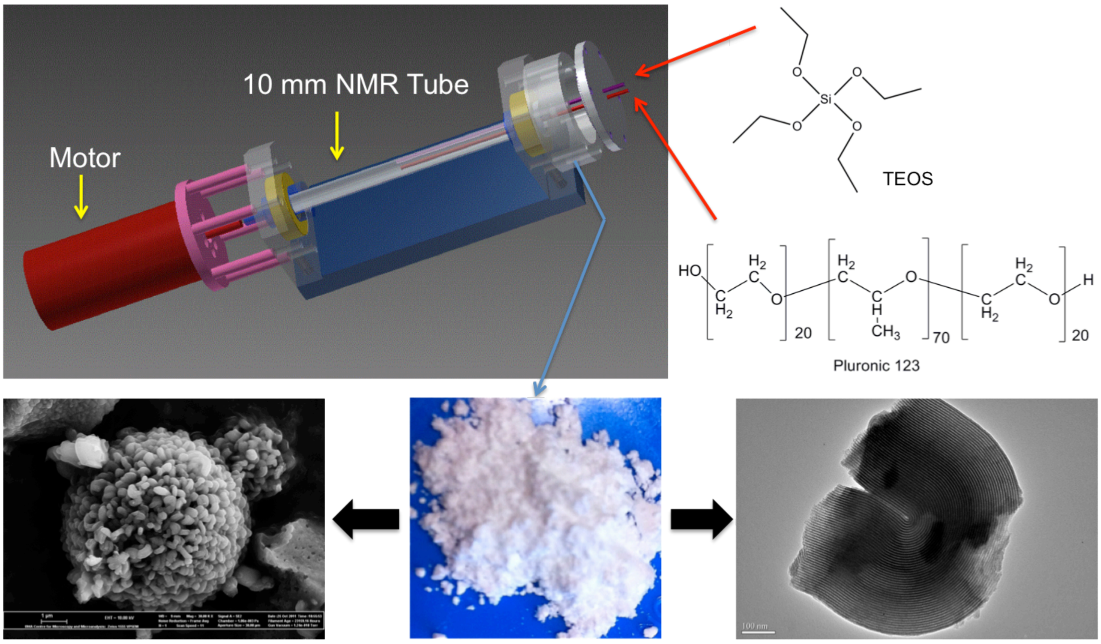

This chapter is reformatted from a paper published in ***RSC Advances***, Year 2013, Vol. 3, Issue 41, Pages 18767-18770.

3.1. Abstract

Mesoporous silica SBA-15 is formed at room temperature, with significantly shortened pre-calcining reaction times, down to minutes under continuous flow conditions using a vortex fluidic device (VFD). This is associated with controllable pore size by varying the shear on the preformed micelles, from 2.8 nm to 3.8 nm, and a constant wall thickness at ~ 5 nm.

3.2. Introduction

Mesoporous silica was discovered in 1970, with limited attention thereafter until the discovery in the 1990s of ordered mesoporous nanomaterial, which was named Mobil Crystalline Material, MCM-41.[1] It has a large surface area, typically > 1000 m^2g^{-1}, and pore diameters of 2 to 10 nm.[2, 3] However, MCM-41 has low hydrothermal stability which relates to the thin pore walls, 1 – 2 nm.[4] Zhao *et al.* subsequently developed a well-ordered 2D hexagonal mesoporous silica, SBA-15, using a non-ionic amphiphilic triblock copolymer as the structure directing agent,[5] in place of cationic cetyltrimetylammonium bromide (CTAB) used in the synthesis of MCM-41.[6] The properties of MCM-41 can be tailored by changing the wall composition,[7] and MCM-41 type mesoporous silica nanoparticles (MSNs) ~ 100 nm are available for bio-medical applications[8] with low cytotoxicity.[9] SBA-15 also has a large surface area, 400 to 900 m^2g^{-1}, with uniform pore size up to 30 nm in diameter,[10] but thicker walls than MCM-41, at 3.1 to 6.4 nm.[5] SBA-15 has applications in, for example, catalysis, absorption, separation, biosensors and drug delivery.[10-12]

Typically SBA-15 is prepared under acidic conditions using the triblock copolymer Pluronic® P-123 ($EO_{20}PO_{70}EO_{20}$, where EO is ethylene oxide and PO is propylene oxide) as the template, and tetraethyl orthosilicate (TEOS) as the silica precursor.[5, 10, 13, 14] The crucial step is the hydrothermal treatment, which can affect the mesoscopic regularity of the material, with aging temperature in the range of 35 to 100 °C, under autogenous pressure in a Teflon-lined autoclaves for 24 to 48 hours.[5, 14-17] There are several challenges associated with the synthesis of SBA-15, including generating materials with relatively small particles size, controlling the pore diameter and the wall thickness, and reducing the processing time, as well as avoiding batch processing, which can suffer from anisotropic mixing and heat transfer, and the reduction in processing time is advantageous.

Shear flow in a Couette cell operating under laminar flow conditions has been used to prepare mesoporous silica, affording helical micellar structures without altering the cell parameters of the material.[18] The use of a VFD has been developed in this dissertation, operating under turbulent flow conditions to prepare SBA-15 at room temperature (Figure 3.1) which dramatically shortens the processing time and the number of steps required. Here the high shear greatly influences the kinetics of the synthesis, enabling control of pore size and pore wall thickness. The use of the VFD in a continuous flow mode herein is akin to the use of a rotating tube processor operating exclusively in a horizontal position, which has been used for the fabrication of ultrafine crystalline drug nanoparticles,[19] cationic curcumin nanoparticles,[20] and cerium(III) phosphate nanorods.[21] The shear in the thin films in the VFD results in fast kinetics and a significant reduction in processing time, eliminating the conventional hydrothermal step. Also important is the ability to adjust the micellar structure of the copolymer, and in consequence the ability to adjust the pore size. In addition, the wall thickness and the morphology of SBA-15 can be controlled by varying the shear rates. The ability to alter the structure of the polymer micelles using the VFD relates to the use of the same device to exfoliate graphene and sheets of boron nitride in N-methyl pyrrolidone,[22] and the disassembly of molecular capsules in water, albeit under confined mode rather than continuous flow, where there is still shear from the effect of gravity on the tube inclined at $\theta = 45^\circ$.[23] The 45° optimised tilt angle for these studies is consistent with a maximum percent dimerization of cyclopentadiene at the same angle, for the VFD operating in the confined mode, where a finite volume of liquid is maintained in the tube, rather than moving under continuous flow conditions.[24]

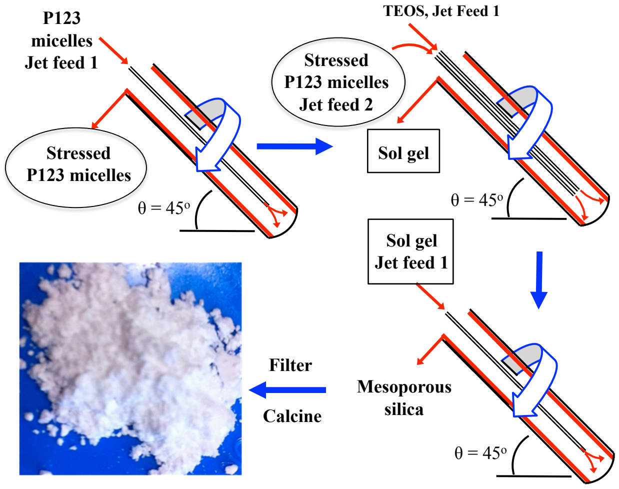

Figure 3.1. *Synthesis of mesoporous silica using VFD under continuous flow.*

3.3. Experimental

The VFD is equipped with a 10 mm glass tube and adjustable tilt angle, with multiple jet feeds for directing reactants to the base of the tube, and with variable controlled rotational speeds (see details in Figure 3.2). At high speeds a uniform thin film forms along the tube with shear arising from the viscous drag, and from the interplay of the gravitational force due to the tilting angle.[22] To control the pore size of the mesoporous silica, the polymer micelles in solution were pre-stressed using the VFD, also under continuous flow conditions (Figure 3.1). The pre-sheared P-123 solution was passed through one jet feed and another solution of the silica precursor through another jet feed, both at the closed end of the tube at room temperature (Figure 3.1), with the resulting solution then passed though the same 10 mm tube. The materials are denoted as S-1-*X*, where *X* is the pre-shear rate, as well as the hydrolyzed silica solution shear rate in the second and final step (Figure 3.1), in revolution per minute (rpm). Filtration and calcination at 550 ˚C for 6 hours afforded the mesoporous material.

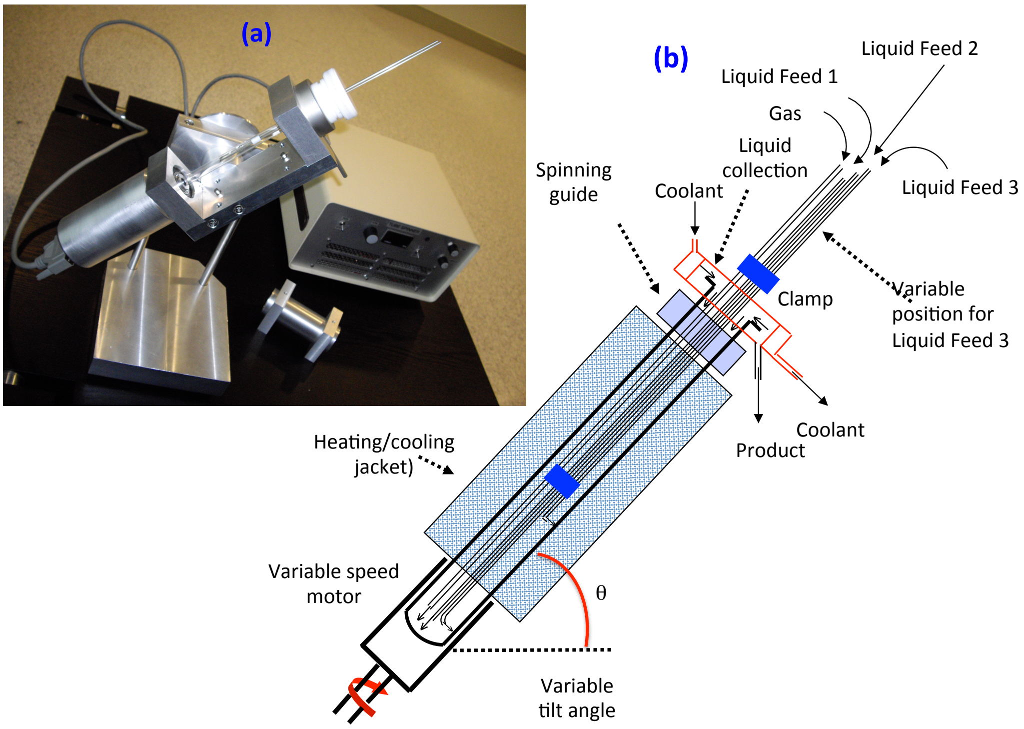

Figure 3.2. *Photograph and schematic drawing of the vortex fluidic device are shown in (a) and (b) respectively.*

3.3.1. Sample preparation

Synthesis of the mesoporous silica: 2.0 g Pluronic ® P-123 ($EO_{20}PO_{70}EO_{20}$, averaged M_w 5800, Sigma Aldrich), was dissolved in 50 mL of deionized water with 10 mL of hydrochloric acid (32%, Aldrich). The solution was stirred vigorously in a water bath at 40 to 45 °C to dissolve the P-123. After half an hour, the solution was cooled and fed into the VFD at a flow rate of 1 mL/min with the rotational speed set at 7000 rpm, with a 45˚ tilt angle, operating at room temperature, *ca.* 20 ˚C. After collecting the pre-sheared micelles solution, the solution was then fed into the VFD again through liquid feed 1. At the same time, 4.4 mL of tetraethyl orthosilicate (TEOS, 98%, Sigma Aldrich) was added through liquid feed 2 (Figure 3.1). This resulted in some sol gel precipitation arising from surfactant micelle assembly and aggregation,[8] and the mixture was then fed separately into a VFD for further shear induced processing. The resulting white material was collected by filtration, washed with deionized water, and dried at 80 ˚C overnight, prior to calcining in air at 550 ˚C for 6 hours to remove the polymer template. The final chemical composition of the mixture was 2 g P-123: 0.02 mol TEOS: 0.32 mol HCl: 2.78 mol H_2O. Approximately 0.8 g of calcined sample was collected and the yield was calculated to be 67.5%. The sample is denoted as S-1. For comparison, mesoporous silica SBA-15 was prepared using the method reported by Zhao *et al.*,[5] with the sol gel precipitate dried at 80 ˚C overnight then calcined at 550 ˚C for 6 hours. The final chemical composition of the mixture was 2 g P-123: 0.02 mol TEOS: 0.32 mol HCl: 2.78 mol H_2O.

3.3.2. Sample characterization

Scanning electron micrographs (SEM) were obtained using a ZEISS 1555 instrument at an accelerating voltage of 5 – 15 kV. Samples were spin-coated with platinum of 3 nm in thickness to avoid charging effect and for better imaging quality. Transmission electron micrographs (TEM) were obtained using a JEOL 2100 instrument operating voltage of 120 kV. Calcined sample was dispersed in ethanol, sonicated for 5 minutes, and drop-casted onto a carbon coated copper grid and allowed to dry before imaging.

Small-angle powder X-ray diffraction (SAXRD) data were collected on a PANalytic Empyrean diffractometer system, using Nickel-filtered Cu Kα radiation at 40 kV and 40 mA. Thermogravimetric analyses (TGA) were performed under the flow of air on a TA Instruments TGA- Q50 unit with a heating rate of 10 °C/min. Nitrogen adsorption-desorption studies were performed using a Micromeritics TriStar^{TM} II 3020 system. The samples were outgassed at 200 °C for 16 hours prior to gas adsorption which was carried out at 77K. The specific surface area, S_{BET}, was determined from the linear part of the BET equation ($P/P_o = 0.09 - 0.40$). Equating the rate of condensation of gas molecules to the rate of evaporation from the absorbed layer, led to determining the surface area using the following equation:[25]

$$\frac{P}{V_a(P_o - P)} = \frac{1}{V_m C} + \frac{C-1}{V_m C}\left(\frac{P}{P_o}\right) \qquad (3.1)$$

where V_a refers to the adsorbed volume, V_m is the micropore volume, and P_o is the saturation pressure of the gas. The pore size distribution and pore volume were evaluated using the Barrett- Joyner- Halenda (BJH) method. The total pore volume reported was taken from the amount of gas adsorbed at a relative pressure (P/P_o) at 0.995.

3.3.3. Molecular modeling

Materials Studio V6.0 was used for modeling of the Pluronic® P-123 structures. The Sketch Atom module was used to draw a molecule of the triblock copolymer and the structure was then 'cleaned' for unorthodox bond lengths and angles. For micelle construction, a manual structure manipulation of a molecule was undertaken to produce a 'v' shape as a starting geometry which was further cleaned and minimized. For energy minimization, the Discover Module was used with the PCFF forcefield and the Atom-based summation method with Fine quality. The Steepest Descent method was used with a convergence criterion of 0.001 kcal/mol/Å. Molecular dynamics simulations were carried out using the NVT ensemble at 298 K with a time step of 1.0 fs and 100,000 steps using the Nose thermostat.

3.4. Results and Discussion

The powder diffraction pattern (XRD) of calcined SBA-15 has four strong peaks at d-spacings of 93.1 Å, 55.4 Å, 48.6 Å, and 36.8 Å respectively, with the unit cell parameter, a = 107.5 Å, Figure 3.3(I)(a). Calcined S-1-7000, Figure 3.3(I)(b), has three peaks at d-spacings of 82.6 Å, 48 .6 Å and 37.6 Å with a = 95.4 Å. The material prepared using conventional processing at ambient temperature has one weak peak at d-spacing of 74.8 Å, Figure 3.3(I)(c).

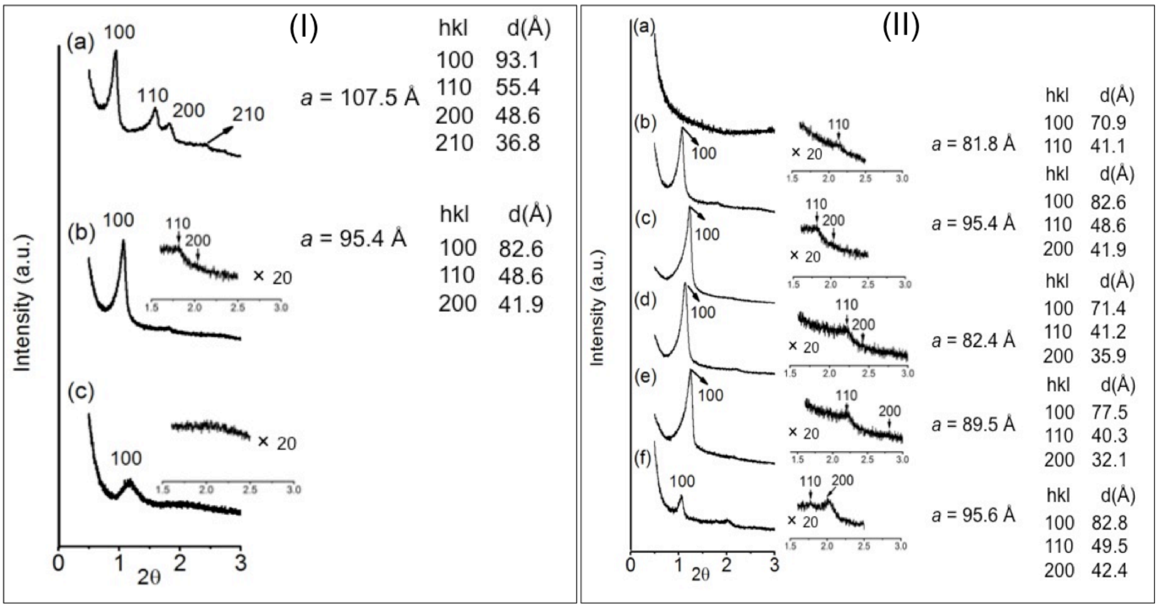

Figure 3.3. *XRD for (I) calcined (a) SBA-15 showing 4 peaks, (b) S-1-7000 (Table 3.1) showing 3 peaks, and, (c) SBA-15 synthesized at room temperature showing one weak peak, and (II) (a) S-1-3500, with no ordered structure, (b) S-1-5500, (c) S-1-7000, (d) S-1-8500, and (e) S-1-7000^c, without pre-sheared micelle solution and the solution sheared at 7000 rpm, and (f) SBA-15^b, prepared according to conventional method without hydrothermal treatment,(Table 3.1), showing peaks with d-spacings for the 2D hexagonal structure.*

The as-synthesized S-1-7000 resulted in a 50% weight loss (TGA) over three distinct steps between 25 – 180 °C, 180 – 400 °C, > 400 °C, Figure 3.4(a), which corresponds respectively to desorption of water, decomposition of the polymer template, and loss of water content formed from condensation of silanol groups in the silica framework.[26, 27] The calcined material showed approximately 4% weight loss from 0 – 100 °C, Figure 3.4(b), with no significant weight loss > 100 °C, which is consistent with uptake of a small amount of moisture post calcining, and that the polymer was removed at 550 °C.

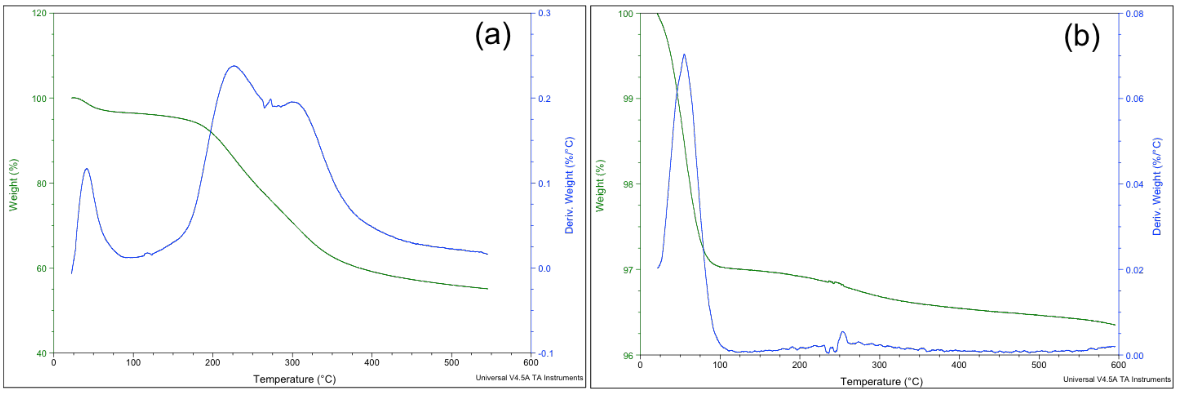

Figure 3.4. *(a) TGA data showing the weight loss of as-synthesized sample S-1-7000 as a function of temperature between 10 to 550 °C. (b) TGA data showing the weight loss of the calcined sample S-1-7000 as a function of temperature between 10 to 600 °C. The negative of the first derivative (%/°C) is also plotted for each analysis.*

SEM of S-1-7000 mesoporous silica after calcination revealed both chain and toroidal "doughnut" structures with the latter assembled into spheroidal arrays approximately 6 µm in diameter, Figure 3.5(a) and (c). In contrast to the use of a Couette cell where the shear eventually stretches and twists the bundles of micelles,[18] the formation of toroids in the present study presumably arises from the intense shear distorting the cylindrical micelles.[28] Given the likely variation in the length of the cylindrical micelles, the bending energy required for toroid formation will vary resulting in the co-existence of chains and toroids during the growth of the silica. Sample SBA-15 shows the expected chain-like structures, Figure 3.5(e), where the shear from stirring is insufficient for significant bending of the cylindrical micelles. No chain like structures was evident for the material prepared using the conventional method at room temperature, Figure 3.5(g).

TEM micrographs of calcined S-1-7000 show a well-ordered 2D hexagonal structure, as well as the curvature of the material identified using SEM, Figure 3.5(b) and (d). Calcined SBA-15 also shows a well-ordered structure (Figure 3.5(f)), but the calcined SBA-15 synthesized at room temperature had no regular array of mesoporous channels (Figure 3.5(h)). Thus SEM and TEM (Figure 3.5(g) and 3(h)), show that well-ordered mesoporous silica is not formed using conventional processing at room temperature, which is consistent with the results from XRD, Figure 3.3(I)(c).

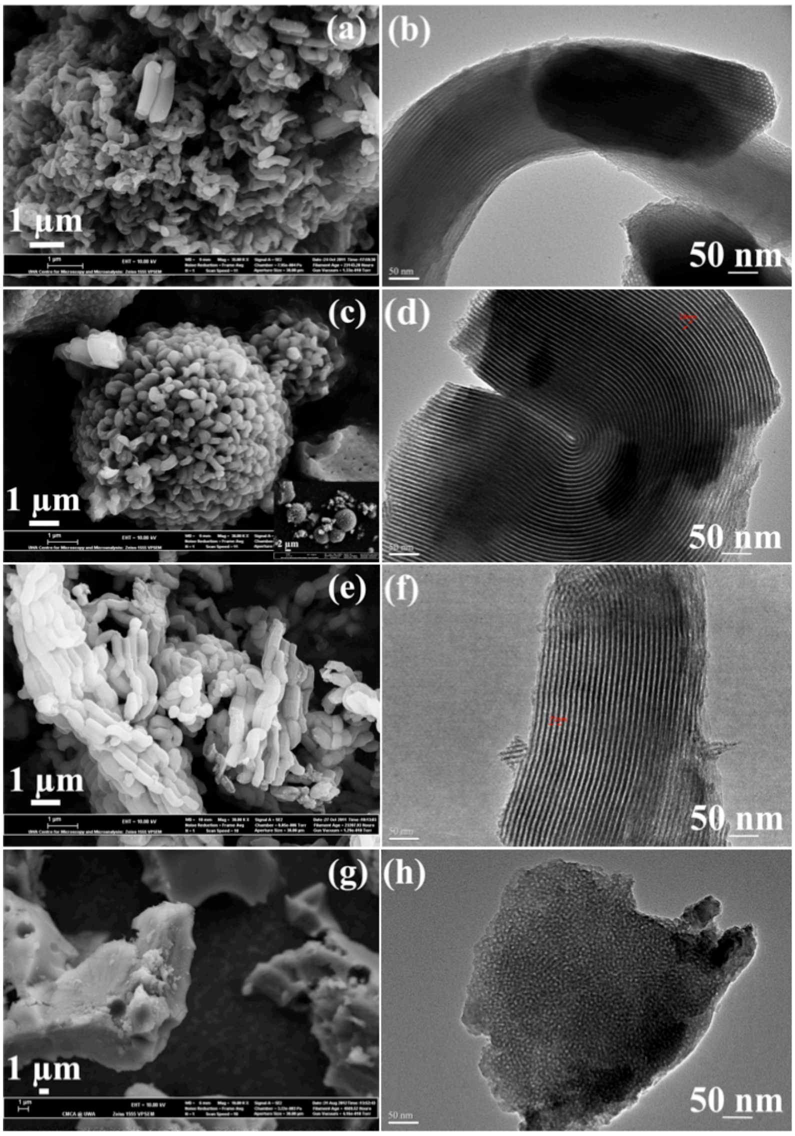

Figure 3.5. *SEM and TEM images of S-1-7000 (Table 3.1), showing a chain-like structure, (a) and (b), and ring/toroidal structures assembled into a sphere, (c) and (d), and for comparison an SEM image of SBA-15, (e) and (f), and prepared using the conventional method, (g) and (h) the conventional method at room temperature.*

Table 3.1. Variation in structural parameters of mesoporous silica S-1 for variation in shear on P-123 micelles.

Sample ID[a]	S_{BET} (m^2g^{-1})	V_t (cm^3g^{-1})	Dp (Å)	d (Å)	a (Å)	b (Å)
S-1-3500	591	0.51	34.0	–	–	–
S-1-5500	575	0.36	29.6	70.9	81.8	52.2
S-1-7000	510	0.36	28.8	82.6	95.4	66.6
S-1-8500	530	0.40	30.1	71.4	82.4	52.3
S-1-7000[c]	529	0.53	39.1	77.5	89.5	49.6
SBA-15[b]	642	0.70	44.7	82.8	95.6	52.1

[a] Last 4 digits refer to the pre-shearing and the hydrolyzed solution rotational speed in rpm [b] Prepared according to conventional method without hydrothermal treatment. [c] Without pre-sheared micelle solution, for the solution sheared at

7000 rpm. * XRD unit cell parameter *a* calculated based on 2d100/√3; *b*, wall thickness based on *b* = *a* – pore diameter; S_{BET}, BET specific surface area determined from linear plots (P/Po from 0.1 to 0.4); V_t, pore volume at relative pressure of 0.995 and D*p*, pore diameter determined from BJH adsorption.

Table 3.1 shows the pore structure parameters of S-1-X and SBA-15 prepared by the conventional method.[5, 29] Clearly the higher the shear, the smaller the pore diameter (Figure 3.6). Moreover the effect of micro-mixing experienced by the micelles in the VFD leads to homogeneity of the sample, as evidenced by the narrower pore size distribution of the mesoporous compared to the conventional method. At 8500 rpm, a larger pore size and BET surface area results which may arise from different micro-mixing in much thinner films formed at higher shear rates.

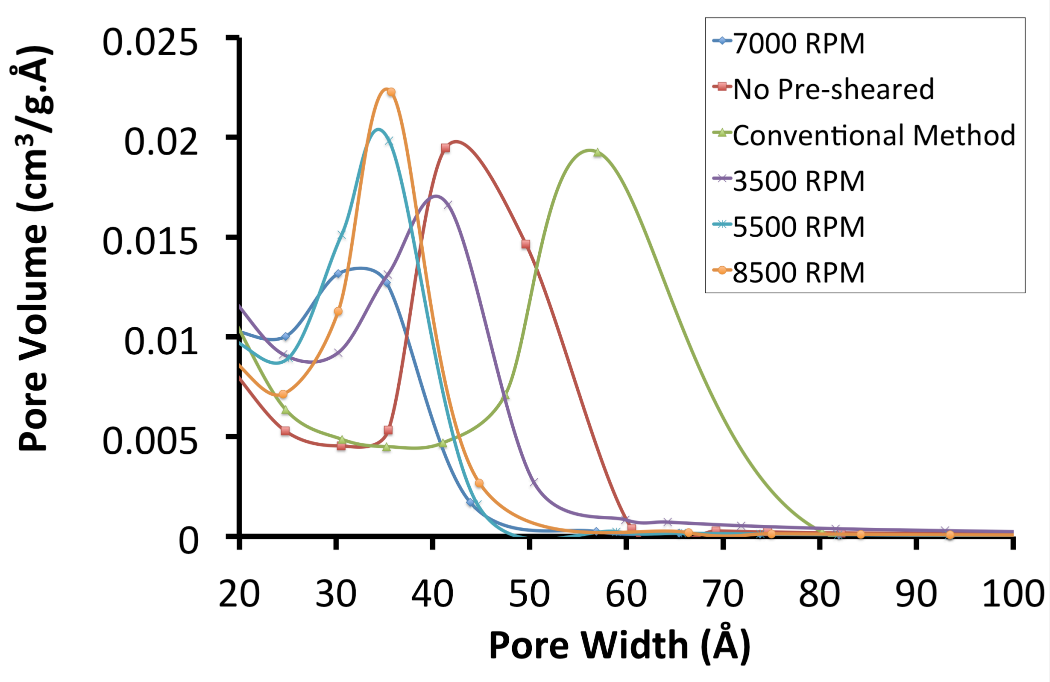

Figure 3.6. *Pore size distribution of sample S-1-7000 (Table 3.1) associated with variation in shear rates associated with change in rotational speed of a 10 mm diameter tube in the VFD, inclined 45 degrees, and with flow rates of reactants at 1 mL/min.*

In establishing the effect of shear in controlling pore diameter, small angle XRD patterns of calcined S-1-*X* samples are compared (Figure 3.3(II)). At 3500 rpm, no peak was evident from XRD (Figure 3.3(II)(a)), which may arise from the meso-regularity not being fully formed at this shear rate. At 5500 rpm, only 2 peaks are evident (Figure 3.3(II)(b)), which may due to the immature formation of the mesostructure at this shear rate. At 7000 and 8500 rpm (Figure 3.3(II)(c) and (d)), both exhibited 3 well-resolved peaks, which are indexed as (100), (110), and (200), and can be associated to the 2D hexagonal symmetry.

The intense (100) peak of S-1-7000 gives a *d*-spacing of 82.6 Å with a large unit cell parameter, (*a* = 95.4 Å).[1] Without pre-stressing the micelle (Figure 3.3(II)(e)), 3 peaks are observed with weaker intensity, but with a larger pore diameter. As discussed above, the conventional method at room temperature is unsuccessful. Under 40 °C, mesostructured material can be produced (Figure 3.3(II)(f)), and without hydrothermal treatment the intensity of the peaks are weak, and this is why hydrothermal treatment is important to enhance the meso-regularity.

Molecular dynamics simulations were carried out to understand the variation in pore size diameter of the mesoporous silica synthesized using the VFD, Table 3.1. At critical micelle concentrations (CMC), Pluronic (Figure 3.7(a)) starts forming mi-cellar structures displayed as different orientations in Figure 3.7(b) and (c). These were used as starting geometries for the molecular dynamics simulations to mimic the evolution of the micelles under shear stress akin to VFD conditions. In normal conditions, the micelle grows in the direction shown by the black arrows, Figure 3.7(c), producing a rod-like structure with a diameter of 26.5 nm. The diameter corresponds to the hydrodynamic radius, but not necessarily corresponding to the mesotructure after adding TEOS. However, in the VFD, the intense shear leads to ‘wrapping’ of the hydrophobic core with the hydrophilic tails thus blocking further growth of the micelles. The final structure is spherical with the hydrophilic tails wrapped around the micelle to protect the hydrophobic core, with an overall diameter of ~13 nm, Figures 3.7(d) and (e). The effect of shear on the nature of micelles has been noted by Yu *et al.* in the context of forming a toroid of triblock polymers.[28] The reduction in size of the micelle translates to inefficient interdigitation and thus closer packing of the micelles which is consistent with the reduction in pore size diameter of the mesoporous silica after calcination, and also smaller *d*-spacings, Table 3.1.

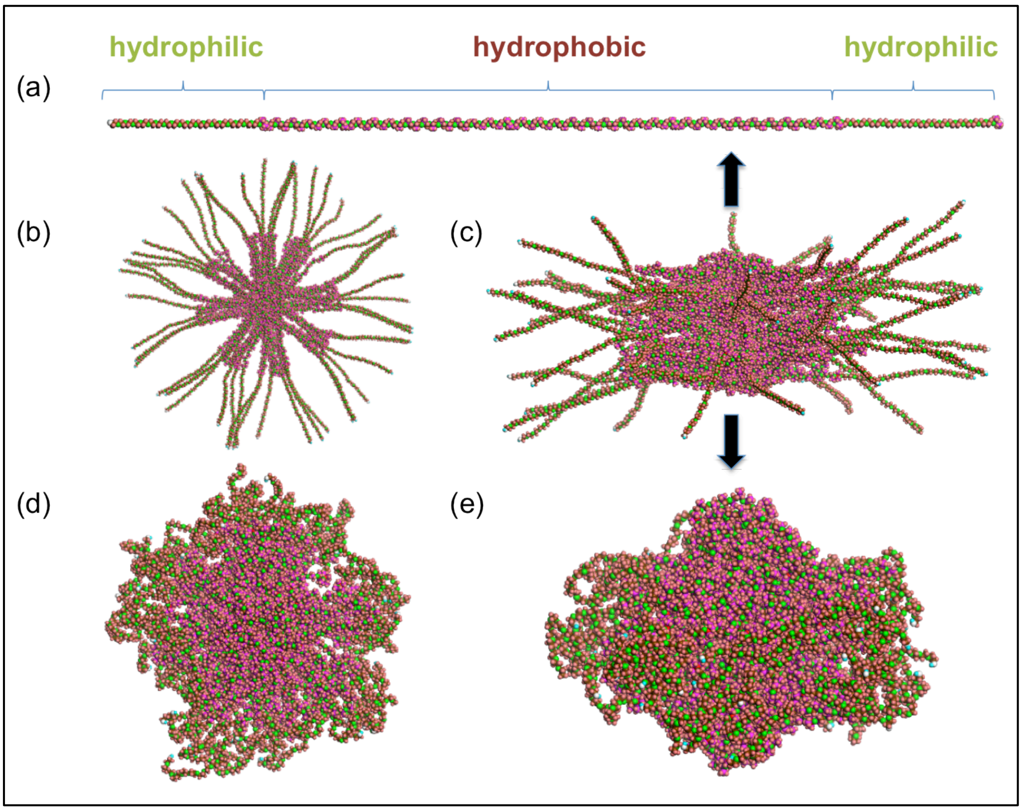

Figure 3.7. *Pluronic structures in CPK format. (a) Linear Pluronic ® P-123 molecule showing hydrophobic core and the hydrophilic tails. (b) and (c) showing different orientations of the starting geometry of the micelle. (d) and (e) showing different orientations of the final geometry of the micelle after molecular dynamic simulations. Atoms are coloured by forcefield type.*

3.5. Conclusions

A new strategy for preparing mesoporous silica has been established, using continuous flow processing involving a vortex fluidic device (VFD) prior to the necessary calcining to remove the polymer template. The overall duration of this synthesis for *ca.* 60 mL of solution is less than 5 hours (with the actual processing time using the VFD less than 1 hour). This is in contrast to the now traditional exclusively batch hydrothermal process, which requires more than 48 hours.[1]

Moreover there is now the ability to control the pore size for fine tuning the property of the mesoporous silica which is without precedent, as is the formation of the pre-calcined material under continuous flow conditions which addresses the ability to scale up the chemical processing at the inception of the science. This has potential for the synthesis of mesoporous materials in general, where the shear in the thin films in the VFD can be varied to change the pore size, arising from the stretching of the micelles, and also in controlling the thickness of the pore walls. This is important in increasing the thermal stability of the material, for high temperature applications.

Continuous flow processing prior to calcining ensures a more uniform product with all reactants being treated in the same way, and for the present process there is a significant reduction in energy consumption with the process operating at ambient temperature and atmospheric pressure.

3.6. Acknowledgement

Support from the Australian Research Council and the Centre for Microscopy, Characterisation and Analysis (The University of Western Australia), is gratefully acknowledged, as is graphical support from Bob Northeast, Flinders University.

3.7. References

1. C. T. Kresge, M. E. Leonowicz, W. J. Roth, J. C. Vartuli and J. S. Beck, Ordered mesoporous molecular sieves synthesized by a liquid-crystal template mechanism, *Nature*, 1992, **359**, 710-712.

2. V.-T. Hoang, Q. Huang, M. Ei*f*á, T.-O. Do and S. Kaliaguine, Structure and Diffusion Characterization of SBA-15 Materials, *Langmuir*, 2005, **21**, 2051-2057.

3. A. Y. Khodakov, V. L. Zholobenko, R. Bechara and D. Durand, Impact of aqueous impregnation on the long-range ordering and mesoporous structure of cobalt containing MCM-41 and SBA-15 materials, *Microporous Mesoporous Mater.*, 2005, **79**, 29-39.

4. W. Guo, X. Li and X. S. Zhao, Understanding the hydrothermal stability of large-pore periodic mesoporous organosilicas and pure silicas, *Microporous Mesoporous Mater.*, 2006, **93**, 285-293.

5. D. Zhao, J. Feng, Q. Huo, N. Melosh, G. H. Fredrickson, B. F. Chmelka and G. D. Stucky, Triblock Copolymer Syntheses of Mesoporous Silica with Periodic 50 to 300 Angstrom Pores, *Science*, 1998, **279**, 548-552.

6. J. Y. Ying, C. P. Mehnert and M. S. Wong, Synthesis and Applications of Supramolecular-Templated Mesoporous Materials, *Angew. Chem. Int. Ed.*, 1999, **38**, 56-77.

7. X. S. Zhao, G. Q. Lu and G. J. Millar, Advances in Mesoporous Molecular Sieve MCM-41, *Ind. Eng. Chem. Res.*, 1996, **35**, 2075-2090.

8. Z. Li, J. C. Barnes, A. Bosoy, J. F. Stoddart and J. I. Zink, Mesoporous silica nanoparticles in biomedical applications, *Chem. Soc. Rev.*, 2012, **41**, 2590-2605.

9. F. Tang, L. Li and D. Chen, Mesoporous Silica Nanoparticles: Synthesis, Biocompatibility and Drug Delivery, *Adv. Mater.*, 2012, **24**, 1504-1534.

10. J. r. P. Thielemann, F. Girgsdies, R. Schlögl and C. Hess, Pore structure and surface area of silica SBA-15: influence of washing and scale-up, *Beilstein J. Nanotechnol.*, 2011, **2**, 110-118.

11. L. Y. Chen, S. Jaenicke and G. K. Chuah, Thermal and hydrothermal stability of framework-substituted MCM-41 mesoporous materials, *Microporous Mater.*, 1997, **12**, 323-330.

12. S. Lin, L. Shi, M. M. L. Ribeiro Carrott, P. J. M. Carrott, J. Rocha, M. R. Li and X. D. Zou, Direct synthesis without addition of acid of Al-SBA-15 with controllable porosity and high hydrothermal stability, *Microporous Mesoporous Mater.*, 2011, **142**, 526-534.

13. R. Che, D. Gu, L. Shi and D. Zhao, Direct imaging of the layer-by-layer growth and rod-unit repairing defects of mesoporous silica SBA-15 by cryo-SEM, *Journal of Materials Chemistry*, 2011, **21**, 17371-17381.

14. M. S. Morey, S. O'Brien, S. Schwarz and G. D. Stucky, Hydrothermal and Postsynthesis Surface Modification of Cubic, MCM-48, and Ultralarge Pore SBA-15 Mesoporous Silica with Titanium, *Chem. Mater.*, 2000, **12**, 898-911.

15. A. Galarneau, H. Cambon, F. Di Renzo, R. Ryoo, M. Choi and F. Fajula, Microporosity and connections between pores in SBA-15 mesostructured silicas as a function of the temperature of synthesis, *New J. Chem.*, 2003, **27**, 73-79.

16. Y. Wan and D. Zhao, On the Controllable Soft-Templating Approach to Mesoporous Silicates, *Chem. Rev.*, 2007, **107**, 2821-2860.

17. H. I. Lee, J. H. Kim, G. D. Stucky, Y. Shi, C. Pak and J. M. Kim, Morphology-selective synthesis of mesoporous SBA-15 particles over micrometer, submicrometer and nanometer scales, *J. Mater. Chem.*, 2010, **20**, 8483-8487.

18. W.-J. Kim and S.-M. Yang, Preparation of Mesoporous Materials from the Flow-Induced Microstructure in Aqueous Surfactant Solutions, *Chem. Mater.*, 2000, **12**, 3227-3235.

19. S. Dev, K. S. Iyer and C. L. Raston, Nanosized drug formulations under microfluidic continuous flow, *Lab Chip*, 2011, **11**, 3214-3217.

20. S. Dev, P. Prabhakaran, L. Filgueira, K. S. Iyer and C. L. Raston, Microfluidic fabrication of cationic curcumin nanoparticles as an anti-cancer agent, *Nanoscale*, 2012, **4**, 2575-2579.

21. J. Fang, C. W. Evans, G. J. Willis, D. Sherwood, Y. Guo, G. Lu, C. L. Raston and K. S. Iyer, Sequential microfluidic flow synthesis of CePO4 nanorods decorated with emission tunable quantum dots, *Lab Chip*, 2010, **10**, 2579-2582.

22. X. Chen, J. F. Dobson and C. L. Raston, Vortex fluidic exfoliation of graphite and boron nitride, *Chem. Commun.*, 2012, **48**, 3703-3705.

23. A. D. Martin, R. A. Boulos, L. J. Hubble, K. J. Hartlieb and C. L. Raston, Multifunctional water-soluble molecular capsules based on p-phosphonic acid

calix[5]arene, *Chem. Commun.*, 2011, **47**, 7353-7355.

24. L. Yasmin, X. Chen, K. A. Stubbs and C. L. Raston, Optimising a vortex fluidic device for controlling chemical reactivity and selectivity, *Sci. Rep.*, 2013, **3**, 2282.

25. W. Paul A, Clyde Orr, in *Analytical Methods in Fine Particle Technology*, Micromeritics Instrument Corporation, Georgia, 1997, ch. 3, p. 59.

26. M. Kruk, M. Jaroniec, C. H. Ko and R. Ryoo, Characterization of the Porous Structure of SBA-15, *Chem. Mater.*, 2000, **12**, 1961-1968.

27. C.-Y. Chen, S. L. Burkett, H.-X. Li and M. E. Davis, Studies on mesoporous materials II. Synthesis mechanism of MCM-41, *Microporous Mater.*, 1993, **2**, 27-34.

28. H. Yu and W. Jiang, Effect of Shear Flow on the Formation of Ring-Shaped ABA Amphiphilic Triblock Copolymer Micelles, *Macromolecules*, 2009, **42**, 3399-3404.

29. D. Zhao, Q. Huo, J. Feng, B. F. Chmelka and G. D. Stucky, Nonionic Triblock and Star Diblock Copolymer and Oligomeric Surfactant Syntheses of Highly Ordered, Hydrothermally Stable, Mesoporous Silica Structures, *J. Am. Chem. Soc.*, 1998, **120**, 6024-6036.

Chapter Four

One-Pot Synthesis of PdO/SBA-15 Under Neutral Condition: Synthesis, Characterization, and Catalytic Properties

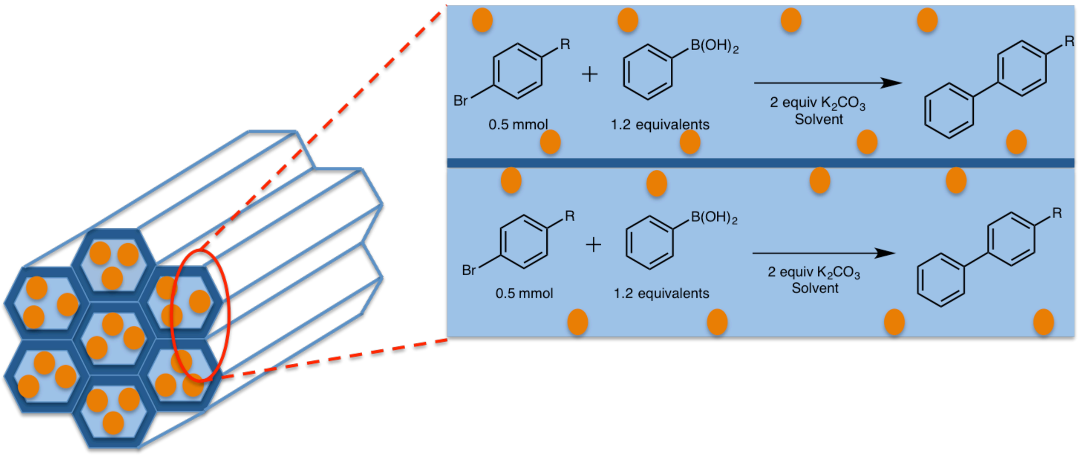

This chapter is prepared in form of a manuscript to be submitted for publication in an international peer-reviewed journal.

4.1. Abstract

A high surface area heterogeneous catalyst has been synthesized using a vortex fluidic device (VFD) under neutral pH and ambient conditions, generating palladium oxide nanoparticles embedded in a mesoporous silica, SBA-15. The overall processing time takes only five hours, a near five-fold improvement from the conventional hydrothermal synthesis which takes up to 24 hours for hydrolysis and condensation, then an additional 24 hours for hydrothermal treatment. Catalytic performance is tested using a Suzuki cross-coupling reaction between 4-nitro bromobenzene and phenylboronic acid, in the presence of potassium carbonate and ethanol under reflux. The reaction goes to completion (> 99% conversion) in 1.0 hour for 3.0 mol% palladium loading.

4.2. Introduction

Palladium (Pd) nanoparticles are often used as catalysts in carbon-carbon cross- couplings such as in Buchwald-Harwig, Heck, Sonogashira, Stille, and Suzuki-Miyaura reactions.[1-4] They have large surface-to-volume ratio and thus have higher catalytic activity.[5-8] However, there are drawbacks on the homogeneous Pd catalyst using metal nanoparticles, in particular the challenge in recovering and reusing (recycling) the catalyst,[4] and that Pd nanoparticles readily agglomerated with catalytic deactivation.[8] Ordered mesoporous silica such as MCM-41 and SBA-15 are considered ideal supports in developing heterogeneous catalyst because of their large surface area and ease of separation from reaction mixtures. Overall, the unique characteristics of these materials allow for a higher activity and selectivity in chemical transformations. Pd doped mesoporous silica is an excellent catalyst for cross coupling reactions and has been widely studied over recent decades.[2, 9] Pd nanoparticles are typically introduced into the mesoporous silica supports through wetness impregnation, ion exchange, vapour-phase deposition, and the use of a two-solvent method.[10-12] However, these methods have disadvantages such as uneven distribution of the particles, with particles also on the surface of the material rather than in the pores, and low incorporation of the metal,[10, 11] with the catalytic performance of such heterogeneous catalysts heavily dependent on the composition, size, and shape of the particles. In addition, the pore size distribution and the organization of the porous network are important.[11] With these complexities, designing the catalysts with the nanoparticles uniform in size, evenly distributed through the material, and not present on the surface of the particles is challenging.

The synthesis of SBA-15 is usually performed under acidic conditions, which involves a lengthy hydrothermal process.[13] Typically a parent support SBA-15 is prepared using the aforementioned hydrothermal method, and the palladium catalyst is impregnated using a post-grafting method, which accounts for another 12 hours of processing time, for both impregnation and drying.[14] I previously established that ordered mesoporous silica, SBA-15, can be readily prepared under acidic conditions using a vortex fluidic device (VFD), operating under continuous flow conditions at room temperature, and avoiding long hydrothermal processing times.[15] With this established, knowing that the high shear in the dynamic thin film in the VFD is effective in controlling the pore size, as well as the pore thickness, developing the synthesis of mesoporous silica under neutral pH with *in situ* incorporation of palladium oxide nanoparticles was undertaken, and subsequent results are the basis of this chapter of the dissertation. Indeed this heterogeneous palladium catalyst can be successfully produced under neutral pH, within 5 hours (*ca.* 60 mL volume), under continuous processing prior to calcination. This represents a significant improvement upon the conventional method, which requires at least 48 hours hydrothermal batch processing.

4.3. Experimental

4.3.1. Synthesis of PdO/SBA-15

The synthesis was carried out according to the method reported by Song *et al.*,[11] but now using continuous flow processing within a VFD. Pluronic® P-123 ($EO_{20}PO_{70}EO_{20}$, averaged M_w 5800, Sigma Aldrich), tetramethyl orthosilicate (TMOS, 98%, Sigma Aldrich), palladium acetylacetonate ($[Pd(acac)_2]$, 99%, Sigma Aldrich), and sodium fluoride (99.9%, Sigma Aldrich) were used as received. Initially 2.5 g Pluronic ® P-123 was dissolved in 50.5 mL of deionized Milli-Q water, and the solution was stirred vigorously in a water bath at 40 to 45 °C to dissolve all of the polymer. Then 0.10 g of $Pd(acac)_2$ was added into the micelles solution and the mixture was stirred for one additional hour, before being fed into a VFD for shearing at 5000 rpm @ 45 ° tilt angle, for a flow rate of 1 mL/min. Using this pre-stressing of the polymer micelles in solution using a VFD allows for a better control of the pore diameter of the mesoporous silica. The collected pre-stressed micelle solution with the palladium precursor was then added with 0.375 mL of 0.5 M NaF aqueous solution, and the solution fed into the VFD through one feed jet, with 4.0 mL TMOS simultaneously fed through a separate feed jet at the same flow rate (Figure 4.1). The resulting brownish mixture was collected by vacuum filtration, washed with deionized water, and then dried at 120 °C overnight. Finally, the material was calcined under hydrogen at 550 °C for 6 hours to remove the polymer template.

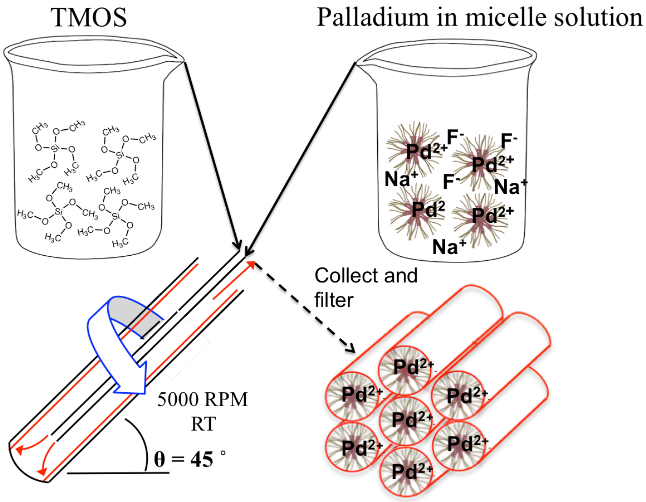

Figure 4.1. *Diagrammatic representation of the in situ synthesis of heterogeneous catalyst Pd/SBA-15 using VFD.*

4.3.2. Characterization techniques

Scanning electron micrographs (SEM) were obtained using a Quanta 450 instrument. Samples were placed on a carbon tap and pre-coated with 5 nm thickness of platinum. The images were taken using a secondary electron detector, at an accelerating voltage of 5 kV. Elemental mapping were obtained also using the SEM, the sample being pre-coated with a 3 nm layer of platinum. The analysis was carried out using back-scattered electron detector, at an accelerating voltage of 7 kV.

Transmission electron micrographs (TEM) were obtained using a FEI Tecnai ^{TM} G^2 Spirit instrument at an operating voltage of 120 kV. Sample was dispersed in ethanol and placed in ultrasonication bath for 5 min. A 7 μL of solution was then dropped casting onto a continuous carbon coated copper grid, and allowed to dry in air prior to imaging.

Small Angle X-ray Scattering (SAXS) measurements were performed at the Western Australian Small Angle Scattering Facility within Curtin University. The instrument used was a Bruker AXS Nanostar SAXS system with a copper anode in a sealed tube for the x-ray source (the operating wavelength is 1.541 Å). The system makes use of a HI-STAR detector, which is a two dimensional xenon gas wire detector (1024 x 1024 pixels). The detector is positioned 11 cm from the sample stage so that a q-range of 0.03 Å^{-1} to 0.85 Å^{-1}. As the samples are isotropic the two dimensional data is reduced to one dimensional data by averaging in the radial direction with the commercial software. This presents an intensity profile as a function of the scattering vector, q.

Nitrogen adsorption–desorption studies were performed using a Micromeritics TriStar^{TM} II 3020 system. The samples were outgassed at 200 °C for 16 hours prior to gas adsorption which was carried out at 77K. The specific surface area, S_{BET}, was determined from the linear part of the BET equation ($P/P_o = 0.05 – 0.30$). The pore size distribution and pore volume were evaluated using the Barrett–Joyner–Halenda (BJH) method. The total pore volume reported was taken from the amount of gas adsorbed at a relative pressure (P/P_o) at 0.990.

Palladium content in PdO/SBA-15 sample was obtained using inductively coupled plasma mass spectrometry (ICP-MS), conducted by TSW Analytical Pty. Ltd. (Perth, WA). The sample was accurately weighed into a Teflon beaker and digested using hydrochloric acid (15 mL, 32% wt. ultra-pure), nitric acid (5 mL, 65% wt. ultra-pure) and hydrofluoric acid (8 mL, 50% wt. A.R.). The digestate was reduced to incipient dryness then the residue dissolved with hydrochloric acid (0.5 mL 32% wt. ultra-pure), nitric acid (0.2 mL, 65% wt. ultra-pure) and water (5 mL, 18 MΩ.cm). The solution was quantitatively transferred to a suitable container and made up to 10 mL. This solution was diluted to incorporate the internal standard (Rhodium at 2ppb) and assayed by ICP-MS (Agilent 7500cs) against high-purity standards (Choice Analytical, SpecPure ICP-MS Standards).

The element composition of the sample were obtained using X-ray photoelectron spectroscopy (XPS), conducted by Surface and Chemical Analysis Network (SCAN) at The University of Melbourne. XPS data was acquired using a VG ESCALAB220i-XL spectrometer equipped with a hemispherical analyzer. The incident radiation was monochromatic Al Kα X-rays (1486.6 eV) at 220 W (22 mA and 10kV). Survey (wide) and high resolution (narrow) scans were taken at analyzer pass energies of 100 eV and 50 eV, respectively. Survey scans were carried out over the binding energy range from 0 – 1200 eV with 1.0 eV step size and 100 ms dwell time. Narrow high resolution scans were run over 20 eV binding energy range with 0.05 eV step size and 250 ms dwell time. Base pressure in the analysis chamber was below 7.0×10^{-9} mbar and during sample depth profile analysis 1.5×10^{-7} mbar. A low energy flood gun was used to compensate the surface charging effect. Argon ions at 5 keV beam energy were used to sputter off approximately 18 nm surface layers at a rate of ~3 Å/second. The ion source gave a crater of approximately 3 x 3 mm. All data were processed using CasaXPS software and the energy calibration was referenced to the C 1s peak at 285.0 eV.

4.3.3. Catalytic performance testing and characterization

Reactions were carried out in air. Ethanol was fractionally distilled over K_2CO_3 onto 4Å molecular sieves under N_2, and dichloromethane (DCM) were distilled under an atmosphere of nitrogen from CaH_2 onto Linde 4Å molecular sieves, which had been activated at 180°C for 20 hours. Reaction glassware was prewashed with AR grade, concentrated (68%) HNO_3 and rinsed with deionized water, followed by AR grade acetone before flame drying and cooling *in vacuo*. Hydrochloric acid (HCl) was removed from deuterated chloroform ($CDCl_3$) by passing it through activated aluminium oxide 70 – 290 mesh (Scharlau, activity degree 1, grain size 0.05 – 0.2 mm) and stored over silver foil/molecular sieves. Other reagents were purchased from Sigma Aldrich and used without further purification.

A mixture of 4-nitrobromobenzene, phenylboronic acid (1.2 molar equivalents), K_2CO_3 (2 molar equivalents) and palladium catalyst (0.6-3.0 mol%) in 0.1 M anhydrous ethanol was stirred at reflux temperature in a preheated oil bath until TLC indicated completion. The mixture was then cooled to room temperature and filtered under gravity. The crude solid material was then sonicated in ethanol for 5 minutes, filtered under gravity and washed with DCM and then deionised water. The recollected catalyst was then dried at 80°C for 1 hour and then placed under vacuum to reuse for subsequent experiments.

Analytical thin-layer chromatography (TLC) was performed on Merck Kiesegel 60 F254 silica aluminium backed sheets, and was visualised under UV light and/or developed using potassium permanganate ($KMnO_4$) dip. $KMnO_4$ dip was prepared by the addition of 20 g K_2CO_3 and 5% NaOH (5 mL) to a solution of deionised water (300 mL), followed by the addition of 3 g $KMnO_4$. The mixture was stirred for 15min in air and then stored in the dark.

Nuclear Magnetic Resonance (NMR) spectra were recorded with a Bruker UltraShield Avance III 400 MHz or 600 MHz NMR Spectrometer running the TopSpin 2.1 software package at 299 K and 293 K, respectively. $CDCl_3$ was used as the solvent and as an internal lock. Chemical shifts (δ) are measured in ppm. ^1H NMR chemical shifts were referenced to δ7.26. Conversion was calculated from crude NMR integration of characteristic product peaks in comparison to the aryl halide starting material.

4.4. Results and Discussion

Kim *et al.* reported the synthesis of highly ordered silica mesostructures in the presence of fluoride ions over a range of pH (0 – 9) using TMOS as the silica precursors.[16] Nevertheless, this approach still involved a lengthy processing time of 24 hours with additional 24 hours aging period, prior to calcination. In this work, the use of TMOS as the silica precursor provides rapid hydrolysis, however, silica gel precipitation is retarded under neutral pH,[17] thus, trace amount of 0.5M NaF was added as the source of fluoride ions for increasing the rate of condensation and promoting precipitation.[16] In addition, the shearing forces within the thin film of VFD provide even micro-mixing and high mass transfer, which consequently intensified both the rate of hydrolysis and condensation and shortened the processing time drastically. Jin *et al.* reported that by introducing halide species such as Br^- or Cl^- during the synthesis of Pd nanocrystals greatly reduces the rate of reduction, which is an important parameter in controlling the nucleation that leads to large particles formation.[18] Using an electro-deposition approach, Maniam *et al.* deposited Pd onto carbon support by using a chloride precursor solution under acidic medium.[19] They also conducted a study on the effect of the precursor concentration and found out that a concentration beyond 1 mM resulted in aggregation of PdNPs due to fast formation of the large nuclei followed by an increase of crystal growth.[19] $Pd(acac)_2$ was chosen as the palladium precursor in this work given that its hydrophobic character is compatible with the polymer micelle P-123 solution, without the need to prepare the precursor in solution to enable higher loading and yet, achieving the small particles size for high catalytic activity. Also, the micelles can act as a stabilizing agent for the colloidal PdNPs, ensuring the PdNPs are encapsulated inside the channels.

To evaluate the mesoregularity of the as-synthesized material, small-angle X-ray scattering (SAXS) spectra were recorded using a Bruker AXS Nanostar SAXS system with a copper anode in a sealed tube for the X-ray source (the operating wavelength is 1.541 Å). The small angle pattern only show weak peaks at q = 0.569 nm^{-1}, which corresponds to *d*-spacing of 11.0 nm and a unit cell parameter, a = 12.7 nm (Figure 4.2). The weak peak of PdO/SBA-15 is possibly consequence of the washed out by Guinier features (from the size of the Pd particles) causing a decrease in scattering contrast between the pore walls and the pore channels when palladium nanoparticles are incorporated inside the pores.[20]

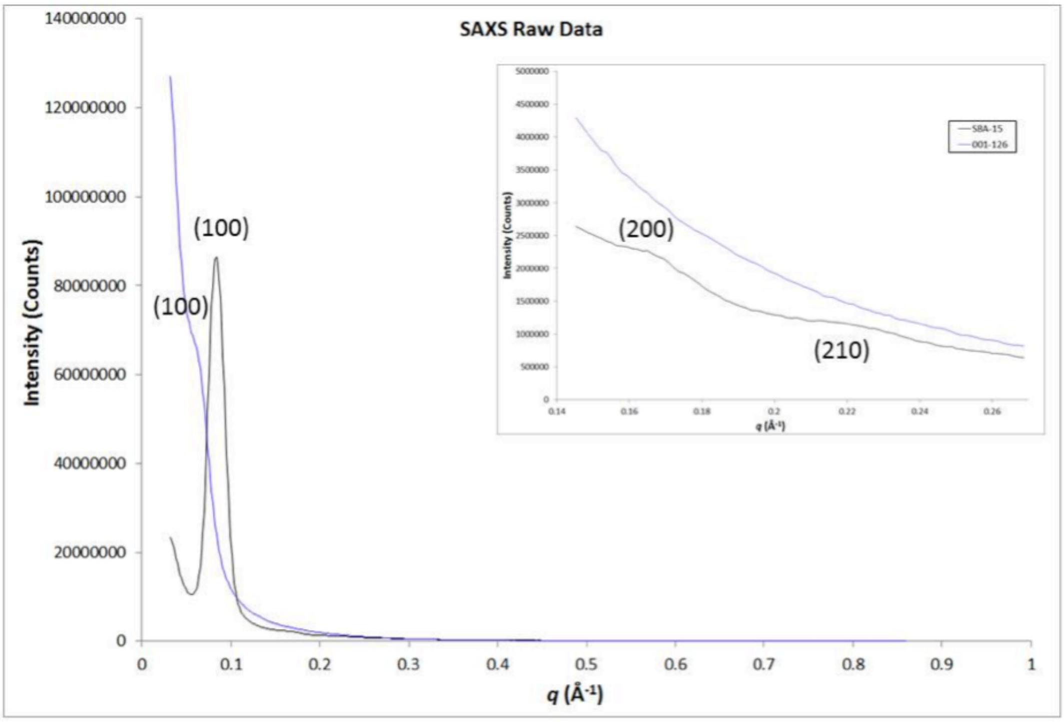

Figure 4.2. *Raw data collected for the PdO/SBA-15 and SBA-15 showing the common (100) reflection and the (200) and (210) reflections in SBA-15.*

Surface morphology of the calcined material was studied using scanning electron microscopy (SEM) and the short section chain-like structures interconnected throughout were observed, Figure 4.3(a). The transmission electron microscopy (TEM) revealed the ordered mesostructure with palladium nanoparticles embedded within the channels (Figure 4.3(b)).

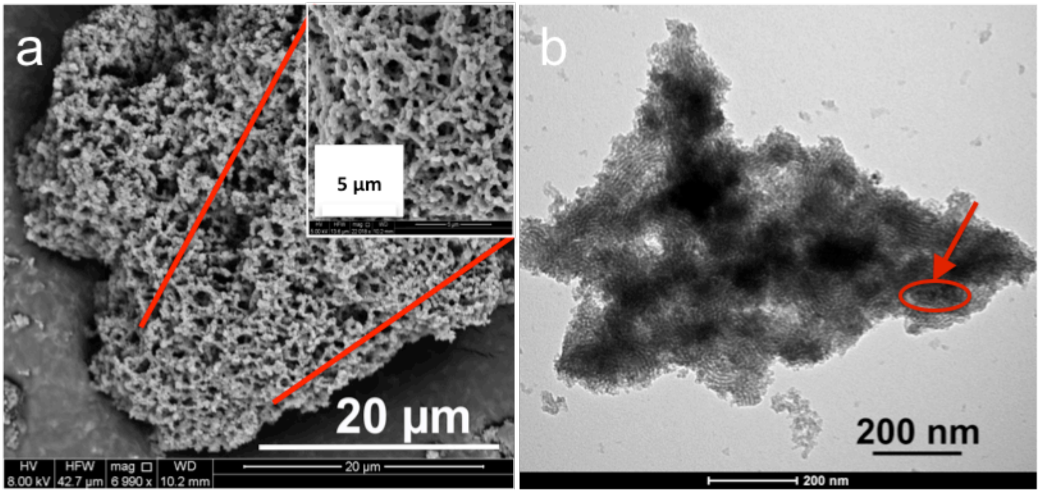

Figure 4.3. *(a) SEM image and (b) TEM image of PdO/SBA-15 synthesized using VFD at neutral pH.*

The estimated pore diameter from the TEM micrograph was 5.0 – 5.5 nm. The nitrogen adsorption-desorption isotherm of the PdO/SBA-15 obtained is a type IV isotherm and exhibited a H-1 hysteresis loop according to the IUPAC classification (Figure 4.4).[21] The structural parameter of the PdO/SBA-15 was listed in Table 4.1. The BJH calculations showed an average pore diameter of 5.5 nm, which was in good agreement with the estimation from the TEM image. All other parameters showed a close resemblance of SBA-15 mesostructure synthesized using VFD previously reported.[15]

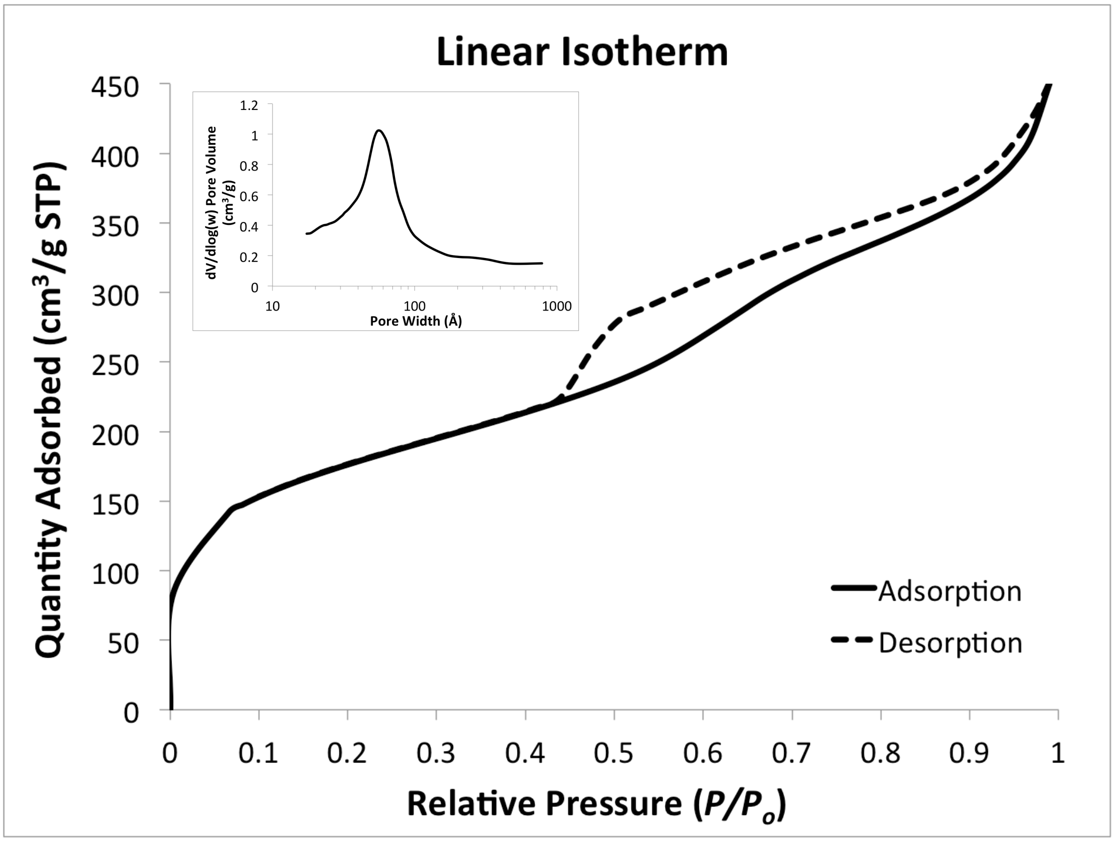

Figure 4.4. *Linear isotherm plot of Pd/SBA-15 exhibited type IV and H-1 hysteresis loop in accordance to IUPAC classification; with the BJH pore diameter distributions of adsorption (inset).*

Table 4.1. Structural parameter of PdO/SBA-15 using N_2 sorption data.

	S_{BET} (m^2/g)	V_t (cm^3/g)	D_p (Å)	d_{100} (Å)	a (Å)	b (Å)
PdO/SBA-15	596.7	0.70	55.0	110.4	127.5	72.0

* S_{BET}, BET total surface area determined from N_2 adsorption/desorption; V_t, total pore volume and D_p, pore diameter determined from BJH adsorption branch; XRD unit cell parameter a calculated based on $2d_{100}/\sqrt{3}$; b, wall thickness based on b = a - pore diameter.

The final palladium content of 1.0 wt% in the catalyst was determined using inductively coupled plasma mass spectrometry (ICP-MS). Energy-dispersive X-ray spectroscopy (EDS) via SEM was conducted with a full area scanned and mapped for individual elements, silica (Si), oxygen (O) and palladium (Pd), proved the existence of the elements

(Figure 4.5). However, the results showed low concentration using this technique, which relies on the interaction of the x-ray excitation and the sample, whereby the detection and measurement depends on a number of factors such as the energy of the X-ray, the amount, and density of material. Thus, quantitative element analysis cannot be relied on using this technique.

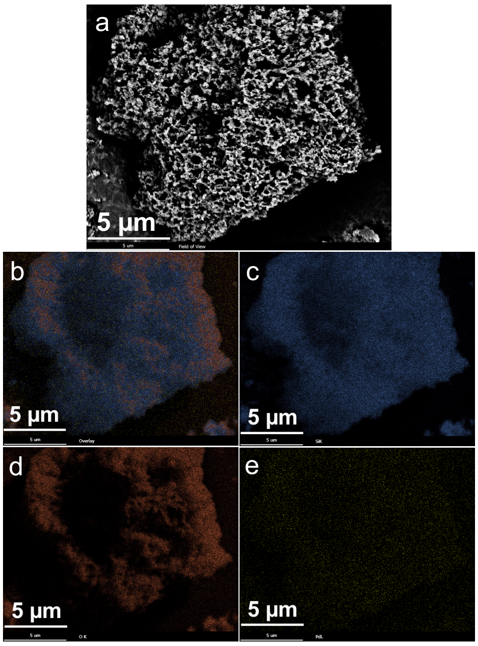

Figure 4.5. *SEM image of PdO/SBA-15 after calcination, and (b) the overlay elemental mapping image of the area showed in (a), (c) silica mapping micrograph, (d) oxygen mapping micrograph, and (e) palladium mapping micrograph.*

The high resolution X-ray photoelectron spectra obtained for the heterogeneous catalyst is shown in Figure 4.6, where the peaks of Pd3d$_{5/2}$ and Pd3d$_{3/2}$ binding energy at 337.4 eV and 342.8 eV were observed by deconvolution, indicating an oxidation state of Pd(II).[22] The shift in binding energy to a higher energy contribution can be attributed to the bulk and dispersed and extremely small PdO particles.[14]

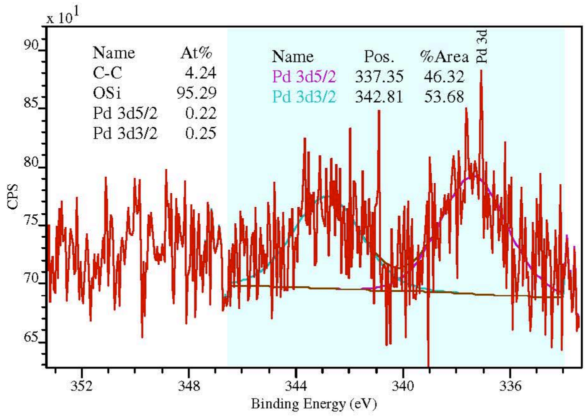

Figure 4.6. *XPS spectra of PdO/SBA-15.*

The catalyst was tested for its performance using the Suzuki-Miyaura cross-coupling reaction. Here a mixture of 4-nitrobromobenzene, phenylboronic acid (1.2 molar equivalents), K_2CO_3 (2 molar equivalents) and palladium catalyst (0.6 - 3.0 mol%) in 0.1 M anhydrous ethanol was stirred at reflux temperature in a preheated oil bath until TLC indicated completion (Scheme 1). Conversion was monitored using ^{1}H NMR spectroscopy on extracts, by integration of characteristic product peaks in comparison to those of the aryl bromide precursor material. These crude extracts were analysed by ^{1}H NMR at consecutive intervals based on preparative thin layer chromatographic monitoring (permanganate dip).

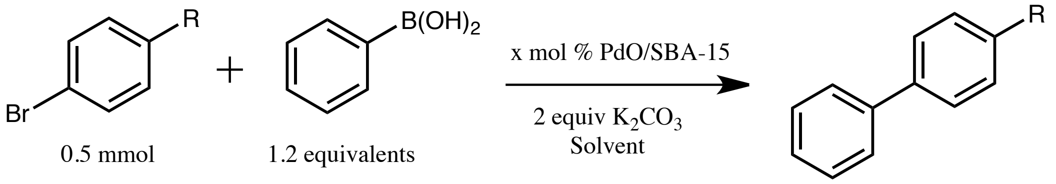

Scheme 4.1. The Suzuki-Miyaura cross-coupling reaction.

The crude extract was allowed to cool to room temperature before evaporation of the solvent *in vacuo*, and the organic material then dissolved in $CDCl_3$, with the insoluble K_2CO_3 and catalyst allowed to settle, to the bottom of the NMR tube before data collection. No starting material peaks were evident from the baseline, and 100% conversion was assumed. The crude extracts did not undergo an aqueous workup which could potentially result in the removal of either the precursor aryl bromide or the resultant biphenyl material, and lead to inaccurate results. A measure of reaction conversion was analysed by the integration of ^{1}H NMR resonances starting material signals (usually the two equivalent Ar-H atoms at the ortho position) with those of the product material. An example set of NMR crude extracts from the reaction between 4-nitro bromobenzene and phenyl boronic acid is shown in Figure 4.7. Integrations are 2H with respect to the two protons at the *ortho* position to the bromine.

The mixture was then cooled to room temperature and filtered under gravity. The crude solid material was then sonicated in ethanol for 5 minutes using a ultrasonic bath with power rating of 150 W, filtered under gravity and washed with dichloromethane (DCM) and then deionised water. The recollected catalyst was then dried at 80 ˚C for 1 hour and then placed under vacuum to reuse for subsequent experiments.

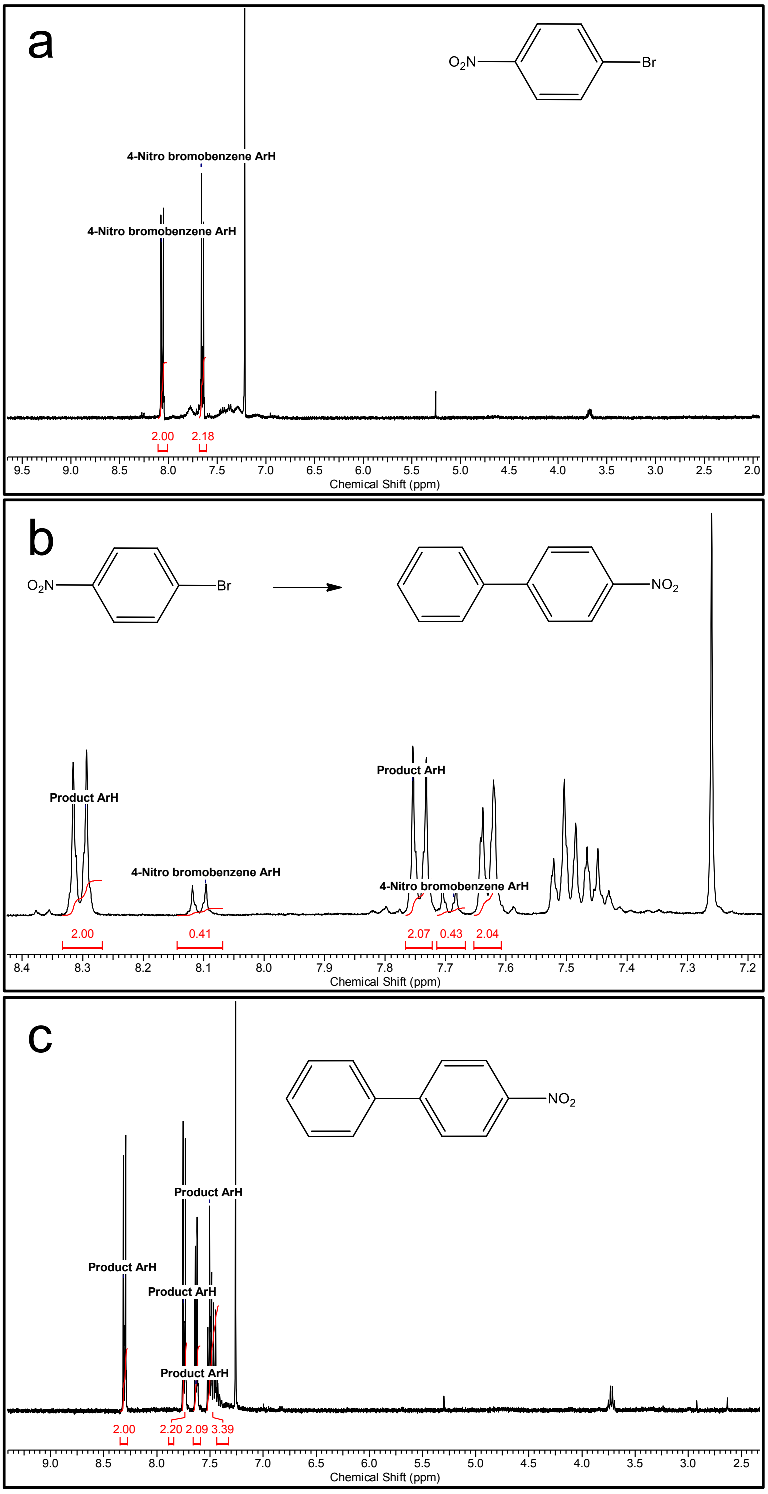

Figure 4.7. *^{1}H NMR (400 MHz) spectrum in $CDCl_3$ of the crude extract of a reaction between 4-nitro bromobenzene and phenyl boronic acid in ethanol (PdO/SBA-15, 1.8 mol%) of (a) 4-nitro bromobenzene, (b) after 115 minutes at reflux temperature, and (c) at completion.*

As summarized in Table 4.2, PdO/SBA-15 synthesized under the VFD processing is an effective catalyst for the Suzuki-Miyaura cross-coupling reaction. In order to investigate the efficiency of the catalyst, the lab-synthesized material was tested with a commercial catalyst Silia*Cat*® S-Pd by Sillicycle, palladium-based catalysts synthesized from a mercapto and diphenylphosphine functionalized silica matrix via a sol– gel process, which are highly reactive, air stable, reusable and leach-resistant.[23] Initially, when the catalyst was used untreated, the commercial catalyst out-performed the materials herein to a large extent. However, grinding the starting materials separately with a mortar and pestle to a fine powders before starting the reaction reduced the reaction time five-fold for the lab synthesized catalyst in the present study. The outcome for pre-grinding the Silia*Cat*® S-Pd was not substantial, which is expected as the commercial product comes in a fine powder form and is easily dispersed into reagents. However, the lab-synthesized catalyst showed a significant reduction in reaction time, decreasing it from 5 hours initially before grinding, to 1 hour after the catalyst where the catalyst was ground in a mortar and pestle. The as synthesized sample was vacuum filtered and dried in an oven prior to calcination, with the filtered cake compressed into flakes. These would have been difficult to disperse in the reagents, and thus with the active sites not being fully accessed. Grinding the materials prior to reaction increased the surface area exposed, therefore enhanced the performance. The substrate scope was upheld in order to focus primarily on the loading effects of palladium on reaction conversion times.

Table 4.2. PdO/SBA-15 catalytic performance under Suzuki-Miyaura cross-coupling reaction.*

Catalyst source, loading	Time to 100% Conversion
Silia*Cat*® S-Pd, 0.5 mol%	1.5 hrs[a]
PdO/SBA-15, 3.0 mol%	5.0 hrs[a]
Silia*Cat*® S-Pd, 0.5 mol%	55 min[b]
PdO/SBA-15, 3.0 mol%	1.0 hrs[b]
PdO/SBA-15, 2.4 mol%	1.25 hrs[b]
PdO/SBA-15, 1.8 mol%	2.5 hrs[b]
PdO/SBA-15, 1.2 mol%	4.0 hrs[b]
PdO/SBA-15, 0.6 mol%	10.25 hrs[b]

[*] Reactions are carried out with 4- nitrobromobenzene and phenylboronic acid, based on scheme 4.1.
[a] catalysts were used untreated;
[b] catalysts were pre-ground with a mortar and pestle into a fine powder.
Experiments are conducted in ethanol under reflux.

From Table 4.2, 3.0 mol% loading of catalyst showed the optimum performance in term of time taken to achieve 100% conversion. The recyclability of the newly discovered palladium catalyst was assessed at the loading of 3.0 mol%. Subsequent re-runs of the Suzuki-Miyaura catalysis were carried out using a purification procedure for the catalyst whereby the crude filtered solid was washed with DCM, water and then sonicated in ethanol before filtering again and repeating the washing process. The filtered catalyst was then dried in an oven at 80 ˚C for 1 hr and placed *in vacuo*. Sonication for 1 hour resulted in reduction catalytic activity upon recycling, with only 70% conversion after 4 hours, as compared to the first cycle catalytic performance with full conversion achieved in one hour. Thus, sonication time was reduced and sonication of the catalyst for 5 minutes proved more beneficial, and the recycled catalyst achieved full conversion in approximately 2 hours. The scale was modified to accommodate for the loss of any catalyst upon the filtration/sonication processes. Even though the time taken for full reaction conversion was doubled after each run, the catalyst was found to be active for four consecutive runs, without appreciable degradation of the catalyst. The results of these recycling experiments are summarised in Table 4.3.

Table 4.3. Recyclability test for PdO/SBA-15.

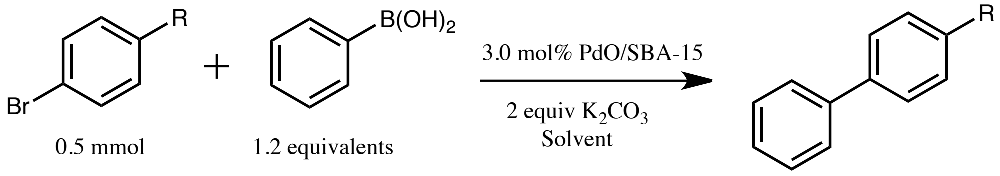

No. of cycle	Loading (mol%)	Time to 100% conversion
1	3.0	1 hr
2	3.0	1 hr 55 min
3	3.0	4 hrs 30 min
4	3.0	8 hrs 15 min

Experiments are conducted in ethanol under reflux.

The reduction in catalytic activity was likely from two factors, the leaching of palladium and the collapse of pore structure. The former was less profound as ICP-MS results from different runs showed an average of less than 20 ppm of palladium found in the product. The latter hypothesis was proven by N_2 adsorption-desorption analysis whereby the BET surface area has dropped from 596.7 m^2/g to 28.5 m^2/g, so did the pore volume from 0.70 cm^3/g down to 0.22 cm^3/g. A TEM image also revealed the collapse of pore structure (Figure 4.8). Theoretically, the hydrothermal stability of SBA-15 was better compared to MCM-41, which is attributed to its thicker pore wall.[24] However, studies have shown the basic condition of Suzuki-Miyaura reaction is the main cause of the degradation of the pore structure.[2] Since the reaction still proceeded to full conversion, it can be concluded that the catalyst was not fully degraded, but the partial collapse of the pore structure successively traps some active Pd species, and thus requires longer reaction time after each run.

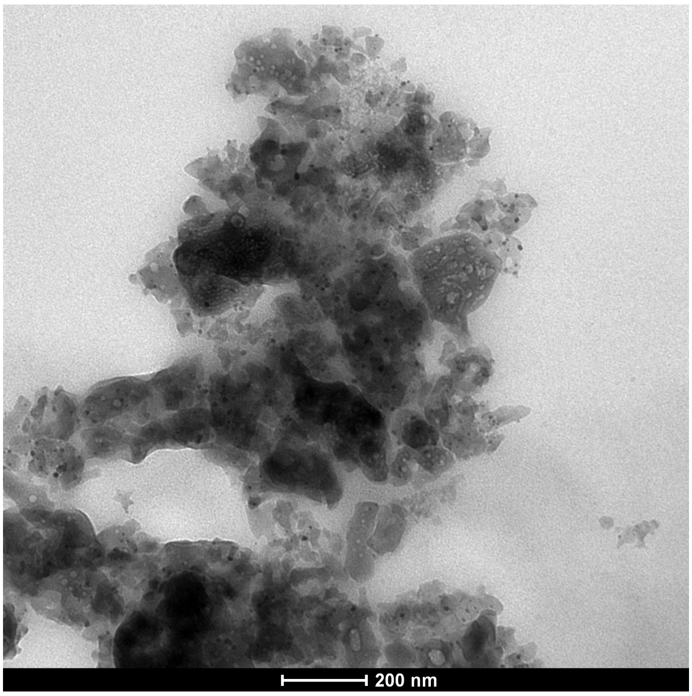

Figure 4.8. *TEM image of the PdO/SBA-15 catalyst after four recycled runs.*

From Table 4.2, 3.0 mol% showed the optimum catalytic performance and 2.4 mol% also showed a reasonable performance. Thus, these two different loadings were chosen to test the performance by changing the substrate scope and catalytic activity. The results are summarized in Table 4.4. As the substrate is replaced with bulkier compound, it requires longer time in achieving 100% conversion.

Table 4.4. Catalytic activity of PdO/SBA-15 for different substrate.[a]

R	Loading (mol%)	Time to 100% conversion (hr)
OCH_3	3.0	7.2
OCH_3	2.4	9.0
$N(CH_3)_2$	2.4	16.5
NO_2*	2.4	3.8

R referring to different substrate attaching to the bromobenzene.
[a] reactions are carried out based on scheme 4.1.
* reaction was carried out with 4-chloro phenylboronic acid.
Experiments are conducted in ethanol under reflux.

4.5. Conclusions

A new method has been developed to synthesise PdO/SBA-15 as a heterogeneous catalyst using a VFD, as an *in situ* single pass process under continuous flow, except for the necessary calcining. This method substantially decreases the processing time by at least five-fold compared to material prepared using hydrothermal processing, and ensures that the catalyst is impregnated within the pores, in minimising the presence of the catalyst on the surface of the particles. The materials prepared using this facile method showed good catalytic performance for Suzuki-Miyaura cross-coupling reaction at the loading of 3.0 mol%. Even though the material did not show an outstanding performance and reusability compared to a commercial product, it is nonetheless cost efficient, and as a one-pot synthesis it warrants further investigations. Additional studies are also warranted in optimizing the processing conditions in preparing the heterogeneous catalyst.

4.6. Acknowledgement

This work is supported by the Australian Research Council, The Perth Mint, and the Government of South Australia. The authors acknowledge the facility and support from the Australian Microscopy & Microanalysis Research Facility (AMMRF) at Flinders University. Craig E. Buckley acknowledges ARC RIEF grant R00107962 which enabled the SAXS studies to be conducted. Also, special thanks to Ruhani Singh for digestion preparation for ICP-MS analysis.

4.7. References

1. N. E. Leadbeater and M. Marco, Ligand-Free Palladium Catalysis of the Suzuki Reaction in Water Using Microwave Heating, *Org. Lett.*, 2002, **4**, 2973-2976.

2. B. W. Glasspoole, J. D. Webb and C. M. Crudden, Catalysis with chemically modified mesoporous silicas: Stability of the mesostructure under Suzuki–Miyaura reaction conditions, *J. Catal.*, 2009, **265**, 148-154.

3. N. Miyaura and A. Suzuki, Palladium-Catalyzed Cross-Coupling Reactions of Organoboron Compounds, *Chem. Rev.*, 1995, **95**, 2457-2483.

4. Yin and J. Liebscher, Carbon−Carbon Coupling Reactions Catalyzed by Heterogeneous Palladium Catalysts, *Chem. Rev.*, 2006, **107**, 133-173.

5. S. Abate, S. Perathoner and G. Centi, Performances of Pd Nanoparticles on Different Supports in the Direct Synthesis of H2O2 in CO2-Expanded Methanol, *Top. Catal.*, 2011, **54**, 718-728.

6. R. Narayanan, Recent Advances in Noble Metal Nanocatalysts for Suzuki and Heck Cross-Coupling Reactions, *Molecules*, 2010, **15**, 2124-2138.

7. J. Zou, K. Swaminathan Iyer, S. G. Stewart and C. L. Raston, Scalable synthesis of catalysts for the Mizoroki-Heck cross coupling reaction: palladium nanoparticles assembled in a polymeric nanosphere, *New J. Chem.*, 2011, **35**, 854-860.

8. B. Karimi, S. Abedi, J. H. Clark and V. Budarin, Highly Efficient Aerobic Oxidation of Alcohols Using a Recoverable Catalyst: The Role of Mesoporous Channels of SBA-15 in Stabilizing Palladium Nanoparticles, *Angew. Chem. Int. Ed.*, 2006, **45**, 4776-4779.

9. S. MacQuarrie, B. Nohair, J. H. Horton, S. Kaliaguine and C. M. Crudden, Functionalized Mesostructured Silicas As Supports for Palladium Catalysts: Effect of Pore Structure and Collapse on Catalytic Activity in the Suzuki−Miyaura Reaction, *J. Phys. Chem. C.*, 2009, **114**, 57-64.

10. P. Han, X. Wang, X. Qiu, X. Ji and L. Gao, One-step synthesis of palladium/SBA-15 nanocomposites and its catalytic application, *J. Mol. Catal. A: Chem.*, 2007, **272**, 136-141.

11. H. Song, R. M. Rioux, J. D. Hoefelmeyer, R. Komor, K. Niesz, M. Grass, P. Yang and G. A. Somorjai, Hydrothermal Growth of Mesoporous SBA-15 Silica in the Presence of PVP-Stabilized Pt Nanoparticles: Synthesis, Characterization, and Catalytic Properties, *J. Am. Chem. Soc.*, 2006, **128**, 3027-3037.

12. P. Wang, X. Luo, X. Wu, X. Wei, L. Zhou and X. Zheng, Structure and catalytic properties of Pd encapsulated in mesoporous silica SBA-15 fabricated by two-solvent strategy, *J. Porous Mater.*, 2013, **20**, 1-6.

13. C. T. Kresge, M. E. Leonowicz, W. J. Roth, J. C. Vartuli and J. S. Beck, Ordered mesoporous molecular sieves synthesized by a liquid-crystal template mechanism, *Nature*, 1992, **359**, 710-712.

14. S. Ganji, P. Bukya, V. Vakati, K. S. R. Rao and D. R. Burri, Highly efficient and expeditious PdO/SBA-15 catalysts for allylic oxidation of cyclohexene to cyclohexenone, *Catal. Sci. Technol.*, 2013, **3**, 409-414.

15. C. L. Tong, R. A. Boulos, C. Yu, K. S. Iyer and C. L. Raston, Continuous flow tuning of ordered mesoporous silica under ambient conditions, *RSC Adv.*, 2013, **3**, 18767-18770.

16. J. M. Kim, Y.-J. Han, B. F. Chmelka and G. D. Stucky, One-step synthesis of ordered mesocomposites with non-ionic amphiphilic block copolymers: implications of isoelectric point, hydrolysis rate and fluoride, *Chem. Commun.*, 2000, 2437-2438.

17. D. Zhao, J. Feng, Q. Huo, N. Melosh, G. H. Fredrickson, B. F. Chmelka and G. D. Stucky, Triblock Copolymer Syntheses of Mesoporous Silica with Periodic 50 to 300 Angstrom Pores, *Science*, 1998, **279**, 548-552.

18. M. Jin, H. Liu, H. Zhang, Z. Xie, J. Liu and Y. Xia, Synthesis of Pd nanocrystals enclosed by {100} facets and with sizes <10 nm for application in CO oxidation, *Nano Res.*, 2011, **4**, 83-91.

19. K. K. Maniam, V. Muthukumar and R. Chetty, Approaches towards Improving the Dispersion of Electrodeposited Palladium on Carbon Supports, *Energy Procedia*, 2014, **54**, 281-291.

20. A. Martin, G. Morales, F. Martinez, R. van Grieken, L. Cao and M. Kruk, Acid hybrid catalysts from poly(styrenesulfonic acid) grafted onto ultra-large-pore SBA-15 silica using atom transfer radical polymerization, *J. Mater. Chem.*, 2010, **20**, 8026-8035.

21. Z. Luan, E. M. Maes, P. A. W. van der Heide, D. Zhao, R. S. Czernuszewicz and L. Kevan, Incorporation of Titanium into Mesoporous Silica Molecular Sieve SBA-15, *Chem. Mater.*, 1999, **11**, 3680-3686.

22. D. Wang, S. Lu, P. J. Kulesza, C. M. Li, R. De Marco and S. P. Jiang, Enhanced oxygen reduction at Pd catalytic nanoparticles dispersed onto heteropolytungstate-assembled poly(diallyldimethylammonium)-functionalized carbonnanotubes, *PCCP*, 2011, **13**, 4400-4410.

23. M. Lemay, V. Pandarus, M. Simard, O. Marion, L. Tremblay and F. Béland, SiliaCat ® S-Pd and SiliaCat DPP-Pd: Highly Reactive and Reusable Heterogeneous Silica-Based Palladium Catalysts, *Top. Catal.*, 2010, **53**, 1059-1062.

24. K. Cassiers, T. Linssen, M. Mathieu, M. Benjelloun, K. Schrijnemakers, P. Van Der Voort, P. Cool and E. F. Vansant, A Detailed Study of Thermal, Hydrothermal, and Mechanical Stabilities of a Wide Range of Surfactant Assembled Mesoporous Silicas, *Chem. Mater.*, 2002, **14**, 2317-2324.

Chapter Five

Nitrate Uptake Using Mesoporous Silica Embedded with Zero-Valent Palladium Nanoparticles

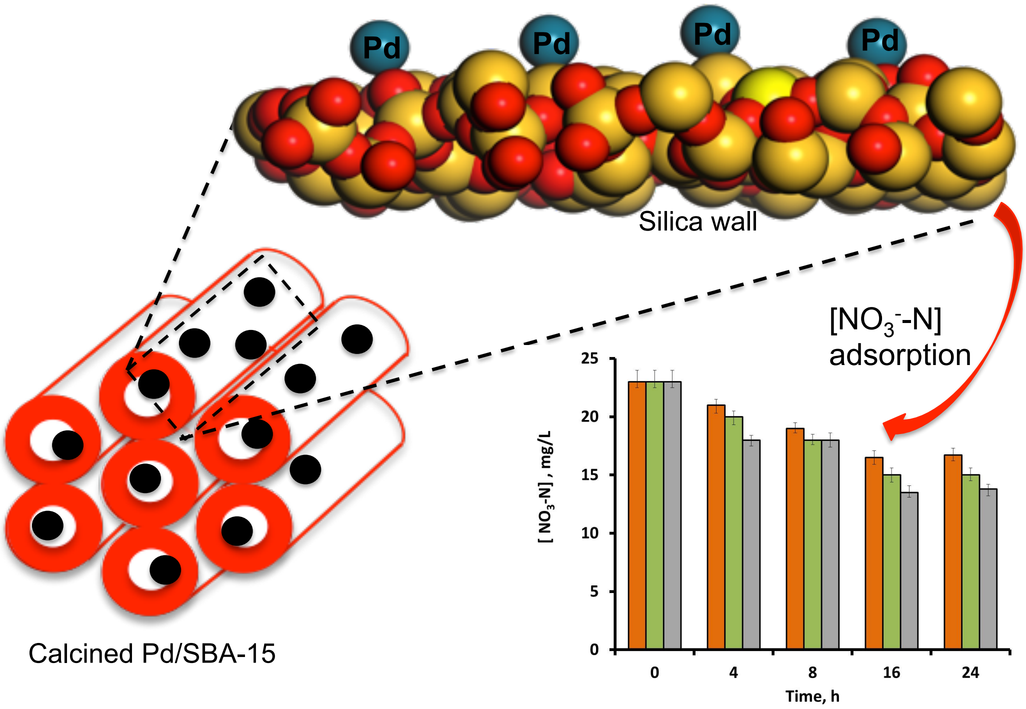

This chapter is reformatted from a paper submitted to ***RSC Advances***, 17 December 2014.

5.1. Abstract

In situ reduction of palladium(II) acetylacetonate during the synthesis of SBA-15 mesoporous silica affords material impregnated with palladium nanoparticles. The synthesis is at neutral pH and ambient conditions using a continuous flow vortex fluidic device with high shear dynamic thin films, followed by calcination. The SBA-15 is available with considerably reduced processing time relative to the conventional synthesis of mesoporous silica, with the material being effective for nitrate-nitrogen [NO_3^-–N] removal from aqueous solutions, at 41% within the first 16 hours, or around 36% for the same period after being recycled.

5.2. Introduction

SBA-15 is a mesoporous silica prepared using a non-ionic amphiphilic copolymer template,[1] possessing novel physical characteristics and hydrothermal stability. Well defined pores in the material relate to its application in catalysis, separation science, drug delivery, and biosensors.[2-4] Advances have been made in improving the synthesis with finer control on the structure and morphology of the material.[5-9] Most of the focus has been on the chemistry, as in functionalizing the material,[10] or adding swelling agents for pore expansion.[11-13] Nevertheless, the synthesis follows the conventional hydrothermal process, which typically takes 48 hours for an individual batch, and reducing this time has been challenging. To this end, I made progress in reducing the processing time, using a vortex fluidic device (VFD) for the pre-calcining stage, and detailed in chapter 3 under section 3.3.1, here the reactions are under shear and are not diffusion controlled.[14] Indeed there is limited literature on the synthesis of silica involving such external shear enhancement. Amorphous silica has been prepared using shear flow in a Couette cell under neutral conditions, albeit without much detail provided on the characterization of the material.[15] Kim *et al.* prepared mesoporous silica involving shear flow in a Couette cell operating under laminar flow conditions, although this involved multiple steps and different operating temperatures.[16] The aforementioned synthesis of SBA-15 using a VFD under ambient conditions,[14] significantly reduced the processing time to *ca.* 5 hours, prior to the calcination step. Here the turbulent shear condition within the device circumvents the need for hydrothermal aging.[14] The simplicity of the VFD processing approach offers scope for customizing the synthesis, depending on the target application, for example nitrate remediation, which is the focus herein.

Heavy usage of artificial fertilizers has resulted in nitrate contamination of ground and surface water.[17] The standard regulations for nitrate-nitrogen concentration [NO_3^--N] in drinking water is less than 10 mg/L.[18] Nitrate removal has been established for a number of techniques, including ion exchange, biological denitrification,[19, 20] electro-reduction and electro-coagulation,[17] chemical denitrification, reverse osmosis, electrodialysis, and catalytic denitrification.[21] Among these commonly used treatment methods, they all have the disadvantage of requiring post-treatment.[22] This can be overcome using desorption methods.[22] Adsorbents such as activated carbon, sepiolite, and slag have been studied in nitrate removal.[23] However, much attention has been devoted to the performance of low cost readily materials such as tree bark, wood charcoal, saw dust, alum sludge, and red mud.[24] There are also studies on the catalytic reduction of nitrate using palladium based catalyst and hydrogen gas as the reducing agent, but they have been limited to bench-scale processing. This relates to technical challenges such as catalytic fouling.[25] Combining two approaches of utilizing an adsorption method followed by a hydrodeoxygenation reaction would be advantageous. Incorporating palladium in SBA-15 as an adsorbent offers scope for recovery and recycling of the material while avoiding fouling of the catalyst. This chapter focuses on the *in situ* synthesis of SBA-15 loaded with zero-valent palladium nanoparticles, and the utility of the material in the removal of nitrate from waste effluent. The reduced palladium nanoparticles provide an active site for catalytic reduction of nitrate via hydrodeoxygenation.[25] Noteworthy, there are no reports on the use of Pd/SBA-15 as an adsorbent for nitrate removal.

The synthesis herein involves the use of the VFD for the *in situ* incorporation of metal nanoparticles within the pores of SBA-15 using a Pd(II) precursor. We recently reported a detailed study of the synthesis of SBA-15 using the VFD under acidic and ambient conditions, establishing the ability to control the pore size over a range of operating conditions.[14] In a related study the VFD was used to prepare mesoporous silica (Chapter 7) in the absence of a copolymer, for direct impregnation of particles of an anti-microbial compound into the material, at neutral pH and under ambient conditions, for controlled release at physiological pH.[26] These findings form the basis of the present study, with now a focus on gaining access to an adsorbent material for nitrate removal. Here the synthesis is carried out under neutral pH which enables direct deposition of metal oxide, in the presence of a copolymer template.

5.3. Experimental

5.3.1. Synthesis of Pd/SBA-15

The synthesis was carried out using a variation of the method reported by Song *et al.*,[27] taking it from strictly batch processing to using the vortex fluidic device (VFD). Pluronic ® P-123 ($EO_{20}PO_{70}EO_{20}$, averaged M_w 5800, Sigma Aldrich), tetramethyl orthosilicate (TMOS, 98%, Sigma Aldrich), palladium(II) acetylacetonate ($[Pd(acac)_2]$, 99%, Sigma Aldrich), and sodium fluoride (99.9%, Sigma Aldrich) were used as received. Pluronic ® P-123 ($EO_{20}PO_{70}EO_{20}$), 2.55 g, averaged M_w 5800, Sigma Aldrich), was dissolved in 50 mL of deionized Milli-Q water. The solution was stirred vigorously in a water bath at 40 to 45 °C to dissolve the P-123. Then 106.8 mg of $Pd(acac)_2$ was added into the micelles solution which was stirred for another hour. The resulting mixture was then fed at 1 mL/min into the VFD with the 18.0 mm internal diameter tube (20.0 mm external diameter) rotating at 5000 rpm at 45 ° tilt angle. This processing was carried out under a mixture of N_2 and H_2 with the gas flow rate controlled at 80 sccm and 20 sccm, respectively, where the hydrogen is effective in reducing the palladium(II) precursor. Aqueous NaF (0.375 mL of 0.5 M) was then added to the collected pre-stressed micelle solution containing palladium nanoparticles, and the resulting solution fed into the VFD through one feed jet, with 4.0 mL TMOS fed into the VFD through a separate feed jet at ambient temperature, using the same VFD processing parameters. The purging gas flow rate of N_2/H_2 was changed to 70/30 sccm to ensure the formation of palladium nanoparticles. The overall processing time of the synthesis was 5 hours, with the residence time of a finite volume of liquid in the tube at *ca.* 3 minutes (Figure 5.1). The resulting greyish material was collected by filtration, washed with deionized water, and dried *in vacuo*, followed by calcining at 550 °C under a mixture of H_2 and Ar at a flow rates of 40 and 960 sccm respectively, for 6 hours, to remove the polymer template. The material was then cooled under argon to room temperature.

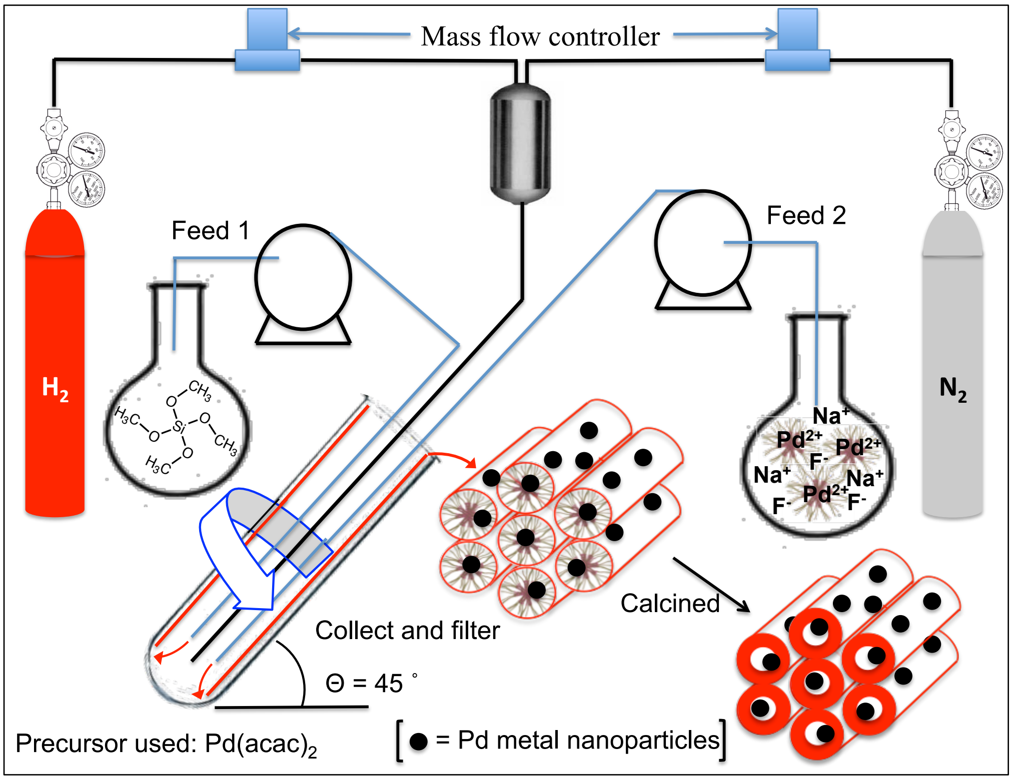

Figure 5.1. *Schematic of the continuous synthesis of Pd/SBA-15 using a vortex fluidic device (VFD).*

5.3.2. Characterization techniques

Scanning electron micrographs (SEM) were obtained using a Quanta 450 instrument. Samples were placed on a conductive carbon tape and pre-coated with 5 nm thick platinum. Images were taken using a secondary electron detector, at an accelerating voltage of 5 kV. Element mapping was obtained also using the same instrument with the samples pre-coated with a 3 nm layer of platinum. The analysis was carried out using a back-scattered electron detector, at an accelerating voltage of 8 kV.

Transmission electron micrographs (TEM) were obtained using a FEI Tecnai ^{TM} G^2 Spirit instrument at an operating voltage of 120 kV. The sample was dispersed in ethanol and placed in an ultrasonication bath for 5 min. A 7 µL aliquot was then dropped cast onto a continuous carbon coated copper grid, and the sample air dried before imaging.

Small Angle X-ray Scattering (SAXS) measurements were performed at the Western Australian Small Angle Scattering Facility within Curtin University. The instrument used was a Bruker AXS Nanostar SAXS system with a copper anode in a sealed tube for the x-ray source (the operating wavelength is 1.541 Å). The system makes use of a HI-STAR detector, which is a two dimensional xenon gas wire detector (1024 x 1024 pixels). The detector is positioned 22.5 cm from the sample stage yielding a q-range of 0.03 Å^{-1} to 0.85 Å^{-1}. Given that the samples are isotropic, the two dimensional data was reduced to one dimensional data by averaging the radial direction with the commercial software. This presents an intensity profile as a function of the scattering vector, q.

Nitrogen adsorption–desorption studies were performed using a Micromeritics TriStar^{TM} II 3020 system. The samples were outgassed at 200 °C for 16 hours prior to gas adsorption which was carried out at 77 K. The specific surface area, S_{BET}, was determined from the linear part of the Brunauer–Emmett–Teller (BET) equation (P/P_o = 0.05 – 0.30). The pore size distribution and pore volume were evaluated using the Barrett–Joyner–Halenda (BJH) method. The total pore volume reported was taken from the amount of gas adsorbed at a relative pressure (P/P_o) at 0.990.

The palladium content in Pd/SBA-15 was determined using inductively coupled plasma mass spectrometry (ICP-MS), conducted by Marine and Freshwater Research Laboratory Environmental Science at Murdoch University (Perth, WA). The sample was accurately weighed into a Teflon beaker and digested using hydrochloric acid (15 mL, 32% wt. ultra-pure), nitric acid (5 mL, 65% wt. ultra-pure) and hydrofluoric acid (8 mL, 50% wt. A.R.). The digestate was reduced to incipient dryness with the residue then dissolved with hydrochloric acid (0.5 mL 32% wt. ultra-pure), nitric acid (0.2 mL, 65% wt. ultra-pure) and water (5 mL, 18 MΩ.cm). The solution was quantitatively transferred to a suitable container and made up to 10 mL gravimetrically, and was assayed using an Agilent 7700x ICP - MS.

Elemental compositions of the samples were determined using X-ray photoelectron spectroscopy (XPS), conducted by Surface and Chemical Analysis Network (SCAN) at the University of Melbourne. XPS data was acquired using a VG ESCALAB220i-XL spectrometer equipped with a hemispherical analyzer. The incident radiation was monochromatic Al Kα X-rays (1486.6 eV) at 220 W (22 mA and 10 kV). Survey (wide) and high resolution (narrow) scans were taken at analyzer pass energies of 100 eV and 50 eV, respectively. Survey scans were carried out over the binding energy range from 0 – 1200 eV with 1.0 eV step size and 100 ms dwell time. Narrow high resolution scans were run over 30 eV binding energy range with 0.05 eV step size and 250 ms dwell time. Base pressure in the analysis chamber was below 7.0 x 10^{-9} mbar and during sample depth profile analysis it was 1.5 x 10^{-7} mbar. A low energy flood gun was used to compensate the surface charging effect. Argon ions at 5 keV beam energy were used to sputter off approximately 18 nm surface layers at a rate of ~3 Å/second. The ion source gave a crater of approximately 3 x 3 mm. All data were processed using CasaXPS software and the energy calibration was referenced to the C 1s peak at 285.0 eV.

5.3.3. Nitrate removal test

Palladium(0) doped mesoporous silica (Pd/SBA-15) samples were individually mixed with an artificial aquatic-media at a buffered pH of around 7.5 which is mainly composed of phosphates, nitrates, carbonate buffer, micronutrients and vitamins.[28] Three different loadings of the same adsorbent (10 mg; 25 mg; 50 mg) were separately mixed with nitrate containing aquatic media (1.5 mL). Each mixture was then hand-vortexed for about 60 seconds for initiating the experiments, followed by gentle mixing throughout the entire experiment with an Eppendorf tube Rotator (Stuart Rotator, SB3) at a constant rotational speed of 25 rpm. The amount of nitrate ions remaining in the solution was monitored at various time intervals (0, 4, 8, 16, and 24 hours). Before each analysis, the mixtures were centrifuged at 9390 x *g* for 5 minutes, and particle-free supernatants were collected for their spectrophotometric analysis. Collected liquid samples were subjected to nitrate-nitrogen (NO_3^--N) assay via colorimetric "cadmium reduction method".[29] Nitrate analyzing kits (HACH®, NitraVer® Nitrate Reagent Powder Pillows) were employed before reading the nitrate-nitrogen concentration of the supernatant by a colorimeter (HACH® DR/870).

5.4. Results and Discussion

A small angle X-ray scattering (SAXS) pattern of the calcined material was collected and a strong diffraction peak for the (1 0 0) plane appeared at $q = 0.0555 \pm 0.0014$ Å^{-1} (Figure 5.2), which corresponds to a *d*-spacing of 113.2 ± 2.86 Å (Table 5.1) and a unit cell parameter, a_o of 130.7 ± 3.30 Å (Figure 5.3). No obvious secondary diffraction of (1 1 0) and (2 0 0) plane were observed in the sample. These second order peaks will be washed out by Guinier features (from the size of the Pd particles) causing a decrease in scattering contrast between the pore walls and the pore channels when palladium nanoparticles are incoporated inside the pores.[30]

This is proven by comparing the SAXS patterns of SBA-15 and Pd/SBA-15 (Figure 5.3).

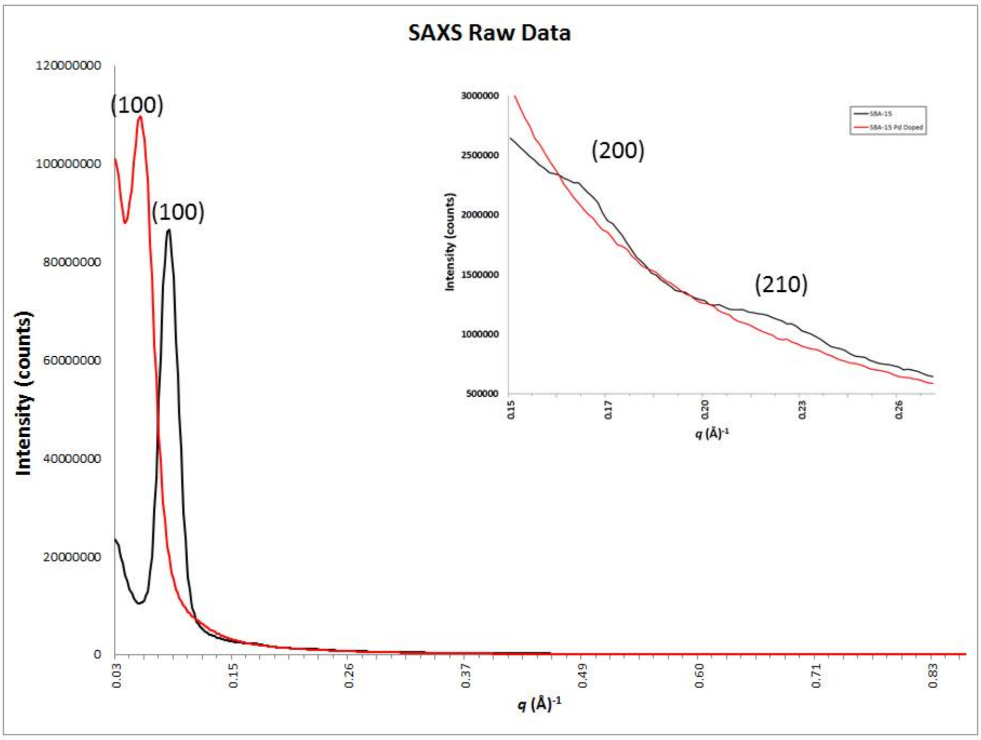

Figure 5.2. *Raw SAXS data collected for SBA-15 and Pd/SBA-15. The (100) reflection is labelled for the two data sets, and the (200) and (210) reflections are shown in the inset for the SBA-15 data set.*

The *d*-spacing for the reflections identified above can be calculated from Braggs law expressing sin (θ) in terms of the scattering vector q.[31]

$$\lambda = 2d_{hkl}\sin(\theta) \tag{5.1}$$

$$\lambda = 2d_{hkl}\cdot\frac{q\lambda}{4\pi} \tag{5.2}$$

$$d_{hkl} = \frac{2\pi}{q} \tag{5.3}$$

Table 5.1. Calculated *d*-spacings for reflections identified in Figure 5.2.

	SBA-15				Pd(0)/SBA-15			
Reflection	*q* (Å^{-1})	+/-	*d* (Å)	+/-	*q* (Å^{-1})	+/-	*d* (Å)	+/-
(100)	0.0839	0.0014	74.9	1.25	0.0555	0.0014	113.2	2.86
(200)	0.1650	0.0128	38.1	2.95	-	-	-	-
(210)	0.2233	0.0298	28.1	3.76	-	-	-	-

To calculate the unit cell parameter a_0 consider the hexagonal formula below ($a_0 = b_0 \neq c_0$; $\alpha = \beta = 90°$ & $\gamma = 120°$)

$$\frac{1}{d_{hkl}{}^2} = \frac{4}{3}\left(\frac{h^2+hk+k^2}{a_0{}^2}\right) + \frac{l^2}{c_0{}^2} \qquad (5.4)$$

So for $h = 1$, $k = 0$, and $l = 0$

$$\frac{1}{d_{(100)}{}^2} = \frac{4}{3}\left(\frac{1}{a_0{}^2}\right) \qquad (5.5)$$

Then using the lattice spacing calculated above we can calculate $a_0 = 86.47 \pm 1.44$ Å and $a_0 = 130.72 \pm 3.30$ Å for the SBA-15 and Pd/SBA-15 samples respectively. Alternatively, unit cell parameter of the material was calculated corresponding to the d-spacing based on equation, $a_o = 2d_{100}/\sqrt{3}$, which is derived for a hexagonal structure. Lastly, pore wall thickness, denoted as b, was obtained by subtracting pore diameter from unit cell parameter.

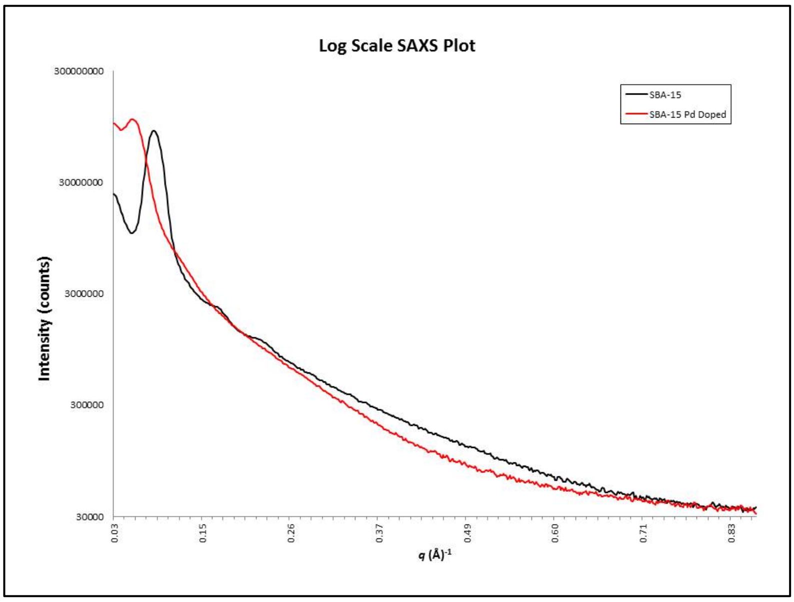

Figure 5.3. *SAXS Log(I) vs q plots for SBA-15 and Pd/SBA-15.*

The surface area, pore volume and pore diameter of the heterogenous catalyst were investigated using nitrogen adsorption-desroption. The calcined material exhibits a typical type IV isotherm with H1 hysteresis loop according to IUPAC classification (Figure 5.4), indicating a uniform mesostructure and cylindrical channels.[32] The step increase at relative pressure around 0.45–0.5 was attributed to the capillary condensation of N_2 into the mesopores. The material has a Brunauer–Emmett–Teller

(BET) surface area of 700.1 $m^2.g^{-1}$ and pore volume of 0.76 $cm^3.g^{-1}$. The narrow pore size distribution of the adsorption branch (inset of Figure 5.4) according to Barrett–Joyner–Halenda (BJH) method was centred at 5.4 nm.

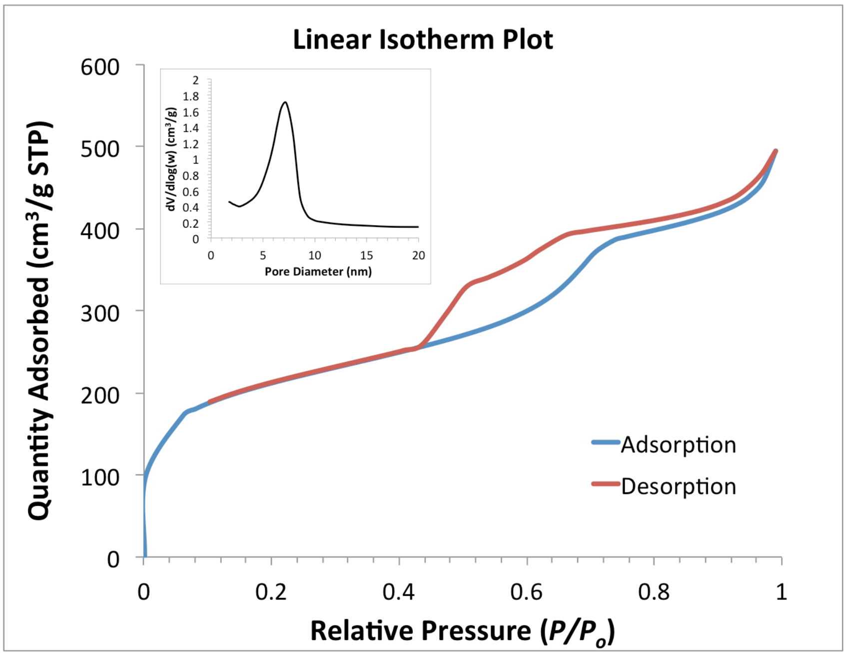

Figure 5.4. *N_2 adsorption-desorption of Pd/SBA-15 and the pore size distribution of the adsorption branch (inset).*

Scanning electron microscopy (SEM) showed the formation of short-chain like sections interconnected throughout, Figure 5.5(a). Energy-dispersive X-ray spectroscopy (EDS) via SEM was conducted with a full area scanned and mapped for individual elements, silica (Si), oxygen (O) and palladium (Pd), establishing the presence of the elements (Figure 5.6). Inductively coupled plasma mass spectrometry (ICP-MS) gave 1.53 wt% of palladium content in the calcined material, which impart high palladium incorporation, at 81%, into the final product. Transmission electron microscopy (TEM) revealed the inner pore structure of the material, showing a well-ordered mesostructure with estimated pore diameter around 5.5 – 6 nm which was close to the average pore diameter reported using the BJH method based on N_2 adsorption-desorption analysis. Palladium nanoparticles (PdNPs) were revealed as darker contrast regions in the TEM images, with estimated diameters of ~ 4 – 5 nm, and are embedded within the pore channels (Figure 5.5(b)). Ruas *et al.* utilized an alcohol reduction method to prepare a suspension of Pd(0) solution using $Pd(acac)_2$ as the metal precursor, and polyvinylpyrrolidone (PVP) as a stabilizer, with a particle size distribution at 5.8 ± 1.1 nm, which agrees with our finding.[33] In addition, using palladium (II) hexafluroacetylacetonate [Pd(hfac)$_2$] as precursor, the Pd crystallite sizes impregnated into SBA-15 range from 6.0 to 7.9 nm, and the post deposition required 3 to 8 hours under supercritical carbon dioxide (scCO$_2$).[34]

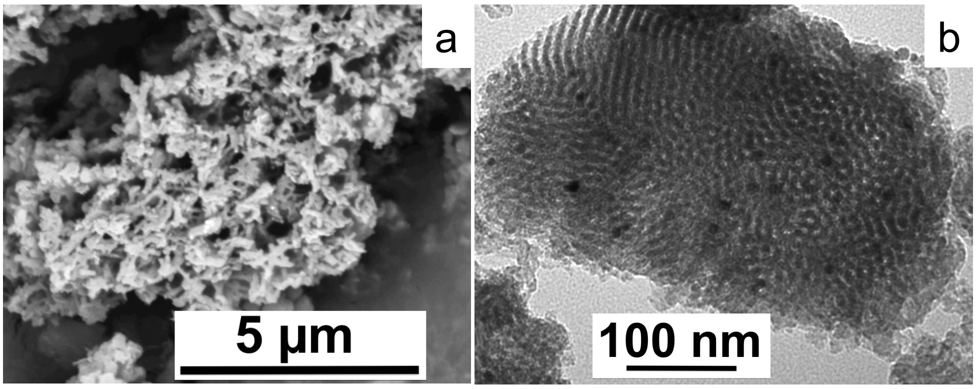

Figure 5.5. *(a) SEM image of Pd/SBA-15 and (b) TEM image of Pd/SBA-15.*

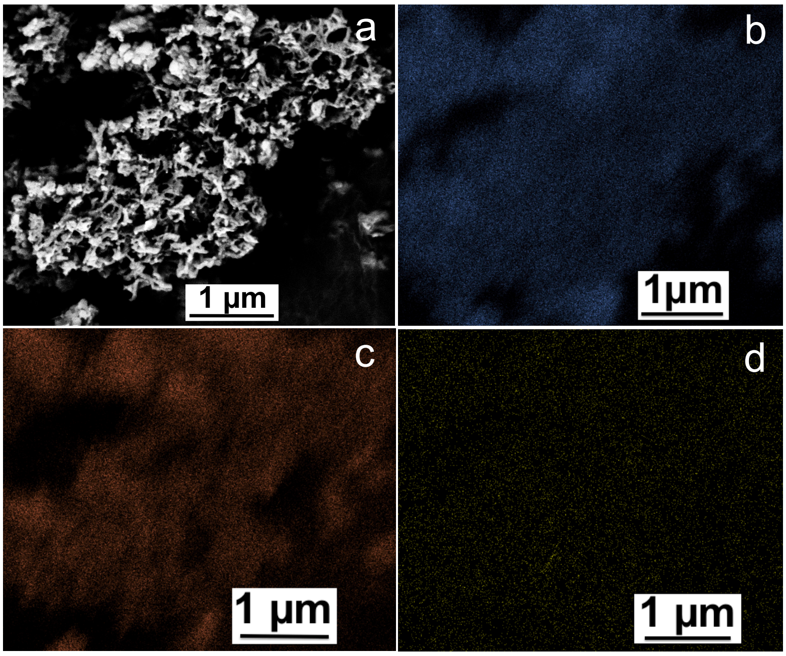

Figure 5.6. *(a) Image of the mapping area, (b) image of Si mapping, (c) image of O mapping, and (d) image of Pd mapping.*

As mentioned above, the synthesis was carried out under H$_2$ to act as a reducing agent in forming elemental palladium nanoparticles. X-ray photoelectron spectroscopy (XPS) was performed to ascertain the oxidation state of the element in the final sample. Survey scans were carried out over the binding energy range 0 – 1200 eV with 1.0 eV step size and 100 ms dwell time, but no visible Pd peak was observed. Since most of the palladium nanoparticles were clearly incorporated inside the pore channels, an argon ion beam was used to etch the silica surface. A crater area of 3 x 3 mm with approximately 18 nm of the surface layer being sputtered off, was investigated by high resolution scans at analyzer pass energies of 50 eV. The peaks of Pd3d$_{5/2}$ and Pd3d$_{3/2}$ binding energy at 335.7 eV and 341.0 eV were observed by deconvolution, indicating an oxidation state of Pd(0) (Figure 5.7).

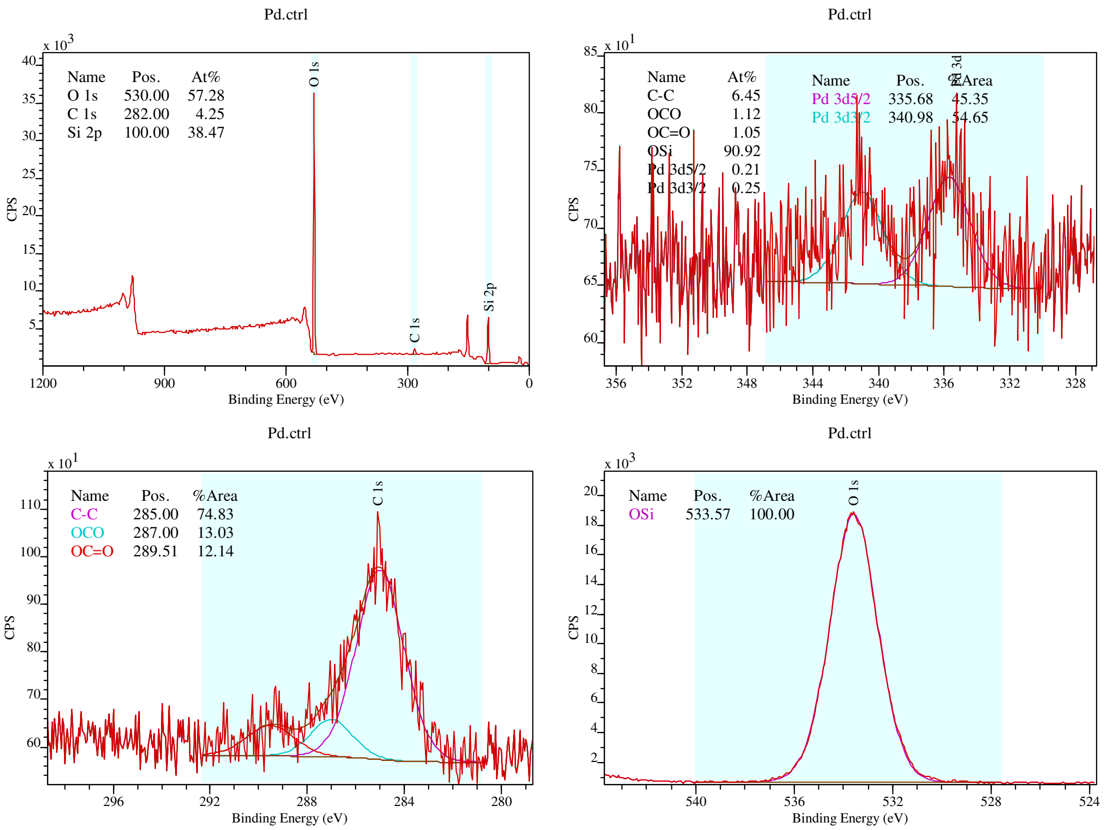

Figure 5.7. *XPS spectra of Pd/SBA-15 with survey scan and high resolution scans under pass energy of 100 eV and 50 eV, respectively.*

Figure 5.8 shows the amount of NO_3^--N concentration of the aqueous media at various time intervals, after being exposed to Pd/SBA-15 samples. Initially, the NO_3^--N concentration in the untreated aqueous media was 23 mg.L^{-1}. The increase in the amount of adsorbent loading had an affirmative effect on the amount of nitrate-nitrogen adsorbed from the liquid media. All of these three loading capacities achieved their maximal nitrate removal efficiencies after 16 hours, which stabilized thereafter. As shown in Figure 5.8, 50 mg of adsorbent yielded the highest nitrate-nitrogen adsorption value of 9.5 mg.L^{-1} (41% removal efficiency of the initial value), which was followed by 8.0 mg.L^{-1} adsorption (35% removal efficiency) by the 25 mg sample, and 6.5 mg.L^{-1} adsorption (28% removal efficiency) by the 10 mg sample. The control experiment with only-silica samples was also investigated using the same amount of adsorbent loadings, with little nitrate removed. This also confirms that the zero valence palladium nanoparticles of the sample are responsible for the nitrate removal. In this context, palladium metal, either monometallic or bimetallic forms, notably Pd-Cu, Pd-Sn or Pd-In, are effective catalysts for the adsorption and catalytic reduction of nitrate.[18]

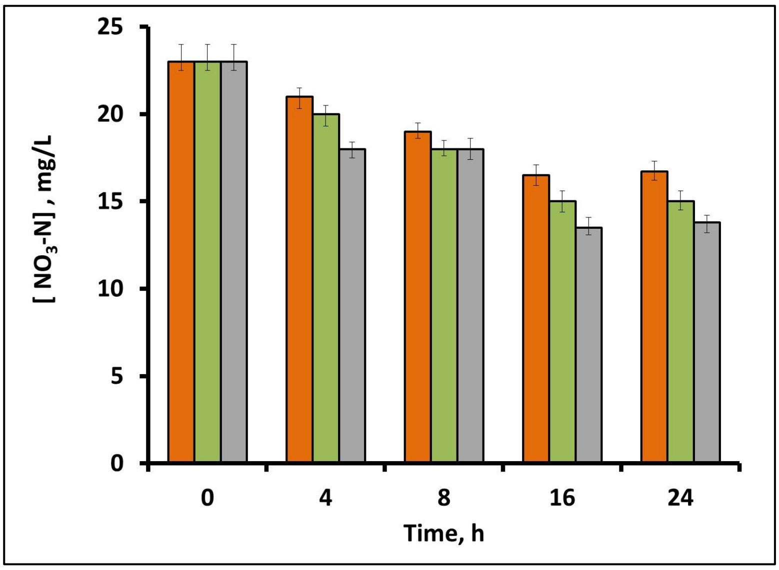

Figure 5.8. *Nitrate-nitrogen [NO_3^--N] content of aqueous media in mg/L versus time for three different Pd/SBA-15 loading concentrations: **(1)** 10 mg adsorbent (brown column); **(2)** 25 mg adsorbent (green column); and **(3)** 50 mg adsorbent (grey column).*

Based on the results shown in Figure 5.8, 16 hours was chosen as the optimal time-interval for testing the recycling potential of the adsorbent. Here, used samples were washed with deionized water through hand-vortexing for 1 minute, followed by removal of the supernatant after centrifugation at 9391 x *g* for 5 minutes. Remaining samples were then mixed again with nitrate-containing fresh media (1.5 mL), while the final nitrate-nitrogen content of the second batch was analyzed after 16 hours of that cycle. Recycling results showed that the Pd/SBA-15 samples were still effective for the removal of nitrate during their second cycle (Table 5.2), albeit with a slight decrease in their maximum removal efficiencies. The Pd/SBA-15 samples were retrieved and analysed using XPS to investigate if the palladium nanoparticles were oxidized after the treatment. From the spectra, the peaks of $Pd3d_{5/2}$ and $Pd3d_{3/2}$ binding energy at 335.5 eV and 340.7 eV were observed by deconvolution, indicating palladium in its elemental form (Figure 5.9).

Table 5.2. Nitrate-nitrogen [NO_3^--N] removal efficiencies of Pd/SBA-15 by two consecutive cycles.*

[NO_3^--N] removal efficiencies (mg/L)	Amount of Pd/SBA-15		
	10 mg	25 mg	50 mg
1st cycle, maximum [NO_3^--N] removal[a]	6.5 ± 0.6	8.0 ± 0.6	9.5 ± 0.5
2nd cycle, maximum [NO_3^--N] removal[a]	4.5 ± 0.3	6.5 ± 0.4	8.2 ± 0.4
Total [NO_3^--N] removal for two consecutive batches[b]	11.0 ± 0.7	14.5 ± 0.7	17.7 ± 0.6

* The numbers given here represent the amount of nitrate-nitrogen [NO_3^--N] ions removed from the solution, rather than the amount present in the solution.

[a] Errors reported were deviations from the mean.

[b] Reported overall errors for each batch are calculated using the standard error propagation formula.

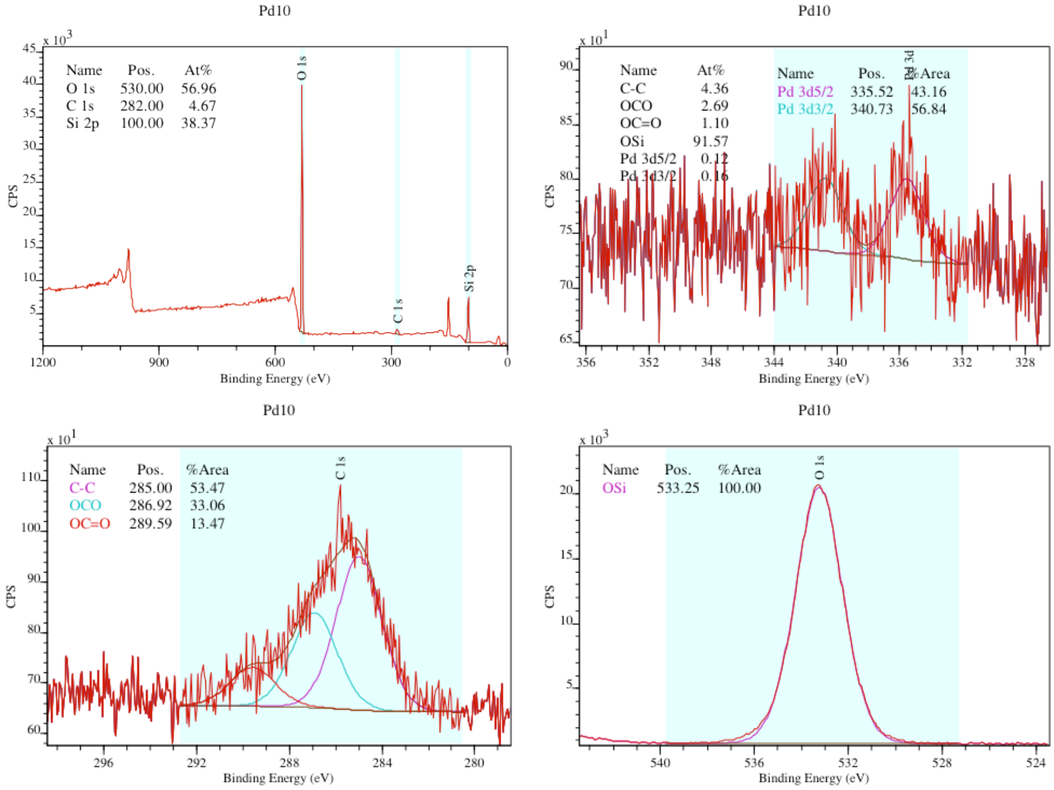

Figure 5.9. *XPS spectra of Pd/SBA-15 after two consecutive cycles of nitrate removal, with survey scan and high resolution scans under pass energy of 100 eV and 50 eV, respectively.*

5.5. Conclusions

An efficient method involving the use of the VFD has been developed for preparing mesoporous silica loaded with elemental palladium nanoparticles at neutral pH. This material is effective in wastewater treatment in targeting nitrate-nitrogen removal, showing a maximum nitrate-nitrogen removal efficiency of 41% after 16 hours. Recyclability of the same adsorbent was examined, establishing 36% maximum nitrate-nitrogen removal efficiency after being recycled. While this is lower, it nevertheless is promising given that Pd/SBA-15 can be easily separated from the liquid effluent.

The novel processing technology of VFD has the advantages of operating under ambient conditions and having a five-fold reduction in processing time relative to the synthesis of conventional hydrothermal processed SBA-15. Also noteworthy is the inherent cost savings in the production of SBA-15 and the analogous material loaded with palladium nanoparticles. This is potentially attractive to industry, as is the ability to generate metal nanoparticles almost exclusively embedded in the pores of the material, rather than on the surface, thereby minimising different outcomes for particles in different environments.

5.6. Acknowledgement

This work is supported by the Australian Research Council, The Perth Mint, and the Government of South Australia. The authors acknowledge the facility and support from the Australian Microscopy & Microanalysis Research Facility (AMMRF) at Flinders University. Craig E. Buckley acknowledges ARC RIEF grant R00107962 which enabled the SAXS studies to be conducted.

5.7. References

1. D. Zhao, J. Feng, Q. Huo, N. Melosh, G. H. Fredrickson, B. F. Chmelka and G. D. Stucky, Triblock Copolymer Syntheses of Mesoporous Silica with Periodic 50 to 300 Angstrom Pores, *Science*, 1998, **279**, 548-552.

2. J. r. P. Thielemann, F. Girgsdies, R. Schlögl and C. Hess, Pore structure and surface area of silica SBA-15: influence of washing and scale-up, *Beilstein J. Nanotechnol.*, 2011, **2**, 110-118.

3. L. Y. Chen, S. Jaenicke and G. K. Chuah, Thermal and hydrothermal stability of framework-substituted MCM-41 mesoporous materials, *Microporous Mater.*, 1997, **12**, 323-330.

4. S. Lin, L. Shi, M. M. L. Ribeiro Carrott, P. J. M. Carrott, J. Rocha, M. R. Li and X. D. Zou, Direct synthesis without addition of acid of Al-SBA-15 with controllable porosity and high hydrothermal stability, *Microporous Mesoporous Mater.*, 2011, **142**, 526-534.

5. D. Zhao, Q. Huo, J. Feng, B. F. Chmelka and G. D. Stucky, Nonionic Triblock and Star Diblock Copolymer and Oligomeric Surfactant Syntheses of Highly Ordered, Hydrothermally Stable, Mesoporous Silica Structures, *J. Am. Chem. Soc.*, 1998, **120**, 6024-6036.

6. R. Ryoo, C. H. Ko, M. Kruk, V. Antochshuk and M. Jaroniec, Block-Copolymer-Templated Ordered Mesoporous Silica: Array of Uniform Mesopores or Mesopore-Micropore Network?, *The Journal of Physical Chemistry B*, 2000, **104**, 11465-11471.

7. D. Zhao, J. Sun, Q. Li and G. D. Stucky, Morphological Control of Highly Ordered Mesoporous Silica SBA-15, *Chem. Mater.*, 2000, **12**, 275-279.

8. H. I. Lee, J. H. Kim, G. D. Stucky, Y. Shi, C. Pak and J. M. Kim, Morphology-selective synthesis of mesoporous SBA-15 particles over micrometer, submicrometer and nanometer scales, *J. Mater. Chem.*, 2010, **20**, 8483-8487.

9. Y. Wan and D. Zhao, On the Controllable Soft-Templating Approach to Mesoporous Silicates, *Chem. Rev.*, 2007, **107**, 2821-2860.

10. D. Margolese, J. A. Melero, S. C. Christiansen, B. F. Chmelka and G. D. Stucky, Direct Syntheses of Ordered SBA-15 Mesoporous Silica Containing Sulfonic Acid Groups, *Chem. Mater.*, 2000, **12**, 2448-2459.

11. P. Schmidt-Winkel, W. W. Lukens, D. Zhao, P. Yang, B. F. Chmelka and G. D. Stucky, Mesocellular Siliceous Foams with Uniformly Sized Cells and Windows, *J. Am. Chem. Soc.*, 1998, **121**, 254-255.

12. J. S. Lettow, Y. J. Han, P. Schmidt-Winkel, P. Yang, D. Zhao, G. D. Stucky and J. Y. Ying, Hexagonal to Mesocellular Foam Phase Transition in Polymer-Templated Mesoporous Silicas, *Langmuir*, 2000, **16**, 8291-8295.

13. L. Cao and M. Kruk, Synthesis of large-pore SBA-15 silica from tetramethyl orthosilicate using triisopropylbenzene as micelle expander, *Colloids Surf., A*, 2010, **357**, 91-96.

14. C. L. Tong, R. A. Boulos, C. Yu, K. S. Iyer and C. L. Raston, Continuous flow tuning of ordered mesoporous silica under ambient conditions, *RSC Adv.*, 2013, **3**, 18767-18770.

15. S. Patwardhan, N. Mukherjee and S. Clarson, Formation of Fiber-Like Amorphous Silica Structures by Externally Applied Shear, *J. Inorg. Organomet. Polym.*, 2001, **11**, 117-121.

16. W.-J. Kim and S.-M. Yang, Preparation of Mesoporous Materials from the Flow-Induced Microstructure in Aqueous Surfactant Solutions, *Chem. Mater.*, 2000, **12**, 3227-3235.

17. A. S. Koparal and Ü. B. Öğütveren, Removal of nitrate from water by electroreduction and electrocoagulation, *J. Hazard. Mater.*, 2002, **89**, 83-94.

18. Y. Wang, J. Qu, H. Liu and C. Hu, Adsorption and reduction of nitrate in water on hydrotalcite-supported Pd-Cu catalyst, *Catal. Today*, 2007, **126**, 476-482.

19. E. Eroglu, V. Agarwal, M. Bradshaw, X. Chen, S. M. Smith, C. L. Raston and K. Swaminathan Iyer, Nitrate removal from liquid effluents using microalgae immobilized on chitosan nanofiber mats, *Green Chem.*, 2012, **14**, 2682-2685.

20. M. H. Wahid, E. Eroglu, X. Chen, S. M. Smith and C. L. Raston, Functional multi-layer graphene-algae hybrid material formed using vortex fluidics, *Green Chem.*, 2013, **15**, 650-655.

21. A. Kapoor and T. Viraraghavan, Nitrate Removal From Drinking Water—Review, *J. Environ. Eng.*, 1997, **123**, 371-380.

22. A. Bhatnagar and M. Sillanpää, A review of emerging adsorbents for nitrate removal from water, *Chem. Eng. J.*, 2011, **168**, 493-504.

23. N. Öztürk and T. E. l. Bektaş, Nitrate removal from aqueous solution by adsorption onto various materials, *J. Hazard. Mater.*, 2004, **112**, 155-162.

24. Y. Cengeloglu, A. Tor, M. Ersoz and G. Arslan, Removal of nitrate from aqueous solution by using red mud, *Sep. Purif. Technol.*, 2006, **51**, 374-378.

25. B. P. Chaplin, M. Reinhard, W. F. Schneider, C. Schüth, J. R. Shapley, T. J. Strathmann and C. J. Werth, Critical Review of Pd-Based Catalytic Treatment of Priority Contaminants in Water, *Environ. Sci. Technol.*, 2012, **46**, 3655-3670.

26. C. L. Tong, U. Stroeher, M. H. Brown and C. L. Raston, Continuous flow vortex fluidic synthesis of silica xerogel as a delivery vehicle for curcumin, *RSC Adv.*, 2014.

27. H. Song, R. M. Rioux, J. D. Hoefelmeyer, R. Komor, K. Niesz, M. Grass, P. Yang and G. A. Somorjai, Hydrothermal Growth of Mesoporous SBA-15 Silica in the Presence of PVP-Stabilized Pt Nanoparticles: Synthesis, Characterization, and Catalytic Properties, *J. Am. Chem. Soc.*, 2006, **128**, 3027-3037.

28. C. S. Bolch and S. Blackburn, Isolation and purification of Australian isolates of the toxic cyanobacteriumMicrocystis aeruginosa Kütz, *J. Appl. Phycol.*, 1996, **8**, 5-13.

29. APHA, ed., *Standard methods for the examination of water and wastewater*, Washington DC, 1992.

30. A. Martin, G. Morales, F. Martinez, R. van Grieken, L. Cao and M. Kruk, Acid hybrid catalysts from poly(styrenesulfonic acid) grafted onto ultra-large-pore SBA-15 silica using atom transfer radical polymerization, *J. Mater. Chem.*, 2010, **20**, 8026-8035.

31. Martin Ermrich and D. Opper, *XRD for the analyst*, PANalytical GmbH, Germany, 2011.

32. R. Che, D. Gu, L. Shi and D. Zhao, Direct imaging of the layer-by-layer growth and rod-unit repairing defects of mesoporous silica SBA-15 by cryo-SEM, *J. Mater. Chem.*, 2011, **21**, 17371-17381.

33. C. P. Ruas, D. K. Fischer and M. A. Gelesky, PVP-Stabilized Palladium Nanoparticles in Silica as Effective Catalysts for Hydrogenation Reactions, *J. Nanotechnol.*, 2013, **2013**, 6.

34. J. Morère, M. J. Tenorio, M. J. Torralvo, C. Pando, J. A. R. Renuncio and A. Cabañas, Deposition of Pd into mesoporous silica SBA-15 using supercritical carbon dioxide, *J. Supercrit. Fluids*, 2011, **56**, 213-222.

Chapter Six

In Situ Synthesis of Phosphate Binding Mesocellular Siliceous Foams Impregnated with Iron Oxide Nanoparticles

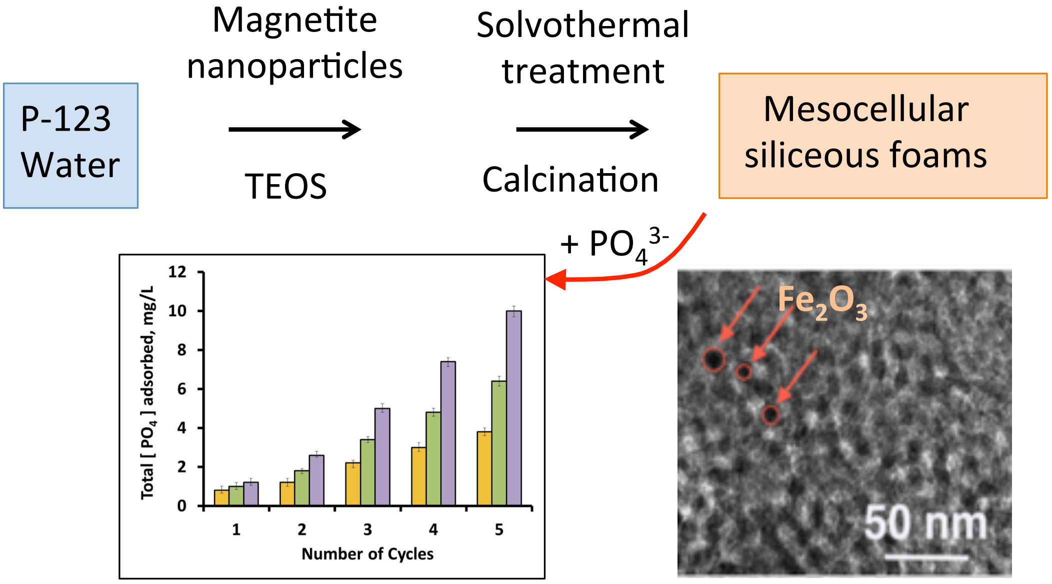

This chapter is reformatted from a paper published in ***RSC Advances***, Year 2014, Vol. 4, Issue 87, Pages 46718-46722.

6.1. Abstract

Mesocellular siliceous foams (MCFs) loaded with preformed magnetite nanoparticles *ca*. 8 nm in diameter are readily prepared in water under neutral conditions. The calcined composite nanomaterial with 0.72% weight of iron is effective for the adsorption of phosphate ions from liquid effluents, with the overall adsorption capacity maintained on cycling five times, at 79.2 mg PO_4^{3-} per gram.

6.2. Introduction

Mesostructured cellular foams (MCFs), also known as mesocellular foams, were developed by Stucky *et al.* in 1998.[1] They were prepared in acidic medium, in a similar way to the synthesis of Santa Barbara Amorphous (SBA-15), under acidic condition, using 1,3,5-trimethylbenzene (TMB) as the organic co-solvent. TMB acts as a swelling agent to increase the pore size of the silica framework,[2] with the resulting MCFs having a unique three-dimensional mesostructure comprised of extensively large interconnected pore diameters of 22 to 42 nm and window diameter of 7 to 22 nm.[1-4] Subsequently in 2007, Wang *et al.* reported success in synthesizing siliceous unilamellar vesicles and foams using a non-ionic amphiphilic copolymer as a template, in near-neutral aqueous solutions without using an organic co-solvent.[5] At the time, these mesostructured materials with significantly enlarged pore size immediately caught attention as ideal supports for catalysis, and for use in separation science and biosensors.[3-7]

Magnetic nanoparticles have a number of applications, in catalysis, biotechnology, energy and environmental remediation.[8, 9] However, they tend to agglomerate due to anisotropic dipolar attractions, with loss of superparamagnetic behaviour.[10] Dispersion of such nanoparticles in a non-magnetic matrix can circumvent agglomeration, as well as protect the nanoparticles from corrosion and oxidation.[10] Impregnating magnetic nanoparticles into ordered mesoporous silica has been developed by many researchers, using a number of different methods, for example, sonochemical, temperature-programmed reduction, and grafting.[9-11] Among these, an impregnation and reduction method is successful for preparing ordered mesoporous magnetic silica nanocomposites. However, the impregnation of magnetic nanoparticles inside the pores may lead to clogging of the pores, along with decreasing the surface area and pore volume of the material.[9] Accordingly MCFs with much larger pore size have the potential to impregnate the same nanoparticles with less likelihood of clogging. Lee *et al.* have developed a multi-step synthesis of a surface modified MFC, with γ-Fe_2O_3 nanoparticles inside the pores, which is an effective support for immobilization of enzymes and nanoparticles.[12] In this chapter of the dissertation a robust one pot self assembly process has been developed, to gain access to such MCF bearing ferromagnetic nanoparticles of hematite (Fe_2O_3) and/or its oxidized form, in targeting application in removing phosphate from waste water.

The presence of excess phosphorous in the form of phosphate ions, PO_4^{3-}, in water has the risk of initiating eutrophication.[13] Wastewater treatment using chemical precipitation for removing phosphate had its origins in Switzerland in 1950s.[9] Many other types of removal technologies have been developed since then, including physical separation, biological removal, crystallization, and ion-exchange methods.[13, 14] Adsorbents for water treatment include ferric-oxides, lime, alum, zeolite, fly-ash, sand and red-mud.[8, 15-19] Analogous to AsO_4^{3-},[20] PO_4^{3-} ions are effectively adsorbed on soil-minerals including the oxides of iron and aluminum.[14, 16] The adsorption efficiency of the material can be enhanced by increasing its surface area, by reducing the particle size/aspect ratio,[16] and there has been increasing interest in preparing various nano-sized adsorbents. In this study, the removal of phosphate ions using MCFs incorporated with magnetic iron oxide nanoparticles has been investigated. In principle, MCFs offer higher adsorption capabilities than SBA-15 due to the larger pore volume and pore diameters.[4]

6.3. Experimental

6.3.1. Preparation of magnetite nanoparticles

Monodispersed magnetite nanoparticles were synthesized following a method reported by Sun *et al.*[21] Iron(III) acetylacetonate [$Fe(acac)_3$], 1,2-tetradecanediol, oleic acid, benzyl ether and oleylamine were purchased from Sigma Aldrich and used without further purification: 508.5 mg of $Fe(acac)_3$, 2306.6 mg of 1, 2-tetradecanediol, 21 mL of benzyl ether, 1.69 g of oleic acid and 1.69 g of oleylamine were mixed using a magnetic stirrer under nitrogen (N_2). The mixture was heated to 200 ˚C for 2 hours, then under reflux at 300 ˚C for another hour under a blanket of N_2. The mixture was then cooled to the room temperature and the black precipitate separated by centrifugation. The magnetite was dispersed in hexane and kept under an argon purged round-bottom flask to prevent any oxidation.

6.3.2. Preparation of MCFs with iron oxides nanoparticles

Mesocellular siliceous foam loaded with magnetic nanoparticles was synthesized using a modified literature procedure.[2] Firstly, 2.0 g Pluronic® P-123 ($EO_{20}PO_{70}EO_{20}$, averaged Mw = 5800, Sigma Aldrich) was dissolved in 50 mL of deionized water in a 250 ml conical flask. The solution was stirred vigorously in a water bath with the temperature controlled between 40 to 45 °C to dissolve the P-123. After an hour, 10 mL of 10 mM magnetite in hexane solution was added into the P-123 solution and stirring was continued. After 30 min, 4.4 mL of tetraethyl orthosilicate (TEOS, 98%, Sigma Aldrich) was added dropwise and the resulting mixture stirred for 20 hours whereupon it was transferred to a Teflon-lined autoclave and placed in an oven at an aging temperature of 110 °C for 24 hours. The final material is being collected on cooling to room temperature via vacuum filtration and dried at 80 °C overnight. The resulting solid was calcined in air at 500 °C for 6 hours to remove the polymer template.

6.3.3. Sample characterization

The calcined materials were characterized using a ZEISS 1555 instrument for scanning electron micrographs (SEM) at an accelerating voltage of 5 – 15 kV. Transmission electron micrographs (TEM) were obtained using a JEOL 2100 instrument with an operating voltage of 120 kV. Nitrogen adsorption- desorption studies were performed using a Micromeritics TriStar™ II 3020 system. The samples were outgassed at 110 °C for 16 hours prior to gas adsorption which was carried out at 77K. The specific surface area, S_{BET}, was determined from the linear part of the BET equation (P/P_o = 0.09 – 0.30). The pore size distribution and pore volume were evaluated using the Barrett–Joyner–Halenda (BJH) method. The total pore volume reported was taken from the amount of gas adsorbed at a relative pressure (P/P_o) at 0.995. Magnetic properties were determined using a superconducting quantum interference device (SQUID) magnetometer. The final iron content was obtained using inductively coupled plasma mass spectrometry (ICP-MS), at TSW Analytical Pty. Ltd. (Perth, WA).

6.3.4. *Preparation for phosphate removal study*

Iron oxides/MCFs samples were individually mixed with an artificial aquatic-medium with a buffered pH close to 7.5, which mainly includes phosphates, nitrates, carbonate buffer, micronutrients and vitamins.[22] Three different loadings of the same adsorbent (10 mg; 25 mg; 50 mg) were separately mixed with phosphate containing aquatic media (1.5 mL). Each mixture was then hand-vortexed for about 30 seconds, followed by gentle mixing throughout the entire experiment with an Eppendorf tube Rotator (Stuart Rotator, SB3) at a constant rotational speed of 20 rpm. Mixtures were centrifuged at 9391 g for 5 minutes, and particle-free supernatants were collected for spectrophotometric analysis. Collected liquid samples were subjected to phosphate analysis using the colorimetric "ascorbic acid" method,[23] which is a standard water-analyzing procedure recognized by the United States Environmental Protection Agency. Phosphate analyzing kits in the form of powder pillows (HACH®, PhosVer® 3 Phosphate Reagent) were employed before reading the phosphate concentration of the supernatant by a colorimeter (HACH® DR/870).

6.4. Results and Discussion

The effect of adding a swelling agent such as TMB into the polymer solution during the synthesis of MCFs has been extensively studied.[2, 4] A direct synthesis of MCFs incorporating magnetic nanoparticles *in situ* has been developed, rather than using a a separate process (Figure 6.1) The calcined material has ultra large cavities and high pore volume which affect the physiochemical properties of the material. This is even in the absence of TMB, with a large amount of hexane used as a dispersing agent for the magnetite nanoparticles presumably acting as a pore expander in the same vein. Nevertheless, aromatic hydrocarbons are in general more solubilizing than aliphatic hydrocarbons within Pluronic micelles which features in the synthesis of MCFs.[24]

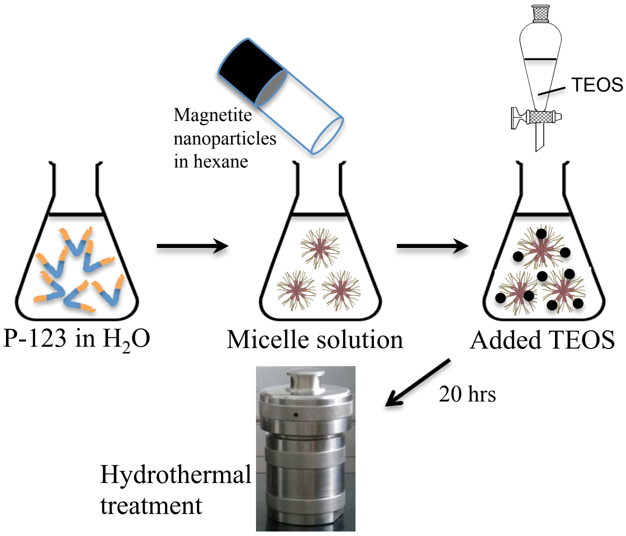

Figure 6.1. *Schematic of the in situ synthesis of iron oxide loaded mesocellular siliceous foams.*

The initial synthesis of MCF in this study had a mass ratio S1 for hexane/P123 of 3.2 and S2 for TEOS/P123 of 2.0. The resulting calcined material had a pore diameter of 28.7 nm and pore volume of 3.5 $cm^3.g^{-1}$, and is designated MCF-1. A second batch of material, designated MCF-2, involved decreasing the mass ratio of S1 and S2 to 0.8 and 1.5, respectively, which resulted in a smaller pore diameter of 13.4 nm, also with a smaller pore volume of 1.59 $cm^3.g^{-1}$. This agrees with the findings of Sridhar *et al.*, in that as the ratio of swelling agent/P123 increases there is an increase in pore diameter, albeit using hexane in the present study rather than TMB.[4] In contrast, the pore diameter increased upon decreasing the ratio of TEOS/P123.[4] Both MCF-1 and MCF-2 exhibited type IV isotherm with H1 hysteresis loop, according to IUPAC definition, Figure 6.2.[25] It should be noted that the BJH method underestimates pore diameter,[26] and many reports have used the proposed modified Broekhoff-de Boer (BdB) method involving the Frenkel–Halsey–Hill (FHH) theory developed by Lukens *et al.* for reporting the pore size distribution of mesocellular foams.[2, 4, 26] Nonetheless, the pore diameters in our study were calculated using the BJH method, given that there was no significant discrepancy with estimated pore diameter from transmission electron micrographs (TEM) images.

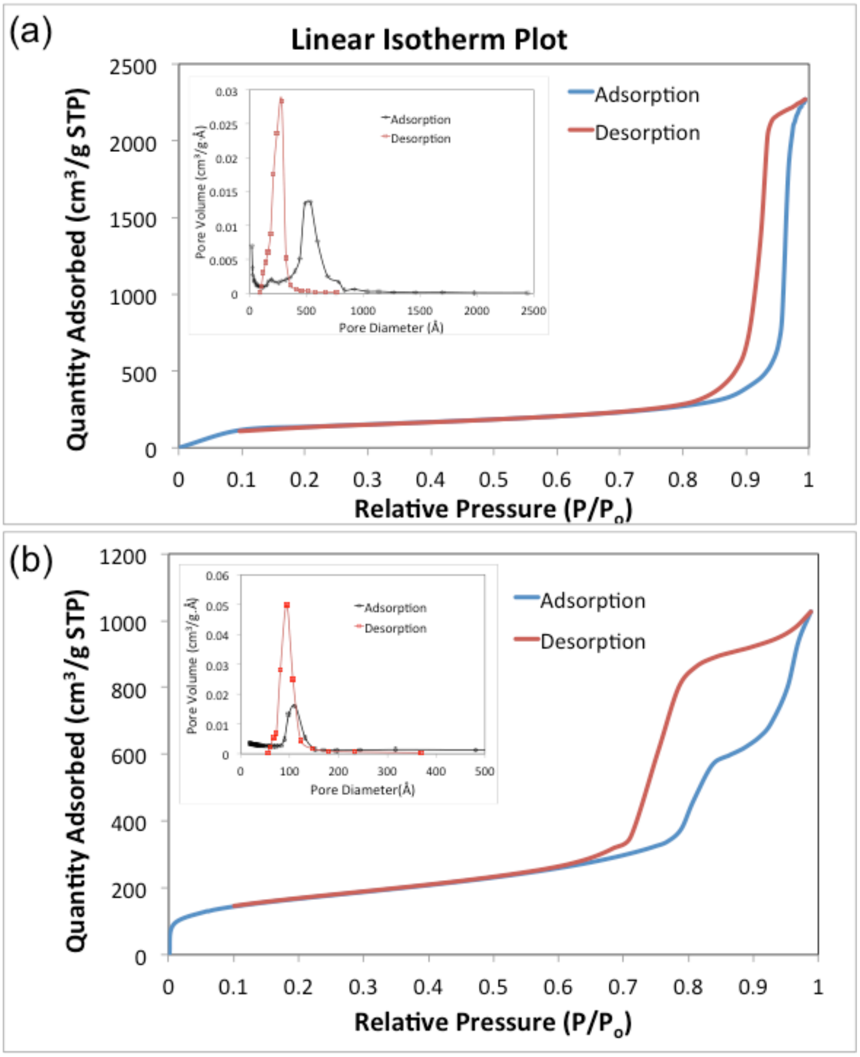

Figure 6.2. *Nitrogen sorption isotherm for (a) MCF-1 and (b) MCF-2 showing a typical type IV hysteresis, with the corresponding pore diameter distributions of adsorption and desorption branch as an inset.*

TEM of the MCFs revealed pore diameter differences resulting from using the two different ratios of hexane/P123 (Figure 6.3). The pores are not regularly packed, with a combination of distorted spherical cellular and indistinct polyhedral cellular foams. Structural transformation from tubules to vesicles occurred by increasing the hydrophobic volume fraction, which also depends on the temperature of the process.[5, 27] When lower the concentration (ratio) of hexane, it not only results in a decrease in pore sizes, but there is now a combination of spherical pores and hexagonal packing of cylindrical pores. This relates to the presence of hexane which has high Flory-Huggins interaction parameters, being a non-ideal solvent for propylene oxide (PO) blocks in micelles.[24] This is consistent with a lower amount of hexane not dramatically enhancing (increasing) the pore diameter. Silica wall thickness determined from TEM images was around 5.0 – 5.5 nm for both samples, being independent of pore diameter.

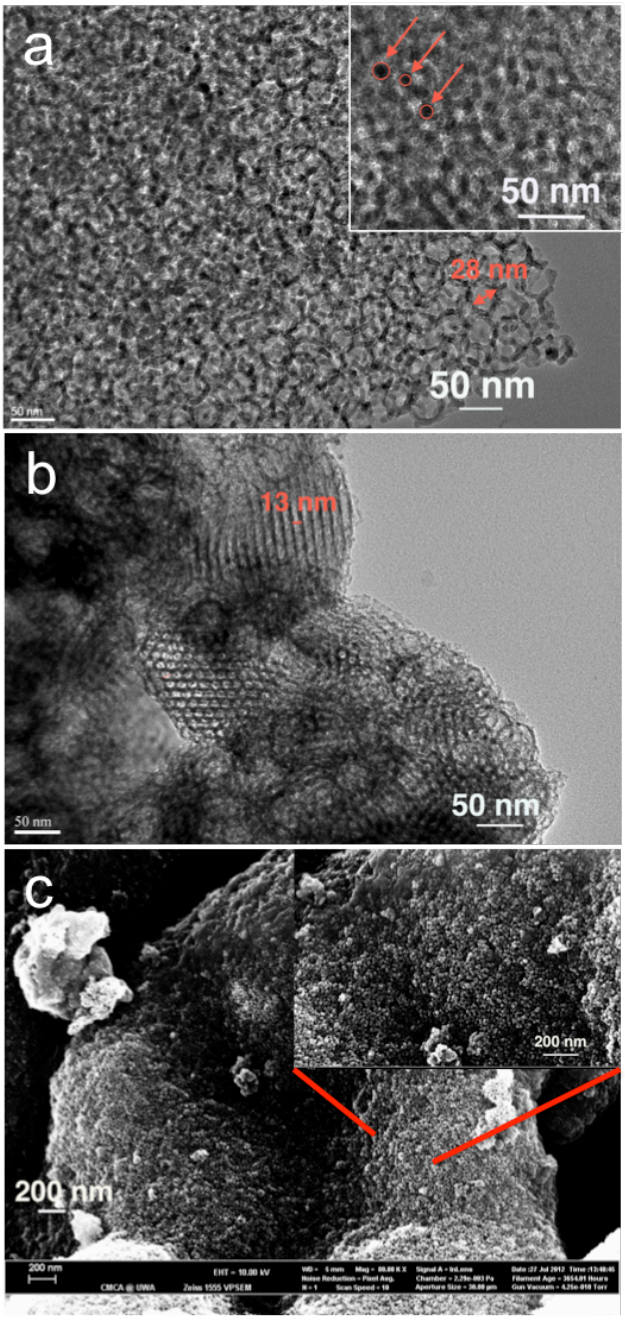

Figure 6.3. *TEM images of (a) MCFs with S1 (see text) value at 3.2, inset showing the magnetite nanoparticles, and (b) S1 value at 0.8. (c) SEM image of MCF-1 with the magnified image of the selected area (inset).*

Monodispersed magnetite was prepared using the method reported by Sun *et al.* and re-dispersed in hexane.[21] The particle sizes determined from TEM were *ca.* 8 nm (Figure 6.4), which is consistent with the diameters determined from TEM images (inset) for the composite material, being approximately 7 – 8 nm in diameter. TEM images of the calcined MCF-1 sample showed the magnetite nanoparticles were successfully loaded within the mesocellular foam network, Figure 6.3. Also, a weak Fe element peak can be observed from the elemental analysis spectrum using energy-dispersive X-ray spectroscopy (EDS) under TEM (Figure 6.5). The amount of magnetite present corresponds to 0.72 wt% of the iron in final sample, as determined using ICP-MS. From SEM micrographs, MCF-1 is comprised of clusters of small spherical particles (Figure 6.3(c)). Under high resolution SEM, it appears as a sponge like surface, where the spaces between the interconnected particles reflect the pore diameter of the material.

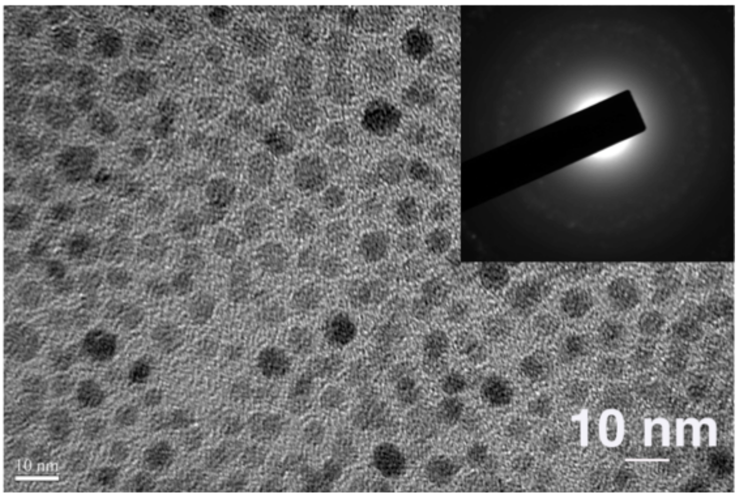

Figure 6.4. *TEM image of magnetite nanoparticles dispersed in hexane, and the diffraction pattern of magnetite (inset).*

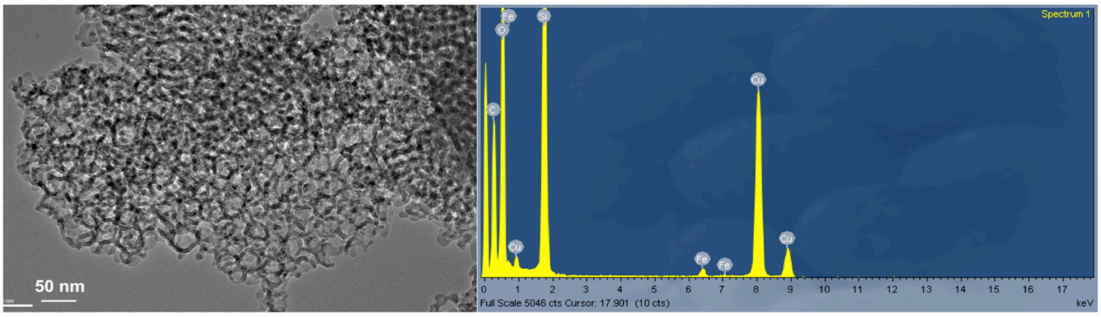

Figure 6.5. *TEM image of MCF-1 (left), and the elemental analysis spectrum using energy-dispersive X-ray spectroscopy (EDS) (right).*

Since the magnetite (Fe_3O_4) nanoparticles were loaded *in situ* during the synthesis of mesocellular foams and has undergone calcination at 500 ˚C under air, oxidation of magnetite to hematite (α-Fe_2O_3) will occur, although this could not be ascertained using XPS or X-ray diffraction (Figure 6.6), because of the low percentage of iron in the samples.

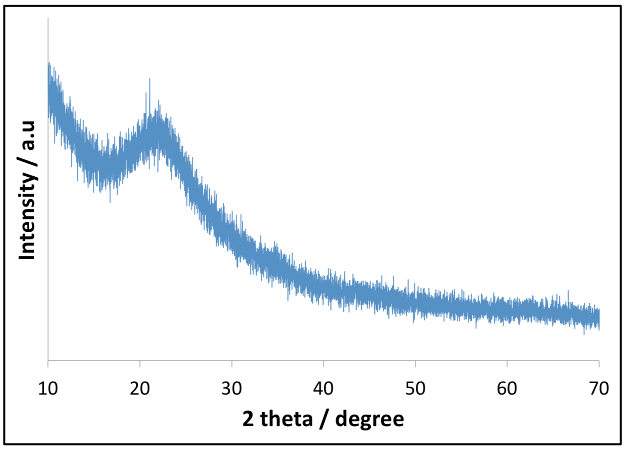

Figure 6.6. *XRD profile for sample MCF-1, which only shows a broad amorphous peak.*

However, Gallagher *et al.* noted that heating pure magnetite above 250 ˚C in air results in the formation of thermodynamically stable α-Fe_2O_3.[28] At room temperature, MCF-1 shows a weak ferromagnetic behaviour with its saturation magnetization and coercivity being 0.22 emu g^{-1} and 13.5 Oe respectively.[29] At 5K, magnetization hysteresis loops of MCF-1 have dual characteristics of ferromagnetic behaviour with a coercivity of Hc = 150 Oe and a saturated magnetization of ~56.7 emu/g, and paramagnetic behaviour where a linear slop is observed at large applied fields (Figure 6.7).[29-31]

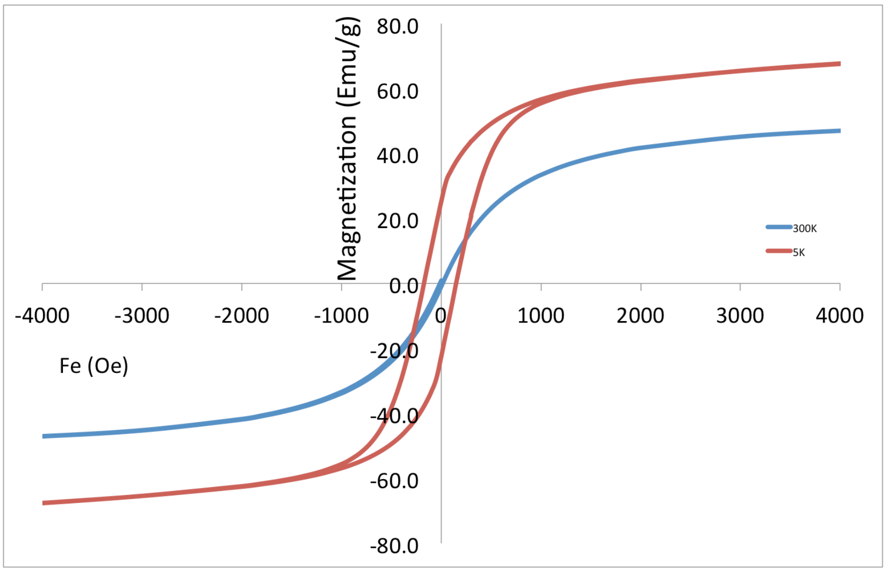

Figure 6.7. *Magnetic hysteresis loops at 5K and 300K for sample MCF-1 was obtained and magnetic properties were determined using a superconducting quantum interference device (SQUID) magnetometer.*

Phosphate removal experiments were conducted to evaluate the performance of the MCFs with respect to their physiochemical properties, which is provided in Table 6.1. A blank experiment was conducted, which involved mixing the phosphate containing media with the mesoporous siliceous samples devoid of any iron oxides loading. This established that there was no significant amount of phosphate removal. Next, three different loadings of MCF-1 (10 mg; 25 mg; 50 mg) were separately mixed with phosphate containing aquatic media (1.5 mL). Data collection was based on the amount of phosphate concentration of the aqueous media at various time intervals, after being exposed to adsorbent MCF-1. Regardless of the loading concentration, MCF-1 resulted in similar phosphate removal values of around 1 mg PO_4^{3-} L^{-1} at given time-intervals (Table 6.2). Adsorption equilibrium was nearly reached within the first 30 minutes of the experiment. Clearly, the iron oxide nanoparticles present within the sample are the main factor responsible for the phosphate removal. Adsorption mechanisms are mainly divided into inner-sphere complexation and outer-sphere complexation.[32] The sorption of PO_4^{3-} ions on the iron oxides first takes place at the active sites on the surface, by forming complexes with surface bound OH^- ligand.[32] The fact that the phosphate adsorption did not significantly differ with various loading concentrations indicates that the iron oxide nanoparticles were not entirely located at the outer surfaces of the adsorbent, while some of them might be hindered within the internal pores of the mesocellular siliceous foams. This is supported by the observations from TEM where the iron oxides (dark contrast) were observed within the pores (Figure 6.3(a) and 6.3(b)). With such a high porosity, MCF can act as a membrane, with the PO_4^{3-} ions permeating from high concentration (outer surface) to low concentration (inner pores), involving a temperature and pressure gradient.

Table 6.1. Physicochemical properties of the mesocellular siliceous foams.

Sample ID	S_{BET} (m^2g^{-1})	V_t (cm^3g^{-1})	Pore diameter (nm)
MCF-1	438.1	3.5	27.8
MCF-2	581.5	1.6	13.4

Table 6.2. Amount of phosphate (PO_4^{3-}) adsorbed from aqueous media in mg.L^{-1} (Initial [PO_4^{3-}]: 16 mg/L) at various time intervals for three different loading concentrations of sample MCF-1.

Time (h)	Amount of Adsorbent		
	10 mg	**25 mg**	**50 mg**
0.5	0.8	1.0	1.2
4.0	1.2	1.2	1.4
24	0.8	1.0	1.2

Since adsorption equilibrium was nearly reached within the first 30 minutes, and because it is more practical to carry out several consecutive cycles at one time, the optimal time-interval for testing the recycling potential of the adsorbent through consecutive cycles was set at 30 minutes. Used samples were then washed with deionized water which involved hand-vortexing for 1 minute, followed by removal of the supernatant after centrifugation at 9391 g for 5 minutes. The remaining samples were then mixed again with phosphate-containing aqueous media (1.5 mL), while the remaining phosphate content of the liquid sample was analysed after the first 30 minute of each cycle, Figure 6.8.

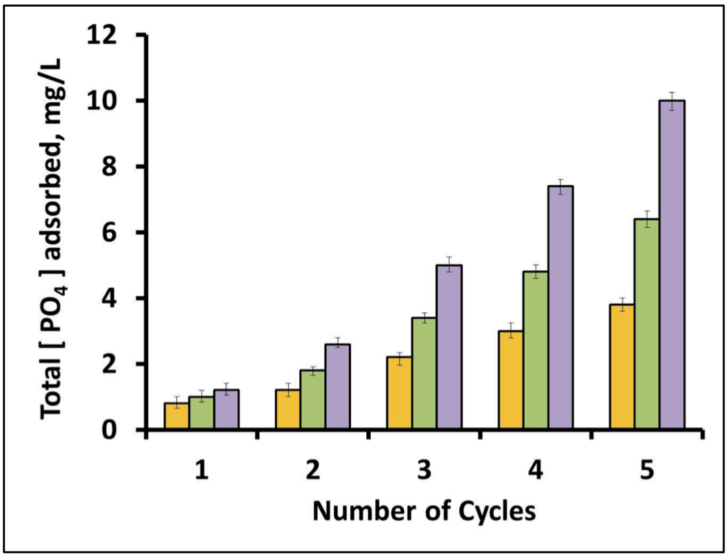

Figure 6.8. *Cumulative amount of* PO_4^{3-} *adsorbed in mg* L^{-1} *after each consecutive cycle, for three different loading concentrations of MCF-1, for (1) 10 mg adsorbent (yellow column); (2) 25 mg adsorbent (green column); and (3) 50 mg adsorbent (purple column).*

The increase in adsorbent loading had a positive effect on the total amount of PO_4^{3-} adsorbed. As shown in Figure 6.8, by the end of the fifth consecutive cycle, 50 mg of adsorbent yielded the highest overall phosphate adsorption value of 10 mg L^{-1}, which was followed by 6.4 mg L^{-1} phosphate adsorption by a 25 mg sample, and 3.8 mg L^{-1} for a 10 mg sample. Since the main component responsible for the PO_4^{3-} removal is the iron oxide component, it is realistic to conclude that the adsorption capacity of the adsorbent is based on the amount of Fe present in the sample, which was 0.72% (w/w). Once phosphate-removal values were converted into adsorption capacities, a reverse correlation was observed between the adsorbent loading and the overall phosphate adsorption capacity. A 10 mg sample yielded an overall adsorption capacity of 79.2 mg PO_4^{3-} per gram Fe, followed by 53.3 mg PO_4^{3-} per gram Fe for a 25 mg sample, and 41.7 mg PO_4^{3-} per gram Fe for a 50 mg sample. These results are within the range of literature data given for adsorbents containing iron oxide nanoparticles.[8, 33] In a related study, diatom frustules coated with magnetite nanoparticles yielded an overall adsorption capacity of around 45 mg PO_4^{3-} per gram Fe.[8] Noteworthy is that MCF-1 can continuously adsorb PO_4^{3-} ions during each consecutive cycle, while the adsorption rate was nearly doubled after the second cycle. This phenomenon aligns with the aforementioned proposed adsorption process, with the phosphate ions being initially adsorbed by the active sites of magnetic nanoparticles located on the surface of the silica, and then they diffuse into the cavities of the mesocellular foams during the recycling process, where the other magnetic nanoparticles reside. Since MCF-1 exhibits higher pore volume, it has a higher capability to continuously adsorb phosphate ions before reaching saturation. Recycling the material for consecutive mechanical-mixing and washing processes might slightly enhance the surface adsorption capacity of the adsorbent.

To establish whether the pore diameter would affect the overall performance, MCF-2 was synthesized with much smaller pore diameter and pore volume (Table 6.1). The iron content of MCF-2 determined by ICP-MS was 0.79% w/w, which was slightly higher than for MCF-1 (0.72% w/w). Given that iron oxide was the main component responsible for the phosphate removal, theoretically a slight increase in the removal rate of phosphate should be expected. The same experimental procedures were carried out, and by the end of the fifth consecutive cycle, 50 mg of MCF-2 yielded the highest overall phosphate adsorption value of 9.5 mg L^{-1}, which was followed by 5.8 mg L^{-1} phosphate adsorption by a 25 mg sample, and 3.0 mg L^{-1} phosphate adsorption by a 10 mg sample, Figure 6.9. This establishes that MCF-2 had a slightly lower PO_4^{3-} ion adsorption capacity than MCF-1 sample, which has the larger pore sizes. Once phosphate-removal values were converted into the adsorption capacities, similar reverse correlation was observed between the adsorbent loading and the overall phosphate adsorption capacity of the adsorbent. A 10 mg sample yielded an overall adsorption capacity of 57.0 mg PO_4^{-3} per gram Fe, followed by 44.1 mg PO_4^{3-} per gram Fe for a 25 mg sample, and 36.1 mg PO_4^{3-} per gram Fe for a 50 mg sample. While the trend of the cumulative adsorption values did not show significant differences, when comparing the overall adsorption capacities per iron content, there was a significant drop in MCF-2. Presumably the smaller pore diameters hinder the adsorption and diffusion of phosphate ions towards the active sites of magnetic nanoparticles, located within the internal pores of MCF-2.

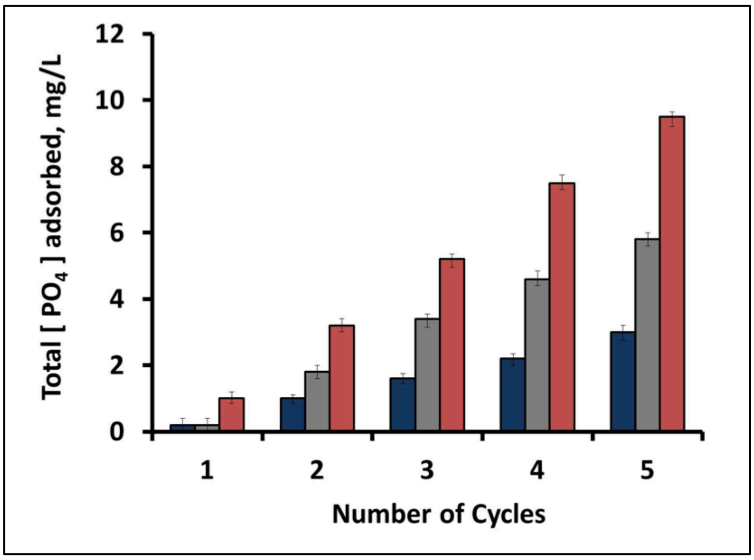

Figure 6.9. *Cumulative amount of* PO_4^{3-} *adsorbed in mg* L^{-1} *after each consecutive cycle, for three different loading concentrations of MCF-2, (1) 10 mg adsorbent (dark-blue column); (2) 25 mg adsorbent (grey column); and (3) 50 mg adsorbent (red column).*

6.5. Conclusions

In summary, mesocellular siliceous foams have been prepared under neutral conditions with *in situ* incorporation of iron oxide nanoparticles. For a minimal iron content (around 0.7% w/w), and rather small particle size (*ca*. 8 nm) of the magnetic nanoparticles within the siliceous foam matrix, the composite materials show a significant overall phosphate adsorption capacities of up to 79.2 mg PO_4^{3-} per gram Fe after five consecutive cycles. This process is relatively benign and cost effective, while allowing the recyclability of the adsorbent. The remaining material can be easily separated by a simple filtration step, allowing the transfer of adsorbed phosphate ions from one environment to another for further applications, including as a fertilizer.

6.6. Acknowledgement

Support from the Government of South Australia, the Australian Research Council and the Centre for Microscopy, Characterisation and Analysis (The University of Western Australia), is gratefully acknowledged, as is the preparation of the magnetite nanoparticles by Ruhani Singh.

6.7. References

1. P. Schmidt-Winkel, W. W. Lukens, D. Zhao, P. Yang, B. F. Chmelka and G. D. Stucky, Mesocellular Siliceous Foams with Uniformly Sized Cells and Windows, *J. Am. Chem. Soc.*, 1998, **121**, 254-255.

2. J. S. Lettow, Y. J. Han, P. Schmidt-Winkel, P. Yang, D. Zhao, G. D. Stucky and J. Y. Ying, Hexagonal to Mesocellular Foam Phase Transition in Polymer-Templated Mesoporous Silicas, *Langmuir*, 2000, **16**, 8291-8295.

3. N. Erathodiyil, S. Ooi, A. M. Seayad, Y. Han, S. S. Lee and J. Y. Ying, Palladium Nanoclusters Supported on Propylurea-Modified Siliceous Mesocellular Foam for Coupling and Hydrogenation Reactions, *Chem. Eur. J.*, 2008, **14**, 3118-3125.

4. M. Sridhar, G. K. Reddy, N. Hu, A. Motahari, D. W. Schaefer, S. W. Thiel and P. G. Smirniotis, Preparation, characterization and lysozyme immobilization studies on siliceous mesocellular foams: Effect of precursor chemistry on pore size, wall thickness and interpore spacing, *Microporous Mesoporous Mater.*, 2014, **190**, 215-226.

5. H. Wang, Y. Wang, X. Zhou, L. Zhou, J. Tang, J. Lei and C. Yu, Siliceous Unilamellar Vesicles and Foams by Using Block-Copolymer Cooperative Vesicle Templating, *Adv. Funct. Mater.*, 2007, **17**, 613-617.

6. Y. Han, S. S. Lee and J. Y. Ying, Pressure-Driven Enzyme Entrapment in Siliceous Mesocellular Foam, *Chem. Mater.*, 2006, **18**, 643-649.

7. S. Wu, H. X. Ju and Y. Liu, Conductive Mesocellular Silica–Carbon Nanocomposite Foams for Immobilization, Direct Electrochemistry, and Biosensing of Proteins, *Adv. Funct. Mater.*, 2007, **17**, 585-592.

8. J. Toster, I. Kusumawardani, E. Eroglu, K. S. Iyer, F. Rosei and C. L. Raston, Superparamagnetic imposed diatom frustules for the effective removal of phosphates, *Green Chem.*, 2014, **16**, 82-85.

9. J. Liu, S. Z. Qiao, Q. H. Hu and G. Q. Lu, Magnetic Nanocomposites with Mesoporous Structures: Synthesis and Applications, *Small*, 2011, **7**, 425-443.

10. S. L. Jun, K. H. Sun, J. H. Nam, W.-S. Seo and J. H. Hae, Fabrication of spherical silica aerogel/magnetite nanocomposite particles, *Mater. Lett.*, 2013, **112**, 153-157.

11. I. Ursachi, A. Vasile, H. Chiriac, P. Postolache and A. Stancu, Magnetic properties of magnetite nanoparticles coated with mesoporous silica by sonochemical method, *Mater. Res. Bull.*, 2010, **46**, 2468-2473.

12. S. S. Lee, S. N. Riduan, N. Erathodiyil, J. Lim, J. L. Cheong, J. Cha, Y. Han and J. Y. Ying, Magnetic Nanoparticles Entrapped in Siliceous Mesocellular Foam: A New Catalyst Support, *Chem. Eur. J.*, 2012, **18**, 7394-7403.

13. L. Zeng, X. Li and J. Liu, Adsorptive removal of phosphate from aqueous solutions using iron oxide tailings, *Water Res.*, 2004, **38**, 1318-1326.

14. G. K. Morse, S. W. Brett, J. A. Guy and J. N. Lester, Review: Phosphorus removal and recovery technologies, *Sci. Total Environ.*, 1998, **212**, 69-81.

15. S. K. Kang, K. H. Choo and K. H. Lim, Use of Iron Oxide Particles as Adsorbents to Enhance Phosphorus Removal from Secondary Wastewater Effluent, *Sep. Sci. Technol.*, 2003, **38**, 3853-3874.

16. A. Zach-Maor, R. Semiat and H. Shemer, Synthesis, performance, and modeling of immobilized nano-sized magnetite layer for phosphate removal, *J. Colloid Interface Sci.*, 2011, **357**, 440-446.

17. J. Xiong, Z. He, Q. Mahmood, D. Liu, X. Yang and E. Islam, Phosphate removal from solution using steel slag through magnetic separation, *J. Hazard. Mater.*, 2008, **152**, 211-215.

18. E. W. Shin, J. S. Han, M. Jang, S.-H. Min, J. K. Park and R. M. Rowell, Phosphate Adsorption on Aluminum-Impregnated Mesoporous Silicates: Surface Structure and Behavior of Adsorbents, *Environ. Sci. Technol.*, 2003, **38**, 912-917.

19. W. Huang, S. Wang, Z. Zhu, L. Li, X. Yao, V. Rudolph and F. Haghseresht, Phosphate removal from wastewater using red mud, *J. Hazard. Mater.*, 2008, **158**, 35-42.

20. A. Violante and M. Pigna, Competitive Sorption of Arsenate and Phosphate on Different Clay Minerals and Soils, *Soil Sci. Soc. Am. J.*, 2002, **66**, 1788-1796.

21. S. Sun, H. Zeng, D. B. Robinson, S. Raoux, P. M. Rice, S. X. Wang and G. Li, Monodisperse MFe_2O_4 (M = Fe, Co, Mn) Nanoparticles, *J. Am. Chem. Soc.*, 2003, **126**, 273-279.

22. C. S. Bolch and S. Blackburn, Isolation and purification of Australian isolates of the toxic cyanobacteriumMicrocystis aeruginosa Kütz, *J. Appl. Phycol.*, 1996, **8**, 5-13.

23. APHA, ed., *Standard methods for the examination of water and wastewater*, Washington DC, 1992.

24. R. Nagarajan, Solubilization of “guest” molecules into polymeric aggregates, *Polym. Adv. Technol.*, 2001, **12**, 23-43.

25. Z. Luan, E. M. Maes, P. A. W. van der Heide, D. Zhao, R. S. Czernuszewicz and L. Kevan, Incorporation of Titanium into Mesoporous Silica Molecular Sieve SBA-15, *Chem. Mater.*, 1999, **11**, 3680-3686.

26. W. W. Lukens, P. Schmidt-Winkel, D. Zhao, J. Feng and G. D. Stucky, Evaluating Pore Sizes in Mesoporous Materials: A Simplified Standard Adsorption Method and a Simplified Broekhoff−de Boer Method, *Langmuir*, 1999, **15**, 5403-5409.

27. R. W. Corkery and A. Fogden, On the Formation and Structure of Nanometric Polyhedral Foams: Toward the Dry Limit, *Langmuir*, 2008, **24**, 10443-10452.

28. K. J. Gallagher, W. Feitknecht and U. Mannweiler, Mechanism of Oxidation of Magnetite to [gamma]-Fe_2O_3, *Nature*, 1968, **217**, 1118-1121.

29. S. Zhang, W. Wu, X. Xiao, J. Zhou, F. Ren and C. Jiang, Preparation and characterization of spindle-like Fe_3O_4 mesoporous nanoparticles, *Nanoscale Research Letters*, 2011, **6**, 1-9.

30. G. A. B. Confalonieri, P. Szary, D. Mishra, M. J. Benitez, M. Feyen, A. H. Lu, L. Agudo, G. Eggeler, O. Petracic and H. Zabel, Magnetic coupling mechanisms in particle/thin film composite systems, *Beilstein J. Nanotechnol.*, 2010, **1**, 101-107.

31. H. Chen, D. C. Colvin, B. Qi, T. Moore, J. He, O. T. Mefford, F. Alexis, J. C. Gore and J. N. Anker, Magnetic and optical properties of multifunctional core-shell radioluminescence nanoparticles, *J. Mater. Chem.*, 2012, **22**, 12802-12809.

32. M. B. McBride, *Environmental chemistry of soils*, Oxford university press, 1994.

33. A. Zach-Maor, R. Semiat and H. Shemer, Adsorption–desorption mechanism of phosphate by immobilized nano-sized magnetite layer: Interface and bulk interactions, *J. Colloid Interface Sci.*, 2011, **363**, 608-614.

Chapter Seven

Continuous Flow Vortex Fluidic Synthesis of Silica Xerogel as a Delivery Vehicle for Curcumin

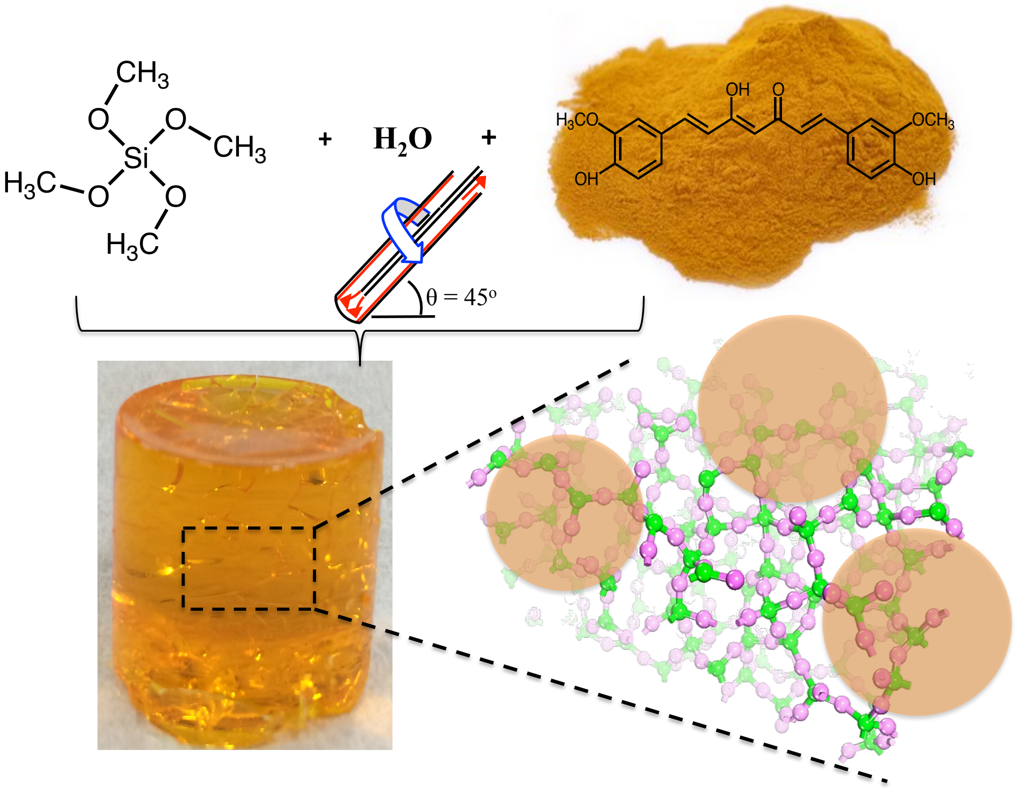

This chapter is reformatted from a paper published in ***RSC Advances***, 2015, **5**, 7953-7958.

Abstract

Sol-gel synthesis of silica xerogel at room temperature is effective using a vortex fluidic device operating under scalable continuous flow conditions, using only tetramethyl orthosilicate as the silica precursor and deionized water. The gelation time of the hydrogel can be as short as 3.5 hours depending on the concentration of the silica. This process is also effective in incorporating preformed sub-micron particles of curcumin, as an effective vehicle for bioavailability of this compound, which was shown by antimicrobial activity against *Staphylococcus aureus*.

7.1. Introduction

Solution-gelation ("sol-gel") technology has been known for decades and it is widely applied for fabricating silica materials. Tetraalkoxysilanes ($SiOR_4$) such as tetraethyl orthosilicate (TEOS) and tetramethyl orthosilicate (TMOS) are commonly used as precursors for preparing monolithic silica or silicate glasses,[1, 2] with the sol-gel reactions involving hydrolysis of alkoxysilanes, followed by room temperature condensation, which is summarized in equations (1–3).[3, 4]

Hydrolysis:

$$Si(OR)_4 + 4H_2O \rightarrow Si(OH)_4 + 4ROH \qquad (7.1)$$

Alcohol condensation:

$$Si(OH)_4 + Si(OR)_4 \rightarrow (OH)_3Si{-}O{-}Si(OR)_3 + ROH \qquad (7.2)$$

Water condensation:

$$Si(OH)_4 + Si(OH)_4 \rightarrow (OH)_3Si{-}O{-}Si(OH)_3 + H_2O \qquad (7.3)$$

Alkoxysilanes are hydrophobic and are only sparingly soluble in water. In general they react slowly with water,[5] although this can be overcome in the presence of ethanol or methanol as a bridging medium. The sol-gel process involves lengthy hydrolysis and condensation, taking up to 1000 hours of gelation for TEOS,[1, 5] with the presence of acid or base speeding up the process.[4, 5] There is limited information available on producing either monolithic silica or silicate glasses without adding acid or base, while achieving a rapid gelation time with appreciable Brunauer–Emmett–Teller (BET) surface area and pore volume. Avnir *et al.* established that rapid gelation of monolithic porous silica can be achieved without the addition of alcohol, however, no characterization data of the solid is available.[6] In addition, Dai *et al.* established that no appreciable pore volume is present in the resulting silica material if only water is used as the reaction medium during the sol-gel process.[2]

Silicate glasses produced *via* sol-gel processing can be used in optical devices due to their excellent transparency,[7, 8] and as delivery vehicles for drugs,[9, 10] and biologically active molecules.[11] *In situ* synthesis of silica gel incorporating different compounds as such a delivery vehicle is challenging given the use of rather constraining conditions which feature in the hydrogel processing.[9] Typically, drug loading into silica is carried out as a multi-step batch process. For example, Smirnova *et al.* have developed a 72 hour, two step synthesis of an aerogel involving the use of acid and base, followed by loading the drugs ketoprofen and griseofulvin under supercritical conditions.[9] Other compounds could also benefit from being incorporated into silica. The bioavailability of curcumin (Figure 7.1), which is derived from the plant *Curcuma longa*, is an ideal compound for incorporation. Curcumin has anti-cancer, anti-oxidant, anti-inflammatory, anti-bacterial, and anti-carcinogenic properties, and is often regarded as a model nutraceutical/molecular pharmaceutical for drug delivery applications.[12-17] Despite such remarkable properties, it suffers from low water solubility and bioavailability, and extreme sensitivity at physiological pH.[12, 13, 18] Zhao *et al.* have developed a novel synthesis of mesoporous silica nanoparticles, for *in vivo* release of curcumin to zebrafish larvae, in developing a system for the treatment of heart failure.[17]

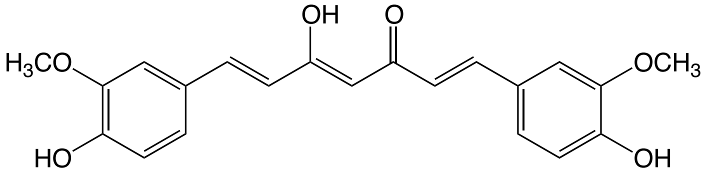

Figure 7.1. *Chemical structure of curcumin.*

The research reported in this chapter focuses on using the recently developed vortex fluidic device (VFD),[11] for carrying out sol-gel processing at room temperature. This avoids the use of alcohol or an acid or base catalyst, with *in situ* incorporation of curcumin particles, which were preformed also using the VFD. The use of the VFD under scalable continuous flow conditions results in much faster kinetics, and offers scope for carrying out reactions under turbulent flow, beyond the limits of a diffusion control. Remarkably the use of the

VFD imparts significant pore volume in the resulting silica, as judged by high BET surface area, in the absence of an organic solvent. Moreover, the use of the VFD avoids the inherent difficulty of traditional batch processing where uneven mass and heat transfer can result in non-uniform processing/products.[19, 20] Overall, the sol-gel processing in the present study is high in green chemistry metrics, in minimising the use of a solvent and auxiliary reagents, and operating the process at room temperature, which is an integral part of developing more benign processes in the anthropocene era.

In an earlier chapter I established that ordered mesoporous silica is readily prepared using a VFD, also operating under continuous flow conditions, at room temperature, thus avoiding long hydrothermal processing times, with the intense shear in the dynamic thin film effective in controlling the pore size, as well as the pore wall thickness.[21] VFD is a versatile microfluidic platform, with processing capabilities also in controlling chemical reactivity and selectivity in organic synthesis,[20, 22-25] exfoliating graphene from graphite,[26] forming graphene-algae hybrid materials,[27, 28] controlling the growth of palladium nanoparticles on carbon nano-onions,**[29]** and controlling the polymorphs of calcium carbonate.[30]

In generating silica hydrogels, deionized Milli-Q water and TMOS were introduced into the base of a rapidly rotating glass tube (borosilicate NMR tube) inclined at an angle relative to the horizontal position via two separate feed jets (Figure 7.2). The high shear generated within the thin film in the VFD is able to overcome the otherwise immiscibility of the two liquids, indeed in forming what appears to be a single phase. This intense micro-mixing and the viscous drag as the liquid whirls up the tube facilitates the reaction, as does the mechanoenergy within the Stewartson-Ekman layers arising from the liquid being driven up the rotating tube with gravity forcing the liquid back.[31] The inclination angle of the tube was set at 45^o, Figure 7.2, given that this has been shown to be the optimum angle for all the aforementioned applications of the VFD.

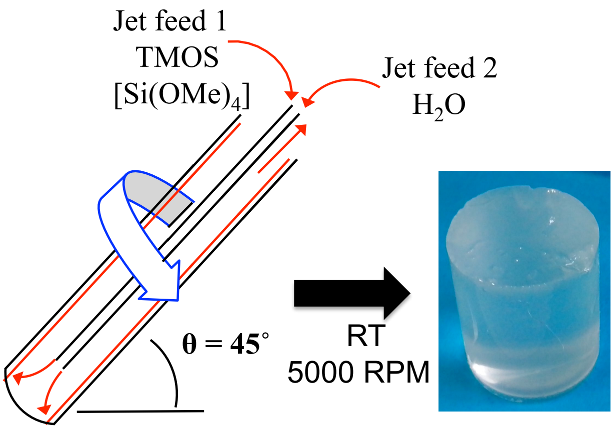

Figure 7.2. *Schematics of the synthesis of silica hydrogels.*

7.2. Experimental

7.3.1. Preparation of silica hydrogel

Silica hydrogel was prepared using the VFD under continuous flow. Tetramethyl orthosilicate (TMOS, Sigma Aldrich) was used without purification and was fed through one feed jet and Milli-Q water fed though another feed jet, with the flow rate in the range 0.8 – 1. 2 mL/min. The molar ratio of H_2O/Si for final sample was adjusted by modulating the volumetric flow rate of both feed jets. The gel samples were subsequently dried in an oven at 110 ˚C overnight and crushed into powder using a mortar and pestle, for further characterizations.

7.3.2. Preparation of curcumin nanoparticles

Curcumin 108 mg was dissolved in 7 mL of ethanol. This solution was then fed into vortex fluidic device (VFD) at ~ 0.6 mL/min though feed jet 1 with Milli-Q water fed through a second feed jet at volumetric flow rate of 1.5 mL/min, while the 18 mm internal diameter borosilicate glass tube (NMR tube) was spun at 5000 rpm at a tilt angle of 45 ˚. The product was collected and then placed in a Rotavac for 5 min to remove the ethanol. The curcumin nanoparticles are well dispersed in water and ready to be used in the silica hydrogel synthesis.

7.3.3. Preparation of curcumin loaded silica hydrogel

This followed a similarly procedure as used for the synthesis of the above silica hydrogel, except the Milli-Q water was replaced by the as formed freshly prepared suspension of curcumin particles. The molar ratio of H_2O/Si in the final product was fixed at 8:1. The final gel sample was dried using a Rotavac, with bath temperature set at 60 ˚C, for 30 min and the solid then converted to a powder using a mortar and pestle. These conditions minimize the likelihood of degradation of curcumin.

7.3.4. Preparation of agar for bacteria growth inhibition test

After removal of the ethanol, the as prepared suspension of curcumin was diluted with Milli-Q water in 15 mL tubes at concentrations from 209 μg.mL^{-1} to 1047 μg.mL^{-1}. Mueller Hinton agar was then added to give a final volume of 10 mL.

Silica powder and powdered curcumin/SiO_2 were added to 15 mL tubes and Mueller Hinton agar was added and mixed to give a final volume of 10 mL. The final curcumin concentration for the curcumin/SiO_2 sample was adjusted to range from 60 μg.mL^{-1} to 300 μg.mL^{-1}. The agar plates were allowed to set and dried for 30 mins at room temperature prior to use.

7.3.5. Characterization techniques

Nitrogen adsorption-desorption studies were performed using a Micromeritics TriStar^{TM} II 3020 system. The samples were outgassed at 110 °C for 16 hours prior to gas adsorption which was carried out at 77 K. The specific surface area, S_{BET}, was determined from the linear part of the Brunauer-Emmett-Teller (BET) equation ($P/P_o = 0.05 – 0.30$). The pore size distribution and pore volume were evaluated using the Barrett–Joyner–Halenda (BJH) method. The total pore volume reported was taken from the amount of gas adsorbed at a relative pressure (P/P_o) at 0.996.

Fourier Transform Infra-Red (FTIR) spectra were recorded on a Nicolet Nexus 870 FT-IR, equipped with a Thermo Scientific ATR-IR 'Smart Orbit Attachment'. The data was collected at 4 cm^{-1} resolution with 64 scans at room temperature.

^{29}Si MAS NMR was performed using a Bruker 400 instrument, single pulse at 5000 Hz rotating speed to determine the poly-condensation degree of the silica. Calculation method is described in Chapter 2, under section 2.3.5 (equation 2.12).

Dynamic light scattering (DLS) measurements were collected using a Malvern Instrument 'High Performance Particle Sizer' model HPP5001. The measurements were performed at room temperature and 10 measurements were taken for each run for 3 runs in total. Correlation data was analyzed using the Malvern Instrument software.

Scanning electron microscopy (SEM) images of curcumin nanoparticles were obtained using a FEI Quanta 450 FEG Environmental Scanning Electron Microscope (ESEM), operating at an accelerating voltage of 5 kV with secondary electron detector under high vacuum. A 5 nm thickness of platinum coating was applied onto the sample surface using Quorumtech K575X sputter coater prior to imaging.

The concentration of curcumin in the final samples was determined using two methods, involving the use of a Varian Cary Eclipse Fluorimeter and Simultaneous Thermal Analyzer (STA), to compare the consistency. For fluorimeter studies, the excitation wavelength was set at 510 nm and emission wavelength at 555 nm. Standard solutions of known curcumin concentration were prepared by dissolving curcumin in ethanol. A calibration curve was plotted by linear fit correlation and the final concentration of curcumin in the sample was determined using the calibration fit equation.

Sample calculation for curcumin content using fluorescence spectroscopy:

A series of known concentration of curcumin solutions in ethanol were prepared and used to obtain a calibration curve, giving a linear equation:

$y = 215.83\ x + 3.1777$ with linear regression $R^2 = 0.9521$; where x is the curcumin concentration in $mg.mL^{-1}$.

The curcumin was extracted from 0.3054 g of agar/composite curcumin/SiO_2 in ethanol, for then recording the fluorescence spectra, affording a concentration of curcumin at 71 $\mu g.mL^{-1}$.

The weight of agar nutrient solution was 9.0 g and 1.25 g curcumin/SiO_2 composite was added:

% Composite silica with curcumin = 1.25/10.25 × 100% = 12.20%

Thus, total weight of composite silica with curcumin in 0.3054 g of gel is:

0.3054 g × 12.20% = 37.26 mg

Therefore, weight percent of curcumin in the composite sample is:

0.071/37.26 × 100% = 0.19% w/w

STA combines thermo-gravimetric analysis (TGA) and differential scanning calorimetry (DSC) for analysis of the thermal properties of inorganic and organic materials. Sample was heated under nitrogen from 30 to 600 ˚C, with the temperature increment rate at 10 ˚C/min.

7.3. Results and Discussion

Studies were undertaken on gelation time post VFD processing, for different silica to water molar ratios, as well as on the effect of using different rotational speeds for a 18.0 mm internal diameter glass tube housed in the VFD. At 5000 rpm, the time for gelation is the shortest regardless of the molar ratio, with overall gelation times consistently within 3 to 4 hours as judged visually, as opposed to most commonly used method, namely rheological measurements.[32] Typically in rheology measurement, the gelation time is recorded corresponding to the onset of gelation by the sudden increase of storage modulus, *G'*,[33] and visual judgement recorded in our study may be overstated. However, at higher rotational speed, changing the water to silica molar ratio affects the gelation time, with the optimum time at 6000 rpm and 7000 rpm corresponding to a H_2O/Si molar ratio of 10:1, Figure 7.3. The variation in gelation time associated with changing the H_2O/Si molar ratio and rotation speed is based on visual observations, noting that the fluid dynamics within the VFD are inherently complex. This is highlighted by our recent findings of a speed dependent vibration induced Faraday wave in the device which dramatically affects rates of reactions.[34] Nitrogen adsorption-desorption analyses show variation in BET surface area and Barrett–Joyner–Halenda (BJH) pore volume (Table 7.1). The BJH pore volume increased with an increase in water to TMOS molar ratio, and the trend was consistent for different rotational speeds. Overall the change in rotational speed for the process only affects the gelation time of the sample post VFD processing, whereas all the physisorption characteristics remained consistent with variation of the H_2O/Si molar ratio.

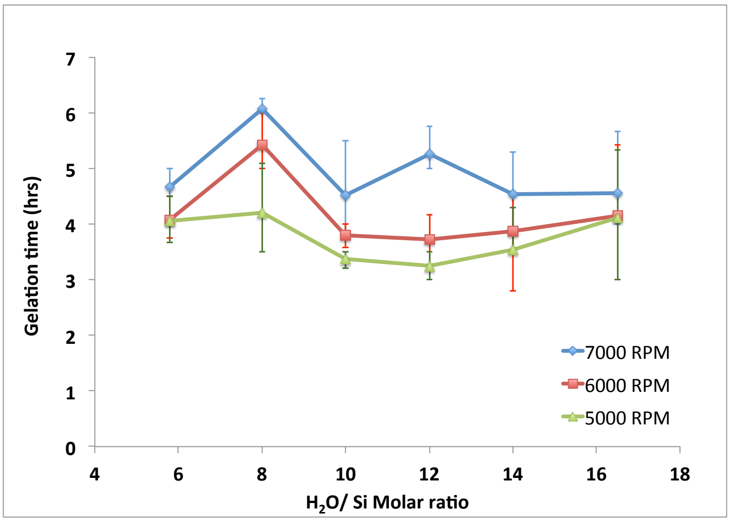

Figure 7.3. *Change in gelation time at different H_2O/Si molar ratios for different rotational speeds (data points in triplicate).*

Table 7.1. Physisorption properties of silica xerogels for different Si/H_2O molar ratios and different rotational speeds on the VFD.

Si/H_2O (mol ratio)	5000 rpm		6000 rpm		7000 rpm	
	S_{BET} (m^2g^{-1})	V_p (cm^3g^{-1})	S_{BET} (m^2g^{-1})	V_p (cm^3g^{-1})	S_{BET} (m^2g^{-1})	V_p (cm^3g^{-1})
1 : 6	646.5	0.39	605.1	0.35	591.3	0.38
1 : 8	590.7	0.32	565.4	0.31	578.0	0.32
1 : 10	566.1	0.31	612.1	0.34	616.4	0.34
1 : 12	624.7	0.35	646.6	0.36	649.6	0.36
1 : 14	718.6	0.40	713.2	0.40	729.6	0.40
1 : 16.5	764.1	0.48	752.4	0.44	804.1	0.48

* S_{BET}, BET total surface area determined from N_2 adsorption desorption; V_p, total pore volume determined from BJH adsorption at relative pressure of 0.996.

For comparing VFD and batch processing, a sample was prepared using conventional batch processing for the same molar ratio of water to silica at 8:1, with the TMOS and deionized Milli-Q water added into a round-bottom flask via two separate feed jets. The solution was stirred at room temperature for 8 min, and the onset of gelation was monitored, which was found to be in excess of 9 hours. The BET surface area of this sample is 459.8 $m^2.g^{-1}$ and pore volume of 0.25 $cm^3.g^{-1}$, both being significantly less than for the material using VFD. FTIR spectra of this batch derived silica xerogel, and that derived from VFD processing, along with that of TMOS itself are shown in Figure 7.4. Both silica xerogel samples show common bands assigned to various vibrations in the gel network. The intense band at 1050 – 1200 cm^{-1} is assigned to Si–O–Si asymmetric stretching vibrations. The symmetric stretching vibrations of Si–O–Si appears at 790 cm^{-1}, with the expected in-plane stretching vibrations of the silanols Si–OH groups at 940 cm^{-1}.[35, 36] Both samples were devoid of any peaks corresponding to –CH vibrations arising from incomplete hydrolysis and condensation. This is despite the short processing time using the VFD, where under continuous flow processing, the residence time for a finite amount of liquid moving along the tube is approximately 3 min. ^{29}Si NMR data show that the xerogel derived from using the VFD has 95% degree of condensation, which is higher compared to the batch process derived xerogel, at 89%, despite the dramatic difference in gelation time.

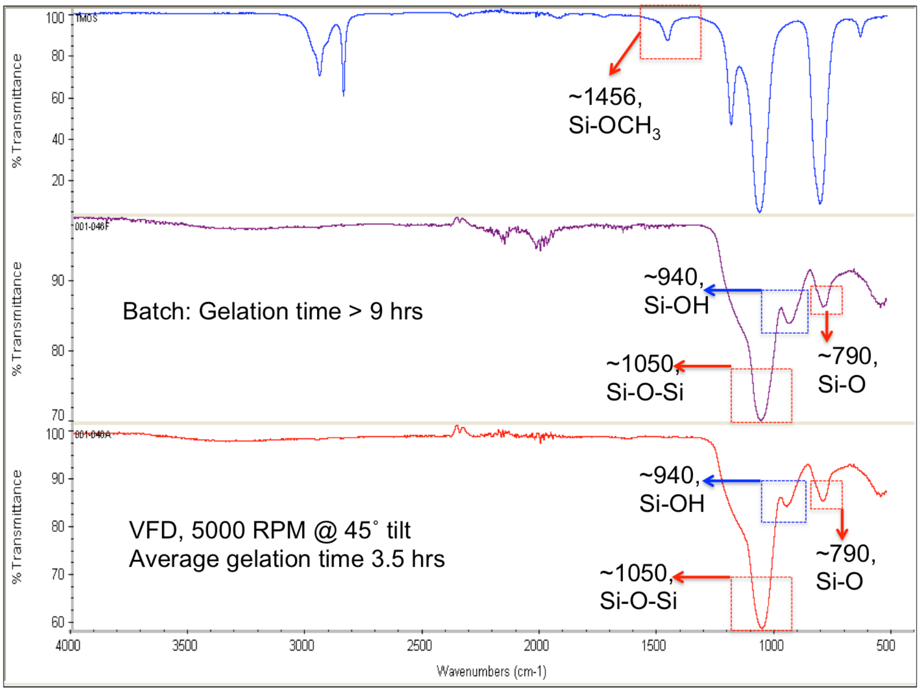

Figure 7.4. *FTIR spectra of TMOS, batch processed silica xerogel, and VFD processed silica xerogel.*

While curcumin is only sparingly soluble in water, it dissolves in organic solvents, and we used this property to form sub-micron size particles of the compound for subsequent incorporating into silica, and possibly for enhanced bioavailability. Initially the curcumin was dissolved in ethanol and introduced into the VFD through one jet feed with excess deionized water added through a second jet feed, also as a continuous flow process. The molar ratio of H_2O: ethanol was fixed at 8:1, with the resulting curcumin in the form of a colloidal suspended in the solvent mixture. Dynamic light scattering (DLS) gave a mean hydrodynamic diameter of 465 nm (Figure 7.5), which is consistent with the estimated particle sizes from scanning electron micrograph (SEM) ranging from 300 – 470 nm (Figure 7.6). Much smaller particles of curcumin ~50 nm in diameter, stabilised by surfactants, are accessible using related rotating tube processing, involving acid-base precipitation.[15] Amorphous spheroidal curcumin precipitates 30 – 40 nm in diameter have been prepared also using the anti-solvent approach with a micromixer, but they agglomerate into *ca.* 140 nm particles, eventually forming needle-shaped curcumin crystals.[37] This finding agrees with our x-ray powder diffraction (XRD) data, with the particles of curcumin formed using the anti-solvent approach on the VFD becoming crystalline on standing, but the curcumin particles embedded in silica immediately after fabrication remain amorphous, Figure 7.7.

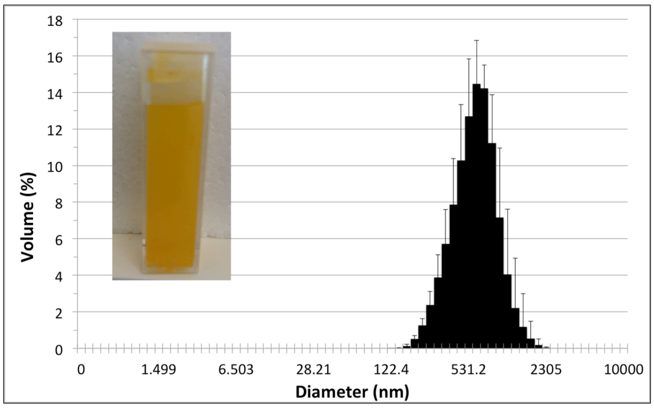

Figure 7.5. *Bar graph of the particle sizes distribution with +/- 1 standard deviation error bars for curcumin particles suspended in Milli-Q water after VFD processing (inset).*

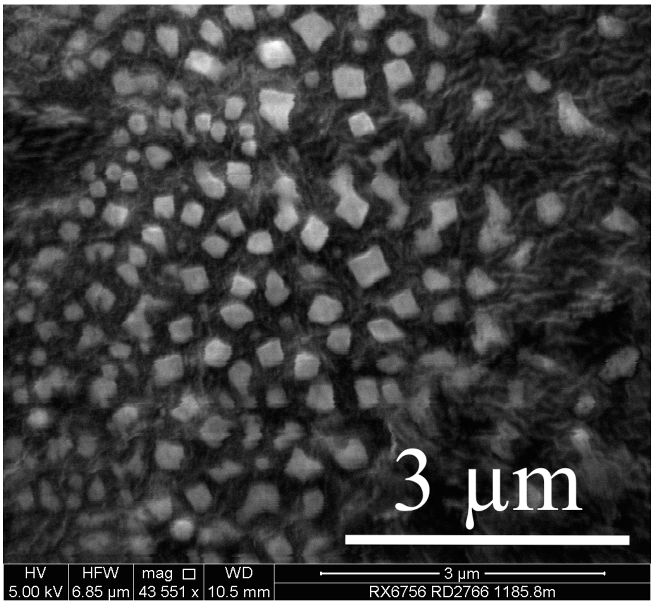

Figure 7.6. *SEM image of curcumin particles prepared using the VFD. A suspension of the particles in deionized water was drop cast onto carbon tape and dried under air.*

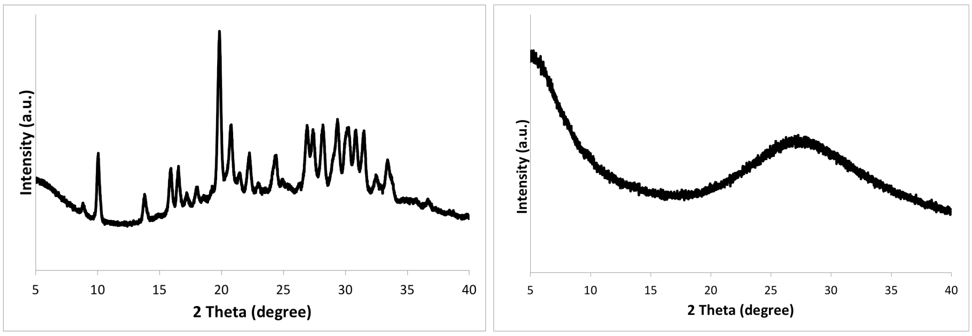

Figure 7.7. *X-ray diffraction pattern of (left) crystalline curcumin and (right) silica xerogel loaded with curcumin.*

The colloidal suspension of curcumin was used to prepare composite silica hydrogel, using a similar procedure to that used for the material devoid of curcumin, as discussed above. TMOS was fed into the same VFD through one jet feed and the curcumin particles suspended in water in another jet fed, which served also as the aqueous medium for the hydrolysis and condensation of TMOS. The volumetric feed rate for these reactants was set at 0.6 mL/min. The molar ratio of H_2O/Si was fixed at 8:1, in order to compare the gelation time with the aforementioned silica gel synthesis. The samples were collected in a vial and allowed to stand at room temperature (~20 ˚C) for gelation. The collected sample was clear orange with no obvious individual curcumin particles present (Figure 7.8). Gelation time of this sample was 8 hours, with the longer gelation time presumably arising from the curcumin particles affecting the growth of silica network. The gel sample was then dried *in vacuo* at 60 ˚C to remove methanol generated during the synthesis of the silica, whereupon the material was ground using a mortar and pestle into a fine powder.

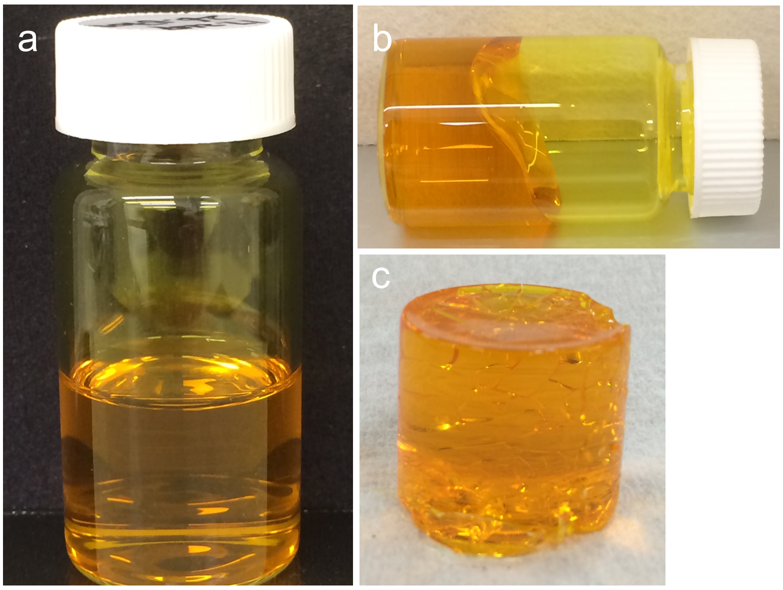

Figure 7.8. *Curcumin loaded silica hydrogel (a) initial appearance from the VFD; (b) partial gelation; and (c) curcumin/SiO_2 gel. The sample was prepared with the VFD operating at 5000 rpm at 45˚ tilt.*

Fluorescence microscopy images identified the presence of curcumin particles, encapsulated within the silica network, and the particle size appears uniform (Figure 7.9). Encapsulation of curcumin in mesoporous silica with a multi-step self-assembly approach has been reported by initially forming an aggregated micellar rods involving the use of surfactant, then loading the curcumin, and lastly hydrolysis of tetraethoxysilane under acidic conditions.[38] This material is effective in the controlled release of curcumin under physiological pH, with photo-stability of the compound within the silica matrix. In the present study, we explored the utility of the composite material for antibacterial activity based on the release of curcumin.[16, 37]

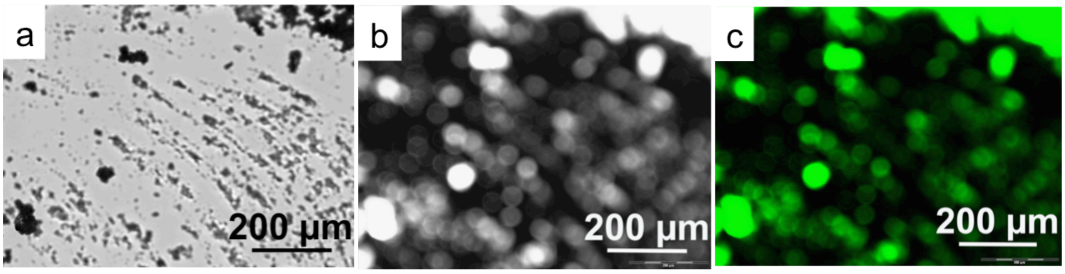

Figure 7.9. *Optical microscopy image of curcumin/SiO$_2$ composite material, (b) bright field image, and (c) fluorescence image.*

The Gram positive bacterium *Staphylococcus aureus* was grown overnight on Mueller Hinton agar at 37 ˚C. Fresh bacterial colonies were then inoculated into Mueller Hinton broth to give a final optical density of 0.01 at an absorbance of 600 nm. Starting with 10^8 colony forming unit (cfu)/mL, bacterial cultures were serially diluted 1:10 into phosphate buffer saline (PBS) and 5 µL of the diluted OD 0.01 bacterial suspension was spotted onto the selective Mueller Hinton agar plates. The bacterial suspension was allowed to dry and the plates were incubated overnight (16 hours) at 37 ˚C. Firstly, a control test was carried out to verify that silica xerogel has no effect on bacteria growth inhibition. Here 1 g of silica powder was added as a dry powder to 15 mL tubes and Mueller Hinton agar was added and mixed to give a final volume of 10 mL. Then 8 different concentrations of bacteria were spotted onto the surface and incubated. After 16 hours, bacterial growth was observed (Figure 7.10). This result indicated that the as-synthesized silica powder devoid of curcumin is non-toxic and has no antimicrobial capability.

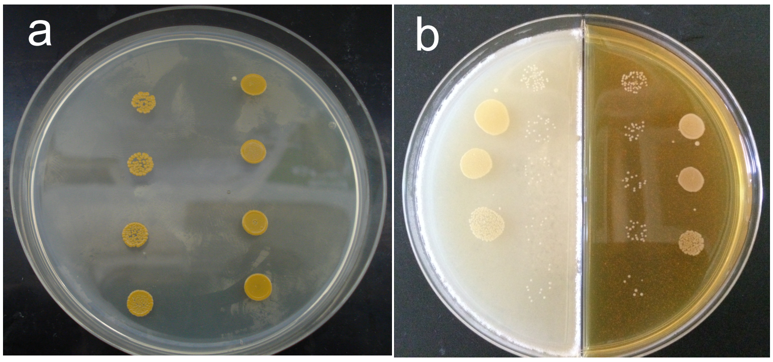

Figure 7.10. *Bacterial growth inhibition test; (a) growth on agar only, (b) growth with 1 g of silica xerogel (left), and a suspension of curcumin particles, with the curcumin at 194 µg.mL^{-1} (right).*

Five different concentrations of curcumin/SiO$_2$ composite and curcumin sub micro-particles suspension (CNPS) were than prepared for the same growth test. The concentration of the curcumin in the sample was determined using two different methods, fluorescence spectroscopy and simultaneous thermal analyser (STA), to compare the integrity of the analysis results. Interpolated data from a linear calibration curve using fluorescence spectroscopy gave 0.19% w/w curcumin in the composite sample (calculation shown under characterization section). STA analysis revealed an endothermic peak at 172 ˚C in the differential scanning calorimetry (DSC) curve, which corresponds to the melt temperature of curcumin.[39, 40] Thermo-gravimetric analysis (TGA) gave 0.24% w/w curcumin present in the composite material (Figure 7.11). Both results are reasonably consistent and the higher limit of 0.24% w/w was used for the determination of curcumin concentration in the composite sample for the bacterial growth inhibition test.

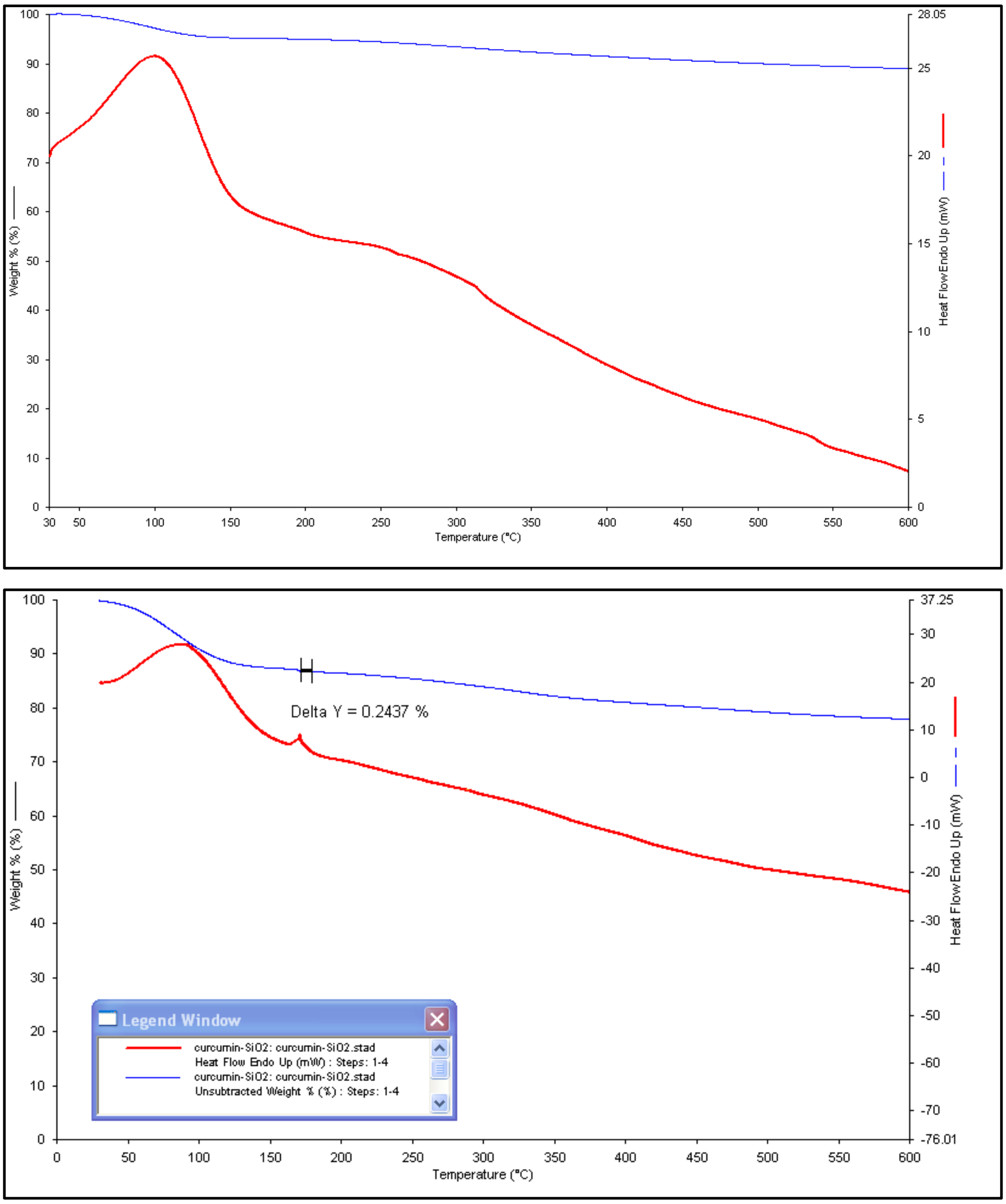

Figure 7.11. *STA plot of silica xerogel devoid of curcumin showing a small weight loss associated with surface hydroxyl groups (top), an endotherm peak at 172 – 179 ˚C , consistent with the decomposition of curcumin in the composite material (bottom).*

Here 0.25 g, 0.50 g, 0,75 g, 1.0 g, and 1.25 g of curcumin/SiO_2 powder, with curcumin concentration of 60, 120, 180, 240 and 300 µg.mL^{-1} respectively, were added and mixed with the Mueller Hinton agar (left side of the Mueller Hinton agar plates) (Figure 7.12). On the right side, different concentrations of CNPS were prepared for performance comparison (Figure 7.12). The curcumin concentrations were 209, 418, 628, 838, and 1047 µg.mL^{-1} respectively (Figure 7.12). For the curcumin/SiO_2 sample, a partial inhibition of the bacterial growth is seen at curcumin concentrations as low as at 120 µg.mL^{-1} (Figure 7.12(b), left), with a more pronounced effect at a concentration of 180 and 240 µg.mL^{-1} (Figure 7.12 (c,d), left). Total growth inhibition is achieved at a concentration of 300 µg.mL^{-1} (Figure 7.12 (e), left). In contrast, the CNPS also showed mild inhibition starting at 628 µg.mL^{-1} (Figure 7.12 (c), right) and full inhibition at 1047 µg.mL^{-1} (Figure 7.12(e), right). Thus, the curcumin/SiO_2 composite outperformed the curcumin particles by four fold for the bacterial growth inhibition tests (Table 7.2).

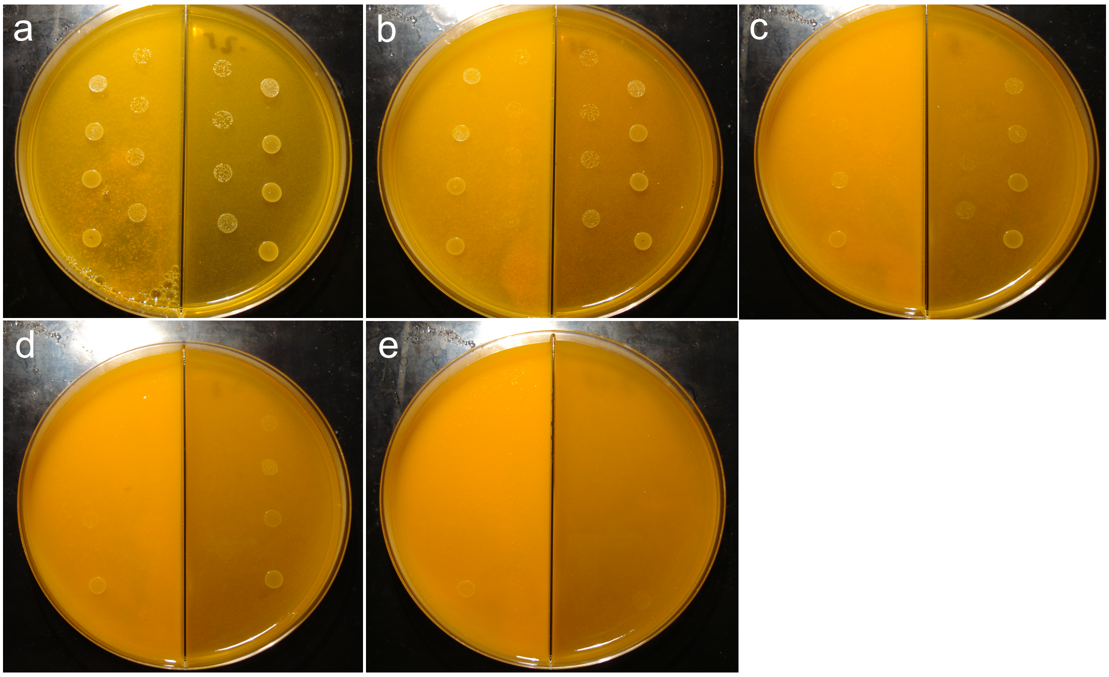

Figure 7.12. *Bacterial growth inhibition test on Mueller Hinton agar plates with curcumin/SiO_2 composite powder added on the left hand side, and CNPS added on the right hand side with concentrations of (a) 60 / 209 µg.mL^{-1}, (b) 120 / 419 µg.mL^{-1}, (c) 180 / 628 µg.mL^{-1}, (d) 240 / 838 µg.mL^{-1}, and (e) 300 / 1047 µg.mL^{-1}.*

Table 7.2. *Staphylococcus aureus* bacteria growth inhibition test comparison.

Sample: Curcumin/SiO_2 composite		Sample: Suspension of curcumin particles	
Curcumin concentration	Inhibition*	Curcumin concentration	Inhibition*
60	None	209	None
120	Mild	419	None
180	6/8	628	2/8
240	7/8	838	4/8
300	Full	1047	Full

* The inhibition numbers show in term of fraction, referring to the successful growth inhibition number out of 8 dilutions.

The improved inhibition of bacterial growth by curcumin in the composite material may be due to the silica network shielding the curcumin from degradation, prior to release/bioavailability. Alternatively, the porous network of silica enhances the adsorption process, allowing the curcumin to slowly diffuse and thus, improves its bioavailability. The shielding is evident by comparing the same sample over a longer period of time. When the 1.0 g and 1.25 g samples were incubated for 48 hours, the bacteria grew fully on the CNPS whereas the curcumin/SiO_2 composite still showed growth inhibition at lower bacterial concentrations, Figure 7.13.

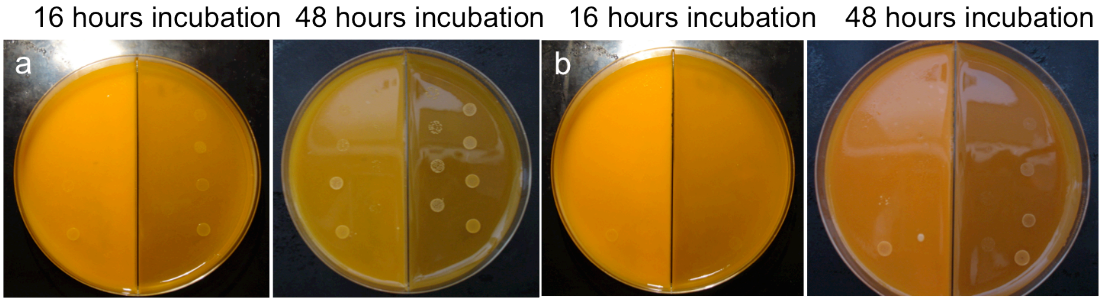

Figure 7.13. *Bacterial growth inhibition for longer incubation periods; (a) 240 / 838 µg.mL^{-1}, and (b) 300 / 1047 µg.mL^{-1}.*

7.4. Conclusions

A benign aqueous synthesis of silica hydrogel has been developed, which is without precedence in terms of a significantly reduced processing time, without the need for a solvent or the addition of an acid or base. Moreover, the same processing can be used for *in situ* incorporation of curcumin particles into the silica. This composite material showed better performance in bacterial growth inhibition compared to neat curcumin. The silica network appears to provide an excellent shielding to the curcumin particles, and better control in diffusion and thus improved bioavailability of this multi-medicinal functional compound. The simplicity of this process greatly promotes the use of silica as a drug delivery vehicle, in minimising the use of chemicals involved throughout the process. Future work can be done in substituting different drugs using the same procedure, along with the general application of the ability to make silica under more benign processing conditions, and presumably involving less energy input, while significantly reducing the generation of waste.

The composite material can be further functionalized by introducing different sources of silica precursor such as mercaptopropyl-trimethoxysilane, aminopropyltrimethoxysi-lane, and vinyltriehtoxysilane during the synthesis, in undergoing co-condensation, instead of post-grafting method. The silica hydrogel is hydrophilic due the –OH group on the surface, and functionalizing the surface of the silica will change the hydrophobicity of the material and thus expand the applications, which will be the focus of further studies.

The high surface tension of the pore liquid in the present study may lead to cracking and shrinkage during the drying process due to the capillary pressure and condensation of surface silanol groups.[40] However, this can be overcome by using supercritical CO_2 drying,[41, 42] solvent exchange,[42, 43] or liquid–paraffin–medium solvent evaporation.[44]

7.5. Acknowledgement

Support from the Government of South Australia, the Australian Research Council and National and Medical Research Council of Australia is gratefully acknowledged, as is Haniff Wahid's fluorescence microscopy help.

7.6. References

1. K. Kajihara, Recent advances in sol–gel synthesis of monolithic silica and silica-based glasses, *J. Asian Ceram. Soc.*, 2013, **1**, 121-133.

2. S. Dai, Y. H. Ju, H. J. Gao, J. S. Lin, S. J. Pennycook and C. E. Barnes, Preparation of silica aerogel using ionic liquids as solvents, *Chem. Commun.*, 2000, 243-244.

3. F. Surivet, M. Lam Thanh, J. P. Pascault and T. Pham Quang, Organic-inorganic hybrid materials. 1. Hydrolysis and condensation mechanisms involved in alkoxysilane-terminated macromonomers, *Macromolecules*, 1992, **25**, 4309-4320.

4. C. J. Brinker, Hydrolysis and condensation of silicates: Effects on structure, *J. Non-Cryst. Solids*, 1988, **100**, 31-50.

5. M. A. Fardad, Catalysts and the structure of SiO_2 sol-gel films, *J. Mater. Sci.*, 2000, **35**, 1835-1841.

6. D. Avnir and V. R. Kaufman, Alcohol is an unnecessary additive in the silicon alkoxide sol-gel process, *J. Non-Cryst. Solids*, 1987, **92**, 180-182.

7. M. C. Kyung, in *Optical Devices in Communication and Computation*, ed. P. Xi, InTech, 2012, ch. 10, p. 230.

8. R. Ciriminna, A. Fidalgo, V. Pandarus, F. Béland, L. M. Ilharco and M. Pagliaro, The Sol–Gel Route to Advanced Silica-Based Materials and Recent Applications, *Chem. Rev.*, 2013, **113**, 6592-6620.

9. I. Smirnova, S. Suttiruengwong and W. Arlt, Feasibility study of hydrophilic and hydrophobic silica aerogels as drug delivery systems, *J. Non-Cryst. Solids*, 2004, **350**, 54-60.

10. U. Guenther, I. Smirnova and R. H. H. Neubert, Hydrophilic silica aerogels as dermal drug delivery systems – Dithranol as a model drug, *Eur. J. Pharm. Biopharm.*, 2008, **69**, 935-942.

11. S. Radin, S. Bhattacharyya and P. Ducheyne, Nanostructural control of the release of macromolecules from silica sol–gels, *Acta Biomater.*, 2013, **9**, 7987-7995.

12. P. Anand, A. B. Kunnumakkara, R. A. Newman and B. B. Aggarwal, Bioavailability of Curcumin: Problems and Promises, *Mol. Pharmaceut.*, 2007, **4**, 807-818.

13. M. M. Yallapu, M. Jaggi and S. C. Chauhan, Curcumin nanoformulations: a future nanomedicine for cancer, *Drug Discov. Today*, 2012, **17**, 71-80.

14. S. Jambhrunkar, S. Karmakar, A. Popat, M. Yu and C. Yu, Mesoporous silica nanoparticles enhance the cytotoxicity of curcumin, *RSC Adv.*, 2014, **4**, 709-712.

15. S. Dev, P. Prabhakaran, L. Filgueira, K. S. Iyer and C. L. Raston, Microfluidic fabrication of cationic curcumin nanoparticles as an anti-cancer agent, *Nanoscale*, 2012, **4**, 2575-2579.

16. P. S. Negi, G. K. Jayaprakasha, L. Jagan Mohan Rao and K. K. Sakariah, Antibacterial Activity of Turmeric Oil: A Byproduct from Curcumin Manufacture, *J. Agric. Food. Chem.*, 1999, **47**, 4297-4300.

17. H. Yan, C. Teh, S. Sreejith, L. Zhu, A. Kwok, W. Fang, X. Ma, K. T. Nguyen, V. Korzh and Y. Zhao, Functional Mesoporous Silica Nanoparticles for Photothermal-Controlled Drug Delivery In Vivo, *Angew. Chem. Int. Ed.*, 2012, **51**, 8373-8377.

18. A. Goel, S. Jhurani and B. B. Aggarwal, Multi-targeted therapy by curcumin: how spicy is it?, *Mol. Nutr. Food Res.*, 2008, **52**, 1010-1030.

19. X. Chen, N. M. Smith, K. S. Iyer and C. L. Raston, Controlling nanomaterial synthesis, chemical reactions and self assembly in dynamic thin films, *Chem. Soc. Rev.*, 2014, **43**, 1387-1399.

20. L. Yasmin, K. A. Stubbs and C. L. Raston, Vortex fluidic promoted Diels–Alder reactions in an aqueous medium, *Tetrahedron Lett.*, 2014, **55**, 2246-2248.

21. C. L. Tong, R. A. Boulos, C. Yu, K. S. Iyer and C. L. Raston, Continuous flow tuning of ordered mesoporous silica under ambient conditions, *RSC Adv.*, 2013, 18767-18770.

22. L. Yasmin, T. Coyle, K. A. Stubbs and C. L. Raston, Stereospecific synthesis of resorcin[4]arenes and pyrogallol[4]arenes in dynamic thin films, *Chem. Commun.*, 2013, **49**, 10932-10934.

23. L. Yasmin, X. Chen, K. A. Stubbs and C. L. Raston, Optimising a vortex fluidic device for controlling chemical reactivity and selectivity, *Sci. Rep.*, 2013, **3**, 2282.

24. L. Yasmin, P. K. Eggers, B. W. Skelton, K. A. Stubbs and C. L. Raston, Thin film microfluidic synthesis of fluorescent highly substituted pyridines, *Green Chem.*, 2014, **16**, 3450-3453.

25. M. N. Gandy, C. L. Raston and K. A. Stubbs, Towards aryl C-N bond formation in dynamic thin films, *Org. Biomol. Chem.*, 2014, **12**, 4594-4597.

26. X. Chen, J. F. Dobson and C. L. Raston, Vortex fluidic exfoliation of graphite and boron nitride, *Chem. Commun.*, 2012, **48**, 3703-3705.

27. M. H. Wahid, E. Eroglu, X. Chen, S. M. Smith and C. L. Raston, Entrapment of *Chlorella vulgaris* cells within graphene oxide layers, *RSC Adv.*, 2013, **3**, 8180-8183.

28. M. H. Wahid, E. Eroglu, X. Chen, S. M. Smith and C. L. Raston, Functional multi-layer graphene-algae hybrid material formed using vortex fluidics, *Green Chem.*, 2013, **15**, 650-655.

29. F. M. Yasin, R. A. Boulos, B. Y. Hong, A. Cornejo, K. S. Iyer, L. Gao, H. T. Chua and C. L. Raston, Microfluidic size selective growth of palladium nano-particles on carbon nano-onions, *Chem. Commun.*, 2012, **48**, 10102-10104.

30. R. A. Boulos, F. Zhang, E. S. Tjandra, A. D. Martin, D. Spagnoli and C. L. Raston, Spinning up the polymorphs of calcium carbonate, *Sci. Rep.*, 2014, **4**.

31. D. A. Bennetts and L. M. Hocking, On Nonlinear Ekman and Stewartson Layers in a Rotating Fluid, *Proc R Soc A*, 1973, **333**, 469-489.

32. A. Ponton, S. Warlus and P. Griesmar, Rheological Study of the Sol–Gel Transition in Silica Alkoxides, *J. Colloid Interface Sci.*, 2002, **249**, 209-216.

33. C. Metin, K. Rankin and Q. Nguyen, Phase behavior and rheological characterization of silica nanoparticle gel, *Appl. Nanosci.*, 2014, **4**, 93-101.

34. J. Britton, S. B. Dalziel and C. L. Raston, Continuous flow Fischer esterifications harnessing vibrational-coupled thin film fluidics, *RSC Adv.*, 2015, **5**, 1655-1660.

35. R. Al-Oweini and H. El-Rassy, Synthesis and characterization by FTIR spectroscopy of silica aerogels prepared using several $Si(OR)_4$ and $R''Si(OR')_3$ precursors, *J. Mol. Struct.*, 2009, **919**, 140-145.

36. M. Ochoa, L. Durães, A. Beja and A. Portugal, Study of the suitability of silica based xerogels synthesized using ethyltrimethoxysilane and/or methyltrimethoxysilane precursors for aerospace applications, *J. Sol-Gel Sci. Technol.*, 2012, **61**, 151-160.

37. Y. He, Y. Huang and Y. Cheng, Structure Evolution of Curcumin Nanoprecipitation from a Micromixer, *Cryst. Growth Des.*, 2010, **10**, 1021-1024.

38. N. W. Clifford, K. S. Iyer and C. L. Raston, Encapsulation and controlled release of nutraceuticals using mesoporous silica capsules, *J. Mater. Chem.*, 2008, **18**, 162-165.

39. Bhawana, R. K. Basniwal, H. S. Buttar, V. K. Jain and N. Jain, Curcumin Nanoparticles: Preparation, Characterization, and Antimicrobial Study, *J. Agric. Food. Chem.*, 2011, **59**, 2056-2061.

40. S. Yun, H. Luo and Y. Gao, Superhydrophobic silica aerogel microspheres from methyltrimethoxysilane: rapid synthesis via ambient pressure drying and excellent absorption properties, *RSC Adv.*, 2014, **4**, 4535-4542.

41. H. Tamon, T. Sone and M. Okazaki, Control of Mesoporous Structure of Silica Aerogel Prepared from TMOS, *J. Colloid Interface Sci.*, 1997, **188**, 162-167.

42. P. B. Wagh, R. Begag, G. M. Pajonk, A. V. Rao and D. Haranath, Comparison of some physical properties of silica aerogel monoliths synthesized by different precursors, *Mater. Chem. Phys.*, 1999, **57**, 214-218.

43. R. Miyamoto, Y. Ando, C. Kurusu, H.-z. Bai, K. Nakanishi and M. Ippommatsu, Fabrication of large-sized silica monolith exceeding 1000 mL with high structural homogeneity, *J. Sep. Sci.*, 2013, **36**, 1890-1896.

44. H. Yang, Q. Shi, B. Tian, S. Xie, F. Zhang, Y. Yan, B. Tu and D. Zhao, A Fast Way for Preparing Crack-Free Mesostructured Silica Monolith, *Chem. Mater.*, 2003, **15**, 536-541.

Chapter Eight

Controlling the Morphology of Mesoporous Silica Using a Vortex Fluidic Device

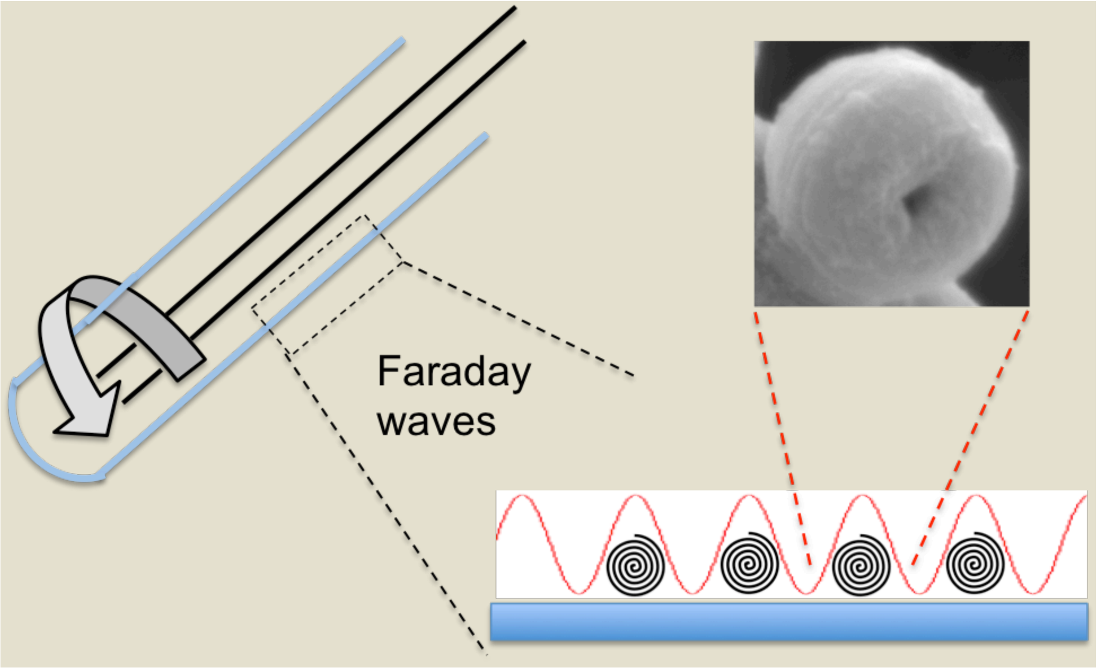

This chapter presents a feasibility study on controlling the morphology of mesoporous silica formed under continuous flow using the VFD.

8.1. Abstract

Surface morphology of SBA-15 can be manipulated by changing the tilt angle of a VFD at a fixed rotational speed of 7000 rpm and a fixed flow rate of 1.0 mL/min. At a rotational speed of 5000 rpm, 1.0 mL/min flow rate, and 45° tilt angle, donut-like SBA-15 particles of the material are formed, ranging from 0.7 to 1.5 μm in diameter, and 300 nm in thickness.

8.2. Introduction

As discussed in Chapter 3, the synthesis of ordered mesoporous silica is effective using a VFD at room temperature and ambient pressure. This method also provides scope for controlling the surface morphology and physicochemical properties of the material, arising from changing the processing parameters of the VFD, in particular the rotational speed and tilt angle. Chapter 3 has revealed that the pore diameter can be tuned by changing the rotational speed at a fixed flow rate, whereas in this Chapter, I investigate the effect of changing the tilt angle on the morphology of mesoporous silica at a fixed rotational speed of 7000 rpm and a fixed flow rate of 1.0 mL/min.

The control of surface morphology of SBA-15 using batch synthesis has required the addition of co-surfactant, co-solvent, or the addition of inorganic salts during the hydrothermal synthesis.[1-3] Zhao *et al*. reported that donut-like SBA-15 can be prepared by using N,N-dimethylformamide (DMF) as a co-solvent. The polar DMF interacts with the amphiphillic copolymer, Pluronic P-123, reducing the local energy of curvature of the silica precursor, tetraethyl orthosilicate (TEOS), resulting in the donut-like macroscopic structure.[1] Katiyar *et al.* employing Zhao's theory, used CTAB as a co-surfactant and ethanol as a co-solvent, to synthesize spheroidal particles of SBA-15 4 to 10 μm in diameter with a pore diameter up to 12.7 nm.[3] The present study focuses on varying the shear within the VFD for controlling the morphology of the product, without the need of surfactants, co-solvents or inorganic salts.

8.3. Experimental

8.3.1. Material preparation

The synthesis of the material followed as previously reported in Chapter 3, section 3.3.1,[4] now changing the tilt angle and comparing the results. The calcined materials are labelled as S-*x*-*y*, where *x* denotes rotational speed and *y* denotes the tilt angle. Based on the studies in Chapter 3, the best mesoregularity product can be obtained under a rotational speed of 7000 rpm. After benchmarking the optimum conditions, all experiments were carried out at 7000 rpm and a flow rate of 1.0 mL/min.

8.3.2. *Sample characterization*

Scanning electron microscopy (SEM) was performed on a Quanta 450 scanning electron microscope at an accelerating voltage of 5 kV. Nitrogen adsorption-desorption measurements were performed on a Micromeritics Tristar II® 3200. The samples were degassed at 473 K for 16 hours and measurements were taken at 77 K. The surface area was calculated based on the Brunauer–Emmett–Teller (BET) method. The pore size distribution and pore volume were evaluated using the Barrett–Joyner–Halenda (BJH) method. Small-angle powder X-ray diffraction (SAXRD) data were collected on a PANalytic Empyrean diffractometer system, using the Nickel-filtered Cu Kα radiation at 40 kV and 40 mA.

8.4. Results and discussion

The underlying chemistry in forming the SBA-15 using the VFD is detailed in Chapter 3. This work follows the same synthetic approach, focusing on the effect of tilt angle on the morphology of SBA-15, studied here using SEM. At a rotational speed of 7000 rpm, the tilt angle was varied from 0° to 60° at 15° intervals. Samples S-7000-0 and S-7000-15 (0 and 15 degrees tilt respectively) had spherical structures, with the particles ranging in size from 2 – 6 µm, Figure 8.1(a) and Figure 8.1(b). As the tilt angle increased, samples S-7000-30 and S-7000-45 (30 and 45 degrees respectively) showed particles with a horseshoe-like morphology, assembled into spheroidal arrays approximately 10 µm in size, Figure 8.1(c) and Figure 8.1(d). At a tilt angle of 60°, sample S-7000-60 showed structures with a ring/toroidal-like morphology randomly interconnected, Figure 8.1(e).

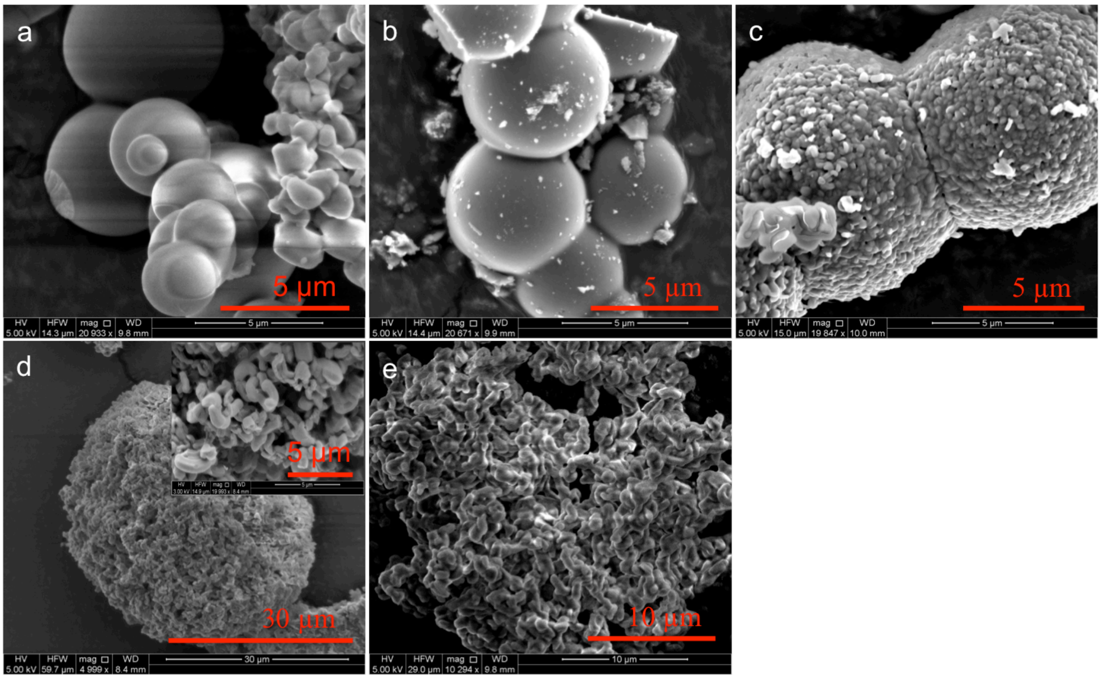

Figure 8.1. *SEM images of SBA-15 synthesized at 7000 rpm, at 0° and 15° tilt angle showing mainly spheroidal structures, (a) and (b), and at 30° and 45° tilt angle showing an horseshoe/bent structures (refer to the inset of Figure 8.1(d)) assembled into spheroidal arrays, (c) and (d), and at 60° tilt angle showing a cluster of intertwined curved structures, (e).*

There were significant changes to the macroscopic structures of the samples, as well as significant effect on their microscopic properties as seen in the large variation in the gad sorption isotherms, the large range in surface are (472 – 627 m^2/g), and the total pore volume (0.31 – 0.55 cm^3/g). The pore diameter of all samples remained consistent at *ca.* 3.0 nm, except for the 45° tilt angle sample which had a larger pore diameter of 3.5 nm. Table 8.1 lists the properties of each sample at different tilt angles. The pore size distribution plot (Figure 8.2) agrees with the pore diameter data shown in Table 8.1. However, from the adsorption isotherm of all the materials prepared at different tilt angles (Figure 8.3), samples prepared at tilt angles of 0°, 15°, and 30° tilt angle showed a rather ill-defined hysteresis loop of Type IV adsorption isotherms, according to the IUPAC definitions.[5] The adsorption isotherm for these three samples closely resembles the Type I adsorption isotherm, which is typically exhibited in microporous solids. As hysteresis occurs when the mechanism of mesopore filling by capillary condensation varies from mesopore emptying, the appearance of hysteresis in the isotherm indicates the presence of mesopores in the final sample. The samples exhibit a H2 type hysteresis, which can be explained as a consequence of the interconnectivity of the pores,[6] which supports the presence of a high ratio of micropores in these samples.

Table 8.1. Effect of tilt angle on the structural parameters of mesoporous silica S-1.

Sample ID	S_{BET} ($m^2 g^{-1}$)	V_t ($cm^3 g^{-1}$)	Pore diameter (nm)	*d*-spacing (Å)	*a* (Å)	b (Å)
S-7000-0	504.6	0.38	3.2	78.1	90.2	57.8
S-7000-15	525.1	0.32	3.0	79.5	91.8	62.2
S-7000-30	472.2	0.31	3.1	81.0	93.5	62.2
S-7000-45	627.7	0.55	3.5	81.7	94.3	58.9
S-7000-60	533.0	0.37	2.9	87.4	100.9	71.8
S-5000-45	510.3	0.41	3.9	73.7	85.1	45.8

* XRD unit cell parameter *a* calculated based on $2d_{100}/\sqrt{3}$; b, wall thickness based on b = a – pore diameter; S_{BET}, BET specific surface area determined from linear plots (P/P_o from 0.1 to 0.4); V_t, pore volume at relative pressure of 0.995; and pore diameter determined from BJH adsorption.

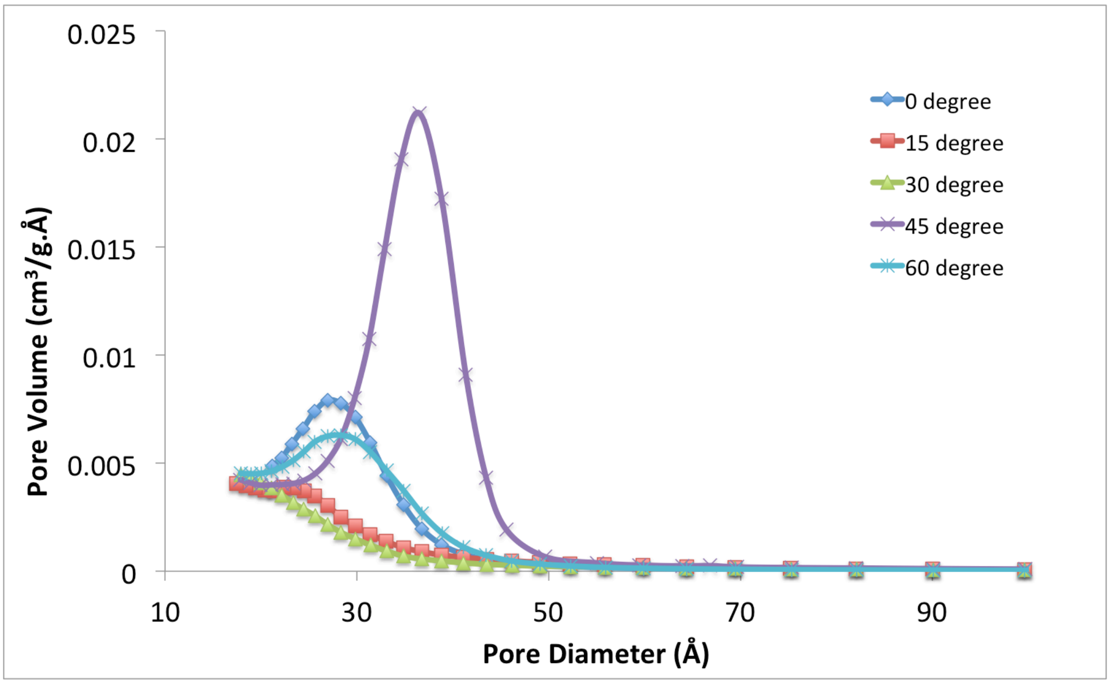

Figure 8.2. *Pore size distribution plot for different tilting angles, in preparing SBA-15 using the VFD under continuous flow, with the tube rotating at 7000 rpm.*

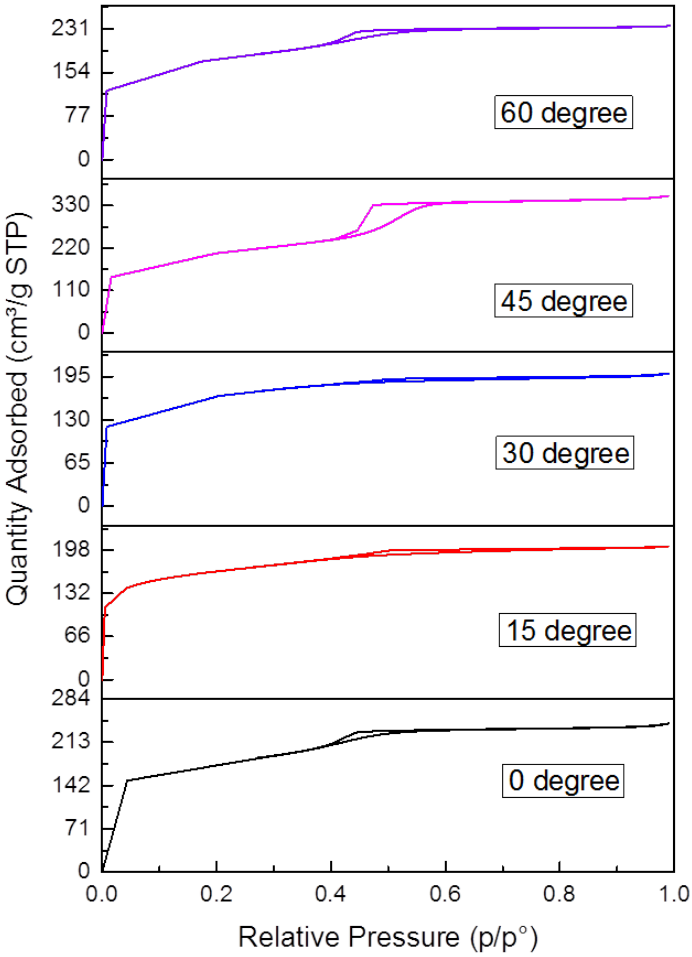

- *Linear isotherm plot of all samples: S-7000-60, S-7000-45, S-7000-30, S-7000-15, and S-7000-0 (from top to bottom), showing Type IV isotherms. The existence of hysteresis indicates the presence of mesopores in all samples. However, the weak hysteresis for samples S-7000-30, S-7000-15, and S-7000-0 may be due to the high proportion of micropores in these samples and thus, the isotherms closely resemble Type I isotherms which are typically exhibited by microporous solids.*

From the above results, the sample prepared at 45˚ tilt showed the best outcome in terms of surface area, pore volume and also pore diameter. Further studies were undertaken to investigate the effect of changing the rotational speed on morphology at a tilt angle of 45˚. This involved maintaining the same chemical processing, with only one variable being changed, namely the rotational speed from 7000 rpm down to 5000 rpm, based on the speculation that the VFD is under the Faraday wave at rotational speed of 500 rpm. This sample is denoted as S-5000-45. SEM images revealed a combination of horseshoe and donut-like morphologies, which are randomly agglomerated, Figure 8.4(a). The size of the donut-like structures ranges from 0.7 to 1.5 µm in diameter, Figure 8.4 (b–f), with a typical thickness of *ca.* 300 nm, Figure 8.4(b).

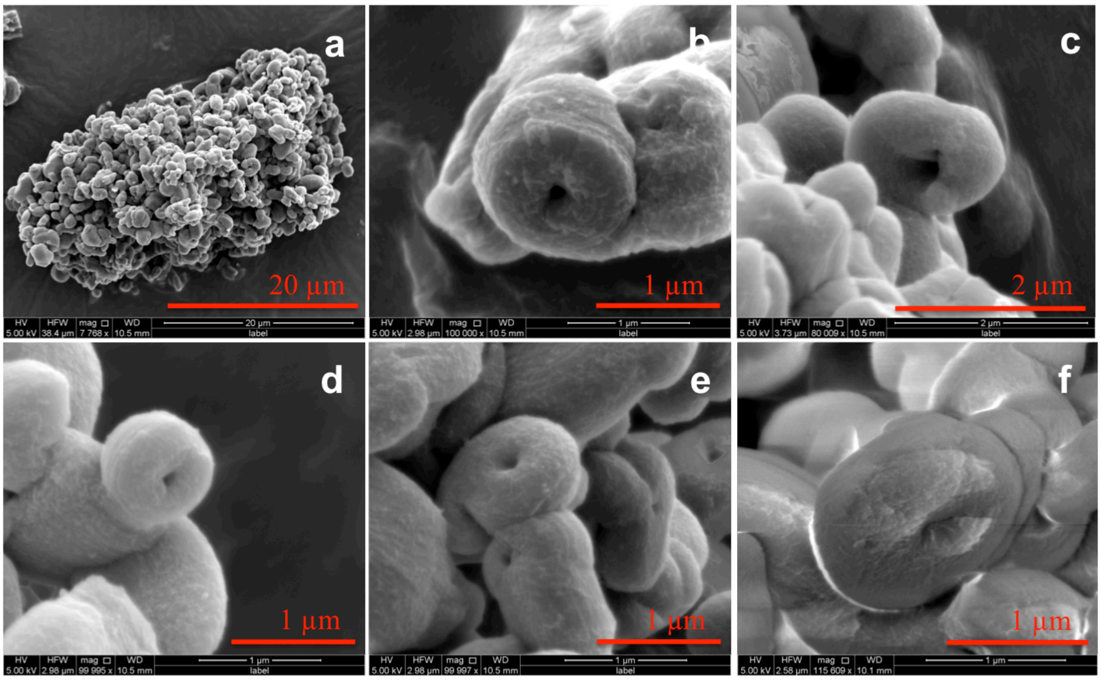

- *SEM images of sample S-5000-45 (5000 rpm rotational speed, 45 degree tilt angle, 1.0 mL/min flow rate) showing horseshoe and donuts-like structures (a), magnified images show donuts-like structures from different locations, (b) – (f).*

TEM images showed that mesoporous silica with well-ordered structures were formed, Figure 8.5(a). As noted from the SEM images, some structures feature elongated donut-like morphologies, which were reflected in the TEM images as well, Figure 8.5(b) and (c). TEM revealed the presence of essentially round donut-like structures in the samples, with SEM images establishing the thickness of the structures up to 300 nm. The TEM image is dark in contrast due to the thickness of the structures, and hence the ordered channels cannot be observed, Figure 8.5(d).

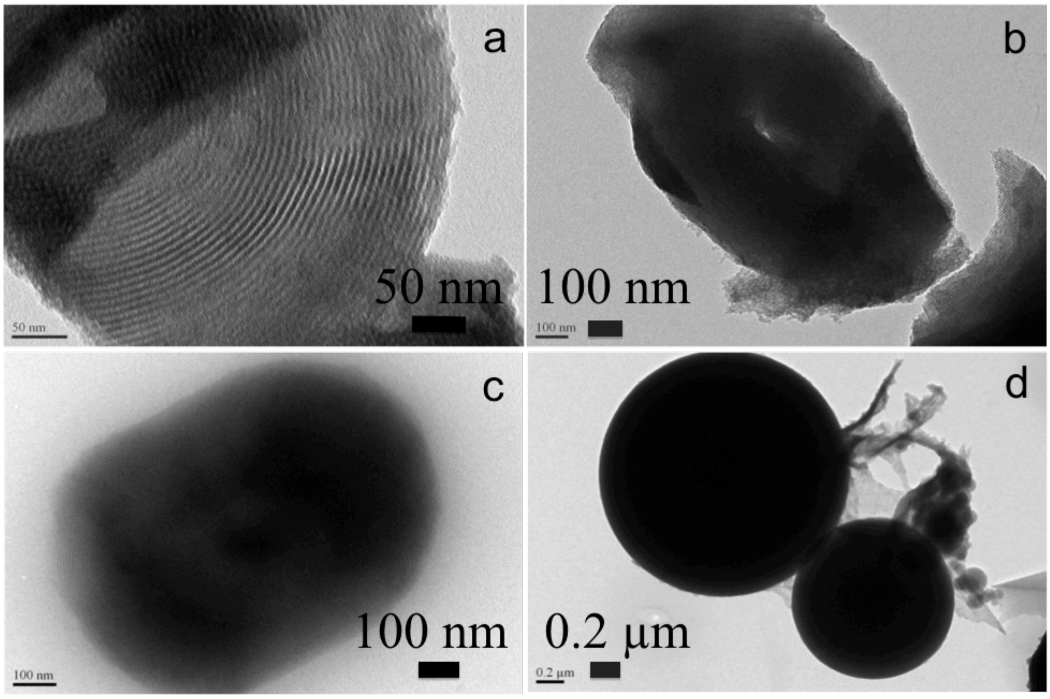

- *TEM images of sample S-5000-45 showing a well-ordered structure (a); elongated donut-like structure which matched SEM images, Figure 8.3(c), (b) and (c); the round donut-like structure which matched SEM image, Figure 8.3(b), (d-e), (d).*

The surface area determined using BET method is 510.3 m^2/g and the BJH pore volume is 0.41 cm^3/g. Compared to the S-7000-45 sample, the slight decrease in both surface area and pore volume is understandable as both ends of the structure have combined, leading to a decrease in available surface area for gas adsorption. The pore diameter determined using nitrogen adsorption desorption is 3.9 nm, which closely agrees with the estimated value of 4.1 nm from the TEM image, Figure 8.5(a).

From the XRD pattern (Figure 8.6), there are four well-resolved peaks. The unit cell parameter of the sample is 85.1 Å with *d*-spacings of 73.7 Å, 43.1 Å, 36.7 Å and 28.8 Å respectively. The calculated pore wall thickness is 4.6 nm, which matches the 4.5 nm thickness from the TEM images, Figure 8.5(a). The larger pore diameter compared to sample S-7000-45 is due to the lower effect of shear on the growth of micelles, which has been reported previously.[4] The S-5000-45 sample showed type IV adsorption isotherms with a H1 hysteresis loop as defined by IUPAC (Figure 8.7).[5]

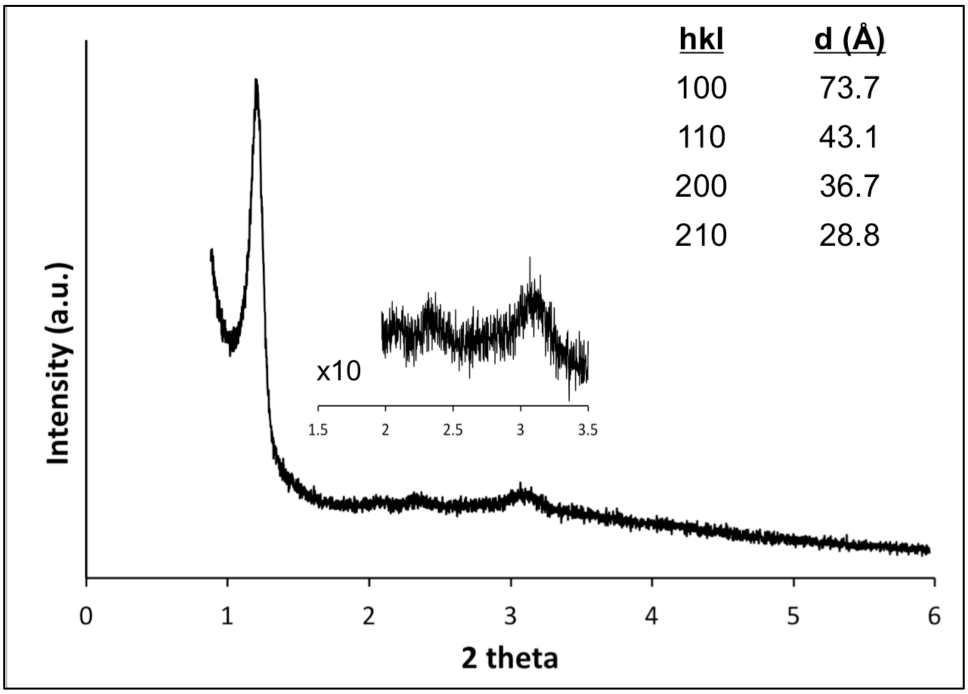

- *XRD for S-5000-45 showing peaks with d-spacings of 2D hexagonal structure.*

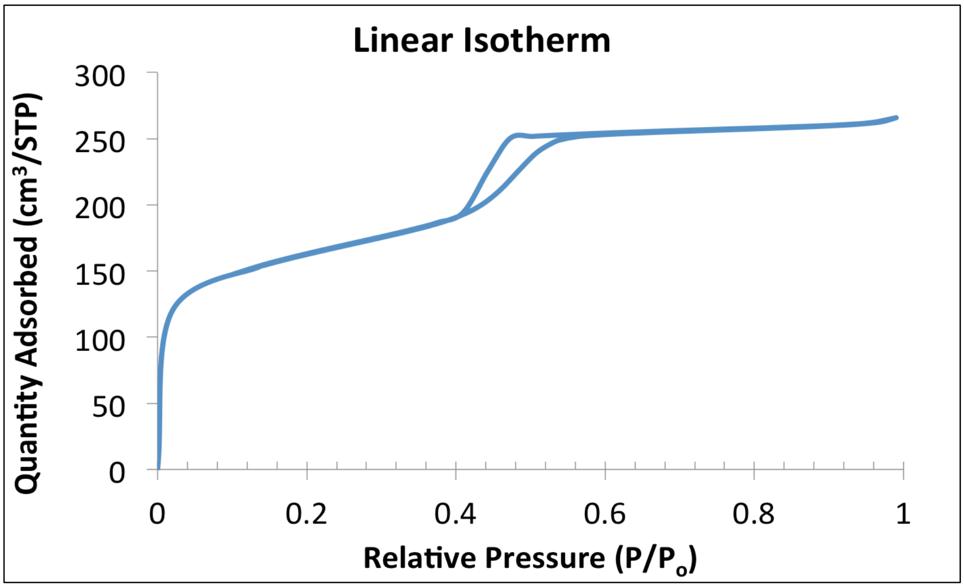

- *Linear isotherm of sample S-5000-45 shows a Type IV adsorption isotherm.*

8.5. Conclusion

The mechanism of the formation of donut-like morphologies of SBA-15 produced at a rotational speed of 5000 rpm and a tilt angle of 45˚ using the VFD is unclear at this point. A possible speculation is at these operating parameters, the medium is under a Faraday wave induced by vibrations, where the associated localised shear is able to control the growth of the curved surface, and curved pores.[7] Indeed, the size of the diameter of the donut-like structures may define half the wavelength of the Faraday wave. Other studies within the research group at Flinders University have established that vibrations within the VFD promote the formation of Faraday waves, which can be used to enhance chemical reactions.[7] A collaboration with Dr Stuart Dalziel, Applied Mathematics, University of Cambridge, is focussing on understanding the mechanism of formation of the Faraday waves in the VFD, along with a mathematical basis for the phenomena. More studies need to be undertaken in order to rationalize the mechanism of the donut-like structures formation.

8.6. Acknowledgement

Support from the Australian Research Council and the Adelaide Microscopy (The University of Adelaide), is gratefully acknowledged. Also, special thanks to Paul Eggers in performing the XRD analysis.

8.7. References

1. D. Zhao, J. Sun, Q. Li and G. D. Stucky, Morphological Control of Highly Ordered Mesoporous Silica SBA-15, *Chem. Mater.*, 2000, **12**, 275-279.

2. K. Kosuge, T. Sato, N. Kikukawa and M. Takemori, Morphological Control of Rod- and Fiberlike SBA-15 Type Mesoporous Silica Using Water-Soluble Sodium Silicate, *Chem. Mater.*, 2004, **16**, 899-905.

3. A. Katiyar, S. Yadav, P. G. Smirniotis and N. G. Pinto, Synthesis of ordered large pore SBA-15 spherical particles for adsorption of biomolecules, *J. Chromatogr. A*, 2006, **1122**, 13-20.

4. C. L. Tong, R. A. Boulos, C. Yu, K. S. Iyer and C. L. Raston, Continuous flow tuning of ordered mesoporous silica under ambient conditions, *RSC Adv.*, 2013, 18767-18770.

5. Z. Luan, E. M. Maes, P. A. W. van der Heide, D. Zhao, R. S. Czernuszewicz and L. Kevan, Incorporation of Titanium into Mesoporous Silica Molecular Sieve SBA-15, *Chem. Mater.*, 1999, **11**, 3680-3686.

6. S. Naumov, Hysteresis Phenomena in Mesoporous Materials,The University of Leipzig, 2009.

7. J. Britton, S. B. Dalziel and C. L. Raston, Continuous flow Fischer esterifications harnessing vibrational-coupled thin film fluidics, *RSC Adv.*, 2015, **5**, 1655-1660.

Chapter Nine

Vortex Fluidic Device in Palladium Catalysed Dehydration of Phenylboronic Acid

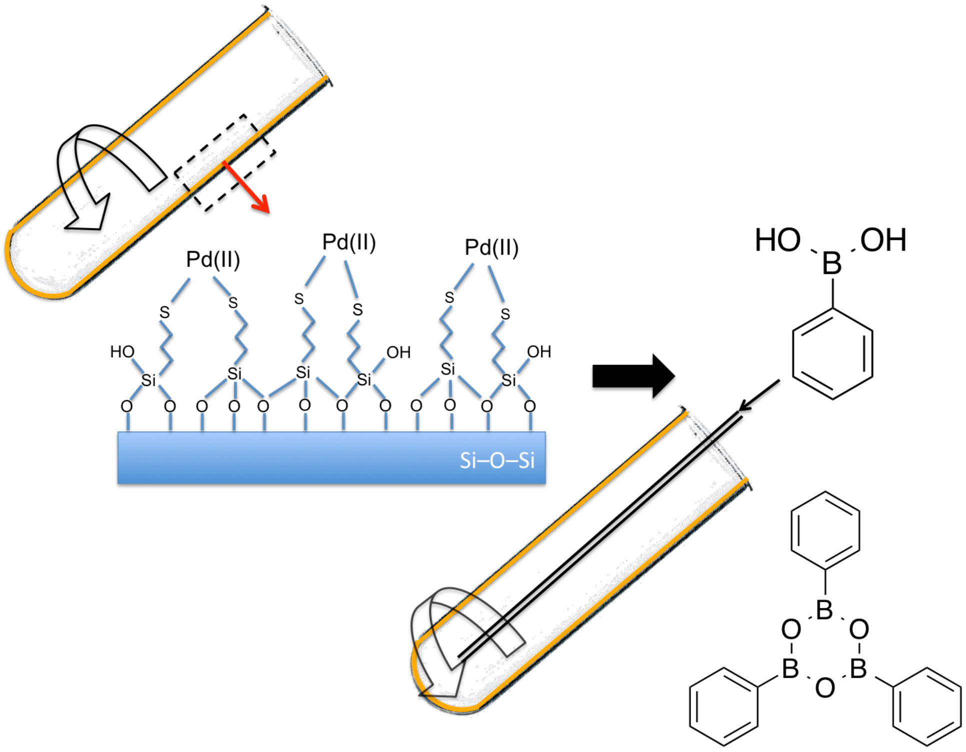

This chapter presents promising research outcomes, which while incomplete and unpublishable, it sets the scene for further studies in catalysis, and applications of the product. Indeed, it potentially forms the basis of a major research in its own right, beyond the scope of this PhD research program, and the results herein are more about supporting research for the dissertation.

Introduction

Boroxines (Figure 9.1(a)), also known as boroxins, or boronic acid anhydrides,[1] are six-membered cyclotrimeric anhydrides of organoboronic acids.[2] Organoboroxine chemistry has recently received much attention because the formation of the boroxine is a powerful tool for the construction of organized architectures.[3] In addition, boroxines have applications in diverse areas such as flame retardant materials,[4] dopants that enhance lithium ion transference in polymer electrolytes,[5-8] and reactants or as catalysts for organic transformations.[9, 10] In general, boroxines are formed by chemical dehydration or by ligand-facilitated trimerization of a boronic acid (Figure 9.1 (b)).[1, 2, 11, 12] No other synthetic methods appear to be available for this reaction. Regardless of the nature of the substituent (R), the formation of a six-membered ring prevails, which is attributed to the resonance stabilization of the conjugated six π-electron system.[12]

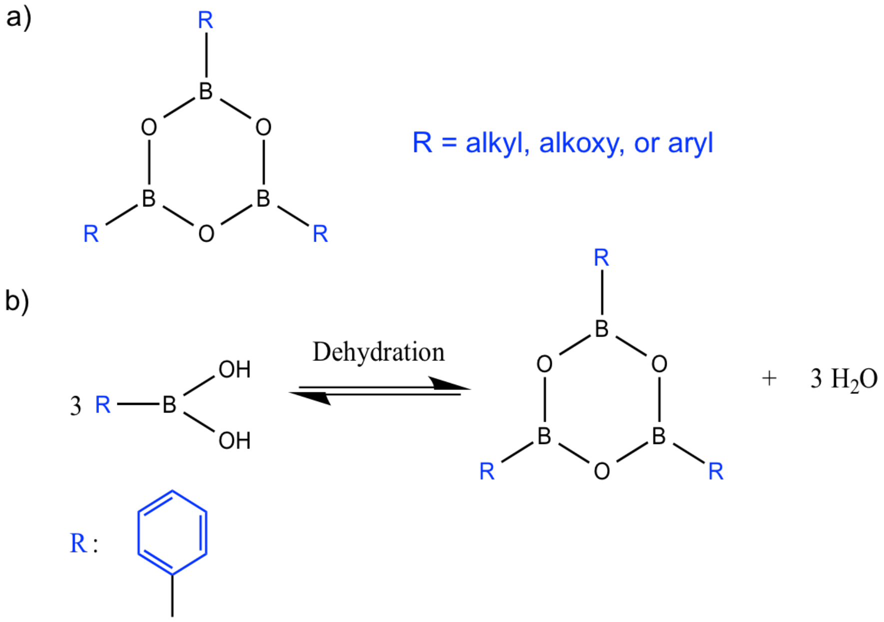

Figure 9.1. *(a) Generalized chemical structure of boroxine with the six-membered ring accessible for a variety of compounds with different substituents, R, and (b) standard chemical reaction of boroxines formation via dehydration process. Studies have been performed in mimicking the same reaction using unorthodox VFD processing, using phenylboronic acid as the substrate.*

Boroxines chemistry has recently come to the forefront with a landmark paper published in 2005 by the Yaghi group, describing the synthesis of the first crystalline boroxines based covalent organic framework (COF-1) (Scheme 2).[13] The synthesis of COF-1 involves heating the 1,4- benzenediboronic acid (BDBA) at 120 ˚C for 72 hours under a mesitylene-dioxane solution in a sealed Pyrex tube, with the final product having a rigid structure, exceptional thermal stabilities, low density, and large specific surface areas.[13]

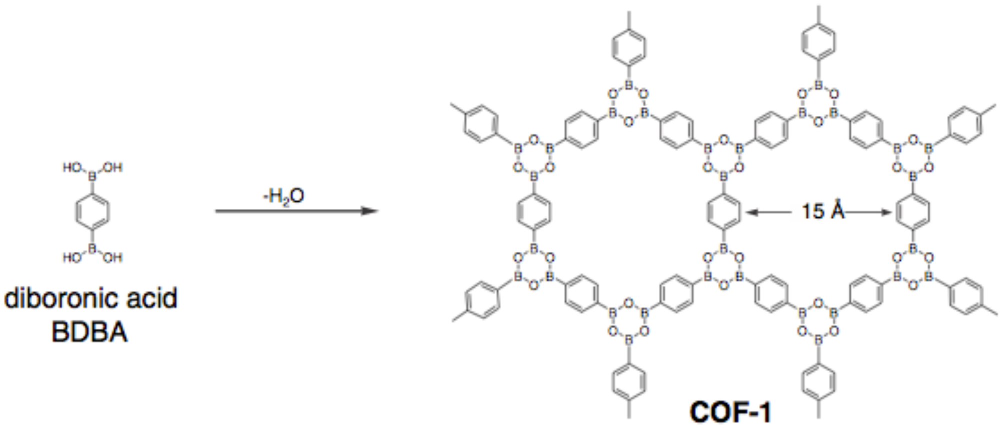

Scheme 1. *Condensation reaction of BDBA used to produce COF-1. Taken from Yaghi et al.*[13]

Herein, an unorthodox synthetic route for producing boroxines has been developed, which uses a vortex fluidic device (VFD), in a reaction catalyzed by Pd/SiO_2 in water under ambient conditions. This is without the need of a purification step for isolating the product. The process involved coating the borosilicate tube in the VFD with a film of silica containing the palladium catalyst. The preliminary catalytic studies was for phenylboronic acid as the substrate, with a systematic change in the operating parameters of the VFD, in particular rotational speed and flow rate. Initially the reaction was discovered in attempting to use the catalyst in the Suzuki reaction between bromobenzene and phenylboronic acid, in the presence of potassium carbonate using 1,4-dioxane as the solvent. However, ^1H NMR spectra revealed the formation of boroxines rather than the expected biphenyl compound. Detailed investigations then followed using phenylboronic acid with base, with the product analysed using gas chromatography-mass spectrometry (GC-MS).

9.1. Experimental

9.2.1. Coating of borosilicate tube with Pd/SiO_2 catalyst

This procedure is carried out using the VFD under confined mode. First, 1.0 mL of deionized water and 1.03 mL of TMOS, with a molar ratio of H_2O/Si of 8, were added into an 18.0 mm ID borosilicate tube with the end of the tube sealed with paraffin film. The VFD was sheared at 6000 rpm, which was selected on the basis that the finite volume of liquid added to the tube will not overflow in the 18.0 mm ID borosilicate tube during rotation. After 30 min, as the hydrolysis and condensation of silica was close to completion, the speed was increased to 6500 rpm and shearing continued for another 30 min to remove the solvent by evaporation. After 1 hour, a semi-dried thin film of silica layer was coated inside of the tube (Figure 9.2(a)).

Then 856.4 μL of 3-mercaptopropyltrimethoxysilane (MPTMS) was added into the tube and the mixture was further sheared at 6500 rpm. After 30 min, the rotational speed was increased to 7000 rpm and shearing continued till the tube was dry. By this stage, it was assumed the silanol thin film coating was partially functionalized with thiol groups (Figure 9.2(b)).

Lastly, 40 mg of palladium acetylacetonate [Pd(acac)$_2$] was dissolved in a combination of 2 mL of ethanol and 1 mL of toluene. This was added to the tube and sheared at 7000 rpm, to create a thin coating of palladium species on top of the thiol-functionalized surface (Figure 9.2(c)). The overflow at the top of the tube was collected and re-introduced into the system till a dry coating developed (Figure 9.3).

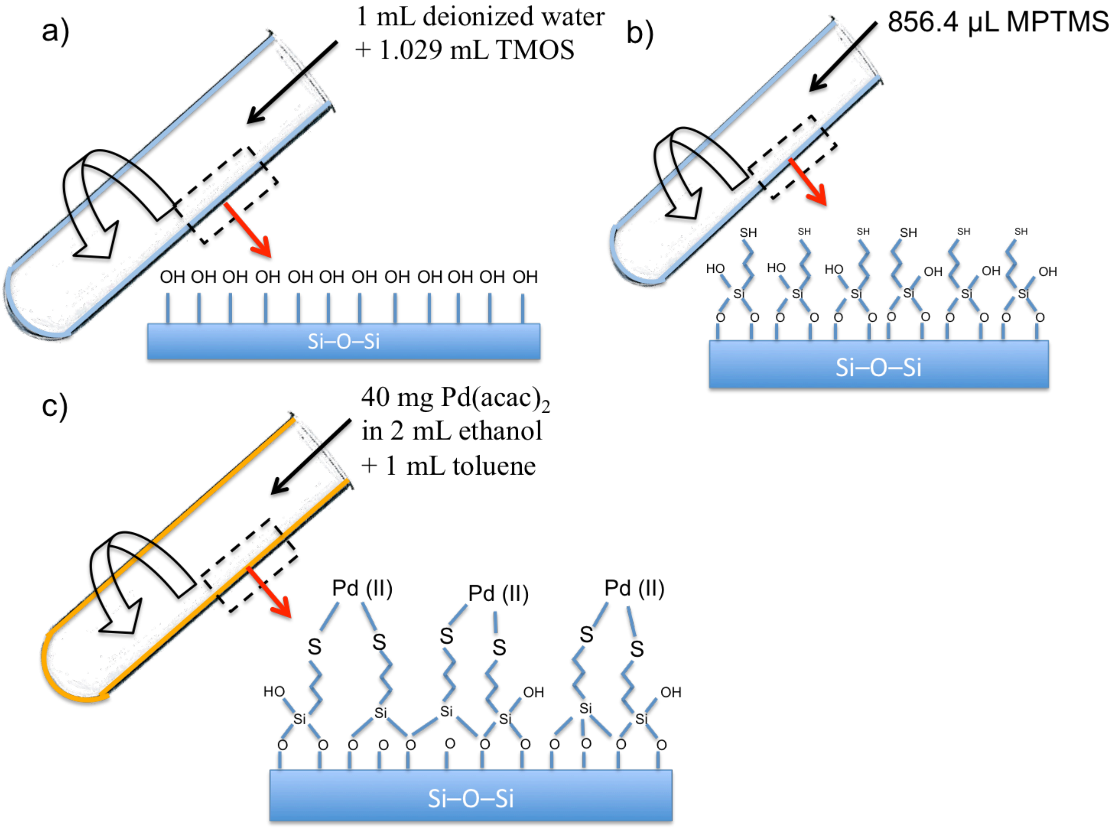

Figure 9.2. *Schematics of Pd/SiO$_2$ catalyst coating procedure using VFD under confined mode.*

Figure 9.3. *Photograph showing the appearance of the coated borosilicate tube with Pd/SiO_2 catalyst. The tilting angle of 45° is employed in this study was based on the results reported by Yasmin et al., where $\theta = 45°$ is the optimum tilt angle for the highest chemical reactivity.*[14]

9.2.2. *Catalytic performance test*

The dehydration process was carried out using the VFD under the continuous flow mode. The overall setup of the experiment is shown in Figure 9.4. Initially 2.4 mmol of phenylboronic acid ($PhB(OH)_2$) was dissolved in 20 mL of deionized water, and this solution was fed into the VFD using a syringe pump at a specific fixed flow rate. Optimization studies were done with the rotational speed and substrate injecting flow rate as variable parameters. The resultant products were collected, dried *in vacuo*, redispersed in chloroform ($CDCl_3$), and analysed using GC-MS.

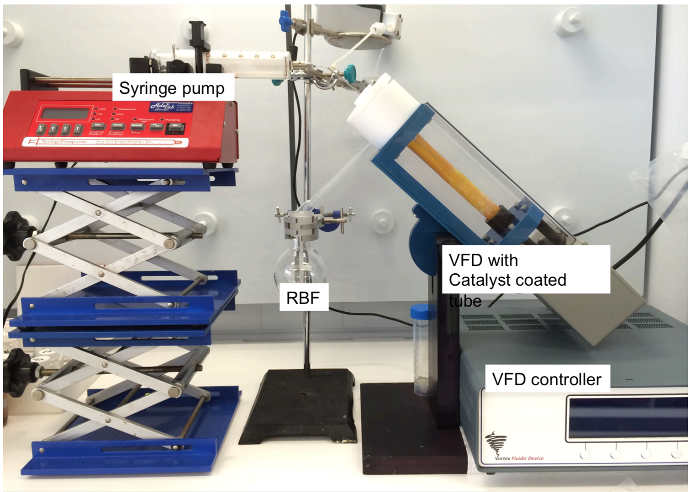

Figure 9.4. *Picture of the overall reaction setup, where the dissolved phenylboronic acid solution is introduced into VFD using a syringe pump at a controlled flow rate, with the product collected in a round bottom flask.*

9.2.3. Sample characterization

Nitrogen adsorption-desorption measurements were performed on a Micromeritics Tristar II® 3200. The samples were degassed at 473 K for 16 hours and measurements were taken at 77 K. The surface area was calculated based on Brunauer–Emmett–Teller (BET) method. The pore size distribution and pore volume were evaluated using the Barrett–Joyner–Halenda (BJH) method.

Elemental compositions of the samples were determined using X-ray photoelectron spectroscopy (XPS), conducted by Surface and Chemical Analysis Network (SCAN) at the University of Melbourne. XPS data was acquired using a VG ESCALAB220i-XL spectrometer equipped with a hemispherical analyzer. The incident radiation was monochromatic Al Kα X-rays (1486.6 eV) at 220 W (22 mA and 10 kV). Survey (wide) and high resolution (narrow) scans were taken at analyzer pass energies of 100 eV and 50 eV, respectively. Survey scans were carried out over the binding energy range from 0 – 1200 eV with 1.0 eV step size and 100 ms dwell time. Narrow high resolution scans were run over 30 eV binding energy range with 0.05 eV step size and 250 ms dwell time. Base pressure in the analysis chamber was below 7.0 x 10^{-9} mbar and during sample depth profile analysis it was 1.5 x 10^{-7} mbar. All data were processed using CasaXPS software and the energy calibration was referenced to the C 1s peak at 285.0 eV.

GC-MS was used to analyse the final product. GC-MS data was acquired using Agilent 7850/5875 GC-MS equipped with Zebron ZB-5ms, 60 m x 0.25 mm x 0.25 μm column. The initial analysis was set to start at 100 ˚C, held for 10 min, then increased at 20 ˚C/min increments up to 200 ˚C, each held for 10 min. This was followed by 10 ˚C/min increment up to 250 ˚C with each held for 30 min, and lastly using the same incremental step, rate the temperature was increased to 310 ˚C with 30 min holding time. The spectra were then compared with the database.

^{13}C Nuclear Magnetic Resonance (NMR) spectra were recorded with a Bruker UltraShield Avance III 400 MHz NMR Spectrometer running the TopSpin 2.1 software package. $CDCl_3$ was used as the solvent and as an internal lock. Chemical shifts (δ) were measured in ppm. ^{13}C NMR chemical shifts were referenced to δ77.16.

9.2. Results and discussion

The coating containing the catalyst was nonporous with very low specific surface area and pore volume, as derived from nitrogen adsorption-desorption analysis, which agrees with the proposed structure formation in Figure 9.2. Since the coating is generated under confined mode, the incorporation rate of palladium would be 100%. Thus, the content of palladium can be calculated based on the initial palladium precursor added and the final weight content of the coating on the borosilicate tube. The coating was carried out on 5 different borosilicate tubes, and the calculated palladium content was 1.22 ± 0.01 wt%.

The catalytic performance was carried out by dissolving 294 mg of $PhB(OH)_2$ in 20 mL of deionized water and sonicating the mixture for 5 min, which was then pumped into the VFD operating under various conditions. Firstly, a bench test was performed where the reagent was introduced into the VFD using a pristine borosilicate tube devoid of catalyst, at a flow rate of 0.5 mL/min, sheared at 6000 rpm. The product was collected and dried *in vacuo*, and then chloroform ($CHCl_3$) was added. However, the product was insoluble in $CHCl_3$ but readily redissolved in deionized water, suggesting no reaction occurred as expected in the absence of the catalyst. The same procedure and testing was performed using silica coated borosilicate tube in the absence of Pd and no reaction was also observed.

Next, the same experiment was performed under the same conditions, using a Pd/SiO_2 coated tube. The product was collected in a round bottom flask (RBF) and dried *in vacuo*. The product readily dissolved in $CHCl_3$ and from GC-MS spectra, it showed a well defined peak with a retention time of 30 min (Figure 9.5).

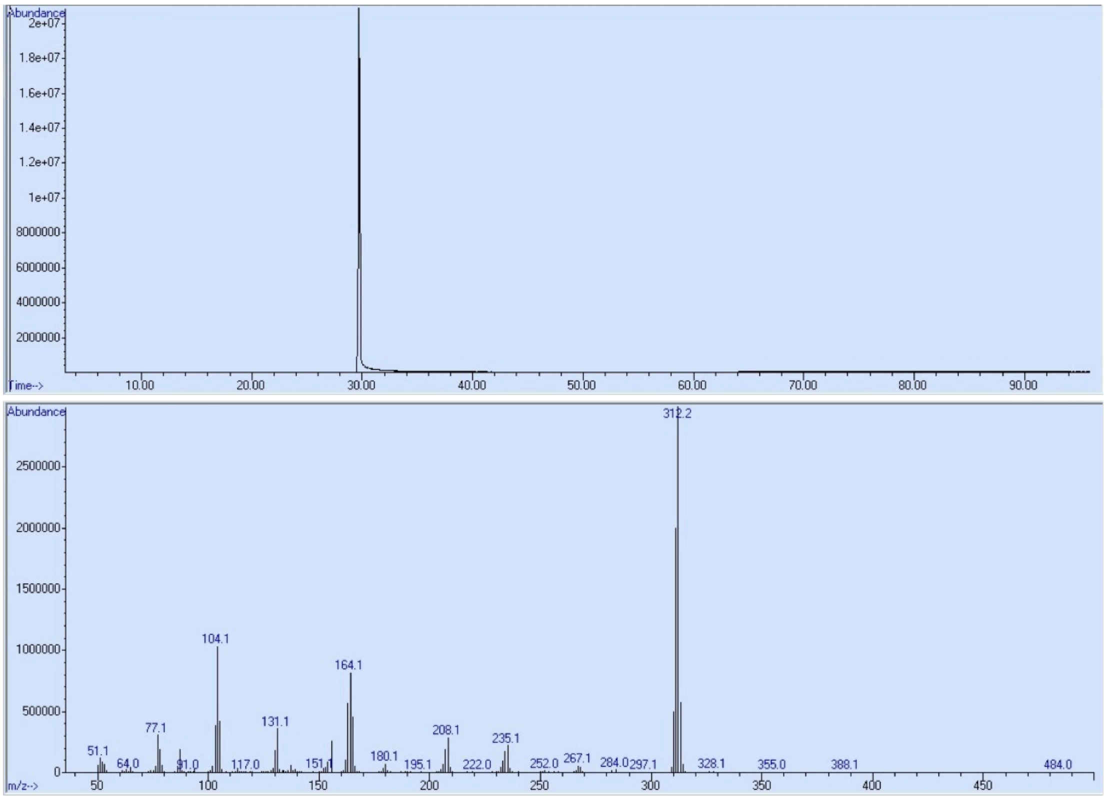

Figure 9.5. *GC-MS spectra of the product showing a single peak with a retention time of 30 min (top), and the mass spectrum of the corresponding peak (bottom), which is consistent with the presence of triphenylboroxine.*

The mass spectrum (m/z 312, m/z 104, m/z 164, m/z 208, and m/z 235) obtained has a 97% agreement with the peaks of triphenylboroxine in the database as shown in Figure 9.6 suggesting the material is mostly product in nature. To further verify it was indeed triphenyboroxine, general crystallographic data was collected on a Bruker X8 Apex II CCD Diffractometer with Mo-Kα radiation (λ = 0.71073 Å). Structure solutions and refinements were performed using the SHELX-97 software package, however, the data set was for a twinned crystal and the structure could not be solved. The unit parameters for the product was a = 10.6969 Å, b = 13.223 Å, c = 23.120 Å, α = 90 °, β =99.881°, and γ = 90°, which closely matches the unit cell parameters for triphenylboroxine, a = 10.715(2) Å, b = 13.652(3) Å, c = 11.703(2) Å, α = 90 °, β = 100.38(1)°, and γ = 90° (from the Cambridge Crystallographic Data Centre (CCDC)), with the exception of the c axis which is double in length. This is consistent with twinning for the present sample, and coupled with ^{13}C NMR spectra (Figure 9.7), the data suggests the product is most certainly triphenylboroxine. Optimizing the formation of this compound was then undertaken as the next step in the research.

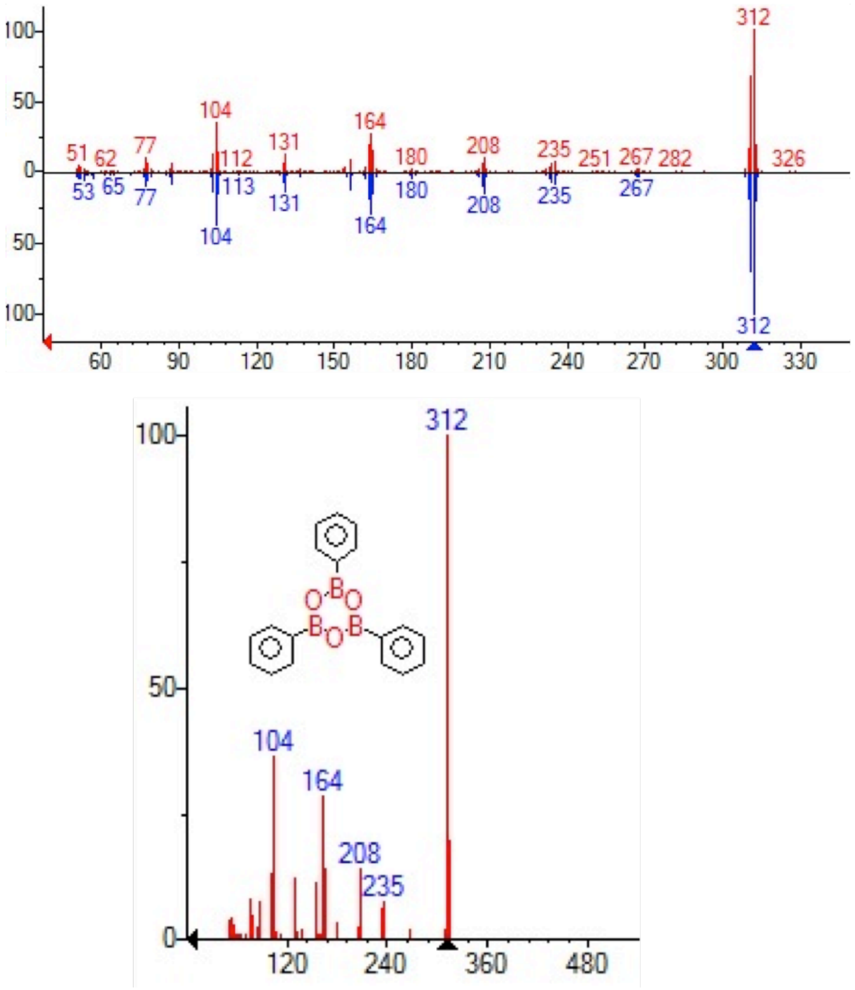

Figure 9.6. *Mass spectra (top) comparison of the product (red) with database compound (blue), (bottom) mass spectra of triphenylboroxine from the MS library.*[15]

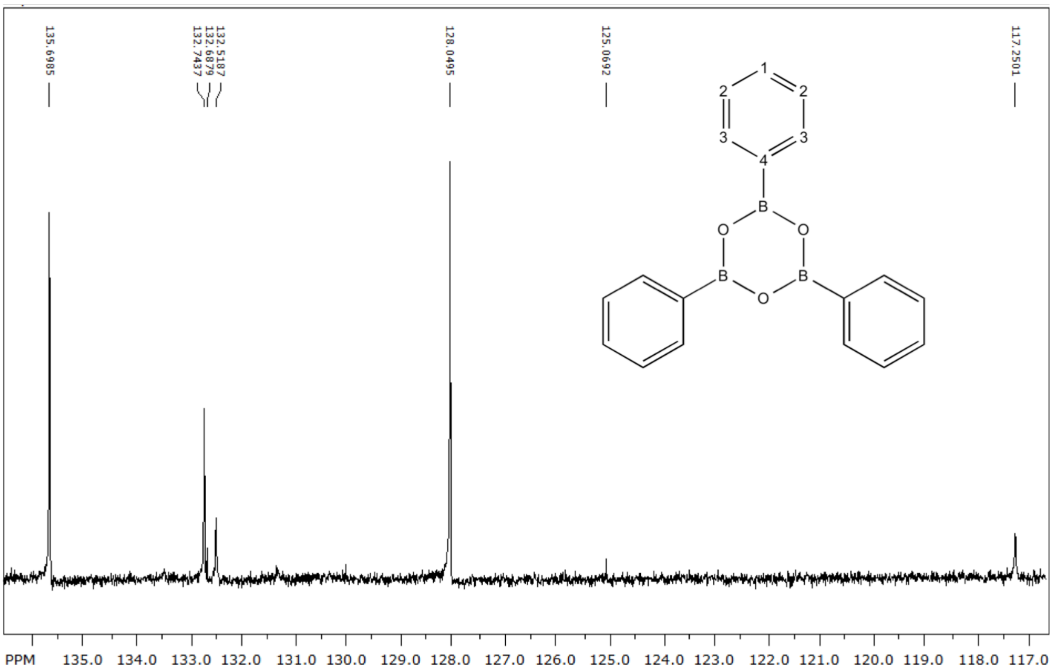

Figure 9.7. *^{13}C NMR spectrum in CDCl$_3$ of the product, ^{13}C NMR (100 MHz, CDCl$_3$): δ117.5(3), 128.0(1), 132.5(4), and 135.7(2), indicated the product is triphenylboroxines*

In optimizing the reaction using VFD processing, the flow rate was maintained at 0.5 mL/min and the percentage yield was compared at different rotational speeds (Table 9.1). The results showed the absence of by-products as demonstrated by a single peak from the GC-MS spectrum (Figure 9.5).

Table 9.1. Percentage yield of triphenylboroxines at different rotational speeds using VFD.

Rotational Speed (rpm)	Run 1 (% Yield)	Run 2 (% Yield)	Run 3 (% Yield)	Run 4 (% Yield)
5000	84.2	54.5	79.8	73
5500	65.1	77.3	78.6	73
6000	94.3	76.5	71.6	78.3
6500	82.0	81.9	79.7	77.5
7000	86.4	79.0	72.7	69.3

The percentage yield is calculated based on mass ratio of the substrate and product and the average percentage yield are plotted as a function of rotational speed (Figure 9.7).

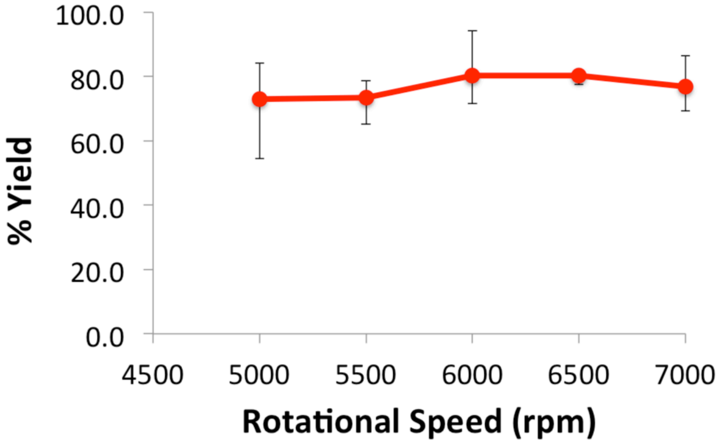

Figure 9.8. *Percentage yield variation as a function of rotational speed for the formation of triphenylboroxine catalysed by Pd/SiO_2 using a VFD. Data points are averaged of quadruplets runs.*

Based on Figure 9.8, 6500 rpm was chosen as the optimum rotational speed, in having the highest yield compared to the yields of other rotational speeds. A set of experiments was carried out to optimise the flow rate of the substrate into the VFD tube while maintaining the speed at 6500 rpm. The percentage yield was plotted as a function of flow rate in mL/min (Figure 9.9).

From both sets of data derived from varying the rotational speed and the flow rate respectively, it is concluded that the optimised conditions for this reaction are 6500 rpm and a flow rate of 0.75 mL/min, using a Pd/SiO_2 coated 18.0 mm ID borosilicate tube.

Since this is a continuous flow processing, the residence time was calculated to be 4.8 min. Importantly, the coated tube was repeatedly used for the reaction, up to 10 cycles, with the final reaction cycle carried out under the same experimental conditions as the first cycle, in ascertaining the catalyst performance. The percentage yield difference for the reaction between consecutive cycles was < 5%. This indicates minimal leaching of palladium, however, ICP-MS analysis is required to identify the actual amount of palladium leaching, if any, which will be undertaken in future studies.

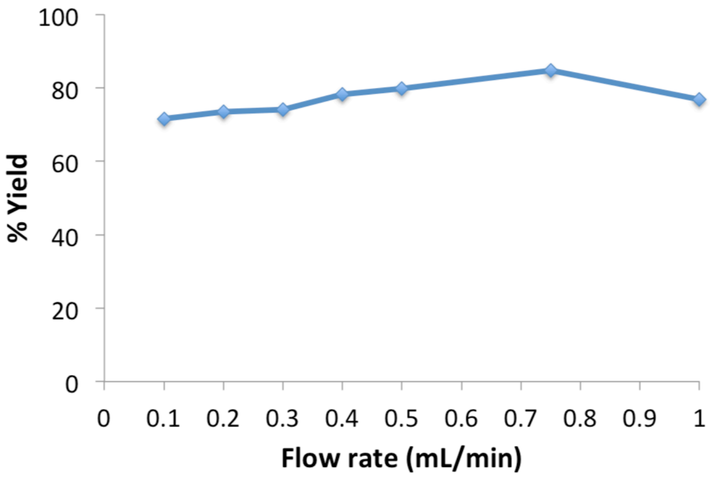

Figure 9.9. *Percentage yield of triphenylboroxines change as a function of flow rate (mL/min) under 6500 rpm rotational speed in the VFD.*

After repeatedly using the coated tube for 10 cycles, the coating was scrapped off and XPS experiments performed to ascertain the oxidation state of palladium after the final cycle. The peaks of $Pd3d_{5/2}$ and $Pd3d_{3/2}$ with binding energy at 337.8 eV and 343.0 eV (Figure 9.10) were observed by deconvolution, indicating an oxidation state of Pd(II).[16, 17]

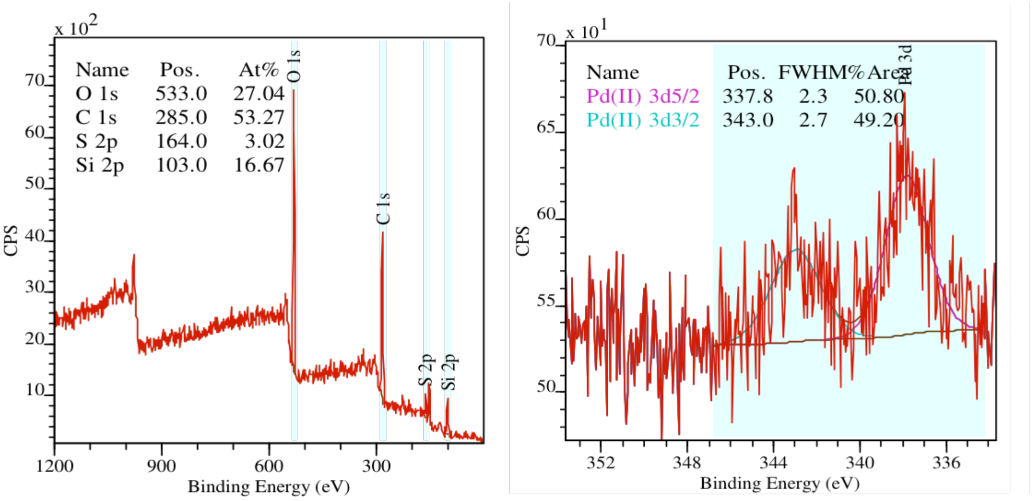

Figure 9.10. *XPS spectra of the catalyst after 10 consecutive runs with survey scan (left) and high resolution scans for Pd (right) under pass energy of 100 eV and 50 eV, respectively.*

9.3. Conclusion

This is an exciting finding, in establishing an unorthodox synthetic approach for gaining access to triphenylboroxines in aqueous medium, under ambient conditions, and continuous flow. However, the reaction mechanism needs to be investigated, along with extending the number of substrates such as 3-aminophenylboronic acid monohydrate, 4-bromophenylboronic acid, 4-chlorophenylboronic acid, 4-flurophenylboronic acid, 4-nitrophenylboronic acid, 2,3,4,6-tetrafluorophenylboronic acid, 4-pyridinylboronic acid, and 4-biphenylboronic acid. In addition, further studies are warranted in using the reaction to prepare COFs[13], with the exciting possibility of controlling the physical and chemical properties of the material for gas storage such as ammonia, carbon dioxide, hydrogen, and methane.[18]

9.4. Acknowledgement

This work is supported by the Australian Research Council and the Government of South Australia. Also, special thanks to Alex Duan for XPS analysis and Scott Dalgarno for single crystal analysis.

9.5. References

1. A. L. Korich and P. M. Iovine, Boroxine chemistry and applications: A perspective, *Dalton Trans.*, 2010, **39**, 1423-1431.

2. K. L. Bhat, G. D. Markham, J. D. Larkin and C. W. Bock, Thermodynamics of Boroxine Formation from the Aliphatic Boronic Acid Monomers R–B(OH)$_2$ (R = H, H$_3$C, H$_2$N, HO, and F): A Computational Investigation, *J. Phys. Chem. A.*, 2011, **115**, 7785-7793.

3. Y. Tokunaga, Boroxine chemistry: from fundamental studies to applications in supramolecular and synthetic organic chemistry, *Heterocycles*, 2013, **87**, 991-1021.

4. A. B. Morgan, J. L. Jurs and J. M. Tour, Aromatic boronic acid flame retardant polymer additives: synthesis and flame retardant testing, *Polym. Prepr. (Am. Chem. Soc., Div. Polym. Chem.)*, 1999, **40**, 553-554.

5. M. A. Mehta and T. Fujinami, Li+ Transference Number Enhancement in Polymer Electrolytes by Incorporation of Anion Trapping Boroxine Rings into the Polymer Host, *Chem. Lett.*, 1997, **26**, 915-916.

6. M. A. Mehta, T. Fujinami and T. Inoue, Boroxine ring containing polymer electrolytes, *J. Power Sources*, 1999, **81–82**, 724-728.

7. Y. Yang, T. Inoue, T. Fujinami and M. A. Mehta, Ionic conductivity and interfacial properties of polymer electrolytes based on PEO and boroxine ring polymer, *J. Appl. Polym. Sci.*, 2002, **84**, 17-21.

8. N. G. Nair, M. Blanco, W. West, F. C. Weise, S. Greenbaum and V. P. Reddy, Fluorinated Boroxin-Based Anion Receptors for Lithium Ion Batteries: Fluoride Anion Binding, Ab Initio Calculations, and Ionic Conductivity Studies, *J. Phys. Chem. A.*, 2009, **113**, 5918-5926.

9. L. Xu, B.-J. Li, Z.-H. Wu, X.-Y. Lu, B.-T. Guan, B.-Q. Wang, K.-Q. Zhao and Z.-J. Shi, Nickel-Catalyzed Efficient and Practical Suzuki−Miyaura Coupling of Alkenyl and Aryl Carbamates with Aryl Boroxines, *Org. Lett.*, 2010, **12**, 884-887.

10. Z. Z. Song, H. N. C. Wong and Y. Yang, in *Pure and Applied Chemistry*, 1996, vol. 68, p. 723.

11. P. Huang, Z. Jiang, G. Chen, Y. Zhu and Y. Sun, Dehydration of Phenylboronic Acid to Boroxine Catalyzed by Aun Nanoclusters with Atom Packing Core–Shell Structure, *J. Nanosci. Nanotechnol.*, 2013, **13**, 5088-5092.

12. K. Ishikawa, N. Kameta, M. Masuda, M. Asakawa and T. Shimizu, Boroxine Nanotubes: Moisture-Sensitive Morphological Transformation and Guest Release, *Adv. Funct. Mater.*, 2014, **24**, 603-609.

13. A. P. Côté, A. I. Benin, N. W. Ockwig, M. O'Keeffe, A. J. Matzger and O. M. Yaghi, Porous, Crystalline, Covalent Organic Frameworks, *Science*, 2005, **310**, 1166-1170.

14. L. Yasmin, X. Chen, K. A. Stubbs and C. L. Raston, Optimising a vortex fluidic device for controlling chemical reactivity and selectivity, *Sci. Rep.*, 2013, **3**, 2282.

15. R. H. Cragg, J. F. J. Todd and A. F. Weston, Mass spectra of organoboron compounds—II: The mass spectra of triphenylboroxine and its precursor phenylboronic acid, *Org. Mass Spectrom.*, 1972, **6**, 1077-1081.

16. D. Wang, S. Lu, P. J. Kulesza, C. M. Li, R. De Marco and S. P. Jiang, Enhanced oxygen reduction at Pd catalytic nanoparticles dispersed onto heteropolytungstate-assembled poly(diallyldimethylammonium)-functionalized carbonnanotubes, *PCCP*, 2011, **13**, 4400-4410.

17. Y. H. Ng, M. Wang, H. Han and C. L. L. Chai, Organic polymer composites as robust, non-covalent supports of metal salts, *Chem. Commun.*, 2009, 5530-5532.

18. S.-Y. Ding and W. Wang, Covalent organic frameworks (COFs): from design to applications, *Chem. Soc. Rev.*, 2013, **42**, 548-568.

Chapter Ten

Conclusions and Recommendations for Future Work

10.1. Conclusions

This dissertation focuses on the use of process intensification methodologies involving the vortex fluidic device for the preparation of mesoporous siliceous and composite siliceous materials. In particular it presents the results of studies in the preparation of ordered mesoporous silica, SBA-15, and silica hydrogel, under continuous flow conditions. The performance of the materials produced were tested in various applications such as catalysis, drug delivery, and adsorption for wastewater treatment, all showing reasonable performances.

The conventional hydrothermal processing of SBA-15 requires at least 48 hours, and overall it can take up to 72 hours to synthesize a batch of material.[1-4] In addition, the synthetic requirements such as temperature and pressure are critical to precisely control the course of the processing in order to tune the physicochemical properties of the material such as pore diameter, pore volume, and pore wall thickness. Comparatively, continuous processing developed herein using the VFD can generate an equivalent volume of a batch within 5 hours. In addition, this process is carried out under atmospheric pressure and room temperature. The process provides the ability for tuning the pore diameter by varying the shear rates within the device, with higher shear rates corresponding to smaller the pore sizes.

Conventional batch processing is ideal for small-scale production such as pharmaceutical industry. Batch processing has low production rates, and in scaling up, the requirements of a large feed tank/reactor vessel, a pump and high power consumption are inevitable in addition to the longer reaction time in reaching equilibrium. These factors significantly contribute to the relatively high production cost of a material. Also noteworthy is that batch processing is much labour intensive as it is rather challenging to fully automate the process, which in turns can result in more frequent intermittent shut down times between batches. SBA-15 produced via conventional hydrothermal processing is only available in the market place through two companies, ACS Chemical in United States and ZECASIN S.A. in Romania. The listing cost for ACS Chemical is USD 200 for 20 g of SBA-15 and for ZECASIN S.A it is EURO 130 for 10 g. This reverberates the aforementioned statement on how currently available batch processing of SBA-15 greatly affects the cost of the materials produced. The estimated cost of raw materials needed for the synthesis of 1.5 g of SBA-15 using VFD processing is less than $1, which could make it a competitive market product.

Batch processing using large containers can suffer from anisotropic mixing and uneven heat transfer, which is overcome using VFD processing through the intense micromixing within the ultra-thin film formed within the high speed rotating tube. The shear in the thin film in the VFD results in fast kinetics arising from an increase in collisions of reacting species otherwise reacting under diffusion control,[5] and thus there is a significant reduction in processing time. In addition, the synthesis of SBA-15 using the VFD is carried out under continuous flow mode with enhanced uniformity of the product.

Impregnation is a commonly used method to incorporate metal oxides into SBA-15 using batch processing, but this post-synthesis grafting method is time consuming and has limited control over the amount and location of the metal oxides loaded onto the support. The work presented in this dissertation establishes the ability of using the VFD to incorporate Pd nanoparticles *in situ* within the pore channel during the synthesis of SBA-15. This is under continuous flow conditions without additional processing time. The overall processing time of the Pd loaded SBA-15 is 5 hours prior to calcination and the palladium incorporation rate in the final product is 81%. This process clearly outperforms batch processing which requires 48 hours to prepare the SBA-15, and an additional 12 hours for post-synthesis Pd impregnation and drying.[6] The present method also has the advantage over the wetness impregnation in minimizing the use of solvent with the initial preparation of metal precursors in solution being unnecessary. Furthermore, it reduces the waste generation, in adhering to the first two principles of green chemistry, namely (1) it is better to prevent waste rather than treat it after its generation and (2) the best synthetic approach should maximize incorporation of all materials used into the final product.[7]

The advantages of using the VFD in the synthesis of SBA-15 include (i) the ability to vary a number of processing parameters to control pore diameter and pore wall thickness without changing the chemical processing, (ii) the ability to prepare the material without the need for heating (reducing utility cost), (iii) the ability to incorporate other material such as palladium *in situ*, and (iv) the intense micromixing and associated fast kinetics allows the incorporation of other metal centres, in place of silicon, with the sites expected to be uniformly dispersed in the solid, in building material with new properties, although this hasn't been tested, and is an important strategy to pursue in the future. Overall the method can be used to create designer mesoporous silica for niche market applications, including specific applications defined by customers.

Silicate glass produced via sol-gel processing has applications in optical devices due to its excellent transparency, and as delivery vehicles for drugs, and biologically active molecules in general. The *in situ* synthesis of silica gel incorporating different compounds, especially biological compound as a delivery vehicle is challenging, given that the components have to withstand the synthetic conditions of the sol gel processing, which involves the use of an acid or base catalyst and an organic solvent.

This dissertation establishes a more benign process for preparing silica xerogel without the need of an acid or base catalyst and an organic solvents, under ambient conditions, and yet achieving a rapid gelation time, as short as 3.5 hours, with appreciable surface area and pore volume. The process only involves using the silica precursor, TMOS and deionized water, which greatly expands the possible applications of using silica gel as a support, promoting the ability to mix in other materials, for example plasmonic particles (gold and silver), drug molecules and nanoparticles thereof, and heat sensitive macromolecules, such as proteins. Most importantly, VFD processing for sol-gel formation has significant reductions in the amount of waste generated.

Under confined mode of VFD processing, a finite volume of silica precursor and water, based on the targeted molar ratio, are added in forming a thin film silica coating in the tube. VFD processing has high heat and mass transfer, and excess water added for the hydrolysis of TMOS, along with the resulting methanol by-product eventually evaporate resulting in the formation of a dry thin coating of silica over the surface of the borosilicate tube. This method was developed to coat the borosilicate tube of VFD with composite siliceous material so that the VFD can be utilized for a wide range of catalytic reactions. The applications of the coated tubes are (i) the high shear flow in the VFD have potential for further controlling chemical reactivity and selectivity of organic reactions beyond diffusion control,[8-12] (ii) the stabilization of active compounds within the silica network provides high surface to volume ratios and thus, minimal amount of catalyst is required, (iii) the continuous flow operation is likely to result in uniformity of all reagents in contact with the catalyst, which can be controlled down to the molecular level, and (iv) the product collected is free of catalyst, and a separation process is not necessary, and (v) the catalyst remains coated and can be recycled, at least 10 times, without an appreciable loss of activity through leaching of the metal.

10.2. Recommendations for Future Work

10.2.1. Preparing hybrid silica materials for application as heavy metals scavenger

As revealed in Chapter 7, silica hydrogel can be synthesized directly in the VFD using only the silica precursor, TMOS and water. Based on this result, preliminary work has been carried out to investigate the feasibility of synthesizing the hybrid silica gel using the same method using a combination of two silica precursors, TMOS and 3-mercaptopropyltrimethoxysilane (MPTMS) with water (Figure 10.1).

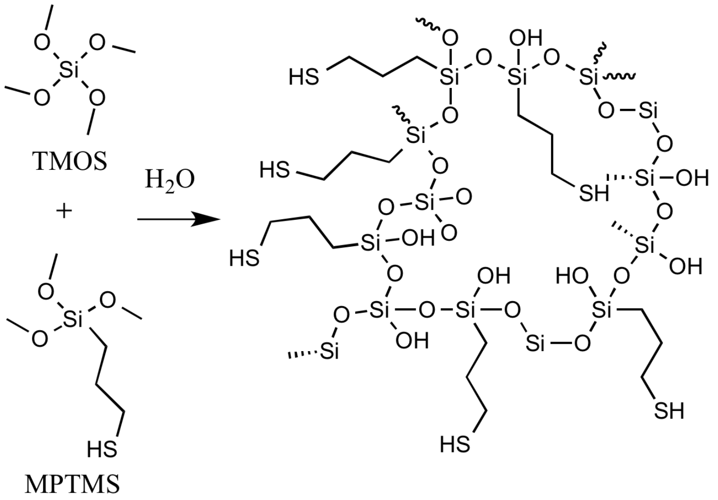

Figure 10.1. *Pseudomicellar aggregates form in the early stage of polycondensation of TMOS/MPTMS hybrid gels.*[13]

In this feasibility study, three separate feed jets were used to introduce water, TMOS, and MPTMS separately into the VFD with gel formation occurring after 1.5 hours (Figure 10.2).

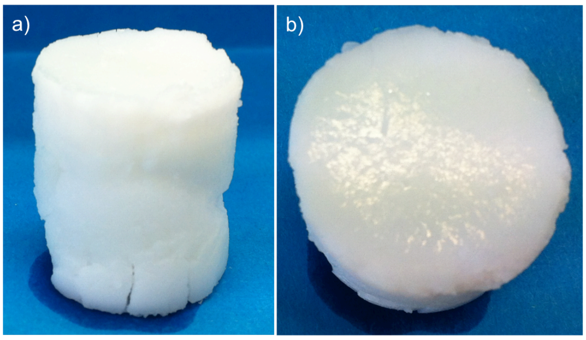

Figure 10.2. *Photo of hybrid silica gel formed by co-condesation of two silica precursors, TMOS and MPTMS after 1.5 hours; (a) front view and (b) top view.*

The preliminary result is encouraging, with characterization of the material required to understand the physicochemical properties of the material, with concomitant optimisation of the process. This of course would lead to new applications. Introducing MPTMS imparts thiol functionality into the material, which was established using ATR-FTIR (Figure 10.3). Potentially this material has application as a scavenging agent for heavy metals such as mercury, gold, silver, copper, nickel, zinc, and palladium. Performance tests would involve filling a column with the hybrid silica gel, then flowing a known concentration of a solution of metal ions through the column and analysing the concentration of the solution using ICP-MS after filtration.

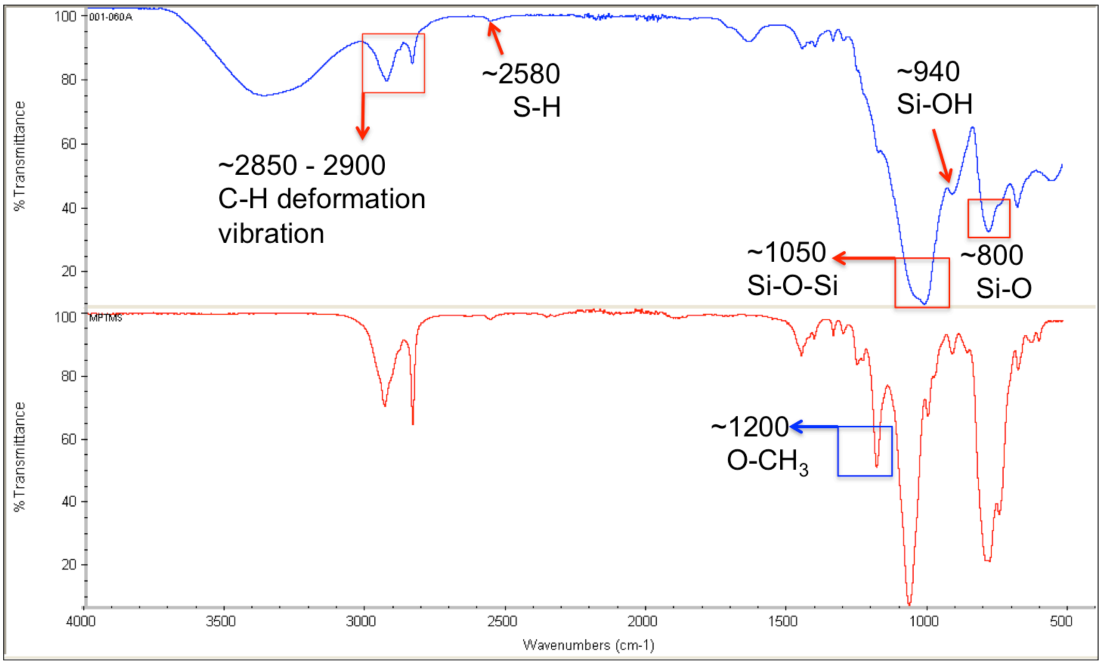

Figure 10.3. *ATR-FTIR spectra of hybrid silica gel (top) synthesized using VFD, and MPTMS (bottom) for comparison. From top spectra, the vibration bands at 800, 1050 and 1640 cm^{-1} correspond to vibration mode of SiO_2, and the peak disappearance at 1200 cm^{-1} indicates complete hydrolysis of the silica precursors. This hybrid silica gel has both the Si-OH and thiol moieties on the surface, from the peak showed at 940 and 2580 cm^{-1} respectively.*

10.2.2. Preparation of covalent organic framework (COF) using the VFD

As discussed in Chapter 9, the VFD is utilized as a reactor with the Pd/SiO_2 catalyst being coated on the borosilicate tube. Results show that this experimental setup affords triphenylboroxine under simple and benign conditions by dehydration of phenylboronic acid. Based on this new result, further studies are warranted to investigate the possibility of forming COF via similar condensation of benzene-1,4-diboronic acid (BDBA).

10.2.3. Immobilization of lipases within silica networks and their use in transesterification reactions

The use of lipases as catalyst results in products with high levels of purity, and it improves both selectivity and yield.[14] However, the high associated cost of lipases and difficulty in recycling them is a major obstacle hindering their use in industrial processes.[14] Britton and Raston have established the use of the VFD in generating high purity biodiesel from sunflower oil at room temperature. Using enzymes immobilized on a porous matrix, it was shown that the reaction kinetics of the reaction followed a Michaelis-Menten kinetic model, in which the overall production rate is determined by the rate of internal mass transfer.[15, 16] The thin film in a VFD which is effective in controlling chemical reactivity and selectivity of organic reactions beyond diffusion control,[9-11, 17] has potential to overcome the mass transfer limitation for enzymes. It is proposed that by immobilizing lipases within the silica network in a thin coating in the borosilicate tube, as discussed in Chapter 9, there is potential for high hydrolytic and transesterification activity of the biocatalyst. If the preliminary results are promising, further studies can proceed to include a wide range of feedstocks, or immobilization of different enzymes in avoiding the use of complex catalysts. The use of biocatalyst would minimize the pollutants generated, and the use of VFD processing could minimize the energy usage, combining both these approaches could thus be advantageous.

In summary, this dissertation has established a novel approach for preparing mesoporous silica, which can be used in many different applications, with a limited number of these being presented. Indeed, there is scope for this approach and associated applications to be taken up by industry. Nevertheless, there is still a major research undertaking required beyond the current studies, in advancing the science further, with new challenging and exciting discoveries awaiting, associated with using the complex fluid dynamics within the VFD.

10.3. References

1. D. Zhao, J. Feng, Q. Huo, N. Melosh, G. H. Fredrickson, B. F. Chmelka and G. D. Stucky, Triblock Copolymer Syntheses of Mesoporous Silica with Periodic 50 to 300 Angstrom Pores, *Science*, 1998, **279**, 548-552.

2. A. Galarneau, H. Cambon, F. Di Renzo, R. Ryoo, M. Choi and F. Fajula, Microporosity and connections between pores in SBA-15 mesostructured silicas as a function of the temperature of synthesis, *New J. Chem.*, 2003, **27**, 73-79.

3. Y. Wan and D. Zhao, On the Controllable Soft-Templating Approach to Mesoporous Silicates, *Chem. Rev.*, 2007, **107**, 2821-2860.

4. H. I. Lee, J. H. Kim, G. D. Stucky, Y. Shi, C. Pak and J. M. Kim, Morphology-selective synthesis of mesoporous SBA-15 particles over micrometer, submicrometer and nanometer scales, *J. Mater. Chem.*, 2010, **20**, 8483-8487.

5. J. Britton, S. B. Dalziel and C. L. Raston, Continuous flow Fischer esterifications harnessing vibrational-coupled thin film fluidics, *RSC Adv.*, 2015, **5**, 1655-1660.

6. S. Ganji, P. Bukya, V. Vakati, K. S. R. Rao and D. R. Burri, Highly efficient and expeditious PdO/SBA-15 catalysts for allylic oxidation of cyclohexene to cyclohexenone, *Catal. Sci. Technol.*, 2013, **3**, 409-414.

7. P. T. Anastas and J. C. Warner, Principles of green chemistry, *Green Chemistry: Theory and Practice*, 1998, 29-56.

8. L. Yasmin, T. Coyle, K. A. Stubbs and C. L. Raston, Stereospecific synthesis of resorcin[4]arenes and pyrogallol[4]arenes in dynamic thin films, *Chem. Comm.*, 2013, **49**, 10932-10934.

9. M. N. Gandy, C. L. Raston and K. A. Stubbs, Towards aryl C-N bond formation in dynamic thin films, *Org. Biomol. Chem.*, 2014, **12**, 4594-4597.

10. L. Yasmin, P. K. Eggers, B. W. Skelton, K. A. Stubbs and C. L. Raston, Thin film microfluidic synthesis of fluorescent highly substituted pyridines, *Green Chem.*, 2014, **16**, 3450-3453.

11. L. Yasmin, K. A. Stubbs and C. L. Raston, Vortex fluidic promoted Diels–Alder reactions in an aqueous medium, *Tetrahedron Lett.*, 2014, **55**, 2246-2248.

12. J. Britton and C. L. Raston, Continuous flow vortex fluidic production of biodiesel, *RSC Adv.*, 2014, **4**, 49850-49854.

13. M. Pagliaro, R. Ciriminna, M. Wong Chi Man and S. Campestrini, Better Chemistry through Ceramics: The Physical Bases of the Outstanding Chemistry of ORMOSIL, *J. Phy. Chem.*, 2006, **110**, 1976-1988.

14. C. Barão, L. de Paris, J. Dantas, M. Pereira, L. Filho, H. de Castro, G. Zanin, F. de Moraes and C. Soares, Characterization of Biocatalysts Prepared with Thermomyces lanuginosus Lipase and Different Silica Precursors, Dried using Aerogel and Xerogel Techniques, *Appl. Biochem. Biotechnol.*, 2014, **172**, 263-274.

15. T. M. Kuo and H. Gardner, *Lipid Biotechnology*, Taylor & Francis, 2002.

16. H.-S. Kim, M. D. Legoy and D. Thomas, Effect of mass transfer limitation on the enzyme reaction in reversed micelle, *Korean J. Chem. Eng.*, 1989, **6**, 35-40.

17. L. Yasmin, X. Chen, K. A. Stubbs and C. L. Raston, Optimising a vortex fluidic device for controlling chemical reactivity and selectivity, *Sci. Rep.*, 2013, **3**, 2282.